Nanostructures for sensors, electronics, energy and environment II

Edited by Nunzio Motta

Imprint

Nanostructures for sensors, electronics, energy and environment II

Nunzio Motta

Editorial

Address:
School of Chemistry, Physics and Mechanical Engineering and
Institute for Future Environments, Queensland University of
Technology, 2 George St., Brisbane 4001, Australia

Email:
Nunzio Motta - n.motta@qut.edu.au

This Thematic Series, "Nanostructures for sensors, electronics, energy and environment II", is a continuation of the series released three years ago and again presents articles in this highly dynamic field. The fields of nanoscale science and technology are rapidly emerging, with a focus on the design, fabrication, and characterization of functional objects. The existing energy crisis could be mediated not only by new and more efficient methods of collecting sunlight, but also by saving resources by applying developments in storage, electronics and sensors.

Conventional energy sources are limited and most of them generate greenhouse gases that pollute the environment. Photovoltaic technology is a potentially viable solution to produce clean energy; however, its production costs are still too high due to the materials and process techniques involved. Moreover, because the sun is an intermittent energy source, the further development of energy storage systems is necessary in order to allow photovoltaic-based power generation to be independent from the grid.

Carbon, one of the most abundant materials found on earth, is the key atomic species in the compounds responsible for green-house gas emission and pollution. However, it can also be used to offset these effects, acting as a valuable material for energy generation, storage, carbon sequestration [1] and sensing [2,3]. Carbon can be employed in one or more of its allotrope forms (e.g., graphene, carbon nanotubes, fullerene) in devices such as organic and inorganic solar cells and supercapacitors [4]. These devices can be produced in large quantities with inexpensive synthesis and process methods based on printing and roll-to-roll techniques, establishing the basis of a new green technology.

Currently, most of the research effort in the field is focused on the synthesis of large quantities of high quality carbon nanomaterials in order to use them for industrial scale production of energy generation and storage devices. However, other interesting advances are appearing and are covered in this series.

Graphene and graphene oxide exhibit interesting properties that can be exploited in room temperature gas sensing devices. The plasmonic effect, generated by the inclusion of metallic nanoparticles, can be used to overcome certain limitations of the carbon materials, especially in organic solar cells [5].

The optical properties of nanomaterials can also be exploited to produce new, powerful devices such as nanolasers, light emitting devices [6] and optical nanosensors.

Nanomaterials continue to intrigue researchers with new properties discovered every year in such low dimensional structures, generating an incredible field of basic and applied research with the expectation of achieving a better, cleaner and more sustainable world.

Nunzio Motta

Brisbane, September 2015

References

1. de Silva, S. W.; Du, A.; Senadeera, W.; Gu, Y. *Beilstein J. Nanotechnol.* **2014,** *5,* 413–418. doi:10.3762/bjnano.5.49
2. Piloto, C.; Notarianni, M.; Shafiei, M.; Taran, E.; Galpaya, D.; Yan, C.; Motta, N. *Beilstein J. Nanotechnol.* **2014,** *5,* 1073–1081. doi:10.3762/bjnano.5.120
3. Li, D.; Pang, Z.; Chen, X.; Luo, L.; Cai, Y.; Wei, Q. *Beilstein J. Nanotechnol.* **2014,** *5,* 346–354. doi:10.3762/bjnano.5.39
4. Liu, J.; Mirri, F.; Notarianni, M.; Pasquali, M.; Motta, N. *J. Power Sources* **2015,** *274,* 823–830. doi:10.1016/j.jpowsour.2014.10.104
5. Notarianni, M.; Vernon, K.; Chou, A.; Liu, J.; Motta, N. *Adv. Device Mater.* **2015,** *1,* 27–32. doi:10.1179/2055031614Y.0000000006
6. Liu, J.; Notarianni, M.; Rintoul, L.; Motta, N. *Beilstein J. Nanotechnol.* **2014,** *5,* 485–493. doi:10.3762/bjnano.5.56

License and Terms

Interaction of iron phthalocyanine with the graphene/Ni(111) system

Lorenzo Massimi[*1], Simone Lisi[1], Daniela Pacilè[2], Carlo Mariani[1]
and Maria Grazia Betti[1]

Abstract

Graphene grown on crystalline metal surfaces is a good candidate to act as a buffer layer between the metal and organic molecules that are deposited on top, because it offers the possibility to control the interaction between the substrate and the molecules. High-resolution angular-resolved ultraviolet photo electron spectroscopy (ARPES) is used to determine the interaction states of iron phthalocyanine molecules that are adsorbed onto graphene on Ni(111). The iron phthalocyanine deposition induces a quenching of the Ni d surface minority band and the appearance of an interface state on graphene/Ni(111). The results have been compared to the deposition of iron phthalocyanine on graphene/Ir(111), for which a higher decoupling of the organic molecule from the underlying metal is exerted by the graphene buffer layer.

Introduction

The interest in the preparation of ordered layers of organic molecules is rapidly growing, because of the possibility to realize advanced electronic- and spin-based devices [1-3]. Transition-metal phthalocyanines (MPcs) are planar molecules that consist of an organic cage formed by four pyrrole and benzene rings with a central metal ion [4]. They represent a class of molecules with potentially large applications thanks to their easily tunable electronic and magnetic properties, which are basically associated with the electronic configuration of the central metal atom [5]. When deposited on surfaces, their inter-

action may be driven by dipolar forces mainly related to the organic cage and by a stronger interaction that is associated with the central metal atom. As an example, the adhesion of iron phthalocyanine (FePc) and cobalt phthalocyanine (CoPc) on a Au substrate is mainly due to the presence of unfilled, out-of-plane oriented, d states that interact with the underlying gold states [6,7].

The magnetic and electronic properties of the adsorbed molecules may be strongly influenced by the interface and can be

potentially tuned by using an appropriate buffer layer. Graphene (Gr), thanks to its unique electronic properties [8] and to the quite easy experimental preparation on many metal substrates [9], is a good candidate to tune the MPc–metal interface. Moreover, the self-assembling capabilities of organometallic molecules offer the possibility to form ordered networks of metal atoms trapped in an organic cage, which is a suitable configuration for the realization of spin-based qubits [10]. Interesting and exemplary cases are represented by MPcs adsorbed on graphene grown on Ni(111) and Ir(111) surfaces. In fact, graphene on Ni(111) and on Ir(111) represents two opposite sides of the graphene–metal interaction: a strong interaction with a strong modification of the free-standing graphene band structure is observed on Ni [11], while a low interaction with an almost unperturbed Dirac cone is present if graphene is grown on Ir [12,13]. Recently it has been shown that graphene acts as a buffer layer that decouples the FePc molecules from Ir(111) and prevents an Ir–FePc interaction [13]. On the other hand, for Gr/Ni(111) a FePc–Ni interaction has been suggested [14-16] despite the presence of the graphene sheet, as it was already observed for CoPc on Gr/Ni(111) [17]. We present a valence band UV photoemission study of the FePc adsorption on Gr/Ni, which brings to light a direct evidence of an interaction between the FePc molecule and the Ni substrate.

Experimental

Experiments were performed in situ in ultra-high-vacuum (UHV) chambers with base pressures in the low 10^{-10} mbar range at the LOTUS laboratory of the Università La Sapienza (Roma). The Ni(111) single crystal was cleaned by several sputtering–annealing cycles (1 keV Ar^+ for 30 min, 600 °C for 10 min). Graphene was obtained by exposing the sample, which was kept slightly below 600 °C to 6000 L of ethylene (1 L = 10^{-6} torr·s). The formation of graphene on the Ni(111) surface is complicated by the segregation of carbon from the bulk, because of the high solubility of carbon in Ni [18-20]. The Ir(111) single crystal was cleaned by several sputtering–annealing cycles (2 keV Ar^+ for 30 min, 1200 °C for 60 s). The preparation of graphene was done by several 120-seconds long exposures to ethylene while flash-heating the sample up to 1100 °C.

The deposition of FePc was carried out by using a custom-made quartz crucible and the molecular deposition was controlled by using a quartz microbalance. One single-layer (SL) is defined as the molecular density of flat molecules fully covering the graphene layer, and it corresponds to a nominal thickness of about 3.4 Å.

Low energy electron diffraction (LEED) was used to check the symmetry of both clean and Gr-covered surfaces. LEED was performed in the energy range of the primary beam of 90–140 eV. High-resolution angular-resolved photoelectron spectroscopy data was carried out by using a SCIENTA SES-200 analyzer with an angular acceptance of ±8° and a resolution of 16 meV. All spectra have been taken along the ΓK direction. The UV radiation, HeIα (21.218 eV) and HeIIα (40.814 eV), was provided by a SCIENTA VUV-5050 monochromatic source.

Results and Discussion

The ARPES band structure of the Gr/Ni(111) and Gr/Ir(111) systems along the ΓK direction of the two-dimensional (2D) Brillouin Zone (BZ) is presented in Figure 1. The corresponding LEED patterns are shown in the insets: for Gr/Ni(111) the graphene lattice is well aligned with the substrate and no corrugation is present, with a resulting (1 × 1) symmetry [21,22], while in Gr/Ir(111) the lattice mismatch, reflected in the additional moiré pattern, introduces a large-scale regular corrugation [23].

The presence of a distinct single π band for both Gr sheets (on Ni and on Ir) reveals the single-layer nature of graphene. For Gr/Ir(111), the Dirac point is localized on a projected bulk band gap and the graphene π band looks very similar to the band of free-standing graphene, the linear dispersion of the π band is preserved close to the K point with only a slight p-doping, which is in agreement with the literature [12,13]. The very tiny doping has also been interpreted as slight hybridization between the Gr-π states and the underlying Ir d bands, which leads to a gap with a width of a few tens of meV [24]. The small size of the gap can be explained by the small difference among the two sublattices, due to the low interaction with the substrate. The band structure of the Gr/Ni(111) system appears to be dominated by the strong projected Ni d bands very close to the Fermi level. Furthermore, the Gr-π band is shifted by 2.5 eV towards higher binding energies as compared to Gr/Ir, and no linear dispersion is observed at the K point, which is in agreement with previous results [11]. Carbon atoms adsorb on two different sites on Ni(111), on top of Ni surface atoms and in fcc-hollow sites of the underlying Ni mesh [21,25]. As a consequence of the different adsorption sites and of the strong interaction, a large asymmetry among the two carbon sublattices is introduced, which induces a band-gap opening [11]. Recent experiments performed along the BZ direction perpendicular to ΓK confirm the strong shift of the Dirac point, while the gap opening is attributed to a strong hybridization of the Gr-$π^*$ states with the Ni d bands [22].

The photoemission data in the low binding energy region for the iron phthalocyanine molecules deposited on the Gr/Ni surface, and on Gr/Ir for comparison, as a function of the thickness of
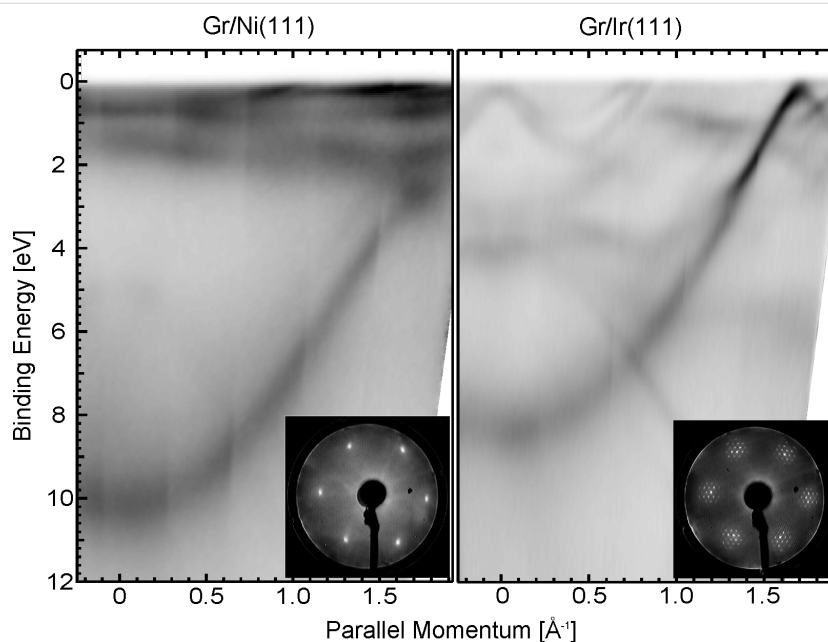
Figure 1: Experimental ARPES band structure for graphene grown on Ni(111) (left) and on Ir(111) (right), taken with 40.814 eV photon energy along the ΓK direction of the 2D BZ. Insets: corresponding LEED patterns taken on Gr/Ni and Gr/Ir, at primary beam energies of 90 eV and 140 eV, respectively. LEED patterns have been obtained by using a different geometry.

the FePc layer is shown in Figure 2. The FePc adsorption on Gr/Ni(111) produces a general reduction of the prevalent d band spectral density of states and a new feature emerges close to the

Fermi level (at about 0.3 eV BE). Its intensity grows upon increasing the molecular coverage up to completion of the first SL, and starts to decrease at higher thicknesses, a behaviour
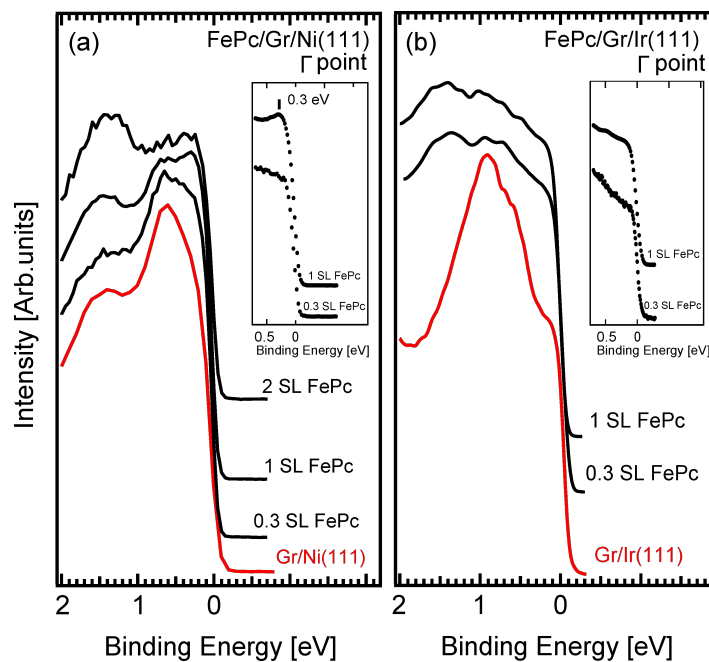
Figure 2: Valence band photoemission data for the adsorption of FePc onto Gr/Ni (a) and onto Gr/Ir (b), as a function of the thickness of FePc layer. Data of clean graphene (red lines) and of the FePc/Gr systems (black lines). Data taken with 40.814 eV photon energy (HeIIα) and around normal emission (±4° angular integration around the Γ point). The data was normalized to the intensity at the Fermi edge and vertically stacked for clarity. In the insets, a zoom around the Fermi level for a coverage of 0.3 and 1 SL of FePc is given.

typical of an interface state. This interface state comes from charge transfer from the Gr/Ni substrate to partially filled d orbitals of the central metal ion [15]. On the other hand, the deposition of FePc on the Gr/Ir surface causes only a general attenuation of the Gr/Ir spectral density, while no new state emerges, which confirms previous results [13]. The presence of an interface state for FePc adsorbed on Gr/Ni but not for FePc adsorbed on Gr/Ir can be very likely related to an interaction of the FePc molecules with the substrate underlying the graphene layer. In fact, the shorter distance of Gr–Ni compared to Gr–Ir [25,26] may induce a larger overlapping of the partially empty out-of-plane d like orbitals of FePc with the hybridized d–π states of Ni–Gr.

In order to better understand the nature of the interaction, we also analyze data at the K point of the BZ, as shown in Figure 3. At the clean Ni(111) surface (Figure 3, bottom spectrum), we observe two main peaks close to the Fermi level, at 0.08 eV and 0.30 eV BE, respectively. As it is well known, the first one is attributed to d electron minority spin with sp-contribution and the second one to the majority spin [27]. The formation of graphene onto Ni(111) induces an increase in intensity accompanied by a very slight shift (−0.02 eV) of the first feature, while the d majority band at 0.3 eV BE remains unchanged and shows only a slight intensity reduction. The observed change of the minority d band originates from a hybridization with the

graphene π bands [25]. The increased intensity of the lowest BE peak is emphasized by the high excitation cross-section for the C π-bands with respect to the Ni d-like states [28], which brings to light the hybrid nature of this first peak. Upon adsorption of a tiny quantity of FePc, this hybrid state is strongly reduced in intensity, while the d majority band appears to be basically unaffected. The strong reduction in intensity of the π–d hybrid state suggests a molecule interaction with the Gr/Ni(111) interface, which validates the suggestion of a molecule–substrate interaction that is mediated by graphene. This is in agreement with recent investigations, in which electron energy loss and photoemission spectroscopy were used [14,15].

Conclusion

When used as a buffer layer between an organic molecule and a metal surface, graphene plays a different role in the molecule–metal interaction that depends on the interaction of graphene with the metal substrate. Graphene on Ni(111) reveals a strong interaction with the substrate and strong alteration of the ideal graphene π band. After deposition of small amounts of FePc molecules, by means of high-resolution UV photoemission we give direct experimental evidence of an interaction of the molecule with Ni through graphene, as shown by the emerging of an interface state at about 0.3 eV binding energy in normal emission and by the quenching of the Gr–Ni π−d hybrid state at the K point of the BZ.

Acknowledgements

References

1. Bogani, L.; Wernsdorfer, W. *Nat. Mater.* **2008,** *7,* 179–186. doi:10.1038/nmat2133
2. Coe, S.; Woo, W.-K.; Bawendi, M.; Bulović, V. *Nature* **2002,** *420,* 800–803. doi:10.1038/nature01217
3. Bao, Z.; Lovinger, A. J.; Dodabalapur, A. *Appl. Phys. Lett.* **1996,** *69,* 3066–3068. doi:10.1063/1.116841
4. Forrest, S. R. *Chem. Rev.* **1997,** *97,* 1793–1896. doi:10.1021/cr941014o
5. Liao, M.-S.; Scheiner, S. *J. Chem. Phys.* **2001,** *114,* 9780. doi:10.1063/1.1367374
6. Gargiani, P.; Angelucci, M.; Mariani, C.; Betti, M. G. *Phys. Rev. B* **2010,** *81,* 085412. doi:10.1103/PhysRevB.81.085412
7. Betti, M. G.; Gargiani, P.; Frisenda, R.; Biagi, R.; Cossaro, A.; Verdini, A.; Floreano, L.; Mariani, C. *J. Phys. Chem. C* **2010,** *114,* 21638–21644. doi:10.1021/jp108734u
8. Geim, A. K.; Novoselov, K. S. *Nat. Mater.* **2007,** *6,* 183–191. doi:10.1038/nmat1849
9. Batzill, M. *Surf. Sci. Rep.* **2012,** *67,* 83–115. doi:10.1016/j.surfrep.2011.12.001
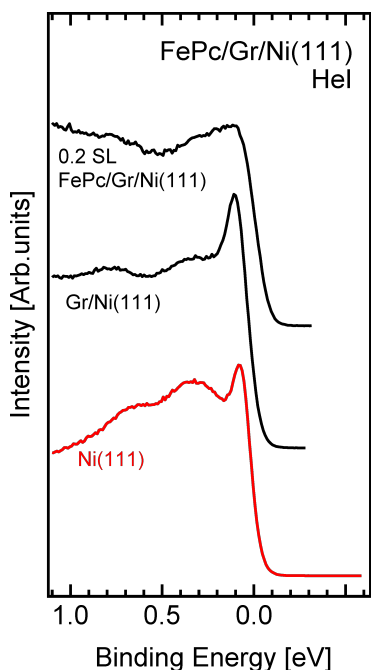
Figure 3: Valence band spectral density of states of clean Ni(111) (red line), of Gr/Ni(111) and of 0.2 SL FePc onto Gr/Ni (black lines), taken at the K point of the BZ (±2° angular integration around K, with 21.218 eV photon energy).

10. Avdoshenko, S. M.; Ioffe, I. N.; Cuniberti, G.; Dunsch, L.; Popov, A. A. *ACS Nano* **2011,** *5,* 9939–9949. doi:10.1021/nn203719a
11. Dedkov, Y. S.; Fonin, M. *New J. Phys.* **2010,** *12,* 125004. doi:10.1088/1367-2630/12/12/125004
12. Pletikosic, I.; Kralj, M.; Pervan, P.; Brako, R.; Coraux, J.; N'diaye, A.; Busse, C.; Michely, T. *arXiv preprint arXiv:0807.2770* **2008**.
13. Scardamaglia, M.; Lisi, S.; Lizzit, S.; Baraldi, A.; Larciprete, R.; Mariani, C.; Betti, M. G. *J. Phys. Chem. C* **2013,** *117,* 3019–3027. doi:10.1021/jp308861b
14. Dou, W.; Huang, S.; Zhang, R.; Lee, C. *J. Chem. Phys.* **2011,** *134,* 094705. doi:10.1063/1.3561398
15. Wei-Guo, Y.; Dan, L.; Xiao-Feng, P.; Wei-Dong, D. *Chin. Phys. B* **2013,** *22,* 117301. doi:10.1088/1674-1056/22/11/117301
16. Dou, W.; Yang, Q.; Lee, C.-S. *Appl. Phys. Lett.* **2013,** *102,* 131606. doi:10.1063/1.4800235
17. Uihlein, J.; Peisert, H.; Glaser, M.; Polek, M.; Adler, H.; Petraki, F.; Ovsyannikov, R.; Bauer, M.; Chassé, T. *J. Chem. Phys.* **2013,** *138,* 081101. doi:10.1063/1.4793523
18. Grüneis, A.; Kummer, K.; Vyalikh, D. V. *New J. Phys.* **2009,** *11,* 073050. doi:10.1088/1367-2630/11/7/073050
19. Lahiri, J.; Miller, T. S.; Ross, A. J.; Adamska, L.; Oleynik, I. I.; Batzill, M. *New J. Phys.* **2011,** *13,* 025001. doi:10.1088/1367-2630/13/2/025001
20. Patera, L. L.; Africh, C.; Weatherup, R. S.; Blume, R.; Bhardwaj, S.; Castellarin-Cudia, C.; Knop-Gericke, A.; Schloegl, R.; Comelli, G.; Hofmann, S.; Cepek, C. *ACS Nano* **2013,** *7,* 7901–7912. doi:10.1021/nn402927q
21. Gamo, Y.; Nagashima, A.; Wakabayashi, M.; Terai, M.; Oshima, C. *Surf. Sci.* **1997,** *374,* 61–64. doi:10.1016/S0039-6028(96)00785-6
22. Varykhalov, A.; Marchenko, D.; Sánchez-Barriga, J.; Scholz, M.; Verberck, B.; Trauzettel, B.; Wehling, T.; Carbone, C.; Rader, O. *Phys. Rev. X* **2012,** *2,* 041017. doi:10.1103/PhysRevX.2.041017
23. N'Diaye, A. T.; Coraux, J.; Plasa, T. N.; Busse, C.; Michely, T. *New J. Phys.* **2008,** *10,* 043033. doi:10.1088/1367-2630/10/4/043033
24. Starodub, E.; Bostwick, A.; Moreschini, L.; Nie, S.; El Gabaly, F.; McCarty, K. F.; Rotenberg, E. *Phys. Rev. B* **2011,** *83,* 125428. doi:10.1103/PhysRevB.83.125428
25. Bertoni, G.; Calmels, L.; Altibelli, A.; Serin, V. *Phys. Rev. B* **2005,** *71,* 075402. doi:10.1103/PhysRevB.71.075402
26. Sun, Z.; Hämäläinen, S. K.; Sainio, J.; Lahtinen, J.; Vanmaekelbergh, D.; Liljeroth, P. *Phys. Rev. B* **2011,** *83,* 081415. doi:10.1103/PhysRevB.83.081415
27. Kreutz, T. J.; Greber, T.; Aebi, P.; Osterwalder, J. *Phys. Rev. B* **1998,** *58,* 1300. doi:10.1103/PhysRevB.58.1300
28. Yeh, J.; Lindau, I. *At. Data Nucl. Data Tables* **1985,** *32,* 1–155. doi:10.1016/0092-640X(85)90016-6

Thermal stability and reduction of iron oxide nanowires at moderate temperatures

Annalisa Paolone[*1], Marco Angelucci[*2], Stefania Panero[3],
Maria Grazia Betti[2] and Carlo Mariani[2]

Address:
[1]CNR-ISC, U.O.S. La Sapienza, Piazzale Aldo Moro 2, I - 00185
Roma, Italy, [2]Dipartimento di Fisica, Università di Roma La Sapienza,
Piazzale Aldo Moro 2, I - 00185 Roma, Italy and [3]Dipartimento di
Chimica, Università di Roma La Sapienza, Piazzale Aldo Moro 2,
I - 00185 Roma, Italy

Email:
Annalisa Paolone[*] - annalisa.paolone@roma1.infn.it;
Marco Angelucci[*] - marco.angelucci@uniroma1.it

* Corresponding author

Keywords:
IR spectroscopy; iron oxide; nanowires; scanning electron microscopy
(SEM); thermogravimetry; XPS

Abstract

Background: The thermal stability of iron oxide nanowires, which were obtained with a hard template method and are promising elements of Li-ion based batteries, has been investigated by means of thermogravimetry, infrared and photoemission spectroscopy measurements.

Results: The chemical state of the nanowires is typical of the Fe_2O_3 phase and the stoichiometry changes towards a Fe_3O_4 phase by annealing above 440 K. The shape and morphology of the nanowires is not modified by moderate thermal treatment, as imaged by scanning electron microscopy.

Conclusion: This complementary spectroscopy–microscopy study allows to assess the temperature limits of these Fe_2O_3 nanowires during operation, malfunctioning or abuse in advanced Li-ion based batteries.

Introduction

The ever-growing need for energy is pushing research towards the study and development of new energy storage and conversion tools with high efficiency such as Li-ion based batteries [1]. The request of stable low-cost components with a high energy-density is leading to the development of nanostructured metal oxides [2-4], because the nanostructuring allows a high specific capacity [5-13]. These considerations brought the development of a new variety of transition metal oxide based

systems [14-24]. Within this context, iron oxide systems are convenient materials because of their low cost and environmental sustainability.

One of the important issues in Li-ion batteries is the chemical and thermal stability of the components. Fe_2O_3 presents a definite chemical phase (Fe^{3+}) with a high chemical stability, while the mixed chemical state of Fe_3O_4 ($Fe^{2+/3+}$) might induce instabilities during its use as electrode material. In the present work, we present a spectroscopic and morphologic characterization of Fe_2O_3 nanowires (NWs), which were produced by means of a hard template method [25] that allows for a good control over the size of the nanoparticles [26]. The characterization was carried out as a function of the annealing temperature in order to assess the thermal stability of the NWs and the temperatures, above which a chemical reduction of the Fe ions takes place. Thermogravimetry measurements distinctly show the mass reduction due to oxygen loss, and infrared transmittance and core-level photoemission measurements allow to follow the reduction process of the iron ions at different temperatures, showing the chemical reduction to Fe_3O_4 starting at moderate temperatures (above 440 K).

Experimental

Thermogravimetry (TGA) measurements were performed by means of a Setaram Setsys Evolution 1200 apparatus, equipped with a mass spectrometer Pfeiffer Vacuum Quadstar QMS200. To identify all possible gaseous products, survey scans in the mass range between 1 and 100 amu were recorded. The TGA measurements were performed by heating in vacuum (approx. 10^{-4} mbar) at 0.5 K/min. Infrared spectra were collected by means of an Agilent Cary 660 spectrometer with a resolution of 1 cm^{-1} in the frequency range between 430 and 1100 cm^{-1}. The spectra were the mean of at least 100 scans for each sample. The NW oxide powders were ground and mixed with dried KBr in a weight ratio of about 1:100. The mixed powders were pressed in a circular die in order to have self-standing pellets. The transmission of each sample was calculated as the ratio between the intensity transmitted by each pellet and the intensity transmitted by a pure potassium bromide pellet, produced in a similar way. Field-emission scanning electron microscopy (SEM) images have been taken at the Sapienza Nanotechnology and Nanoscience Laboratory (SSN-Lab), with a Zeiss Auriga 405 instrument (nominal resolution of 1.0 nm at maximum magnification, beam energy of 10 keV). The X-ray photoemission spectroscopy (XPS) measurements have been carried out at the Lotus laboratory at the "Università di Roma La Sapienza", in an ultra-high vacuum (UHV) system with a base pressure of 1×10^{-10} mbar, un-monochromatized Al Kα photon source ($hv = 1486.7$ eV), hemispherical electron analyzer with a pass energy of 100 eV. The binding energy

(BE) with respect to the Fermi level has been calibrated at the Au-4$f_{7/2}$ core level (84.0 eV BE).

The iron oxide nanowires have been obtained by means of a hard template method. The hard template is mesoporous silica (SBA-15) synthesized through the sol–gel method. In order to embed the iron oxide nanowires, 0.01 M $Fe(NO_3)_3 \cdot 9H_2O$ was dissolved in 50 mL of ethanol and added to 1 g of SBA-15. This solution was mixed at room temperature, dried at 310 K for 1 week, and the resulting powder was sintered at 820 K to promote the decomposition and dehydration of NO_x. After etching, washing and filtering, we obtained the Fe_2O_3 nanowires. A detailed description of the production procedure has been reported elsewhere [25]. For the spectroscopic investigation, the nanowires were finally dispersed in ethanolic solution, deposited onto Si and Cu substrates, and dried in vacuum before analysis.

Results and Discussion

TGA measurements were performed both on the as-produced nanowire sample (sample 1) and on a nanowire specimen heated in vacuum (p < 10^{-4} mbar) for 24 h at 350 K (sample 2), in order to clean the surface and to mimic the baking procedure that was carried out before the XPS measurements. In Figure 1 we report the mass variation of both samples and the correspondent signals detected by the mass spectrometer for $m/z = 32$ (oxygen molecule). Sample 1 displays a smooth, almost linear, loss of mass, which reaches a value of $\Delta m/m \approx -0.03$ around $T_1 = 470$ K and increases further with higher temperatures. Correspondingly, the mass spectrometer detects a high value of the oxygen signal, which decreases with increasing temperatures. In the case of the nanowire specimen with a cleaned surface (sample 2), the mass variation is higher and reaches values of $\Delta m/m \approx -0.04$ around $T_1 = 470$ K, and $\Delta m/m \approx -0.08$ around $T_2 = 560$ K. The mass spectrum of Sample 2 displays a well evident oxygen peak below 470 K. These experiments suggest that oxygen loss from the nanowired samples takes place in any case below 470 K, even if its amount depends on the cleanliness of the surface. Indeed, the higher value of $\Delta m/m$ of the pre-heated sample (sample 2) suggests that the surface of the as-prepared nanowires can be covered by a layer acting as a barrier that prevents oxygen loss. However, these experiments are not conclusive about which iron oxide is obtained after the loss of O_2. Therefore, we used infrared and XPS spectroscopy in order to identify the phase changes that are induced by the thermal treatment.

Infrared (IR) spectroscopy measurements were performed at room temperature (rt) on sample 2 and on two samples, which were obtained by heating sample 2 in vacuum ($\approx 10^{-4}$ mbar) up to 470 K (sample 3) and up to 560 K (sample 4). The IR trans-
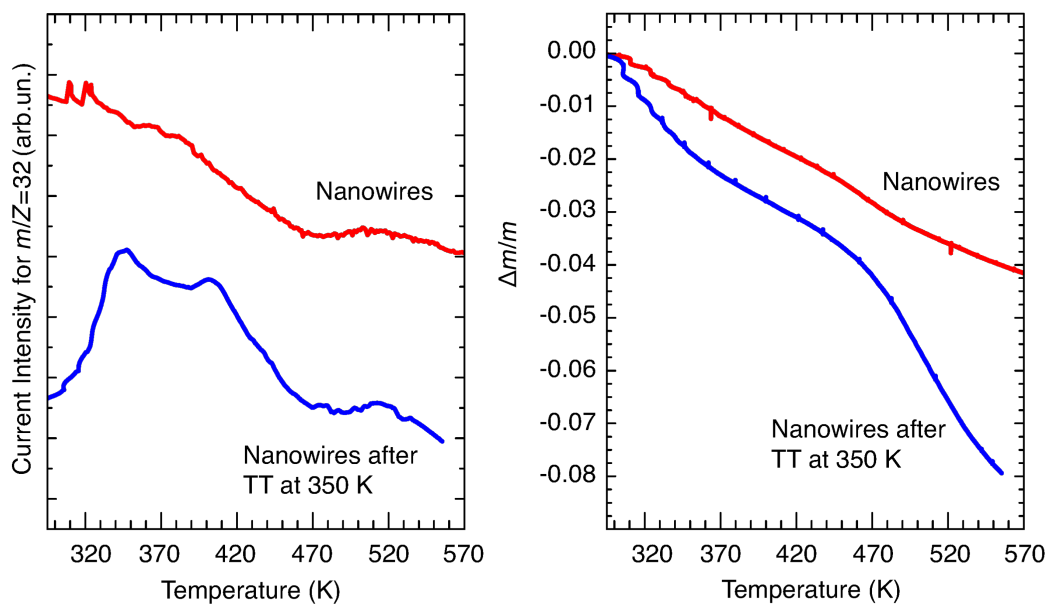
Figure 1: Temperature dependence of the signal of the mass spectrometer for *m/z* = 32 (left) and of the total mass variation Δ*m/m* (right), of the as-produced nanowire sample (red lines, sample 1) and of the nanowire specimen after a thermal treatment (TT) at 350 K for 24 h in vacuum (blue lines, sample 2).

mittance spectra of those samples are reported in Figure 2. Sample 2 shows an IR phonon spectrum that strongly resembles that of hematite, α-Fe$_2$O$_3$ [27], with a smooth transmittance between 500 and 650 cm^{-1} and the broad phonon band
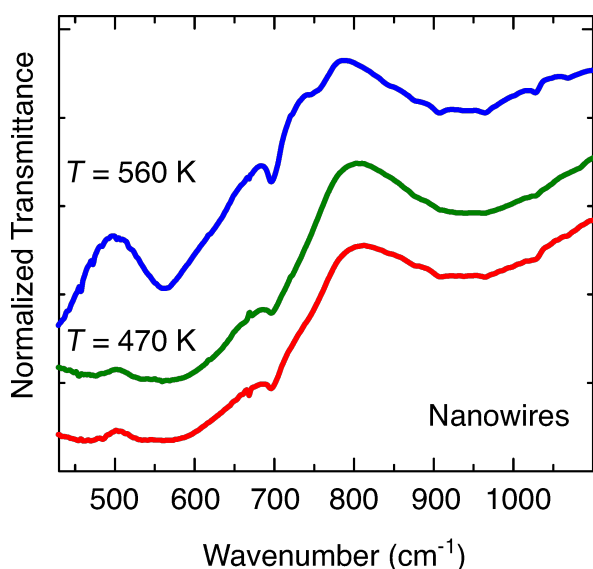

Figure 2: Infrared spectrum (normalized transmittance signal) of the nanowire sample (sample 2, red line), and of the specimen obtained from sample 2 after a thermal treatment at 470 K (sample 3, green line) and at 560 K (sample 4, blue line). In order to compare the transmission of different oxide powders, the transmittance spectra have been normalized. Data are vertically stacked, for the sake of clarity.

centered around 950 cm^{-1}. However, we can observe a minimum of the transmittance around 700 cm^{-1}, which is a fingerprint of maghemite (γ-Fe$_2$O$_3$) [27]. Thus, the clean sample 2 presents features that are typical of a mixture of α- and γ-Fe$_2$O$_3$. The infrared spectrum of the sample heated at 470 K (sample 3) is very similar to that of sample 2, while after the thermal treatment at 560 K (sample 4), the minimum around 700 cm^{-1} becomes deeper and the transmittance below 600 cm^{-1} decreases, which strongly resembles the infrared spectrum of magnetite, Fe$_3$O$_4$ [27].

The evolution of the infrared spectra with temperature indicates that in the pristine α-Fe$_2$O$_3$ material, there is a minor contribution of γ-Fe$_2$O$_3$, the concentration of which remains practically unchanged when the sample is heated to about 470 K, but increases significantly after a thermal treatment at T_2 = 560 K. Moreover, at T_2 a significant part of the sample is transformed into magnetite. We remark that the IR spectra are measured in transmission mode, so that they probe the whole thickness of the NW powders and are not limited to their surface. This issue is important to compare the IR conclusion with the results of the XPS core levels, with higher surface sensitivity.

The iron oxide nanowires have been deposited onto a Si surface and imaged by SEM at rt before and after a thermal treatment at 650 K, to observe whether any morphology modification took place. the resulting images are shown in Figure 3. The NWs assemble in bundles that are a few hundreds of nanometers
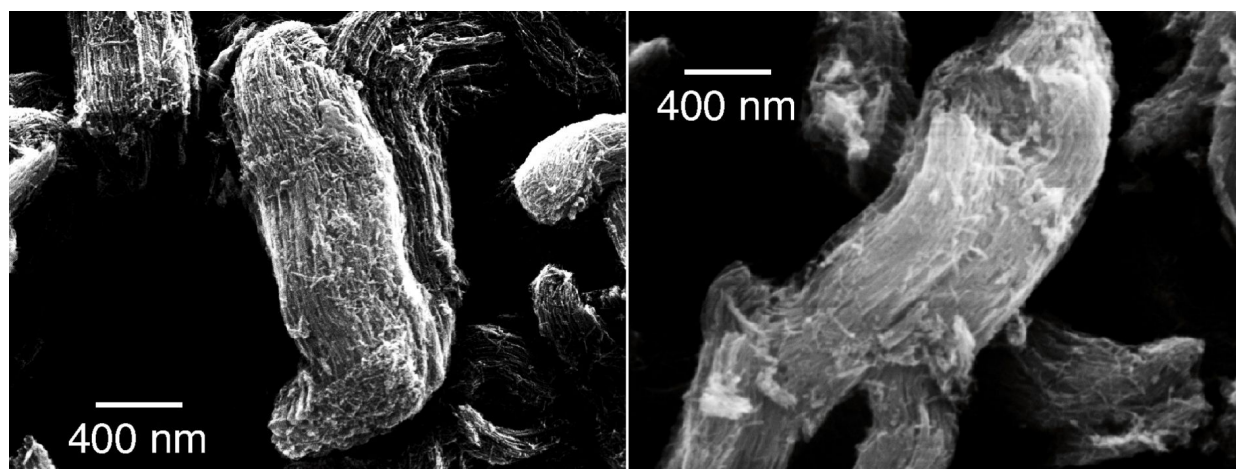
Figure 3: SEM images of the Fe_2O_3 nanowires deposited on a Si surface before (left) and after (right) thermal treatment at 650 K.

thick and several micrometers long. The individual NWs are visible within the bundles, as long parallel nanometer-thick rods. After the thermal treatment that changes the oxidation state of Fe in the NW, they do not change either shape or morphology in the bundled structure. Thus, the thermal treatment causes a chemical reduction, while not affecting the structure of the assembly, which renders the NWs a stable system for potential use in batteries, even after heating. We underline that heating at 650 K is by far a much higher temperature than what is to be expected in any device.

The oxidation state of the Fe atoms can be determined by an analysis of the Fe core levels [28,29]. We confirm the thermally induced reduction at moderate temperatures of the Fe ions in the NWs by the X-ray photoemission spectroscopy analysis of the Fe 3p core level. The XPS Fe 3p core-level data of the Fe_2O_3 NWs, taken at rt and after subsequent steps of thermal annealing, are shown in Figure 4. The Fe 3p signal of the clean Fe_2O_3 system at rt, which is roughly centered at 56 eV BE, presents the characteristic structure that is associated with multiple oxidation states [30-32].
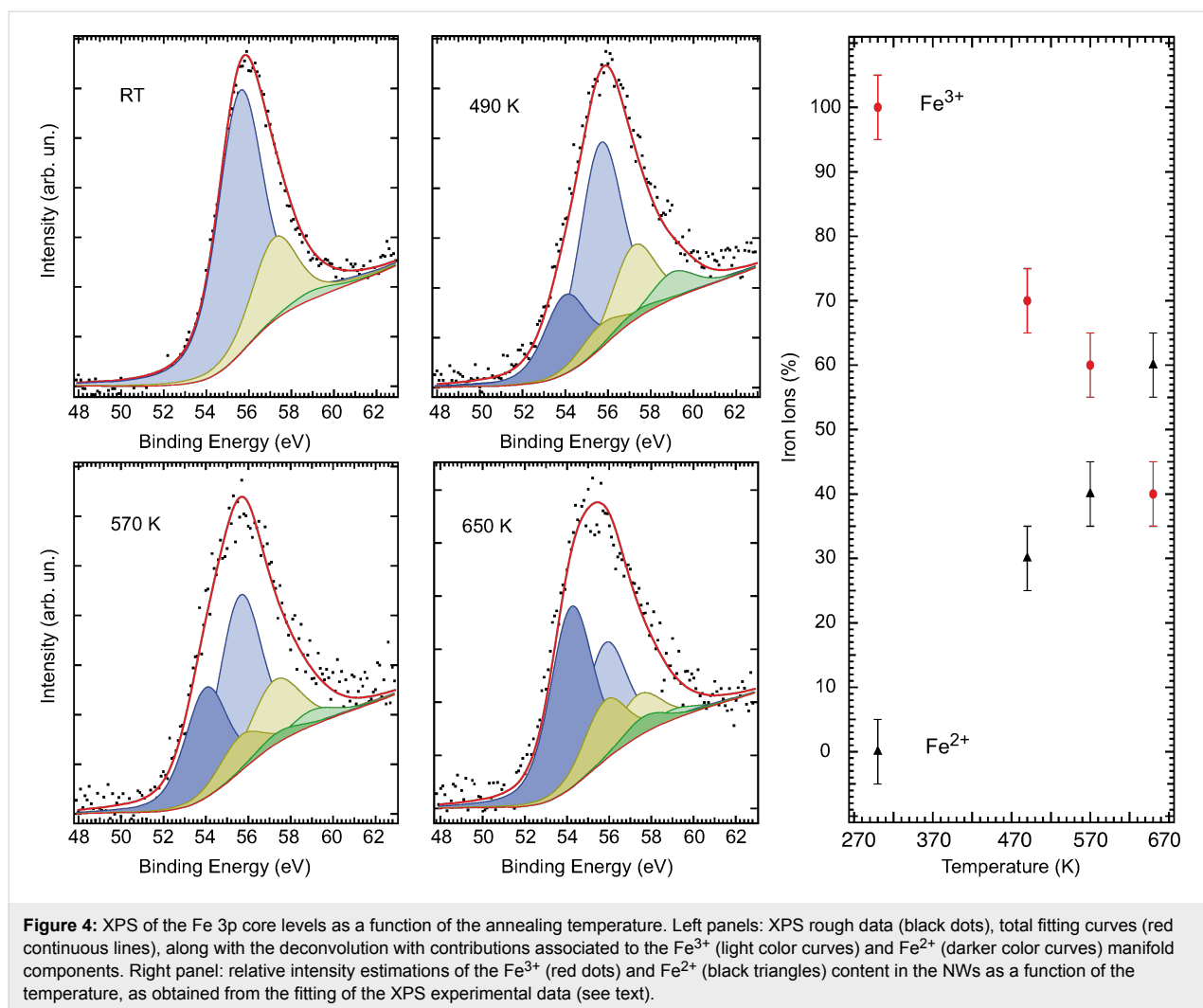
We fit the experimental data with three Voigt (Lorentzian–Gaussian) functions with all peaks having the same Gaussian width (GW = 1.8 eV) and Lorentzian width (LW = 1.0 eV). The lineshape and BE of the Fe 3p core level confirm the Fe^{3+} oxidation state [32] of the Fe_2O_3 NWs. The Fe 3p XPS spectra that were taken after annealing the NWs at increasing temperatures present the emerging of a further manifold of peaks, at lower BE, the relative intensity of which grows as a function of temperature. This lower-BE manifold is associated to the Fe^{2+} oxidation state, and we fit it with three more Voigt functions, in analogy to the previous manifold. The evolution of the relative intensity of the Fe^{3+} and Fe^{2+} signal as

evaluated from the fit, is shown in the right panel of Figure 4. Data analysis shows that already at 470 K, the reduction of iron ions has taken place, and finally a 60:40 ratio of Fe^{2+}/Fe^{3+} is reached at 650 K. These spectroscopic data fully confirm the observed thermal-induced reduction of Fe_2O_3 to Fe_3O_4 at moderate temperatures.

The XPS measurements are more sensitive to the properties of the surface than the infrared spectroscopy measurements, in fact the electron mean free path of the photo-electrons is of the order of 1 nm in this energy range. Both experimental techniques indicate that at 470 K the sample has transformed into Fe_3O_4. However, while infrared measurements show an almost abrupt change from Fe_2O_3 to Fe_3O_4 between 470 K and 560 K, XPS measurements can sensitively detect the progressive change of the iron ion valence above room temperature. In particular, the appearance of divalent Fe ions is clearly visible above 440 K. In fact, XPS probes mainly the physical properties of the very surface. Therefore, the comparison between the data obtained by IR and XPS, strongly indicates that the reduction of iron oxide nanowires starts from their very surface and is completed in the bulk only around 560 K.

Conclusion

We characterized the mass loss and spectroscopic change of Fe_2O_3 nanowires obtained through a hard template method [25], as a function of the annealing temperature, by means of thermogravimetry, IR and XPS spectroscopy. Heating the NWs induces an oxygen loss from the surface and a subsequent reduction of the Fe ions from a 3+ to a prevalent 2+ oxidation state at moderate temperatures (above 440 K). The reduction starts from the NW surface and progressively extends into the bulk, as determined by comparing the IR (bulk sensitive) and XPS (surface sensitive) techniques. Despite the chemical

Figure 4: XPS of the Fe 3p core levels as a function of the annealing temperature. Left panels: XPS rough data (black dots), total fitting curves (red continuous lines), along with the deconvolution with contributions associated to the Fe^{3+} (light color curves) and Fe^{2+} (darker color curves) manifold components. Right panel: relative intensity estimations of the Fe^{3+} (red dots) and Fe^{2+} (black triangles) content in the NWs as a function of the temperature, as obtained from the fitting of the XPS experimental data (see text).

change, the NWs maintain the same shape and size, as imaged by SEM. The chemical reduction is clearly followed and quantified thanks to the thermogravimetry measurements and spectroscopic tools, and it assesses temperature limits for the operation of these nanowires in Li-ion based batteries, establishing the Fe_2O_3 nanowires as stable nanostructured elements for new advanced batteries.

Acknowledgements

References

1. Tarascon, J.-M.; Armand, M. *Nature* **2001,** *414,* 359–367. doi:10.1038/35104644

2. Poizot, P.; Laruelle, S.; Grugeon, S.; Dupont, L.; Tarascon, J.-M. *Nature* **2000,** *407,* 496–499. doi:10.1038/35035045

3. Taberna, P. L.; Mitra, S.; Poizot, P.; Simon, P.; Tarascon, J.-M. *Nat. Mater.* **2006,** *5,* 567–573. doi:10.1038/nmat1672

4. Wu, H. B.; Chen, J. S.; Hng, H. H.; Lou, X. W. D. *Nanoscale* **2012,** *4,* 2526–2542. doi:10.1039/c2nr11966h

5. Larcher, D.; Masquelier, C.; Bonnin, D.; Chabre, Y.; Masson, V.; Leriche, J.-B.; Tarascon, J.-M. *J. Electrochem. Soc.* **2003,** *150,* A133–A139. doi:10.1149/1.1528941

6. Chen, Y. X.; He, L. H.; Shang, P. J.; Tang, Q. L.; Liu, Z. Q.; Liu, H. B.; Zhou, L. P. *J. Mater. Sci. Technol.* **2011,** *27,* 41–45. doi:10.1016/S1005-0302(11)60023-6

7. Chou, S.-L.; Wang, J.-Z.; Chen, Z.-X.; Liu, H.-K.; Dou, S.-X. *Nanotechnology* **2011,** *22,* 265401. doi:10.1088/0957-4484/22/26/265401

8. Wang, Z.; Luan, D.; Madhavi, S.; Li, C. M.; Lou, X. W. D. *Chem. Commun.* **2011,** *47,* 8061–8063. doi:10.1039/c1cc12111a

9. Wang, Z.; Zhou, L.; Lou, X. W. D. *Adv. Mater.* **2012,** *24,* 1903–1911. doi:10.1002/adma.201200469

10. Zhang, Q.; Shi, Z.; Deng, Y.; Zheng, J.; Liu, G.; Chen, G. *J. Power Sources* **2012,** *197,* 305–309. doi:10.1016/j.jpowsour.2011.09.029

11. Koo, B.; Xiong, H.; Slater, M. D.; Prakapenka, V. B.; Balasubramanian, M.; Podsiadlo, P.; Johnson, C. S.; Rajh, T.; Shevchenko, E. V. *Nano Lett.* **2012,** *12,* 2429–2435. doi:10.1021/nl3004286

12. Ding, Y.; Li, J.; Zhao, Y.; Guan, L. *Mater. Lett.* **2012,** *81,* 105–107. doi:10.1016/j.matlet.2012.05.001

13. Zhang, J.; Huang, T.; Liu, Z.; Yu, A. *Electrochem. Commun.* **2013,** *29,* 17–20. doi:10.1016/j.elecom.2013.01.002

14. Zou, Y.; Wang, Y. *ACS Nano* **2011,** *5,* 8108–8114. doi:10.1021/nn2027159

15. Li, X.; Lei, Y.; Li, X.; Song, S.; Wang, C.; Zhang, H. *Solid State Sci.* **2011,** *13,* 2129–2136. doi:10.1016/j.solidstatesciences.2011.08.011

16. Chen, D.; Ji, G.; Ma, Y.; Lee, J. Y.; Lu, J. *ACS Appl. Mater. Interfaces* **2011,** *3,* 3078–3083. doi:10.1021/am200592r

17. Qu, Q.; Yang, S.; Feng, X. *Adv. Mater.* **2011,** *23,* 5574–5580. doi:10.1002/adma.201103042

18. Hsieh, C.-T.; Lin, J.-Y.; Mo, C.-Y. *Electrochim. Acta* **2011,** *58,* 119–124. doi:10.1016/j.electacta.2011.09.008

19. Lee, S.-H.; Sridhar, V.; Jung, J.-H.; Karthikeyan, K.; Lee, Y.-S.; Mukherjee, R.; Koratkar, N.; Oh, I.-K. *ACS Nano* **2013,** *7,* 4242–4251. doi:10.1021/nn4007253

20. Guo, S.; Zhang, G.; Guo, Y.; Yu, J. C. *Carbon* **2013,** *60,* 437–444. doi:10.1016/j.carbon.2013.04.058

21. Wang, G.; Wang, H.; Cai, S.; Bai, J.; Ren, Z.; Bai, J. *J. Power Sources* **2013,** *239,* 37–44. doi:10.1016/j.jpowsour.2013.03.105

22. Jin, B.; Liu, A.-H.; Liu, G.-Y.; Yang, Z.-Z.; Zhong, X.-B.; Ma, X.-Z.; Yang, M.; Wang, H.-Y. *Electrochim. Acta* **2013,** *90,* 426–432. doi:10.1016/j.electacta.2012.11.114

23. Prakash, R.; Fanselau, K.; Ren, S.; Mandal, T. K.; Kübel, C.; Hahn, H.; Fichtner, M. *Beilstein J. Nanotechnol.* **2013,** *4,* 699–704. doi:10.3762/bjnano.4.79

24. Zhao, H.; Pan, L.; Xing, S.; Luo, J.; Xu, J. *J. Power Sources* **2013,** *222,* 21–31. doi:10.1016/j.jpowsour.2012.08.036

25. Hong, I.; Angelucci, M.; Verrelli, R.; Betti, M. G.; Panero, S.; Croce, F.; Mariani, C.; Scrosati, B.; Hassoun, J. *J. Power Sources* **2014,** *256,* 133–136. doi:10.1016/j.jpowsour.2014.01.052

26. Reddy, M. V.; Yu, T.; Sow, C. H.; Shen, Z. X.; Lim, C. T.; Subba Rao, G. V.; Chowdari, B. V. R. *Adv. Funct. Mater.* **2007,** *17,* 2792–2799. doi:10.1002/adfm.200601186

27. Cornell, R. M.; Schwertmann, U. *The Iron Oxides,* 2nd ed.; Wiley-VCH: Weinheim, 2003.

28. Chambers, S. A.; Thevuthasan, S.; Joyce, S. A. *Surf. Sci.* **2000,** *450,* L273–L279. doi:10.1016/S0039-6028(00)00230-2

29. Yamashita, T.; Hayes, P. *Appl. Surf. Sci.* **2008,** *254,* 2441–2449. doi:10.1016/j.apsusc.2007.09.063

30. Yang, D.-Q.; Sacher, E. *J. Phys. Chem. C* **2009,** *113,* 6418–6425. doi:10.1021/jp810171e

31. Mills, P.; Sullivan, J. L. *J. Phys. D: Appl. Phys.* **1983,** *16,* 723. doi:10.1088/0022-3727/16/5/005

32. Zimmermann, R.; Steiner, P.; Claessen, R.; Reinert, F.; Hüfner, S.; Blaha, P.; Dufek, P. *J. Phys.: Condens. Matter* **1999,** *11,* 1657. doi:10.1088/0953-8984/11/7/002

Tensile properties of a boron/nitrogen-doped carbon nanotube–graphene hybrid structure

Kang Xia, Haifei Zhan, Ye Wei and Yuantong Gu[*]

Abstract

Doping is an effective approach that allows for the intrinsic modification of the electrical and chemical properties of nanomaterials. Recently, a graphene and carbon nanotube hybrid structure (GNHS) has been reported, which extends the excellent properties of carbon-based materials to three dimensions. In this paper, we carried out a first-time investigation on the tensile properties of the hybrid structures with different dopants. It is found that with the presence of dopants, the hybrid structures usually exhibit lower yield strength, Young's modulus, and earlier yielding compared to that of a pristine hybrid structure. For dopant concentrations below 2.5% no significant reduction of Young's modulus or yield strength could be observed. For all considered samples, the failure is found to initiate at the region where the nanotubes and graphene sheets are connected. After failure, monatomic chains are normally observed around the failure region. Dangling graphene layers without the separation of a residual CNT wall are found to adhere to each other after failure with a distance of about 3.4 Å. This study provides a fundamental understanding of the tensile properties of the doped graphene–nanotube hybrid structures, which will benefit the design and also the applications of graphene-based hybrid materials.

Introduction

In recent years, low-dimensional structures such as carbon nanotubes (CNT) and graphene have attracted huge attention of the scientific community, because of their excellent performance in the fields of mechanics, photology, electronics and bio-sensing [1,2]. Through the chemical vapor deposition (CVD) method, a graphene–nanotube hybrid structure (GNHS) has been synthesized recently [3-5], which evidently demonstrates an improved performance for the application as field emission device when compared to the previous CNT–bulk-metal structures [6]. The hybrid structure extends the excellent thermal and electrical conductivity of CNT (1D) and graphene (2D) into three dimensions [7], and shows appealing applica-

tions in solar cells [8]. Furthemore, according to Fan et al. [9], owing to the double layer configuration, the CNT–graphene hybrid structures are expected to have a better electrochemical performance, which indicates that the hybrid structure is a good candidate for the usage of electrodes in supercapacitors.

In order to accommodate for various applications, different approaches have been developed to tailor the properties of nanomaterials. Doping is one of such schemes and has been extensively used in synthesizing derivatives from carbon-based materials (e.g., fullerene, nanotubes and graphene) [10]. Boron and nitrogen, which have comparable atomic size with carbon atom and can form strong valence bonds with carbon atoms, are the most frequently used doping elements for carbon-based materials [11]. The presence of boron and nitrogen atom induce significant variations in the electronic structure of graphene layer, which was shown by changes in the Raman spectra [12,13]. According to Panchakarla et al. [14], the doping induces donors and/or acceptors states, which modify the G band (in Raman spectrum) and are essential in facilitating the application of graphene-based electronics. The N-doped graphene is reported by Wang et al. [15] to be also a good candidate for the application as fuel cell electrocatalyst, in field-effect transistors, and in lithium batteries. Thus, especially N-doped nanotube–graphene hybrid structures have been envisioned to have promising potential applications in the field of catalysis, gas storage and energy storage [16].

The majority of the current works that are conducted on graphene variations are focusing on the electrical and chemical properties. However, to facilitate the applications of nanomaterials, a comprehensive understanding of their mechanical properties/performance is crucial. By using molecular dynamics (MD) simulations, Bohayra et al. [10] conclude that the content of nitrogen atoms (up to 6%) has a negligible effect on the Young's modulus of a nitrogen-doped graphene layer, while the presence of nitrogen substitutions reduces the layer strength significantly. Only a few works have been devoted to examine the impact of dopant atoms on the mechanical properties of graphene. Huge efforts are still lying ahead especially for the newly synthesized CNT–graphene hybrid structure. Therefore, in this work, we will examine the impact of different densities and species of dopants on the tensile properties of the GNHS. The emphasis will be placed on Young's modulus, E, yield strength, YS, and yield strain, YP.

Computational details

In order to acquire the influence of the dopants on the mechanical properties of GNHSs, the large-scale atomic/molecular massively parallel simulator (LAMMPS) [17] is utilized to carry out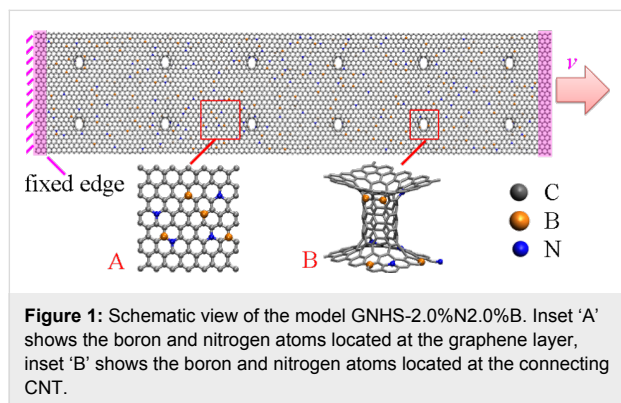 the MD simulations. The pristine GNHS model is constructed by two graphene sheets, with zigzag and armchair edges along the x- and y-axes, respectively. We establish the initial structure according to pervious simulation models [8,18-21], i.e., a specific cylindrical hole is made in the graphene sheet to fit the armchair (4,4)-CNT with a height of 13.8 Å. Basically, three groups of sample structures have been tested, which include GNHS with nitrogen dopant (GNHS-N), GNHS with boron dopant (GNHS-B), and GNHS with both nitrogen and boron dopants (GNHS-NB). Each group contains six doped samples with different percentages of dopants. All structures for the simulations have an identical size of $24.6 \times 5.6 \times 1.4$ nm^3. For the sake of convenience, the percentage of dopants is included in the model name, e.g., a sample name 'GNHS-1.5%N1.5%B means that the hybrid structure contains 1.5% of boron and nitrogen, respectively. The dopants are randomly distributed along the whole structure domain.

Similar to the work of Wei et al. [22], the C–C interatomic interactions are described by the commonly used empirical bond order (REBO) potential [23], which has been shown to represent the binding energy and elastic properties of graphene and CNT well [24]. Basically, the REBO potential is given as

$$E_i = \frac{1}{2} \sum_i \sum_{j \neq 1} \left[E_{ij}^{\text{REBO}} + E_{ij}^{\text{LJ}} + \sum_{k \neq i,j} \sum_{l \neq i,j,k} E_{kijl}^{\text{TORSION}} \right]. \quad (1)$$

Here, the first term represents the interaction between i and j atoms, which strongly depends on the coordination. The second term accounts for a longer-ranged interaction that is depicted by a Lennard-Jones (LJ) potential, while the last term represents an explicit 4-body potential that describes various preferences for dihedral angles in hydrocarbon configurations. A Tersoff potential [25] is adopted to describe the atomic interactions of C–B, C–N and B–N. The N–N bond is considered to be chemically unstable. Thus, two adjacent N atoms are avoided in the model. It must be noted that the cut-off distance for the C–C bond has been modified from 1.7 Å to 2.0 Å according to a previous work [24]. Several studies have already demonstrated that a cut-off distance of 1.7 Å for carbon materials, which was used previously, will produce a spuriously high tensile force and lead to a nonlinear stress–strain curve [26,27]. In addition, the samples with higher densities of dopants contain all the dopant positions of the samples with lower doping percentages to ensure a reasonable comparison. To calculate the stress, the tensile force has been tracked. To lower the computational cost, the GNHS has been assumed as a continuum material, i.e., the cross-sectional area is a product of the width and height. Since we emphasize on the relative mechanical properties (Young's modulus, yield strength) such an approximation will make no difference for the discussion.

At the beginning of the simulation, the conjugate gradient algorithm was applied to relax the model to a minimum energy state. We then used the Nose–Hoover thermostat [28,29] to equilibrate the GNHS at 1 K (NVT ensemble) for 500 ps at a time step of 1 fs. The extremely low temperature was chosen to exclude the thermal fluctuation influence. Figure 1 illustrates the atomic configuration of the GNHS-2.0N2.0B model and the simulation setup. A constant velocity of 0.005 Å/ps was applied to one end of the GNHS to exert the axial load (along the longitudinal *y*-axis), while the other end was held fixed. The equations of motion are integrated over time using a velocity-Verlet algorithm [30]. No periodic boundary conditions have been applied. The system temperature was maintained at 1 K during the simulation.

Figure 1: Schematic view of the model GNHS-2.0%N2.0%B. Inset 'A' shows the boron and nitrogen atoms located at the graphene layer, inset 'B' shows the boron and nitrogen atoms located at the connecting CNT.
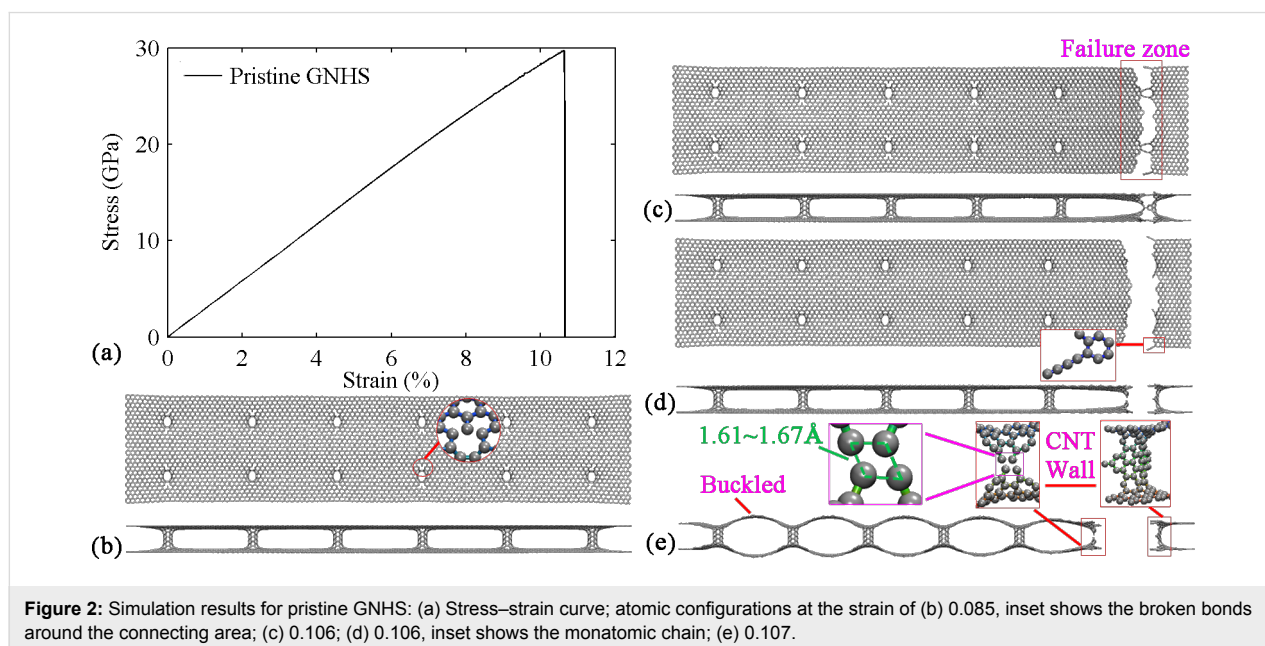
Results and Discussion

Figure 2b and Figure 2c present the atomic configurations of the pristine hybrid structure before and after fracture. It is obvious

that during the period of elastic deformation, all the C–C bonds have been stretched in the loading direction. With the increase of strain, the failure initiates from the region where the nanotubes and graphene sheets are connected. After the bonds begin to break, the hybrid structure quickly fails. This phenomenon is indicated by the sharp decrease of the stress (Figure 2a), which indicates a brittle behavior. Such brittle behavior can be easily explained as the tension loading direction is perpendicular to the axial direction of the CNT. Therefore, the tensile behavior of the GNHS is dominated by the graphene layer rather than by the nanotube and results in a brittle behavior.

During the failure of the structure, several short monatomic chains are formed at the front of the failure region (see inset in Figure 2d). The initial C–C bond length in graphene and CNT is 0.142 nm and is stretched to about 0.160 nm before breaking. It is observed from Figure 2e, that the two separated parts exhibit a bulked configuration eventually after the fracture of the hybrid structure. Strikingly, the upper and lower graphene layers (in the failure zone) are still separated by residual CNT walls. We notice that the length of the elongated C–C bonds in the left region (inset of Figure 2e) ranges from 1.61 to 1.67 Å, which is much longer than the typical length.

Hybrid structures doped with nitrogen

We then evaluate the tensile properties of doped GNHSs with different percentages of dopants. A concentration range of the N-dopants from 0.5% to 4.0% is considered. Figure 3 presents the stress–strain curves obtained from MD simulations. Similar to the pristine GNHS case, all N-doped GNHSs exhibit a linear stress–strain curve during the whole elastic deformation, and

Figure 2: Simulation results for pristine GNHS: (a) Stress–strain curve; atomic configurations at the strain of (b) 0.085, inset shows the broken bonds around the connecting area; (c) 0.106; (d) 0.106, inset shows the monatomic chain; (e) 0.107.

they nearly overlap at low strains (up to 4%). This phenomenon indicates that the Young's moduli are only insignificantly changed. However as shown in Figure 3, yield strength, *YS*, and yield strain, *YP*, experience an apparent degradation. An increase of the dopant concentration, however, does not further reduce *YS* and *YP*. It is interesting to mention that an earlier work reported that 2% of N-doping in graphene monolayers induce a reduction of *YS* of more than 35% [10], which is much
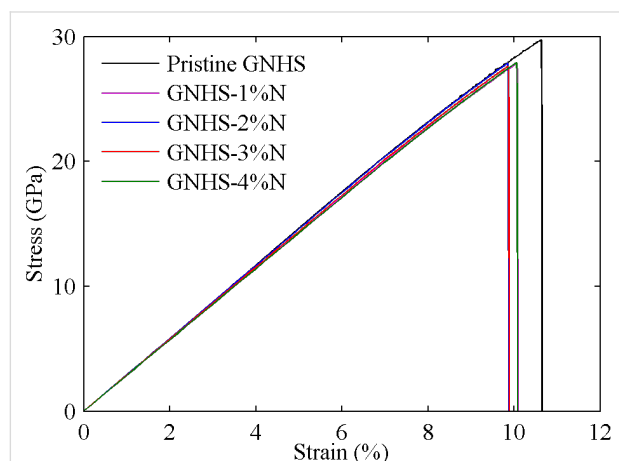
more significant than the reduction observed in the hybrid structures that are studied here. In addition, all stress–strain curves presented in Figure 3 show a sharp decrease of stress, which indicates a brittle behavior of the different GNHSs.

In general, the GNHS with different densities of N-dopants behave similar to the pristine structure. It is found that the GNHS with 0.5%, 1.0%, 1.5%, 2.0%, 2.5% and 3.5% of N-dopants fracture at either the right or the left end of the structure. The atomic configurations of the GNHS with 2% of N-dopants are presented in Figure 4a-d. Before the initiation of failure, a shearing of the CNTs and an elongation of bonds are observed. Similar to the pristine GNHS case, failures start around the connection region (Figure 4a), and are followed by the formation of monatomic chains (Figure 4c). In Figure 4d, the buckled shape is formed because of the stress release after failure. Specifically, after failure, one end of the dangling graphene layers (left in Figure 4d) is separated by the residual CNT wall, and the other end exhibits self-adhesive behavior. Different from these cases, the other two structures with 3% and 4% N-dopant exhibit a fracture region around the middle of the hybrid structure, and the self-adhesive behavior is observed on both sides of the dangling graphene layers (shown in Figure 4h). Particularly, a longer chain is found that contains eight carbon atoms.

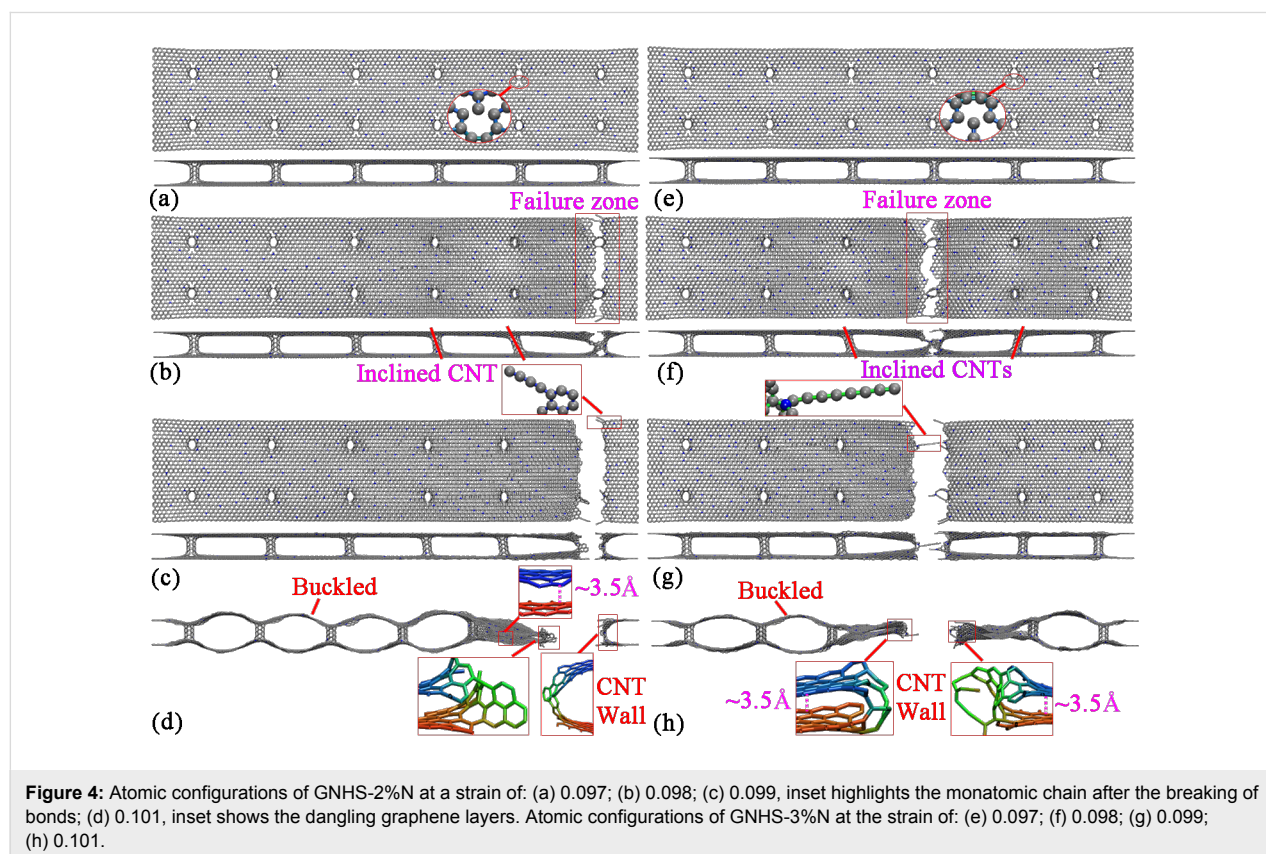**Figure 3:** Stress–strain curves of GNHS with different percentage of N-dopants between 1% and 4%.

Figure 4: Atomic configurations of GNHS-2%N at a strain of: (a) 0.097; (b) 0.098; (c) 0.099, inset highlights the monatomic chain after the breaking of bonds; (d) 0.101, inset shows the dangling graphene layers. Atomic configurations of GNHS-3%N at the strain of: (e) 0.097; (f) 0.098; (g) 0.099; (h) 0.101.

Hybrid structures doped with boron

Besides nitrogen, boron is another common doping element. Thus, we continue our investigation by considering the GNHS with different percentages of B-dopants. Similar to the cases of nitrogen doping, an evident decrease of the yield strength and early yielding are observed (Figure 5). Within the elastic deformation region, the increase of dopant leads to a marginal shift to the slope of the stress–strain curve, which indicates an insignificant reduction in Young's modulus. Of all samples studied, the
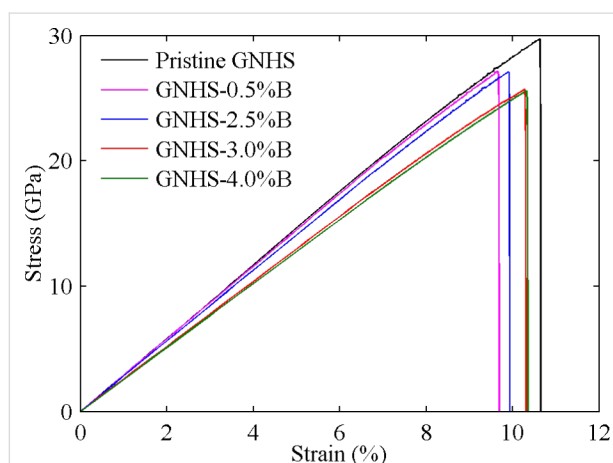

Figure 5: Stress–strain curves of GNHS with different percentage of B-dopant ranging from 0.5% to 4%.

one with 0.5% B-dopant exhibits the highest Young's modulus and *YS*, which are 0.290 TPa and 27.13 GPa, respectively. While the case with 4% B-dopant shows the lowest Young's modulus and *YS*. Importantly, we found that *YS* is not reduced linearly with increasing boron percentage.

Regarding the deformation process the hybrid structures with 0.5%, 1.0%, 1.5%, 2.0% and 2.5% B-dopant share a similar pattern. Specifically, Figure 6a–d illustrate the atomic configurations of GNHS-2.5%B at different strains. As in the previously considered cases, the failure initiates around the connection region and monatomic chains are formed (highlighted in Figure 6c). Interestingly, these monatomic chains have formed three rings around the failure region. After failure, a buckled shaped is formed, and one end the dangling graphene layers are separated by the residual CNT wall, while the other end shows self-adhesive behavior. Besides, in the other three cases (with 3.0%, 3.5% and 4.0% B-dopant) the fracture is observed around the middle area.

Hybrid structures doped with nitrogen and boron

In order to improve the ferroelectric properties and the layer resistivity, N and B doping is widely adopted in thin films studies [31-34]. In this section, we consider a hybrid structure that is doped with both nitrogen and boron. The stress–strain
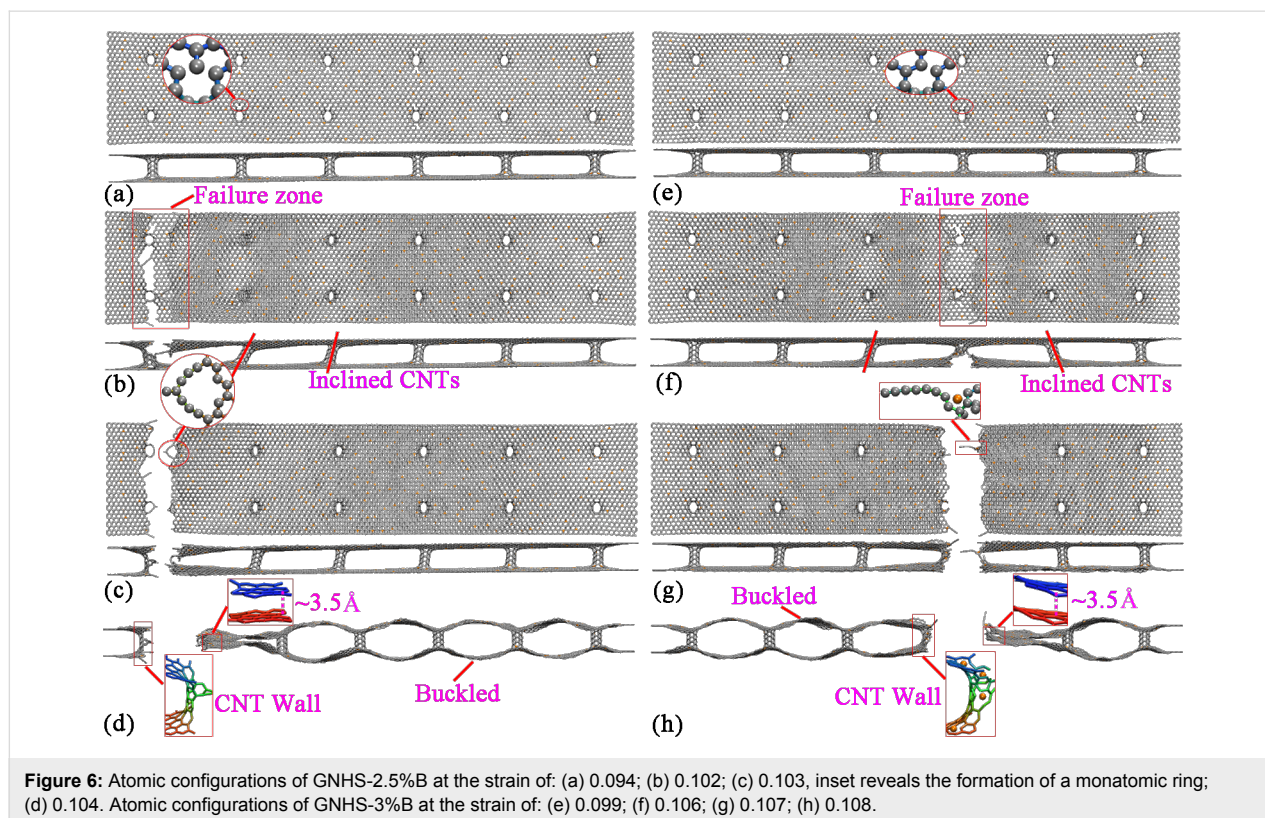

Figure 6: Atomic configurations of GNHS-2.5%B at the strain of: (a) 0.094; (b) 0.102; (c) 0.103, inset reveals the formation of a monatomic ring; (d) 0.104. Atomic configurations of GNHS-3%B at the strain of: (e) 0.099; (f) 0.106; (g) 0.107; (h) 0.108.

curve is presented in Figure 7. As can be seen, GNHS-0.25%N0.25%B has similar *YS* and *YP* as the pristine GNHS, which are 29.27 GPa and 10.55%, respectively. With an increase of the percentage of nitrogen and boron dopants to 0.75%, a considerable drop in *YS* and *YP* is observed (see Figure 7). It is worth to mention that, for GNHS-0.25%N0.25%B and GNHS-075%N0.75%B, the stress does not decrease directly to zero after fracture. An explanation for this phenomenon is given below.
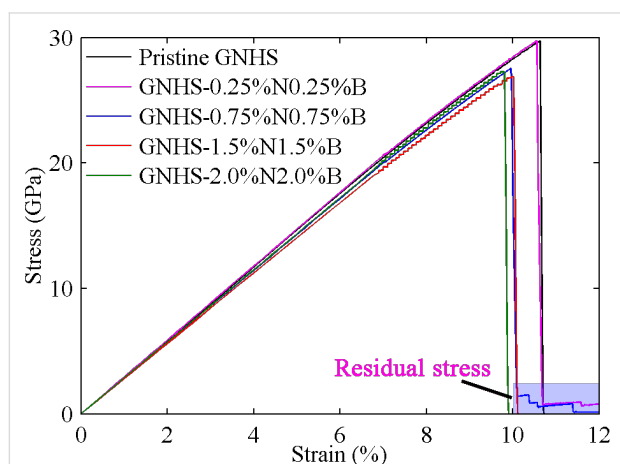

Figure 7: Stress–strain curves of GNHS with different densities of B- and N-dopant.

Besides of the failure around the end of the structure, fractures at other locations are also observed for the hybrid structure with both B- and N-dopants. Figure 8a–d illustrate the atomic configurations of the case with 0.75%B and 0.75%N at different strains. Surprisingly, the hybrid structure is found to fracture around four CNTs. After failure, the upper layer is found to break at the outermost two CNTs at the right end, while the lower layer fractures at the second outermost two CNTs. Such deformation is found to result two dangling layers (upper and lower) that adhere to each other. This adhesive behavior is the reason for the residual stress, which is highlighted in Figure 7. With sufficient elongation, the dangling layers finally separate from each other by van der Waals interaction. The failure of the hybrid structure around the middle region is also witnessed. As shown in Figure 8f, the top and bottom layers of GNHS-1.5%N1.5%B fracture simultaneously around the two connecting CNTs. In all investigated cases, the self-adhesive behavior between the dangling layers and the bulked configuration of the structure is observed after failure. It is necessary to point out that, the boundary condition applied in this work is non-periodic. According to the results presented in Figure 4, Figure 6 and Figure 8, the location of the fracture region is quite random during the simulation. According to previous work on metal nanowires [35] the location of necking is highly related to the strain rate, which could be predicted by the longitudinal wave propagation equation. However, the difference to a
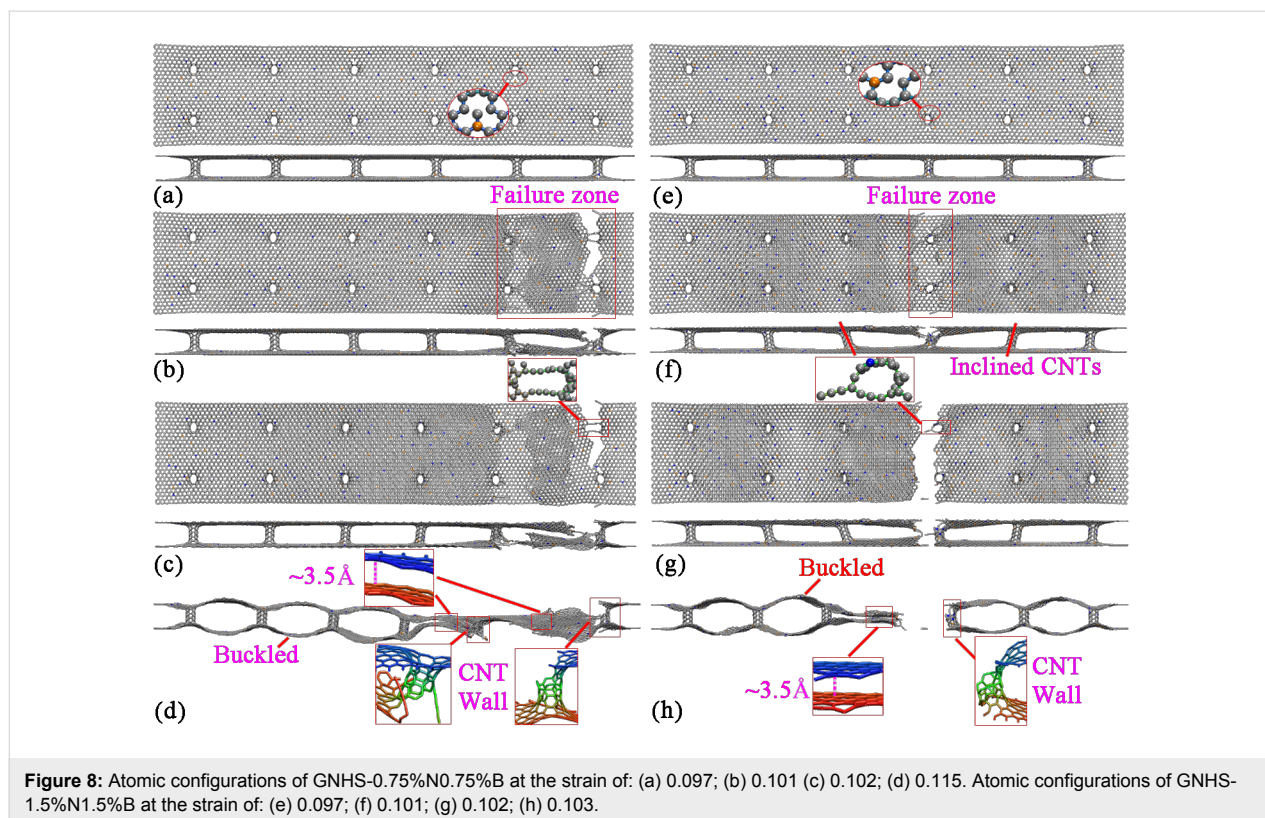

Figure 8: Atomic configurations of GNHS-0.75%N0.75%B at the strain of: (a) 0.097; (b) 0.101 (c) 0.102; (d) 0.115. Atomic configurations of GNHS-1.5%N1.5%B at the strain of: (e) 0.097; (f) 0.101; (g) 0.102; (h) 0.103.

nanowire is that the hybrid structure is intrinsically inhomogeneous. Such an inhomogeneity is believed to introduce a local concentration of stress around the connecting regions, and thus could lead to the phenomenon that the fracture always starts around one of these connecting areas.

Before concluding, we compare the yield strains and Young's moduli of all studied cases. Figure 9a shows the yield strain as a function of the concentration of the dopant. Clearly, the existence of different dopants reduces *YS*. However, the there is no strong correlation between the concentration of the dopant and the reduction of *YS*. For all types of dopants, the reduction is found to fluctuate around 10% (Figure 9a). In most of the circumstances, the hybrid structures with dopants exhibit low Young's moduli. However, for GNHS-0.5%N and GNHS-3.5%N, the Young's modulus is even higher than that of the pristine GNHS, which are 0.292 TPa and 0.295 TPa, respectively. Figure 9b shows that increase of boron doping results in a sharp reduction of the Young's modulus, while the other considered cases exhibit Young's moduli around 0.29 TPa.

Conclusion

Basing on the large-scale MD simulation, the tensile properties of a graphene–carbon nanotube hybrid structure with different dopants have been investigated. It is found that with the presence of dopants, the hybrid structures usually exhibit a lower yielding strength, Young's modulus, and earlier yielding when compared to a pristine hybrid structure. Young's modulus and yielding strength are not reduced when the concentration of dopants increases further. For all considered samples, the failure is found to initiate in the region where the nanotubes and graphene sheets are connected. After failure, monatomic chains are normally observed around the failure region. The dangling

graphene layers are found to adhere to each other through van der Waals interactions with a distance of around 3.4 Å. This study provides a fundamental understanding of the tensile properties of the doped graphene–nanotube hybrid structures, which will benefit the design and also the applications of graphene-based hybrid materials.

Acknowledgements

References

1. Zhu, Y.; Murali, S.; Cai, W.; Li, X.; Suk, J. W.; Potts, J. R.; Ruoff, R. S. *Adv. Mater.* **2010,** *22,* 3906–3924. doi:10.1002/adma.201001068
2. Wang, J. *Electroanalysis* **2005,** *17,* 7–14. doi:10.1002/elan.200403113
3. Zhu, Y.; Li, L.; Zhang, C.; Casillas, G.; Sun, Z.; Yan, Z.; Ruan, G.; Peng, Z.; Raji, A.-R. O.; Kittrell, C.; Hauge, R. H.; Tour, J. M. *Nat. Commun.* **2012,** *3,* No. 1225. doi:10.1038/ncomms2234
4. Das, S.; Seelaboyina, R.; Verma, V.; Lahiri, I.; Hwang, J. Y.; Banerjee, R.; Choi, W. *J. Mater. Chem.* **2011,** *21,* 7289–7295. doi:10.1039/C1JM10316D
5. Du, F.; Yu, D.; Dai, L.; Ganguli, S.; Varshney, V.; Roy, A. K. *Chem. Mater.* **2011,** *23,* 4810–4816. doi:10.1021/cm2021214
6. Yan, Z.; Ma, L.; Zhu, Y.; Lahiri, I.; Hahm, M. G.; Liu, Z.; Yang, S.; Xiang, C.; Lu, W.; Peng, Z.; Sun, Z.; Kittrell, C.; Lou, J.; Choi, W.; Ajayan, P. M.; Tour, J. M. *ACS Nano* **2013,** *7,* 58–64. doi:10.1021/nn3015882
7. Wang, X.; Zhi, L.; Müllen, K. *Nano Lett.* **2008,** *8,* 323–327. doi:10.1021/nl072838r
8. Zhan, H. F.; Xia, K.; Gu, Y. T. *Int. J. Comput. Mater. Sci. Eng.* **2013,** *2,* 1350020. doi:10.1142/S2047684113500206
9. Fan, Z.; Yan, J.; Zhi, L.; Zhang, Q.; Wei, T.; Feng, J.; Zhang, M.; Qian, W.; Wei, F. *Adv. Mater.* **2010,** *22,* 3723–3728. doi:10.1002/adma.201001029
10. Mortazavi, B.; Ahzi, S.; Toniazzo, V.; Rémond, Y. *Phys. Lett. A* **2012,** *376,* 1146–1153. doi:10.1016/j.physleta.2011.11.034
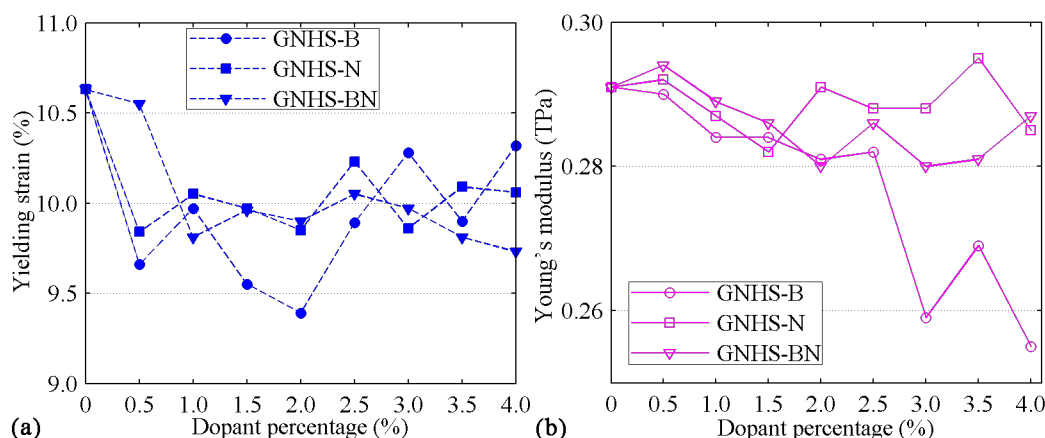

Figure 9: Yield strain, *YP*, and Young's modulus, *E*, as a function of the concentration of N-, B-, and NB-dopants.

11. Wang, Y.; Shao, Y.; Matson, D. W.; Li, J.; Lin, Y. *ACS Nano* **2010,** *4,* 1790–1798. doi:10.1021/nn100315s

12. Panchakarla, L. S.; Subrahmanyam, K. S.; Saha, S. K.; Govindaraj, A.; Krishnamurthy, H. R.; Waghmare, U. V.; Rao, C. N. R. *Adv. Mater.* **2009,** *21,* 4726–4730. doi:10.1002/adma.200901285

13. Voggu, R.; Das, B.; Rout, C. S.; Rao, C. N. R. *J. Phys.: Condens. Matter* **2008,** *20,* 472204. doi:10.1088/0953-8984/20/47/472204

14. Ohta, T.; Bostwick, A.; Seyller, T.; Horn, K.; Rotenberg, E. *Science* **2006,** *313,* 951–954. doi:10.1126/science.1130681

15. Wang, H.; Maiyalagan, T.; Wang, X. *ACS Catal.* **2012,** *2,* 781–794. doi:10.1021/cs200652y

16. Lv, R.; Cui, T.; Jun, M.-S.; Zhang, Q.; Cao, A.; Su, D. S.; Zhang, Z.; Yoon, S.-H.; Miyawaki, J.; Mochida, I.; Kang, F. *Adv. Funct. Mater.* **2011,** *21,* 999–1006. doi:10.1002/adfm.201001602

17. Plimpton, S. *J. Comput. Phys.* **1995,** *117,* 1–19. doi:10.1006/jcph.1995.1039

18. Matsumoto, T.; Saito, S. *J. Phys. Soc. Jpn.* **2002,** *71,* 2765–2770. doi:10.1143/JPSJ.71.2765

19. Dimitrakakis, G. K.; Tylianakis, E.; Froudakis, G. E. *Nano Lett.* **2008,** *8,* 3166–3170. doi:10.1021/nl801417w

20. Novaes, F. D.; Rurali, R.; Ordejón, P. *ACS Nano* **2010,** *4,* 7596–7602. doi:10.1021/nn102206n

21. Varshney, V.; Patnaik, S. S.; Roy, A. K.; Froudakis, G.; Farmer, B. L. *ACS Nano* **2010,** *4,* 1153–1161. doi:10.1021/nn901341r

22. Wei, Y.; Zhan, H. F.; Xia, K.; Sang, S. B.; Gu, Y. T. *Beilstein J. Nanotechnol.* submitted.

23. Brenner, D. W.; Shenderova, O. A.; Harrison, J. A.; Stuart, S. J.; Ni, B.; Sinnott, S. B. *J. Phys.: Condens. Matter* **2002,** *14,* 783. doi:10.1088/0953-8984/14/4/312

24. Zhang, Y. Y.; Wang, C. M.; Cheng, Y.; Xiang, Y. *Carbon* **2011,** *49,* 4511–4517. doi:10.1016/j.carbon.2011.06.058

25. Tersoff, J. *Phys. Rev. B* **1988,** *37,* 6991–7000. doi:10.1103/PhysRevB.37.6991

26. Belytschko, T.; Xiao, S. P.; Schatz, G. C.; Ruoff, R. S. *Phys. Rev. B* **2002,** *65,* 235430. doi:10.1103/PhysRevB.65.235430

27. Jeong, B.-W.; Lim, J.-K.; Sinnott, S. B. *Appl. Phys. Lett.* **2007,** *90,* 023102–023102-3. doi:10.1063/1.2430490

28. Hoover, W. G. *Phys. Rev. A* **1985,** *31,* 1695–1697. doi:10.1103/PhysRevA.31.1695

29. Nosé, S. *J. Chem. Phys.* **1984,** *81,* 511. doi:10.1063/1.447334

30. Verlet, L. *Phys. Rev.* **1967,** *159,* 98–103. doi:10.1103/PhysRev.159.98

31. Turgut, G.; Keskenler, E. F.; Aydin, S.; Sönmez, E.; Doğan, S.; Düzgün, B.; Ertuğrul, M. *Superlattices Microstruct.* **2013,** *56,* 107–116. doi:10.1016/j.spmi.2013.01.004

32. Jun, Y.-K.; Moon, W.-T.; Chang, C.-M.; Kim, H.-S.; Ryu, H. S.; Kim, J. W.; Kim, K. H.; Hong, S.-H. *Solid State Commun.* **2005,** *135,* 133–137. doi:10.1016/j.ssc.2005.03.038

33. Arbiol, J.; Cerdá, J.; Dezanneau, G.; Cirera, A.; Peiró, F.; Cornet, A.; Morante, J. R. *J. Appl. Phys.* **2002,** *92,* 853–861. doi:10.1063/1.1487915

34. Klissurska, R. D.; Brooks, K. G.; Reaney, I. M.; Pawlaczyk, C.; Kosec, M.; Setter, N. *J. Am. Ceram. Soc.* **1995,** *78,* 1513–1520. doi:10.1111/j.1151-2916.1995.tb08846.x

35. Koh, S. J. A.; Lee, H. P. *Nanotechnology* **2006,** *17,* 3451. doi:10.1088/0957-4484/17/14/018

A catechol biosensor based on electrospun carbon nanofibers

Dawei Li, Zengyuan Pang, Xiaodong Chen, Lei Luo, Yibing Cai and Qufu Wei[*]

Full Research Paper

Address:
Key Laboratory of Eco-Textiles of Ministry of Education, Jiangnan University, Wuxi 214122, P. R. China

Email:
Qufu Wei[*] - qfwei@jiangnan.edu.cn

* Corresponding author

Abstract

Carbon nanofibers (CNFs) were prepared by combining electrospinning with a high-temperature carbonization technique. And a polyphenol biosensor was fabricated by blending the obtained CNFs with laccase and Nafion. Raman spectroscopy, Fourier transform infrared spectroscopy (FTIR) and field emission scanning electron microscope (FE-SEM) were, respectively, employed to investigate the structures and morphologies of the CNFs and of the mixtures. Cyclic voltammetry and chronoamperometry were employed to study the electrocatalysis of the catechol biosensor. The results indicated that the sensitivity of the biosensor was 41 $\mu A \cdot mM^{-1}$, the detection limit was 0.63 μM, the linear range was 1–1310 μM and the response time was within 2 seconds, which excelled most other laccase-based biosensor reported. Furthermore, the biosensor showed good repeatability, reproducibility, stability and tolerance to interferences. This novel biosensor also demonstrated its promising application in detecting catechol in real water samples.

Introduction

Nowadays, carbon nanomaterials attract a great deal of attention due to their high surface area, excellent electronic conduction and biocompatibility. Among these, mesoporous carbon [1-8], activated or porous carbon nanofibers [9-19] have been widely studied. Notably, the carbon nanofibers (CNFs) possess a history of more than a century, the carbon filaments discovered in 1889 may be the earliest CNFs [20]. After more than a century of development, various methods used for CNFs preparation are established, such as arc-discharge [21], laser ablation [22], chemical vapor deposition (CVD) methods [23]. Electrospinning, which is known as a facile and convenient process, can produce nanofibers or microfibers with different diameters while using a variety of polymers. The carbonization of electrospun polyacrylonitrile nanofibers can be employed to

fabricate CNFs [24]. Lin et al. reported that an electrospun-CNF-modified carbon-paste electrode (CNF–CPE) could be used for the mediatorless detection of NADH [25]. Electrodes modified with Pd/CNFs showed excellent electrocatalytic activities towards dopamine (DA), uric acid (UA) and ascorbic acid (AA) [26]. NiCF-paste (NiCFP) electrodes displayed excellent electrocatalytic capacity for the oxidation of glucose [27]. These works indicate that electrospun CNFs (ECNFs) harbor excellent electrocatalytic properties. However, it is rarely reported that ECNFs were utilized directly in the design of enzyme-based biosensors.

Phenolic compounds, which widely occur in processes of agriculture and industry, often cause severe health problems in human beings and animals [28]. So it is important to develop fast and effective methods to detect phenolic compounds. Laccase (benzendiol:oxygen oxidoreductases; EC 1.10.3.2), a multicopper oxidase widely distributed in plant and fungal species, can reduce oxygen directly to water through a four-electron transfer step, and this chemical reaction does not produce hydrogen peroxide (H_2O_2) [29]. Based on this, laccase has been utilized to fabricate a variety of biosensors, including biosensors for phenolic compounds [30]. Nafion, a linear perfluorosulfonate polymer possesses good cation-exchange properties, biocompatibility and film-forming properties and has been widely applied in the fields of fuel cells and sensors [31,32].

In the present work, we prepared ECNFs by carbonizing electrospun PAN nanofibers, and a novel catechol biosensor was fabricated through dropping a mixture solution made of ECNFs, laccase and Nafion on a processed glass-like-carbon electrode (GCE). Our results showed that the Laccase–Nafion–ECNFs sensor exhibited a noticeable eletrocatalytic ability towards catechol, and had a linear response range from 1 μM to 1310 μM with a detection limit of 0.63 μM, which all excelled

most other laccase-based biosensors [33-36]. The biosensor was successfully applied in the detection of catechol in real water samples.

Results and Discussion
Morphology analysis

The SEM images of ECNFs and laccase–Nafion–ECNFs/GCE are shown in Figure 1. As can be seen from Figure 1a, the randomly distributed ECNFs formed a fibrous web with an average fiber diameter of about 200 nm. The insert displays the diameter distribution of the ECNFs, which ranges from 50 to 380 nm and mainly focuses on 100 to 200 nm. Notably, many ECNFs were broken up into short fibers because the thermal treatment process enabled the fibers to become fragile. Figure 1b exhibits the surface morphology of the laccase–Nafion–ECNFs/GCE. It can be clearly seen that most of the short fibers were embedded into the laccase. Here, the short fibers may play a role of connecting the active center of laccase and the surface of GCE, which may be favorable for the electron transfer.

Structure and component analysis

The obtained ECNFs were, respectively, investigated by Raman and FTIR spectroscopy (Figure 2a and Figure 2b). As shown in Figure 2a, there are two characteristic peaks appearing at about 1330 and 1590 cm^{-1}, which were related to the D-band and the G-band, respectively. The D-band was attributed to the defective carbon structure of the ECNFs, and the G-band could be ascribed to the in-plane carbon–carbon stretching vibrations of graphite layers [37]. This demonstrated that the ECNFs possessed polycrystalline structures and massive disordered and defected graphite layers. FTIR was employed to further study the functional groups on the surfaces of the ECNFs (Figure 2b). It is manifest that two distinct absorbance peaks, respectively, appeared at around 1710 and 1450 cm^{-1}. And the two absorbance peaks were ascribed to the stretching vibration of the
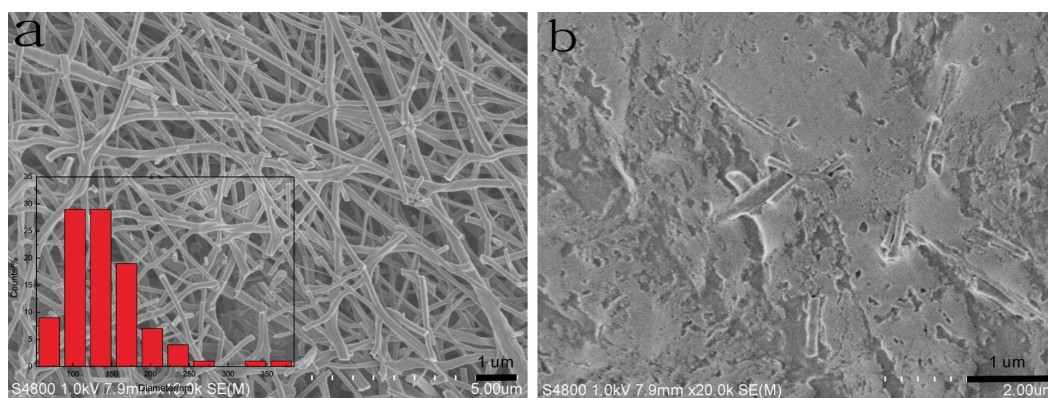

Figure 1: SEM images of the ECNFs (a) and the suface of laccase–Nafion–ECNFs/GCE (b). Insert: the diameter distribution diagram of the ECNFs.
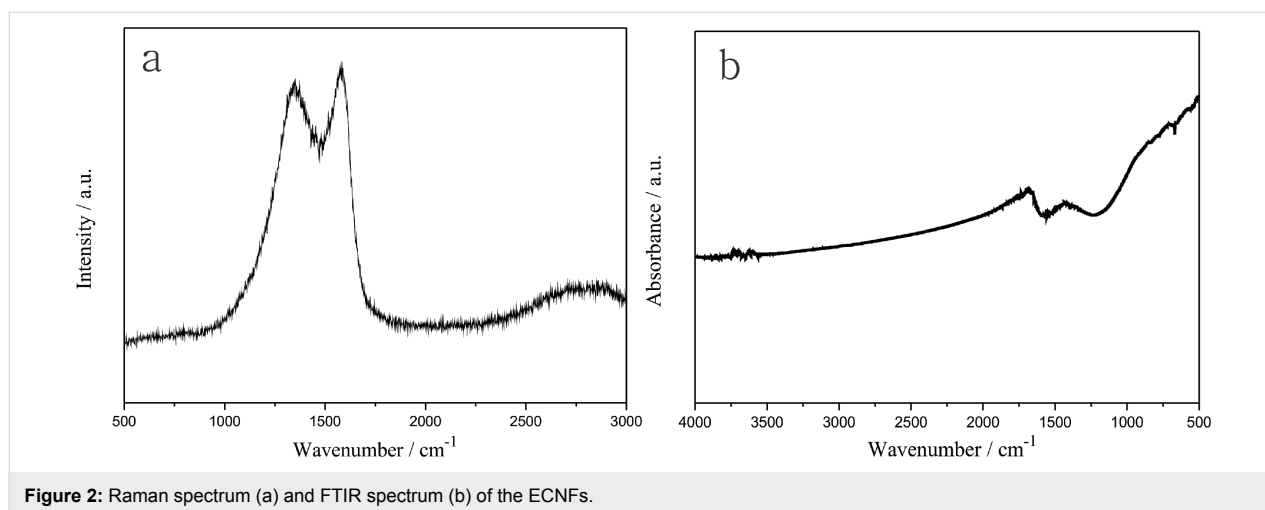
Figure 2: Raman spectrum (a) and FTIR spectrum (b) of the ECNFs.

C=O bond of carboxyl [38] and the O–H bond [39]. This proved that there were numerous carboxyl groups on the surfaces of the ECNFs which were expected to improve the electrocatalytic properties and biocompatibility of the ECNFs [40].

The three solutions, containing laccase, laccase–Nafion, and laccase–Nafion–ECNFs, respectively, were stored in refrigerator at 4 °C for two weeks and a certain amount of the three solutions was dropped onto a glass slide. Three thin films could be obtained after drying the solutions at room temperature. Figure 3 shows the FTIR spectra of the three dried thin films. The characteristic peak at approximately 1670 cm^{-1} could be attributed to the FTIR spectrum of the amide-I band of native laccase [41]. Similarly, some other bands, e.g., at 1066 and 1403 cm^{-1}, which can also be ascribed to laccase, were observed in the three FTIR spectra of Figure 3a–c [41]. It can be clearly seen that the FTIR spectra of laccase–Nafion (Figure 3b) and laccase–Nafion–ECNFs (Figure 3c) solutions were similar with the one of pure laccase solution (Figure 3a), suggesting that laccase in the Nafion and the Nafion–ECNFs mixture both kept its activity and the ECNFs demonstrated their good biocompatibility with laccase. In addition, the laccase activity was also studied. The pristine laccase possessed an enzyme activity of 11.2 U/mg while this value decreased to 10.1 and 10.7 U/mg after the laccase was immobilized in the Nafion and Nafion–ECNFs, respectively. This also confirmed the good biocompatibility of Nafion and ECNFs and showed that the immobilization process had little influence on the activity of laccase.

Direct electrochemistry and electrocatalysis of the laccase–Nafion–ECNFs/GCE

Figure 4 presents the cyclic voltammograms of the laccase–Nafion–ECNFs/GCE in acetate buffer (pH 4.0) with
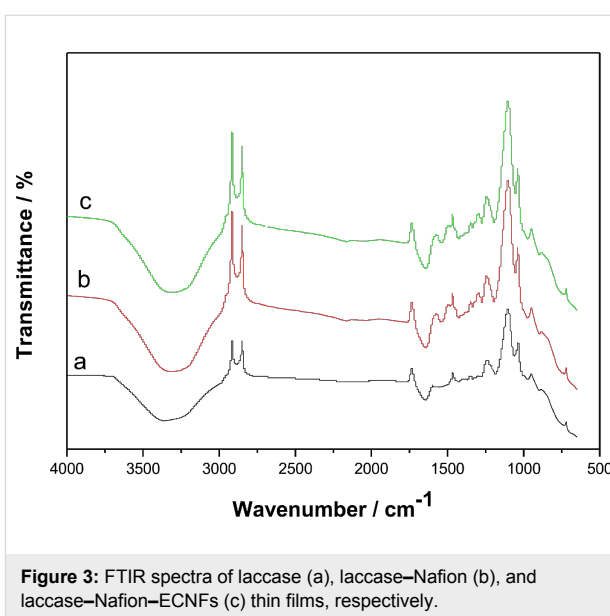
Figure 3: FTIR spectra of laccase (a), laccase–Nafion (b), and laccase–Nafion–ECNFs (c) thin films, respectively.

scan rates from 0.05 to 0.3 V·s^{-1}. It can be clearly seen that a pair of stable and well-defined quasi-reversible anodic and cathodic peaks occur, which can be attributed to the direct electron transfer between the laccase and the GCE. Besides, the anodic peak currents were larger than the peak cathodic currents, indicating a quasi-reversible electrochemical reaction process. Simultaneously, both of the currents increased with the rise of scan rates, the redox peak potentials shifted slightly with an increase in the distance between anodic peak and cathodic peak. As can be seen from the inset of Figure 4, the currents corresponding to redox peaks grew linearly with the scan rates from 0.05 to 0.3 V·s^{-1}. This indicated that the electron transfer occurred easily between the laccase–Nafion–ECNFs composite and the surface of the GC electrode and that the electrochemical activity of the whole process is surface-controlled.
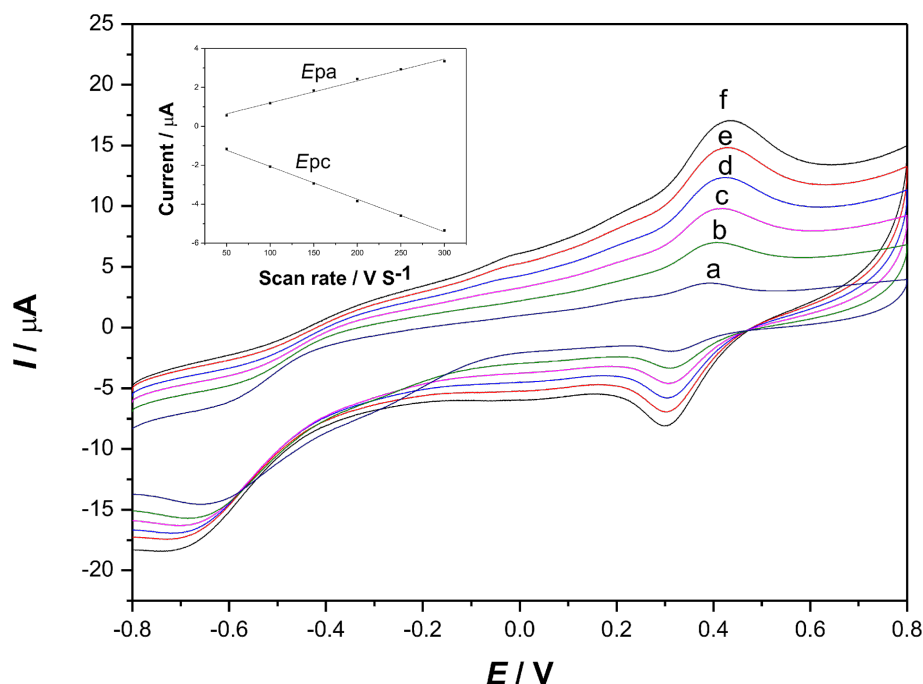
Figure 4: Cyclic voltammograms of the laccase–Nafion–ECNFs/GCE in acetate buffer (pH 4.0) with different scan rates (V·s^{-1}): (a) 0.05; (b) 0.1; (c) 0.15; (d) 0.2; (e) 0.25; (f) 0.3. Inset: Calibration plot of anodic and cathodic peak currents vs scan rates.

Optimization of the enzyme electrodes

Figure 5 shows the cyclic voltammograms of different enzyme electrodes toward 300 µM catechol in 0.2 M acetate buffer (pH 4.0). Compared with the peak current values of laccase/GCE (Figure 5b), those of the laccase–Nafion/GCE (Figure 5a) were smaller, which could be attributed to that Nafion impeded the transfer of electrons, to some extent. It is noticeable that the peak current values of the laccase–Nafion–ECNFs/GCE (Figure 5c) are larger than those of the laccase/GCE and the

separation of peak potentials apparently decreased. This fully demonstrated that the ECNFs enhanced the conductivity of the composite and led to a faster electron transfer. The reaction mechanism is illustrated in Figure 6. First, the catechol on contact with the Lac was oxidized to 1,2-benzoquinone in the presence of molecular oxygen. Subsequently, the 1,2-benzo-quinone was reduced electrochemically at the surface of the GCE.

Figure 5: Cyclic voltammograms of laccase–Nafion/GCE (a), laccase/GCE (b), laccase–Nafion–ECNFs/GCE (c) toward 300 µM catechol in 0.2 M acetate buffer (pH 4.0).
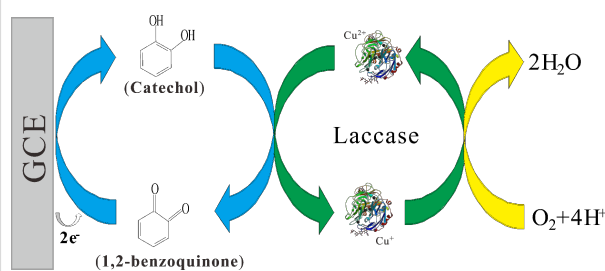
Figure 6: Schematic representation of laccase-catalyzed oxidation of catechol with its subsequent electrochemical reduction on the GCE.

To acquire the optimal amperometric response, the effects of the pH value of the solution and of the applied potential on the current values were, respectively, investigated. As shown in Figure 7a, the current value reached the peak at pH 5.5, and then showed a dramatic decrease, which agreed with a
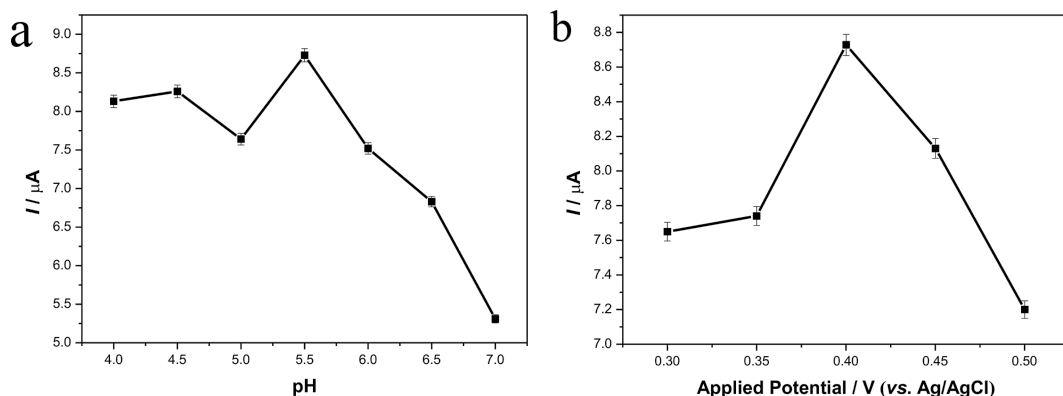
Figure 7: Influences of solution pH (at 0.4 V) (a) and applied potential (pH 5.5) (b) on the steady-state current response of 200 μM catechol in 0.2 M acetate buffer.

previous report [34]. Figure 7b presents the influences of different applied potentials on the amperometric responses. It can be clearly seen that the maximum current value came at 0.4 V. So the applied potential was set at 0.4 V in the following experiments.

Amperometric response of the biosensor

The steady-state amperometric responses of the laccase–Nafion–ECNFs/GCE to different concentrations of catechol were determined by the successive addition of different volumes of 2 mM and 20 mM catechol into 20 mL acetate buffer (pH 5.5). It can be seen from Figure 8b that with the successive addition of catechol, the steady-state current values gradually increased. Figure 8a displays the magnified image of Figure 8b before 400 s, the first current step happened when adding 20 nM catechol into the acetate buffer. The insert in Figure 8a shows the rapid response of the biosensor toward

catechol (attaining 95% of the value of the steady current within 2 s, which is shorter than in a previous report [35]). This sensitive response may be caused by the prompt diffusion of the analytes into the porous composite. The insert in Figure 8b shows the linear calibration curve of the current response on the catechol concentration. It can be seen that the response current increased with the increase in catechol concentration. The linear range was 1–1310 μM (R = 0.998, *n* = 19), which was much wider than for the biosensor based on CNTs and laccase [33]. And the sensitivity was 41 μA·mM^{-1}, the detection limit was as low as 0.63 μM (S/N = 3). The apparent Michaelis–Menten constant (K_M^{app}) was estimated to be 50.64 μM according to the electrochemical version of the Lineweaver–Burk equation [42]. Table 1 compares several laccase-based biosensors. It can be seen that the laccase–Nafion–ECNFs/GCE exhibits a quite outstanding analytical performance and this new sensor could be useful in the detection of catechol.
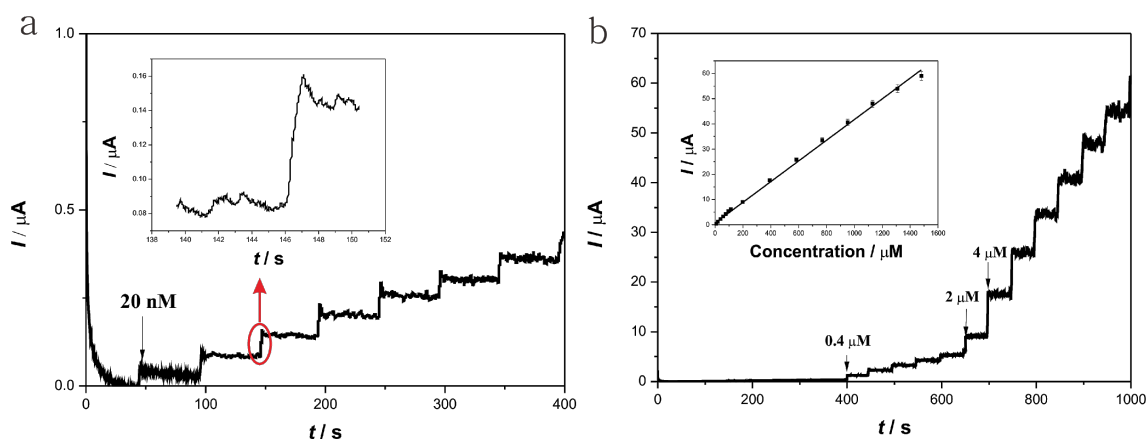
Figure 8: Typical steady-state current response of the laccase–Nafion–ECNFs/GCE on the successive addition of catechol solutions with different concentrations and volumes into 0.2 M acetate buffer (pH 5.5). Inset: A magnification of the third addition of catechol (a); The linear calibration curve of the current response on the catechol concentration (b).

Table 1: Performance comparison of different laccase modified electrodes.

| electrode description	detection limit (µM)	linear range (µM)	sensitivity[a] (µA·mM^{-1})	reference
laccase/CNTs–CS/GCE	0.66	1.2–30	–	[33]
Lac/AP-rGOs/Chit/GCE	7	15–700	15.79	[34]
MB-MCM-41/PVA/lac	0.331	4–87.98	–	[35]
Cu-OMC/Lac/CS/Au	0.67	0.67–13.8	104	[36]
laccase–Nafion–ECNFs/GCE	0.63	1–1310	41	this work

[a]The dash indicates no reported value.

Interferences and biosensor stability

Catechol and some other phenolic compounds, including catechin, epicatechin, gallic acid, guaiacol, phenol and aminophenol, were used to determinate the selectivity of the biosensor (Figure 9). The biosensor showed excellent selectivity for catechol (set to 100%) and exhibited almost no response to other phenolic compounds.
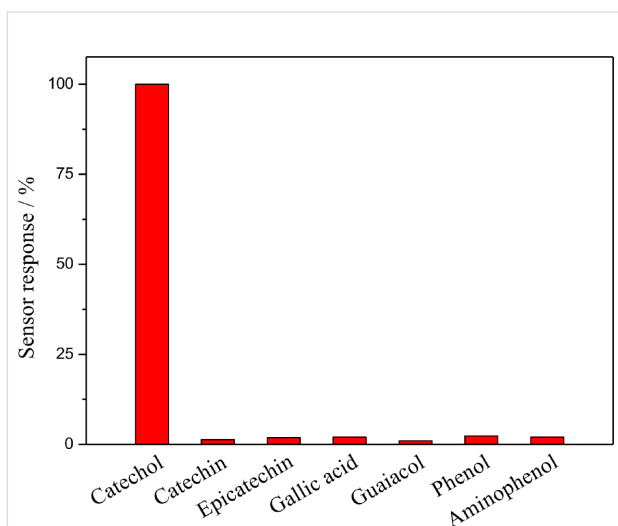
Figure 9: Relative responses of the laccase–Nafion–ECNFs/GCE for different phenolic compounds (catechol, catechin, epicatechin, gallic acid, guaiacol, phenol and aminophenol; 100 µM in 0.2 M acetate buffer (pH 5.5), respectively).

The biosensor showed good repeatability, reproducibility and stability. The biosensor was used to measure successively for 10 times in a certain concentration of catechol solution, and the relative standard deviation (RSD) of the response current value was within 2.0%, which indicating the biosensor possessed good repeatability. Besides, we prepared five biosensors under the same conditions, and the RSD of the response current values of five modified electrodes was 3.5%, which indicates that the biosensor had acceptable reproducibility. Figure 10 shows the storage stability of the laccase–Nafion–ECNFs/GCE in 0.2 M air-saturated acetate buffer (pH 4.0) at 4 °C. It is manifest that

over a storage period of one month, the current response only decreases slightly. Even after 30 days, the current response retained 96.3% of the initial value, which indicated that the laccase preserved its activity well in the mixture of Nafion and ECNFs and that the biosensor possessed good stability.
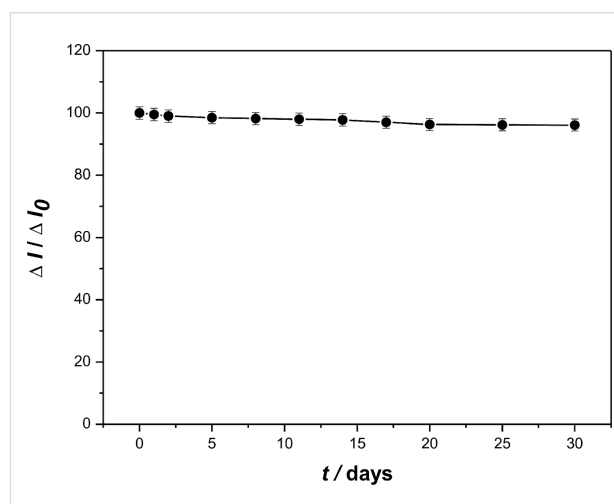
Figure 10: Storage stability of the laccase–Nafion–ECNFs/GCE in 0.2 M acetate buffer (pH 4.0) at 4 °C.

Application to water samples

To demonstrate the practical application of the catechol sensor, the response of the sensor in water samples was investigated. As shown in Table 2, based on the equation of calibration curve, $I = 0.041c + 0.668$ (I in µA, c in µM), the corresponding amount of catechol could be calculated. The recoveries looked satisfactory, confirming that the biosensor can realize its practical application in detecting phenols in real samples.

Conclusion

Carbon nanofibers with excellent electrochemical properties and biocompatibility were fabricated by electrospinning and high temperature carbonization techniques. And the ECNFs were employed to design a novel laccase-based biosensor, which displayed outstanding sensitivity to catechol with a wide linear range, a low detection limit and a fast response. Further-

Table 2: Recovery experiment of detection of catechol in real water samples.

sample	c_{added} (µM)	c_{found} (µM)	recovery (%)	RSD (%)
tap water	100	101.7	101.7	1.6
		99.2	99.2	
		99.7	99.7	
		98.6	98.6	
		97.3	97.3	
Taihu Lake water	100	103.4	103.4	3.5
		102.1	102.1	
		96.1	96.1	
		97.2	97.2	
		96.5	96.5	

more, the biosensor also displayed good repeatability, reproducibility and stability, and was successfully applied in detecting catechol in real samples.

Experimental
Materials
Laccase, Nafion and 2,2'-azinobis(3-ethylbenzothiazole-6-sulfonic acid) (ABTS) were purchased from Sigma-Aldrich. Other chemical reagents were obtained from Sinopharm Group Chemical Reagent Co., Ltd. (Shanghai, China). All reagents were analytical grade and used without further purification. All aqueous solutions were prepared with Milli-Q purified water (>18.0 MΩ·cm). The acetate buffer system (containing 0.2 M HAC-NaAC) was selected as buffer solution.

Apparatus
A Hitachi S-4800 field-emission scanning electron microscope (FE-SEM) was used to examine the surface morphologies of the ECNFs and the laccase–Nafion–ECNFs/GCE. The Raman spectrum analysis was carried out at room temperature using a 3D Nanometer Scale Raman PL Microspectrometer (Tokyo Instruments, Inc., with a 785 nm He–Ne laser). Fourier transform infrared (FTIR) spectra were recorded in the range of 500–4000 cm^{-1} on a Nicolet iS10 FTIR spectrometer (Thermo Fisher Scientific). Electrochemical experiments were carried out at room temperature by using a CHI 660D electrochemical workstation (CH Instruments, Inc., Austin, USA). A UV spectrophotometer (UNNICO Instruments Co., Ltd., Shanghai) was used to calculate the activity of laccase.

Preparation of ECNFs
The ECNFs were prepared by the following steps. Firstly, the electrospinning solution was prepared by dissolving 10 wt % polyacrylonitrile (PAN) powders in DMF with magnetic stirring for 8 h. Secondly, the prepared solution was added into a syringe for electrospinning. The experimental parameters were set to a voltage of 15 kV, a working distance of 15 cm, and a flow rate of 0.5 mL/h respectively. Lastly, a high temperature furnace was employed to stabilize and carbonize the PAN nanofibers. The whole process was conducted in N$_2$ atmosphere and could be divided into two phases: (1) Heating up to 300 °C at a rate of 2 °C·min^{-1} and keeping this temperature for 2 h. This process was for stabilizing the shape of nanofibers. (2) Heating up to 1000 °C at a rate of 5 °C·min^{-1} to carbonize the nanofibers, keeping the highest temperature for 2 h, and then cooling down to room temperature.

Preparation of the modified electrodes
Considering the current response and the stability of modified electrode, in control experiments, the concentrations and mass ratio of Nafion, ECNFs and laccase were optimized. Ultimately, the biosensor was fabricated by using a mixture containing 1.5 wt % Nafion, 0.4 mg·mL^{-1} ECNFs and 3 mg·mL^{-1} laccase.

A typical procedure for the preparation of the laccase–Nafion–ECNFs/GCE is as follows: First, with the help of ultrasonication and stirring, 4 mg ECNFs is added into 10 mL acetate buffer (pH 4.0) to obtain ECNFs suspension. Next, a mixture containing a certain volume of Nafion (5 wt %), ECNFs suspension and the appropriate mass of laccase was kept stirring for 1 h. Finally, the laccase–Nafion–ECNFs/GCE was prepared by dropping 10 µL of the mixture onto the surface of a freshly polished glass carbon electrode. The glass carbon electrode was processed as follows: Firstly, it was polished with alumina. Following that, it was rinsed by water and ultrasonicated in ethanol and water. Finally, it was dried under a nitrogen atmosphere. The dried laccase–Nafion–ECNFs/GCE was kept in storage at 4 °C.

Meanwhile, laccase–Nafion/GCE and laccase/GCE were prepared to compare with the laccase–Nafion–ECNFs/GCE. The laccase/GCE was prepared by using a solution containing 3 mg·mL^{-1} laccase and the laccase-Nafion/GCE was prepared by using a solution containing 1.5 wt % Nafion and 3 mg·mL^{-1} laccase. Herein, the mass of laccase in different electrodes should be kept equal. In addition, all the electrodes were dipped into acetate buffer (pH 4.0) for 30 min to remove the unstable compounds before electrochemical measurements.

Determination of the activity of free and immobilized laccase
To investigate the effect of the immobilization process on the laccase activity we, respectively, studied the free and immobilized laccase activity according to the reported method [43]. The activity of laccase was determined by the UV spectrophotometer at 420 nm using ABTS as the substrate. One unit of

laccase activity was defined as the amount of laccase to catalyse 1 μM of ABTS per minute.

Preparation of water samples

To start with, a microporous membrane was used to filter the prepared water samples (tap water from our lab and water from Taihu Lake). Next, the filtered water samples were added into 0.2 M (pH 5.5) acetate buffer to dilute them (double dilution). Afterward, the diluted water samples were added into 20 mL of 0.2 M air-saturated acetate buffer (pH 5.5). Finally, an amperometric detection (repeated five times) based on the laccase–Nafion–ECNFs/GCE at 0.4 V was conducted after adding 100 μM catechol into the solutions.

Acknowledgements

References

1. Ryoo, R.; Joo, S. H.; Kruk, M.; Jaroniec, M. *Adv. Mater.* **2001,** *13,* 677–681.
   doi:10.1002/1521-4095(200105)13:9<677::AID-ADMA677>3.3.CO;2-3
2. Kim, T.-W.; Park, I.-S.; Ryoo, R. *Angew. Chem.* **2003,** *115,* 4511–4515.
   doi:10.1002/ange.200352224
3. Li, Z. L.; Zhang, J.; Li, Y.; Guan, Y. J.; Feng, Z. C.; Li, C.
   J. Mater. Chem. **2006,** *16,* 1350–1354. doi:10.1039/b512697e
4. Joo, S. H.; Choi, S. J.; Oh, I.; Kwak, J.; Liu, Z.; Terasaki, O.; Ryoo, R.
   Nature **2001,** *412,* 169–172. doi:10.1038/35084046
5. Zhou, H.; Zhu, S.; Honma, I.; Seki, K. *Chem. Phys. Lett.* **2004,** *396,*
   252–255. doi:10.1016/j.cplett.2004.07.120
6. Vinu, A.; Ariga, K.; Mori, T.; Nakanishi, T.; Hishita, S.; Golberg, D.;
   Bando, Y. *Adv. Mater.* **2005,** *17,* 1648–1652.
   doi:10.1002/adma.200401643
7. Lee, J.; Kim, J.; Lee, Y.; Yoon, S.; Oh, S. M.; Hyeon, T. *Chem. Mater.*
   2004, *16,* 3323–3330. doi:10.1021/cm034588v
8. Yang, H.; Yan, Y.; Liu, Y.; Zhang, F.; Zhang, R.; Meng, Y.; Li, M.;
   Xie, S. H.; Tu, B.; Zhao, D. Y. *J. Phys. Chem. B* **2004,** *108,*
   17320–17328. doi:10.1021/jp046948n
9. Tao, X. Y.; Zhang, X. B.; Zhang, L.; Cheng, J. P.; Liu, F.; Luo, J. H.;
   Luo, Z. Q.; Geise, H. J. *Carbon* **2006,** *44,* 1425–1428.
   doi:10.1016/j.carbon.2005.11.024
10. Yang, K. S.; Kim, C.; Park, S. H.; Kim, J. H.; Lee, W. J.
    J. Biomed. Nanotechnol. **2006,** *2,* 103–105. doi:10.1166/jbn.2006.017
11. Kim, C. *J. Power Sources* **2005,** *142,* 382–388.
    doi:10.1016/j.jpowsour.2004.11.013
12. Merino, C.; Soto, P.; Vilaplana-Ortego, E.; de Salazar, J. M. G.;
    Pico, F.; Rojo, J. M. *Carbon* **2005,** *43,* 551–557.
    doi:10.1016/j.carbon.2004.10.018
13. Kim, S.-U.; Lee, K.-H. *Chem. Phys. Lett.* **2004,** *400,* 253–257.
    doi:10.1016/j.cplett.2004.10.124
14. Yoon, S.-H.; Lim, S.; Song, Y.; Ota, Y.; Qiao, W.; Tanaka, A.;
    Mochida, I. *Carbon* **2004,** *42,* 1723–1729.
    doi:10.1016/j.carbon.2004.03.006
15. Luxembourg, D.; Py, X.; Didion, A.; Gadiou, R.; Vix-Guterl, C.;
    Flamant, G. *Microporous Mesoporous Mater.* **2007,** *98,* 123–131.
    doi:10.1016/j.micromeso.2006.08.024
16. Lim, S.; Hong, S.-H.; Qiao, W.; Whitehurst, D. D.; Yoon, S.-H.;
    Mochida, I.; An, B.; Yokogawa, K. *Carbon* **2007,** *45,* 173–179.
    doi:10.1016/j.carbon.2006.07.009
17. Li, P.; Zhao, T.-J.; Zhou, J.-H.; Sui, Z.-J.; Dai, Y.-C.; Yuan, W.-K.
    Carbon **2005,** *43,* 2701–2710. doi:10.1016/j.carbon.2005.05.038
18. Suzuki, M. *Carbon* **1994,** *32,* 577–586.
    doi:10.1016/0008-6223(94)90075-2
19. Li, Y.-Y.; Mochidzuki, K.; Sakoda, A.; Suzuki, M. *Carbon* **2001,** *39,*
    2143–2150. doi:10.1016/S0008-6223(01)00033-1
20. De Jong, K. P.; Geus, J. W. *Catal. Rev.: Sci. Eng.* **2000,** *42,* 481–510.
    doi:10.1081/CR-100101954
21. Zhao, X. F.; Qiu, J. H.; Sun, Y. X.; Hao, C.; Sun, T. J.; Cui, L. W.
    New Carbon Mater. **2009,** *24,* 109–113.
22. Guo, T.; Nikolaev, P.; Rinzler, A. G.; Tomanek, D.; Colbert, D. T.;
    Smalley, R. E. *J. Phys. Chem.* **1995,** *99,* 10694–10697.
    doi:10.1021/j100027a002
23. Boskovic, B. O.; Stolojan, V.; Khan, R. U. A.; Haq, S.; Silva, S. R. P.
    Nat. Mater. **2002,** *1,* 165–168. doi:10.1038/nmat755
24. Wang, Y.; Serrano, S.; Santiago-Avilés, J. J. *Synth. Met.* **2003,** *138,*
    423–427. doi:10.1016/S0379-6779(02)00472-1
25. Liu, Y.; Hou, H.; You, T. *Electroanalysis* **2008,** *20,* 1708–1713.
    doi:10.1002/elan.200804242
26. Huang, J.; Liu, Y.; Hou, H.; You, T. *Biosens. Bioelectron.* **2008,** *24,*
    632–637. doi:10.1016/j.bios.2008.06.011
27. Liu, Y.; Teng, H.; Hou, H.; You, T. *Biosens. Bioelectron.* **2009,** *24,*
    3329–3334. doi:10.1016/j.bios.2009.04.032
28. Singh, S.; Jain, D. V. S.; Singla, M. L. *Sens. Actuators, B* **2013,** *182,*
    161–169. doi:10.1016/j.snb.2013.02.111
29. Chawla, S.; Rawal, R.; Pundir, C. S. *J. Biotechnol.* **2011,** *156,* 39–45.
    doi:10.1016/j.jbiotec.2011.08.008
30. Minussi, R. C.; Pastore, G. M.; Durán, N. *Trends Food Sci. Technol.*
    2002, *13,* 205–216. doi:10.1016/S0924-2244(02)00155-3
31. He, Q.; Joy, D. C.; Keffer, D. J. *J. Power Sources* **2013,** *241,* 634–646.
    doi:10.1016/j.jpowsour.2013.05.011
32. Kumar, S.; Vicente-Beckett, V. *Beilstein J. Nanotechnol.* **2012,** *3,*
    388–396. doi:10.3762/bjnano.3.45
33. Liu, Y.; Qu, X.; Guo, H.; Chen, H.; Liu, B.; Dong, S.
    Biosens. Bioelectron. **2006,** *21,* 2195–2201.
    doi:10.1016/j.bios.2005.11.014
34. Zhou, X.-H.; Liu, L.-H.; Bai, X.; Shi, H.-C. *Sens. Actuators, B* **2013,**
    181, 661–667. doi:10.1016/j.snb.2013.02.021
35. Xu, X.; Lu, P.; Zhou, Y.; Zhao, Z.; Guo, M. *Mater. Sci. Eng., C* **2009,**
    29, 2160–2164. doi:10.1016/j.msec.2009.04.019
36. Xu, X.; Guo, M.; Lu, P.; Wang, R. *Mater. Sci. Eng., C* **2010,** *30,*
    722–729. doi:10.1016/j.msec.2010.03.006
37. Sakae, T.; Yo, T.; Emi, K.; Kiyoshi, O. *Fuel* **2004,** *83,* 47–57.
    doi:10.1016/S0016-2361(03)00211-4

38. Rand, E.; Periyakaruppan, A.; Tanaka, Z.; Zhang, D. A.; Marsh, M. P.; Andrews, R. J.; Lee, K. H.; Chen, B.; Meyyappan, M.; Koehne, J. E. *Biosens. Bioelectron.* **2013,** *42,* 434–438. doi:10.1016/j.bios.2012.10.080

39. Kumar, S.; Lively, B.; Sun, L. L.; Li, B.; Zhong, W. H. *Carbon* **2010,** *48,* 3846–3857. doi:10.1016/j.carbon.2010.06.050

40. Ratinac, K. R.; Yang, W.; Gooding, J. J.; Thordarson, P.; Braet, F. *Electroanalysis* **2011,** *23,* 803–806. doi:10.1002/elan.201000545

41. Mazur, M.; Krywko-Cendrowska, A.; Krysiński, P.; Rogalski, J. *Synth. Met.* **2009,** *159,* 1731–1738. doi:10.1016/j.synthmet.2009.05.018

42. Kamin, R. A.; Wilson, G. S. *Anal. Chem.* **1980,** *52,* 1198–1205. doi:10.1021/ac50058a010

43. Ardhaoui, M.; Bhatt, S.; Zheng, M.; Dowling, D.; Jolivalt, C.; Khonsari, F. A. *Mater. Sci. Eng., C* **2013,** *33,* 3197–3205. doi:10.1016/j.msec.2013.03.052

Neutral and charged boron-doped fullerenes for CO$_2$ adsorption

Suchitra W. de Silva, Aijun Du, Wijitha Senadeera and Yuantong Gu[*]

Abstract

Recently, the capture and storage of CO$_2$ have attracted research interest as a strategy to reduce the global emissions of greenhouse gases. It is crucial to find suitable materials to achieve an efficient CO$_2$ capture. Here we report our study of CO$_2$ adsorption on boron-doped C$_{60}$ fullerene in the neutral state and in the 1e^--charged state. We use first principle density functional calculations to simulate the CO$_2$ adsorption. The results show that CO$_2$ can form weak interactions with the BC$_{59}$ cage in its neutral state and the interactions can be enhanced significantly by introducing an extra electron to the system.

Introduction

The continuous dependence on fossil fuel combustion for the generation of energy has dramatically increased the atmospheric CO$_2$ concentrations over the last century. Despite concerns for global climatic changes and many attempts to sustainably generate energy, fossil fuel combustion continues to be the main source of electricity while releasing 13 Gt of CO$_2$ [1] to the atmosphere each year. Therefore CO$_2$ capture and storage (CCS) technology is a promising solution to reduce atmospheric CO$_2$ emissions [2]. Solvent absorption that is based on amines is the most common technology for the capture of CO$_2$. However this method is criticized for its very high energy consumption and operational limitations such as corrosion, slow

uptake rates, foaming and large equipment. Hence there is a huge interest in solid adsorbent materials for CCS [3-6]. In past few years metal organic frameworks (MOFs) have emerged as solid CO$_2$ adsorbent materials due to their tuneable chemical and physical properties.

Particularly, there is growing interest for metal free carbon-based nanomaterials for gas adsorption. Carbon-based nanomaterials such as fullerene, carbon nanotubes and graphene offer excellent thermal and chemical stability as CO$_2$ adsorbents [7,8]. Heterofullerenes are fullerene structures in which one or more cage carbon atoms are substituted by heteroatoms [9]. In

addition to the properties mentioned above, which are inherent to carbon-based nanomaterials, heterofullerenes also offer excellent tuneable chemical and physical properties [10]. Gas adsorption on heterofullerenes is an appealing subject. B. Gao et al. [11] studied CO_2 adsorption on calcium decorated C_{60} fullerene and F. Gao et al. [12] studied O_2 adsorption on nitrogen-doped fullerene.

Boron-doped C_{60} fullerenes are one of the most structurally stable heterofullerenes [9]. Guo et al. synthesized B-doped C_{60} fullerenes for the first time, in microscopic amounts by laser vaporisation [13]. Zou et al. [14] demonstrated the synthesis of B-doped C_{60} fullerene by using radio frequency plasma-assisted vapour deposition. Recently Dunk et al. [15] introduced a method to produce BC_{59} directly from exposing C_{60} fullerene to boron vapour. Wang et al. [16] stated that substituting a single C atom of the C_{60} fullerene with a B atom does not cause a significant distortion in the cage structure. The net change in the dihedral angle due to the doping is only 1.6% and Kurita et al. [17] predicted that due to the similarity between the C–B bond and the C–C bond, the changes in the bond lengths are less than 5%. Therefore the BC_{59} fullerene has a similar structural and thermal stability as C_{60} fullerene. Despite the numerous study results, which confirm the structural stability of B-doped C_{60} fullerene, very little studies have been done on applications of B-doped fullerene. Here, for the first time we report a study about the CO_2 adsorption on B-doped C_{60} fullerene, in which a single C atom is replaced with a B atom.

Sun et al. [8] predicted an enhanced CO_2 adsorption on $1e^-$- and $2e^-$-charged boron nitride sheets and nanotubes, which show very little chemical affinity towards CO_2 in their neutral state. Also Sun et al. [18] showed that chemical interactions between boron–carbon nanotubes (B_2CNT) and CO_2 can be enhanced by introducing extra electrons to the system. The enhanced interaction of CO_2 with adsorbent materials by electron injection has been further proved by Jiao et al. [19]. Therefore, we will investigate the CO_2 adsorption on BC_{59} fullerene in both the neutral and the $1e^-$-charged states.

Computational Details

First-principles density functional theory (DFT) calculations were carried out to study CO_2 adsorption on the BC_{59} cage. The BC_{59} structure was fully optimized in the given symmetry. The calculations were carried out at B3LYP [20-22] level of theory while using the split valance polarized basis set 6-31G(d). B97d [23,24] with the same basis set was used for calculations when non-covalent interactions are predominant. The CO_2 adsorption on BC_{59} was studied in the neutral state and in the $1e^-$-charged state. The electron distribution and transfer were analysed with Mulliken population analysis method [25].

The adsorption energies were calculated using the following equation.

$$E_{\text{ads}} = E_{CO_2/BC_{59}} - \left(E_{BC_{59}} + E_{CO_2} \right), \qquad (1)$$

where E_{ads} is the adsorption energy, $E_{CO_2 BC_{59}}$ is the total energy of the BC_{59} cage with a CO_2 molecule adsorbed and $E_{BC_{59}}$ and E_{CO_2} are the energies of the isolated BC_{59} cage and CO_2 molecule, respectively. For a favourable adsorption the calculated adsorption energy should have a negative value. To provide more accurate results for the chemisorption energy the counterpoise corrected energy [26,27] was also calculated.

The transition state was located by using the synchronous transit-guided quasi-Newton (STQN) method [28,29], which was then fully optimized by using the Berny algorithm at the B3LYP/6-31G(d) level. The optimized transition structure was used for IRC calculations at the same level of theory [30,31]. All calculations were carried out by using the Gaussian 09 package [32]. The GaussView 5 package [33] was used to visualize the optimized molecular structures, molecular orbitals and charge distributions.

Results and Discussion

The substitution of a C atom in the C_{60} fullerene by a B atom causes a charge transfer between C and B atoms, which results in an unbalanced charge distribution in the fullerene cage. The unbalanced charge distribution forms B–C complex sites for the adsorption of CO_2 (Figure 1). Here we considered two possible sites for the CO_2 adsorption: the B–C atomic site between two hexagonal rings (HH B–C site) and two identical B–C sites between a hexagonal ring and pentagonal ring (HP B–C site).

Adsorption of CO_2 on uncharged BC_{59} fullerenes

According to our simulation results, the CO_2 molecules can only form weak interactions with BC_{59} cage in its neutral state. The physisorption energy is a weak −2.04 kcal/mol (−4.1 kcal/mol for B97D/6-31G(d) calculations) and the weak interactions are mainly van der Waals interactions between the CO_2 molecule and the adsorbent. The CO_2 physisorbed configuration is shown in Figure 2. The CO_2 molecule sits parallel to the boron–carbon plane of the BC_{59} fullerene cage. The B⋯O and C⋯O bond distances are 3.25 Å and 3.71 Å, respectively. The CO_2 molecule undergoes very slight structural changes upon physisorption on the uncharged BC_{59} fullerene cage. The O–C–O angle is slightly bent to 179.7° and the changes to the C=O bond lengths are negligibly small. The doped fullerene cage hardly undergoes any structural change. The charge transfer between CO_2 and BC_{59} is only 0.008e.

Figure 1: Sites for CO_2 adsorption on BC_{59}. The B and C atoms of HH B–C and HP B–C sites are represented as 'ball and bond'-type and the rest of the atoms are represented as 'wireframes'. Atom colour code: grey, carbon; pink, boron.

Figure 2: Configuration of physisorbed CO_2 on neutral BC_{59}. Atom colour code: grey, carbon; pink, boron; red, oxygen.
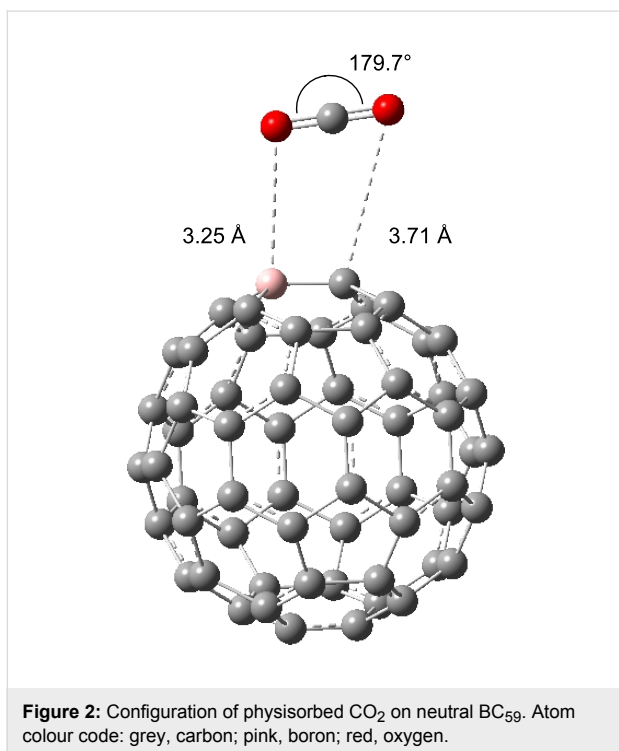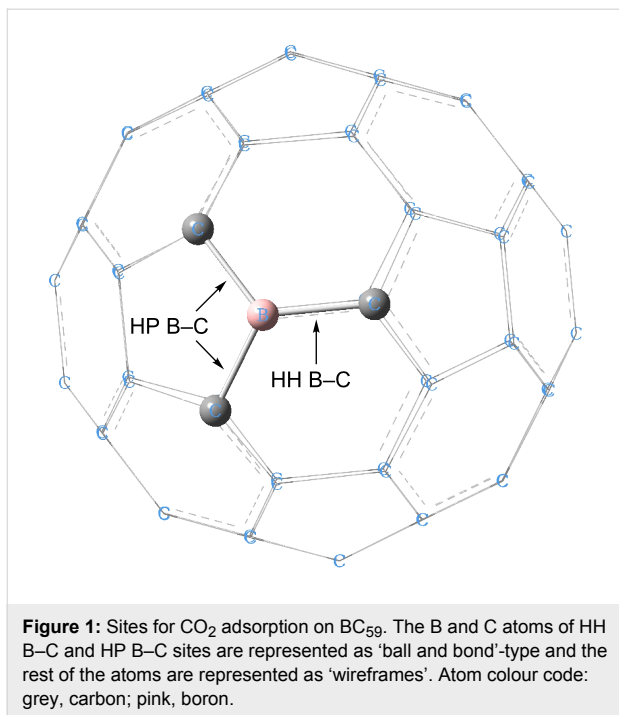
Effects of charges on the structure

Kim et al. [34] predicted that $C_{59}B^-$ should be a stable entity because of the isoelectronic configuration with C_{60}. This claim is further validated by experimental observations by Dunk et al. [15]. The Mulliken charge analysis and the electron density distributions of the lowest unoccupied molecular orbitals

(LUMO) are adopted to assess the influence of changing the charge state of BC_{59}. Figure 3 shows that the LUMO of the neutral BC_{59} is noticeably concentrated on the B atom and the neighbouring C atoms. Furthermore experimental results of Guo et al. [13] showed that boron doping creates an electron defficient site at the B atom. This suggests that an additional electron added to the system will be accepted by the B atom. This hypothesis is consistent with theoretical predictions of Kurita et al. [17] and Xie et al. [35], who stated that the doped B atom in C_{60} fullerene acts as an electron acceptor. The comparison of the Mulliken population analysis of the neutral and the $1e^-$-state of BC_{59} proves that the negative charge introduced to the system is essentially accepted by the B atom. The Mulliken atomic charge of the B atom in the BC_{59} structure in the neutral state has changed from 0.138 to 0.012 upon the introduction of the negative charge, while as shown in Figure 4 the charges on the C atoms are not changed significantly.

Figure 3: LUMO of neutral BC_{59}. The orbitals are drawn at an isosurface value of 0.02. The colours of the orbitals: red, positive wave function; green, negative wave function. Atom colour code: pink, boron; grey, carbon.
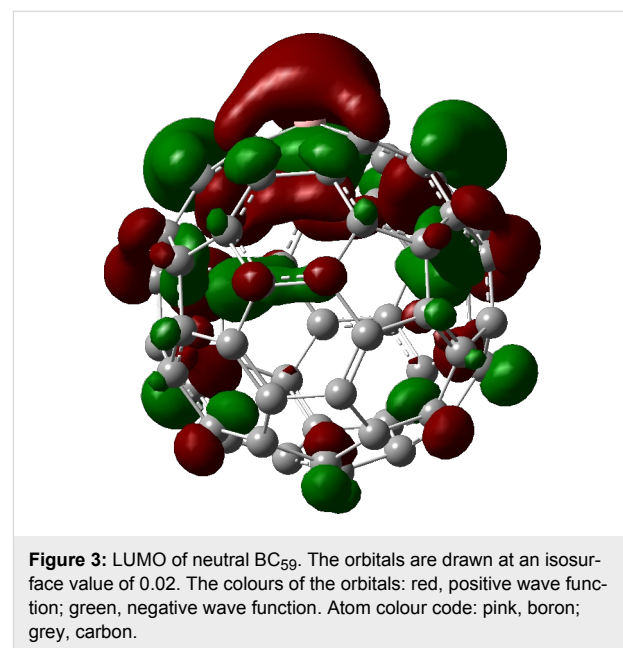
CO_2 adsorption on BC_{59} fullerene in the $1e^-$-state

Next we studied the CO_2 adsorption on a $1e^-$-charged BC_{59} cage. The results confirm that the negatively charged BC_{59} fullerene exhibits a stronger interaction with CO_2. Unlike the neutral BC_{59}, for which the interaction with CO_2 molecule was only physical, here the charged BC_{59} forms a substantial chemical interaction with CO_2 causing the molecule to undergo significant structural deformations. A stable CO_2 adsorption is observed at the HH B–C site. The chemisorption energy of −15.41 kcal/mol (−64.48 kJ/mol) (−13.48 kcal/mol with BSSE correction) agrees well with the ideal range of chemisorption energy (40–80 kJ/mol) for a good CO_2 adsorbent [36].
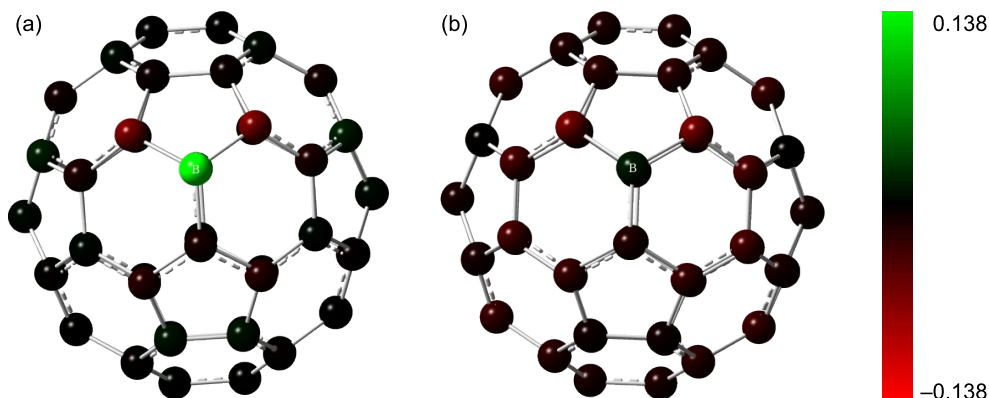
Figure 4: Mulliken charge distribution of (a) neutral BC_{59} and (b) $1e^-$-BC_{59}. The atoms are shaded based on the charge distribution on each atom. The comparison suggests that the most notable charge transfer is on the B atom.

The CO_2 molecule undergoes considerable distortion upon chemically adsorbing on the $1e^-$-charged BC_{59} fullerene. A C=O bond of the CO_2 molecule is broken when one oxygen atom forms a bond with the boron atom (which will be referred as O_a in the following discussion and the other oxygen atom as O_b) and the C atom of the CO_2 molecule forms a bond with the C atom on the HH B–C site of the cage structure. The linear O–C–O bond of CO_2 is bent to 128.0° in the adsorbed form. The $C=O_b$ bond which is originally 1.169 Å (experimentally 1.162 Å [37]) is elongated to 1.208 Å, while the length of the $C–O_a$ bond is expanded to 1.336 Å. The adsorption site of the BC_{59} fullerene also undergoes considerable stretching. The HH B–C site is protruded outwards by about 0.05 Å. The B–C bond of the HH B–C site has stretched from 1.496 to 1.672 Å. The Mulliken population analysis shows that a charge transfer of 0.42 has occurred from the BC_{59} fullerene to the CO_2 molecule.

Comparison of the charge distribution on BC_{59}^- before (Figure 4b) and after (Figure 5c) CO_2 adsorption, confirms that the injected electron is occupied by the CO_2 molecule.

The higher adsorption energy and the significant distortions in the structure confirm a stronger interaction between CO_2 molecule and negatively charged BC_{59} than its neutral state. These interactions can be explained due to the Lewis acidity of CO_2, which prefers to accept electrons [18]. On the other hand the B atom of the BC_{59} becomes less positively charged upon the addition of an extra electron. Therefore it becomes more likely to donate electrons to the CO_2 molecule leading to stronger interactions between the two molecules.

Figure 6 shows the minimum energy pathway for the adsorption from the physisorbed state to the chemisorbed configur-

Figure 5: (a) CO_2 chemisorption and (b) transition structure for CO_2 chemisorption on $1e^-$-charged BC_{59}. Atom colour code: grey, carbon; pink, boron; red, oxygen. (c) Charge distribution after CO_2 chemisorption.

ation. We performed frequency calculations on the optimized transition structure, which confirms that it is a first order saddle point and hence an actual transition structure. From this figure, the activation barrier for the chemisorption i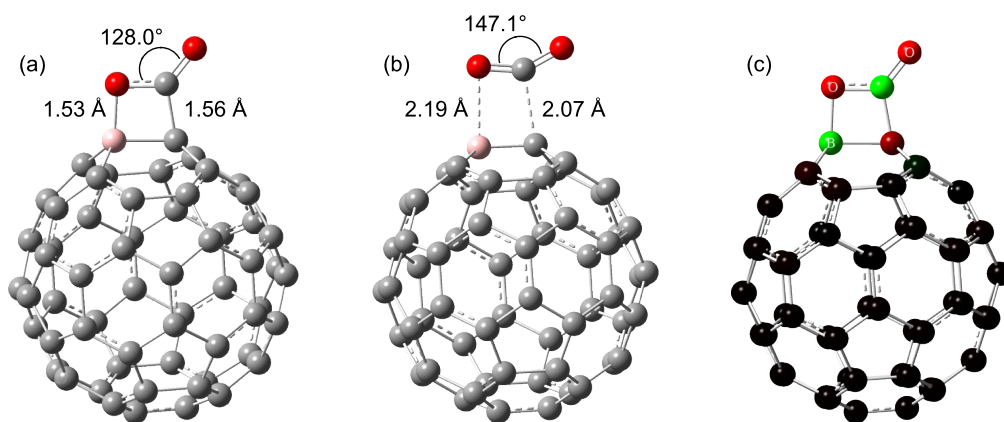s estimated to be 13.25 kcal/mol (55.43 kJ/mol). The low barrier of the reaction indicates that the reaction is energetically favourable.
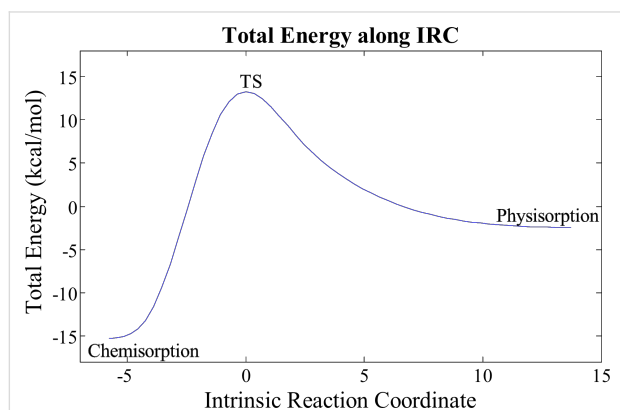

Figure 6: Intrinsic reaction pathway for CO_2 chemisorption on $1e^-$-charged BC_{59} from the physisorbed configuration. The total energy = 0 point corresponds to the total energy of $E_{CO2} + E_{BC59}{}^{-1}$.

For the desorption step, the removal of the added charge will decrease the stability of the bond between CO_2 and the doped fullerene. The thermodynamic analysis of the reaction shows that the CO_2 chemisorption is spontaneous only for temperatures less than 350 K. Therefore we suggest a method of manipulating the charge state and the temperature of the system for adsorbent recycling. Charging the system can be achieved by electrochemical methods, electrospray, and electron beam or gate voltage control methods [8].

Conclusion

By using DFT calculations we have studied the adsorption mechanisms of CO_2 on a C_{60} fullerene cage, in which a single C atom is substituted by a B atom. Our calculation results show that the BC_{59} cage, in its neutral state, shows a low chemical interaction with CO_2 molecule, which only physisorbs with $E_{ads} = -2.04$ kcal/mol. However CO_2 adsorption on the BC_{59} can be significantly enhanced by injecting negative charges into the structure. The CO_2 molecule chemisorbs on the $1e^-$-charged BC_{59} with $E_{ads} = -15.41$ kcal/mol. This study suggests that we can conclude $1e^-$-charged BC_{59} cage structure is a promising CO_2 adsorbent.

Acknowledgements

References

1. International Energy Agency, Ed. *World Energy Outlook 2011;* IEA Publications: Paris, 2011.
2. Kheshgi, H.; de Coninck, H.; Kessels, J. *Mitigation and Adaptation Strategies for Global Change* **2012,** *17,* 563–567. doi:10.1007/s11027-012-9391-5
3. Lee, K. B.; Sircar, S. *AIChE J.* **2008,** *9,* 2293–2302. doi:10.1002/aic.11531
4. Jiao, Y.; Du, A.; Zhu, Z.; Rudolph, V.; Smith, S. C. *J. Mater. Chem.* **2010,** *20,* 10426–10430. doi:10.1039/c0jm01416h
5. Jiao, Y.; Du, A.; Zhu, Z.; Rudolph, V.; Smith, S. C. *J. Phys. Chem. C* **2010,** *114,* 7846–7849. doi:10.1021/jp911419k
6. Sun, Q.; Wang, M.; Li, Z.; Du, A.; Searles, D. J. *J. Phys. Chem. C* **2014,** *118,* 2170–2177. doi:10.1021/jp407940z
7. Lee, H.; Li, J.; Zhou, G.; Duan, W.; Kim, G.; Ihm, J. *Phys. Rev. B* **2008,** *77,* 235101. doi:10.1103/PhysRevB.77.235101
8. Sun, Q.; Li, Z.; Searles, D. J.; Chen, Y.; Lu, G. (M.); Du, A. *J. Am. Chem. Soc.* **2013,** *135,* 8246–8253. doi:10.1021/ja400243r
9. Chen, Z.; King, R. B. *Chem. Rev.* **2005,** *105,* 3613–3642. doi:10.1021/cr0300892
10. Tenne, R. *Adv. Mater.* **1995,** *7,* 965–995. doi:10.1002/adma.19950071203
11. Gao, B.; Zhao, J.-x.; Cai, Q.-h.; Wang, X.-g.; Wang, X.-z. *J. Phys. Chem. A* **2011,** *115,* 9969–9976. doi:10.1021/jp2016853
12. Gao, F.; Zhao, G.-L.; Yang, S.; Spivey, J. J. *J. Am. Chem. Soc.* **2013,** *135,* 3315–3318. doi:10.1021/ja309042m
13. Guo, T.; Jin, C.; Smalley, R. E. *J. Phys. Chem.* **1991,** *95,* 4948–4950. doi:10.1021/j100166a010
14. Zou, Y. J.; Zhang, X. W.; Li, Y. L.; Wang, B.; Yan, H.; Cui, J. Z.; Liu, L. M.; Da, D. A. *J. Mater. Sci.* **2002,** *37,* 1043–1047. doi:10.1023/A:1014368418784
15. Dunk, P. W.; Rodríguez-Fortea, A.; Kaiser, N. K.; Shinohara, H.; Poblet, J. M.; Kroto, H. W. *Angew. Chem.* **2013,** *125,* 333–337. doi:10.1002/ange.201208244
16. Wang, S.-H.; Chen, F.; Fann, Y.-C.; Kashani, M.; Malaty, M.; Jansen, S. A. *J. Phys. Chem.* **1995,** *99,* 6801–6807. doi:10.1021/j100018a008
17. Kurita, N.; Kobayashi, K.; Kumahora, H.; Tago, K.; Ozawa, K. *Chem. Phys. Lett.* **1992,** *198,* 95–99. doi:10.1016/0009-2614(92)90054-Q
18. Sun, Q.; Wang, M.; Li, Z.; Ma, Y.; Du, A. *Chem. Phys. Lett.* **2013,** *575,* 59–66. doi:10.1016/j.cplett.2013.04.063
19. Jiao, Y.; Zheng, Y.; Smith, S. C.; Du, A.; Zhu, Z. *ChemSusChem* **2014,** *7,* 435–441. doi:10.1002/cssc.201300624
20. Becke, A. D. *J. Chem. Phys.* **1993,** *98,* 5648–5652. doi:10.1063/1.464913
21. Lee, C.; Yang, W.; Parr, R. G. *Phys. Rev. B* **1988,** *37,* 785–789. doi:10.1103/PhysRevB.37.785
22. Stephens, P. J.; Devlin, F. J.; Chabalowski, C. F.; Frisch, M. J. *J. Phys. Chem.* **1994,** *98,* 11623–11627. doi:10.1021/j100096a001
23. Grimme, S. *J. Comput. Chem.* **2006,** *27,* 1787–1799. doi:10.1002/jcc.20495
24. Grimme, S.; Ehrlich, S.; Goerigk, L. *J. Comput. Chem.* **2011,** *32,* 1456–1465. doi:10.1002/jcc.21759
25. Mulliken, R. S. *J. Chem. Phys.* **1955,** *23,* 1833–1840. doi:10.1063/1.1740588
26. Simon, S.; Duran, M.; Dannenberg, J. J. *J. Chem. Phys.* **1996,** *105,* 11024–11031. doi:10.1063/1.472902
27. Boys, S. F.; Bernardi, F. *Mol. Phys.* **1970,** *19,* 553–566. doi:10.1080/00268977000101561

28. Peng, C.; Schlegel, H. B. *Isr. J. Chem.* **1993,** *33,* 449–454.
doi:10.1002/ijch.199300051

29. Hratchian, H. P.; Schlegel, H. B. *Finding minima, transition states, and following reaction pathways on ab initio potential energy surfaces;*
Elsevier: Amsterdam, The Netherlands, 2005.

30. Peng, C.; Ayala, P. Y.; Schlegel, H. B.; Frisch, M. J. *J. Comput. Chem.* **1996,** *17,* 49–56.
doi:10.1002/(SICI)1096-987X(19960115)17:1<49::AID-JCC5>3.3.CO;2 -#

31. Gonzalez, C.; Schlegel, H. B. *J. Chem. Phys.* **1989,** *90,* 2154–2161.
doi:10.1063/1.456010

32. *Gaussian 09,* Revision B.01; Gaussian, Inc.: Wallingford, CT, USA, 2009.

33. *GaussView,* Version 5; Semichem Inc.: Shawnee Mission, KS, USA, 2009.

34. Kim, K.-C.; Hauke, F.; Hirsch, A.; Boyd, P. D. W.; Carter, E.; Armstrong, R. S.; Lay, P. A.; Reed, C. A. *J. Am. Chem. Soc.* **2003,** *125,* 4024–4025. doi:10.1021/ja034014r

35. Xie, R.-H.; Bryant, G. W.; Zhao, J.; Smith, V. H., Jr..; Di Carlo, A.; Pecchia, A. *Phys. Rev. Lett.* **2003,** *90,* 206602.
doi:10.1103/PhysRevLett.90.206602

36. Chu, S.; Majumdar, A. *Nature* **2012,** *488,* 294–303.
doi:10.1038/nature11475

37. Foresman, J. B.; Frisch, Æ. *Exploring chemistry with electronic structure methods: A Guide to Using Gaussian;* Gaussian, Inc.: Pittsburgh, PA, USA, 1996.

One-step synthesis of high quality kesterite Cu$_2$ZnSnS$_4$ nanocrystals – a hydrothermal approach

Vincent Tiing Tiong, John Bell and Hongxia Wang[*]

Full Research Paper

Open Access

Abstract

The present work demonstrates a systematic approach for the synthesis of pure kesterite-phase Cu$_2$ZnSnS$_4$ (CZTS) nanocrystals with a uniform size distribution by a one-step, thioglycolic acid (TGA)-assisted hydrothermal route. The formation mechanism and the role of TGA in the formation of CZTS compound were thoroughly studied. It has been found that TGA interacted with Cu^{2+} to form Cu$^+$ at the initial reaction stage and controlled the crystal-growth of CZTS nanocrystals during the hydrothermal reaction. The consequence of the reduction of Cu^{2+} to Cu$^+$ led to the formation Cu$_{2-x}$S nuclei, which acted as the crystal framework for the formation of CZTS compound. CZTS was formed by the diffusion of Zn^{2+} and Sn^{4+} cations to the lattice of Cu$_{2-x}$S during the hydrothermal reaction. The as-synthesized CZTS nanocrystals exhibited strong light absorption over the range of wavelength beyond 1000 nm. The band gap of the material was determined to be 1.51 eV, which is optimal for application in photoelectric energy conversion device.

Introduction

The development of new semiconductor light absorbing materials for applications in photovoltaic technologies is driven by the necessity to overcome the key issues in the current PV technologies: the high production cost of silicon wafer used in the first generation solar cells and the limited availability of raw materials such as tellurium and indium used in CdTe and Cu(Ga, In)Se$_2$ (CIGS) based thin film solar cells, which has

raised significant concerns over their production scale [1]. In the process of developing new PV materials that do not have the above problems, the compound Cu$_2$ZnSnS$_4$ (CZTS) is emerging as a promising new sustainable light absorbing material for PV technologies. As a direct band p-type semiconductor material, CZTS has a theoretical band gap of 1.5 eV and has high light absorption coefficient (>10^4 cm^{-1}) in the range of

visible and near infrared irradiation of solar spectrum [2-4]. Shockley–Queisser balanced calculations have predicted that the theoretical efficiency of PVs using light absorbers like CZTS is 32% [5].

It has been proposed that high-efficiency and low-cost photo-voltaic devices can be made from CZTS nanocrystals [6,7]. This is due to the fact that thin film light absorber layers with controlled thickness can be made from a slurry containing the nanocrystals by a cost-effective method such as doctor blading, spin coating and screen printing which can be scaled-up easily. The recently reported thin film solar cells based on $Cu_2ZnSn(S,Se)_4$ demonstrated a power conversion efficiency of 11.1%, which has approached the benchmark for large scale production [8]. This great achievement shows the bright future for CZTS based PVs. The highest efficiency CZTS solar cell was made using hydrazine based sol–gel method. However, hydrazine is a highly toxic, dangerously unstable solvent and requires extra caution in handling and storage [9]. Therefore, a safer, simple yet convenient method for fabrication of high quality CZTS nanocrystals is desired.

The hydrothermal method has been widely used to synthesize high quality nanocrystals with unique morphology and crystal structure due to its advantage of simplicity of the procedure and low production cost [10-17]. However, to the best of our knowledge, the formation mechanism of CZTS in the hydrothermal reaction has rarely been reported due to the complex reactions involved in the system. Herein we report the synthesis of high quality, pure kesterite phase, monodisperse CZTS nanocrystals by a one-step hydrothermal procedure. Through thoroughly investigating the factors that influence the morphology, crystal size, and growth of CZTS nanocrystals, a mechanism that depicts the formation process of CZTS compound is proposed. It is found that the tiny amount of thioglycolic acid (TGA) used in the precursor is crucial for the formation of pure kesterite CZTS nanocrystals. The roles of TGA in the hydrothermal synthesis are discussed.

Experimental

Materials: All the materials were provided by Sigma Aldrich unless otherwise stated. Chemicals of copper(II) chloride dehydrate ($CuCl_2 \cdot 2H_2O$), zinc chloride ($ZnCl_2$) product of BDH, tin(IV) chloride pentahydrate ($SnCl_4 \cdot 5H_2O$), sodium sulfide nonahydrate ($Na_2S \cdot 9H_2O$), thioglycolic acid (TGA) were all of analytical grade and used as received without further purification. Milli-Q water was used in this work.

Synthesis of CZTS nanocrystals by hydrothermal reaction: In a typical experimental procedure, 0.2 mmol of $CuCl_2 \cdot 2H_2O$, 0.1 mmol of $ZnCl_2$, 0.1 mmol of $SnCl_4 \cdot 5H_2O$, 0.5 mmol of $Na_2S \cdot 9H_2O$ and 18 μL of TGA were dissolved in 34 mL of Milli-Q water under vigorous magnetic stirring. The solution was then transferred to a Teflon-lined stainless steel autoclave (Parr Instrument Company) of 45 mL capacity, which was then sealed and maintained at 240 °C for 24 h. After that, the autoclave was allowed to cool to room temperature naturally. The black precipitate was collected by centrifugation and washed with deionised water and absolute ethanol for several times to remove the ions in the end product. Finally, the product was vacuum-dried at 60 °C for 5 h.

Characterisation: The crystallographic structure of the synthesized samples was identified by X-ray diffraction (XRD, PANanalytical XPert Pro Multi-Purpose Diffractometer (MPD), Cu Kα, λ = 0.154056 nm). The room temperature Raman spectra of the samples were recorded with a Raman spectrometer (Renishaw inVia Raman microscope). The incident laser light with the wavelength of 785 nm was employed as the excitation source in micro-Raman measurement and the spectra were collected by taking the average of 10 different spots. The quantitative elemental analysis of the samples were characterized by field emission scanning electron microscopy (FESEM, JEOL 7001F) at an acceleration voltage of 20.0 kV combined with an energy dispersive X-ray spectroscopy (EDS). Transmission electron microscopy (TEM) images of the samples were performed on a JEOL JEM-1400 microscope. High-resolution TEM (HRTEM) and selected area electron diffraction (SAED) images were obtained using JEOL JEM-2100 microscope at an accelerating voltage of 200 kV. Ultraviolet–visible (UV–vis) absorption spectrum of the sample was measured at room temperature using a Varian Cary 50 spectrometer. The chemical state of each element in the samples was determined using Kratos Axis ULTRA X-ray photoelectron spectrometer (XPS).

Results and Discussion
Synthesis of CZTS nanocrystals

The XRD pattern of the CZTS nanocrystals prepared at 240 °C for 24 h using 18 μL of TGA in the hydrothermal reaction is shown in Figure 1a. All the XRD diffraction peaks can be well indexed to the corresponding crystal planes of kesterite CZTS (JCPDS 01-75-4122) [5,18]. The Raman spectrum of the hydrothermal product is shown in Figure 1b. The strong peak at 336 cm^{-1} together with two shoulder peaks at 288 and 372 cm^{-1} further confirm the formation of CZTS [19]. No other characteristic peaks corresponding to impurities such as $Cu_{2-x}S$ (475 cm^{-1}), SnS_2 (315 cm^{-1}), ZnS (278 and 351 cm^{-1}), Cu_2SnS_3 (297 and 337 cm^{-1}), and Cu_3SnS_4 (318 cm^{-1}) that might form in the hydrothermal reaction are observed, suggesting the highly purity of the synthesized CZTS material [19,20]. The morphology and particle size of the CZTS nanocrystals are shown in Figure 1c, which suggests the CZTS

nanocrystals are monodisperse with crystal sizes around 10 ± 3 nm. High-resolution TEM (HRTEM) image in Figure 1d illustrates the crystal interplanar spacing of 3.12 Å, which can be ascribed to the (112) plane of kesterite phase CZTS. The diffraction spots in the selected area electron diffraction (SAED) pattern illustrated in Figure 1e can all be indexed to the (112), (220), (224) and (420) planes of kesterite CZTS respectively, further confirming the phase purity of the material. The atomic ratio of Cu/Zn/Sn/S in the material is 1.97/1.04/1.03/3.96 according to energy dispersive X-ray spectroscopy (EDS) results (see Table 1), which is consistent with the stoichiometric value of 2/1/1/4 of CZTS (by considering the experimental error of EDS detector).

X-ray photoelectron spectrometry (XPS) measurement was conducted to monitor the valence states of all four elements in the as-synthesized CZTS nanocrystals. Figure 2 displays the high resolution XPS analysis for the four constituent elements: Cu 2p, Zn 2p, Sn 3d and S 2p of CZTS nanocrystals. The spectrum of Cu 2p shows two peaks at 932.14 and 951.99 eV with a

splitting of 19.85 eV, which is in good agreement with the standard separation (19.9 eV) of Cu(I). The peaks of Zn 2p appear at 1022.29 and 1045.46 eV with a split orbit of 23.17 eV, which can be assigned to Zn(II). The peaks of Sn 3d show binding energies at 486.35 and at 494.77 eV respectively, which is in good agreement with the value of Sn(IV). The S 2p peaks are located at 161.76 and 162.92 eV, which are consistent with the binding energy of sulfur in sulfide state of CZTS. These results are in agreement with the reported values of the binding state of the elements of CZTS [18,21].

Influence of different reaction condition

Different reaction conditions such as reaction temperature, reaction duration and concentration of capping agent have been reported to have significant impacts on the morphology, particle size as well as the optical properties of the materials formed in a hydrothermal reaction [17,22]. Hence, a series of experiments under different reaction conditions were carried out to understand the role of TGA and to gain in-depth insight into the formation mechanism of CZTS nanocrystals.
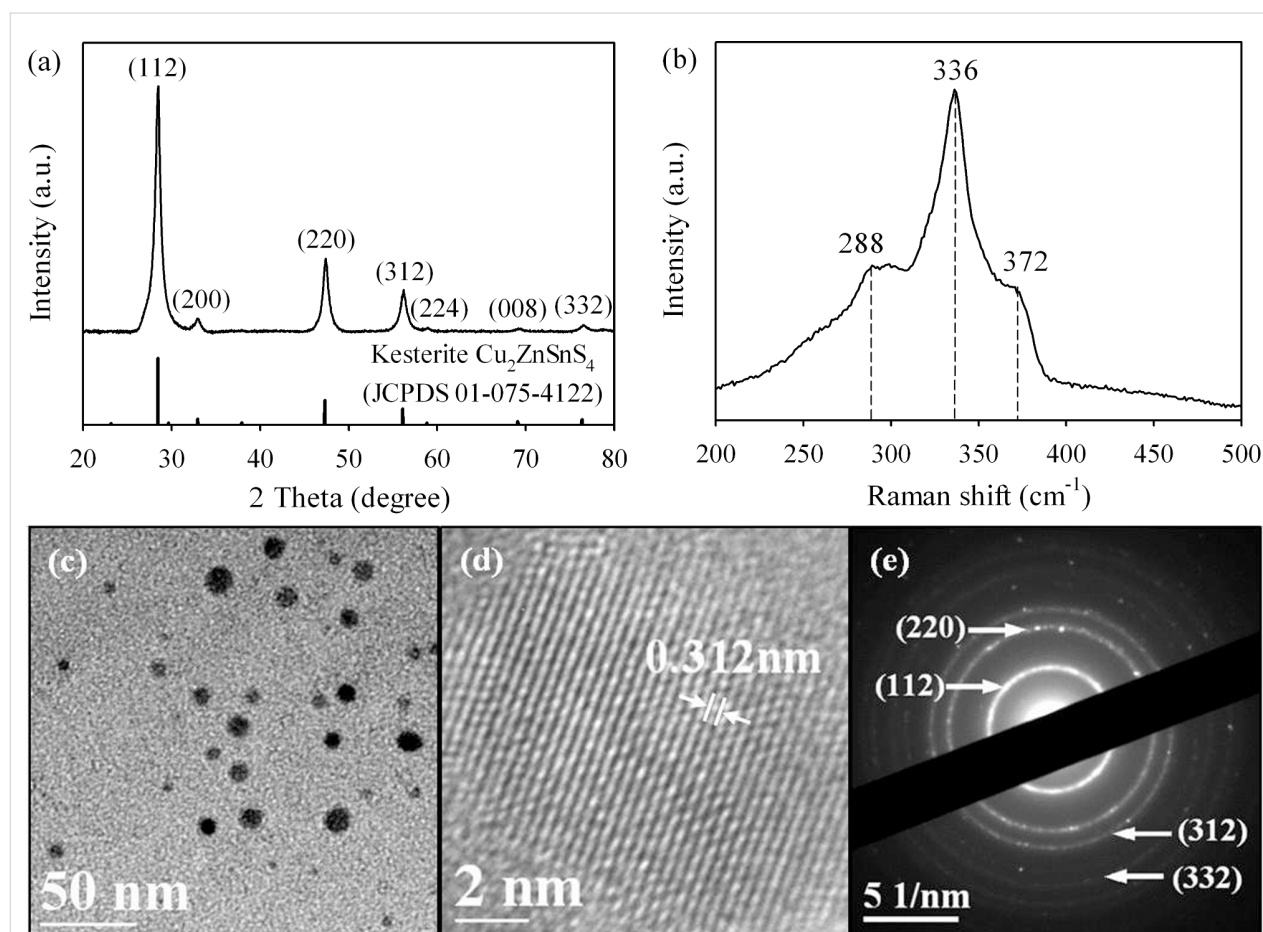
Figure 1: (a) XRD patterns, (b) Raman spectra, (c) TEM image, (d) HRTEM image and (e) SAED pattern of CZTS nanocrystals hydrothermally synthesized at 240 °C for 24 h.
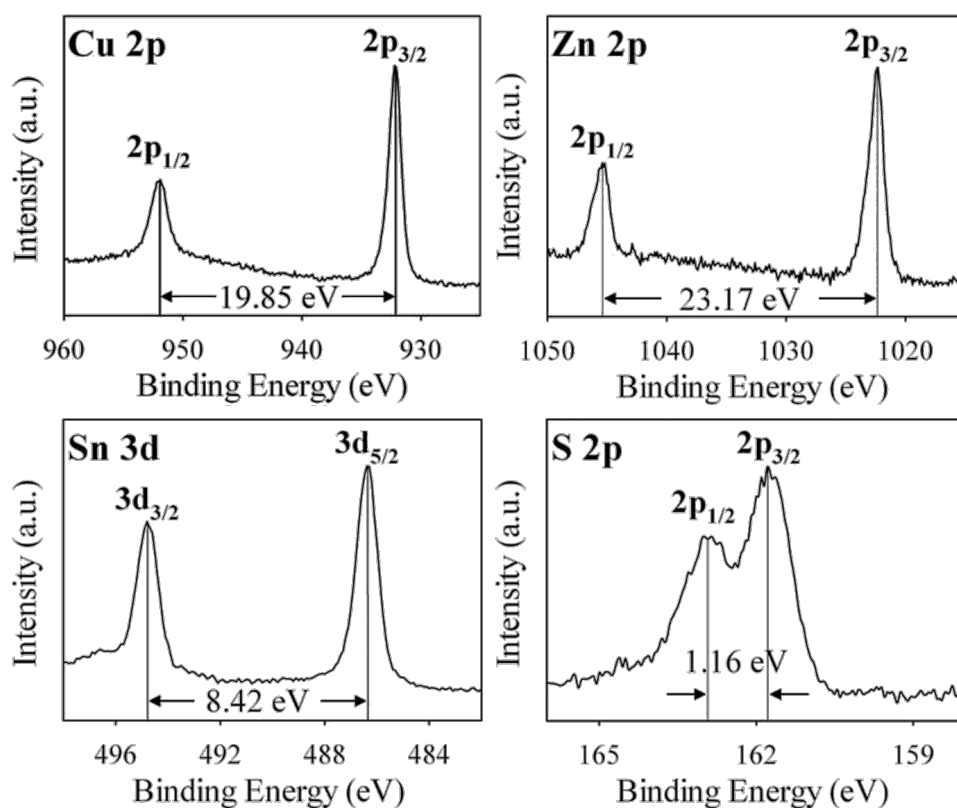
Figure 2: XPS spectra of CZTS nanocrystals synthesized at 240 °C for 24 h.

Influence of TGA concentration

TGA has been widely used in hydrothermal synthesis of metal sulfide such as ZnS, SnS etc. It has been reported that the content of TGA influences the morphology of the hydrothermal product [23,24]. The effect of the content of TGA on the forma-

tion of CZTS compound was investigated in this work. The XRD results of the hydrothermal products synthesized with three different TGA concentrations are shown in Figure 3a. As can be see, when there is no TGA, the XRD pattern of hydrothermal product contains the peaks corresponding to
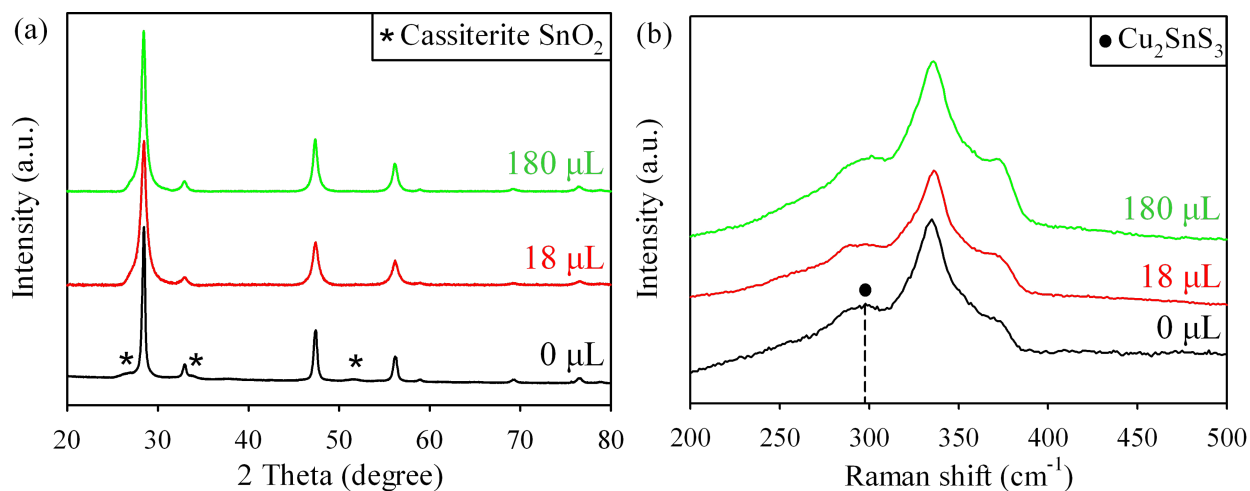
Figure 3: (a) XRD patterns and (b) Raman spectra of the hydrothermal products synthesized with different TGA concentration in the precursor solution.

kesterite CZTS and three other peaks that are attributed to SnO_2 (JCPDS 00-001-0625) impurity. Raman spectra in Figure 3b indicates that, in the absence of TGA, a weak peak located at 298 cm^{-1} which is assigned to ternary Cu_2SnS_3, is detected along with the CZTS peaks. However, the peaks corresponding to impurities disappear when tiny amount of TGA (18 µL) is added to the precursor solution. Further increase the content of TGA does not influence the XRD and Raman results of the material. Thus, the very small amount of TGA in the hydrothermal precursor solution determines the compositional purity of the synthesized CZTS material.

The quantitative elemental analysis of these three CZTS samples (Table 1) shows that the content of Sn element in the hydrothermal sample is very high ([Zn]/[Sn] = 1/1.40) without TGA. And the ratio of Cu/(Zn+Sn) and [Zn]/[Sn] is close to 1 when adding only 18 µL TGA in the hydrothermal reaction system. The Sn rich and Zn poor composition in the sample with no TGA is probably due to the formation of Cu_2SnS_3 and SnO_2 impurity as confirmed by the above XRD and Raman spectrum. The EDS analysis also shows that the elemental composition of the CZTS material using excessive amount of TGA (180 µL) leads to the slightly reduced Sn content relative to Zn.

The morphology of the synthesized CZTS nanocrystals prepared with the three different amounts of TGA measured by TEM is shown in Figure 4. It shows that when there is no TGA in the precursor solution, agglomerates with irregular shape with size ranging from 10–150 nm are obtained. When 18 µL TGA is used in the reaction system, uniform and monodisperse CZTS nanocrystals with an average size of 10 nm are obtained. With increasing the TGA concentration to 180 µL, the size distribution of the CZTS nanocrystals becomes less uniform and some triangular-like shape nanocrystals are observed. The above results demonstrate that high concentration of TGA is not favourable for the formation of monodisperse CZTS nanocrystals. At a high concentration, TGA might form a colloid which wraps a certain surface of CZTS particles, inhibiting the growth of crystals in all directions [25]. Hence, it is rational to conjecture that TGA might play two key roles in this work. One is to prevent aggregation of CZTS nanocrystals by capping on the generated nanocrystals to reduce the surface energy (steric hindrance) during the hydrothermal process; the other role is selective adsorption on certain facets of CZTS nanocrystals and kinetic control of the growth rates of these facets [4,25].

Influence of reaction duration

Figure 5b,c shows the XRD patterns and Raman spectra of the CZTS nanocrystals synthesized at different hydrothermal reaction duration (from 0.5 h to 24 h). The XRD pattern of the precipitate collected from the hydrothermal precursor solution prior to the reaction is shown in Figure 5a. The result suggests

Table 1: Quantitative elemental analysis of CZTS nanocrystals synthesized with different TGA content in the precursor solution of the hydrothermal reaction.

Ratio	0 µL	18 µL	180 µL
Cu/Zn/Sn/S	2.02/0.84/1.18/3.96	1.97/1.04/1.03/3.96	1.96/1.02/0.93/4.09
[Cu]/([Zn+Sn])	1/1.00	1/1.05	1/0.99
[Zn]/[Sn]	1/1.40	1/0.99	1/0.91
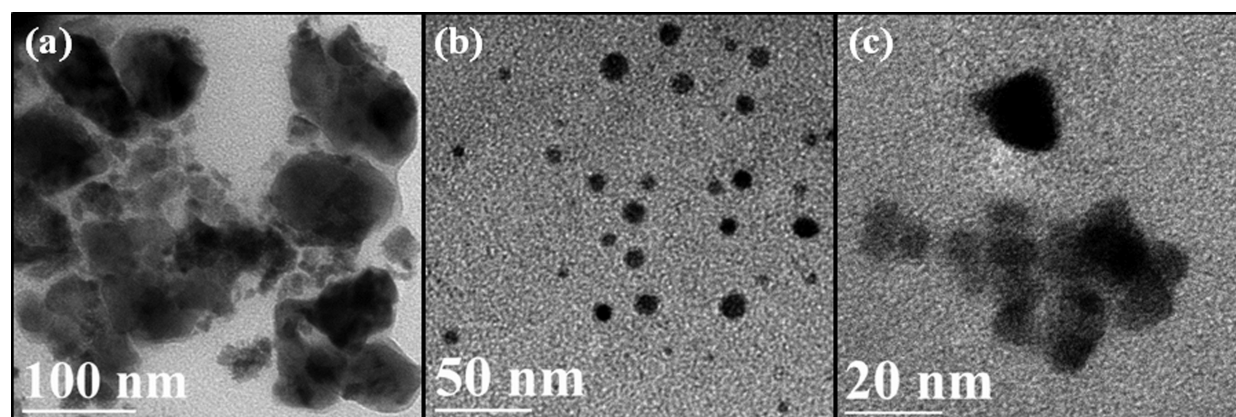
Figure 4: TEM images of CZTS nanocrystals synthesized using (a) 0, (b) 18 and (c) 180 µL of TGA at 240 °C for 24 h.
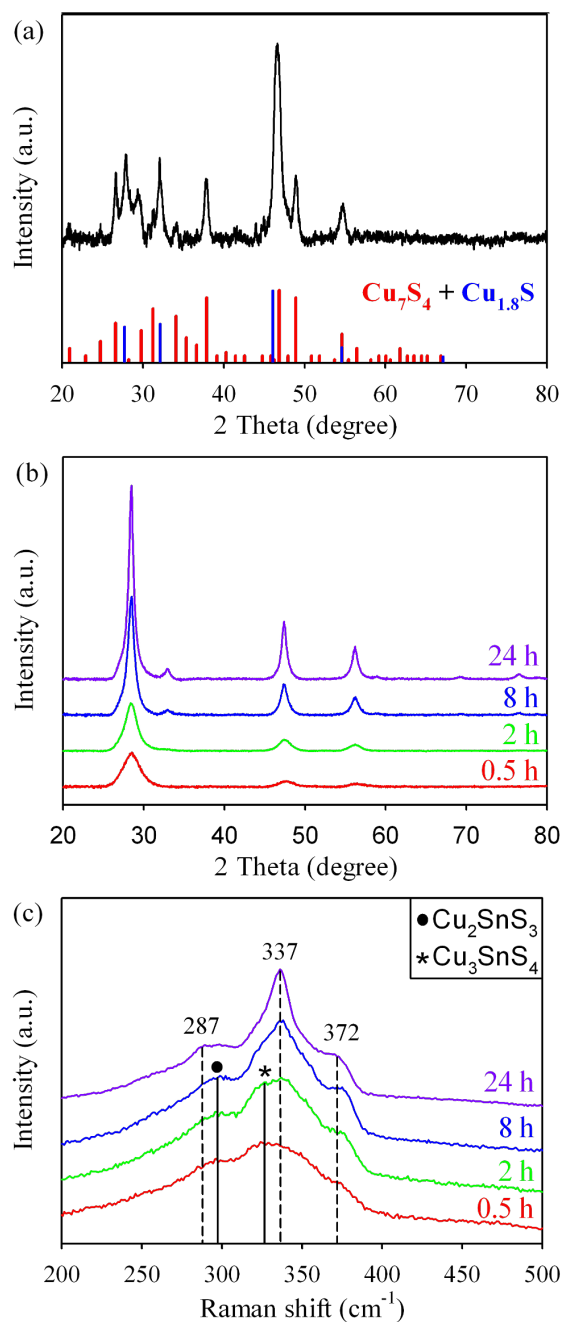
Figure 5: (a) XRD of the precipitate collected from the precursor solution prior to hydrothermal reaction and (b) XRD patterns and (c) Raman spectra of the samples synthesized at different reaction duration.

that Cu_7S_4 (JCPDS 23-0958) and $Cu_{1.8}S$ (JCPDS 56-1256) are formed immediately in the precursor solution prior to the hydrothermal reaction. When the hydrothermal reaction is proceeded for only 0.5 h (Figure 5b), three XRD peaks that can be assigned to kesterite CZTS are observed. The intensity of the diffraction peaks increases gradually with the increase of the reaction time. A characteristic peak located at around 32.9° corresponding to the (200) plane of kesterite CZTS is noticeable only when the reaction duration is extended to 8 h and beyond. The gradual increment of the intensity of diffraction peaks suggests the improvement of crystallinity of the CZTS nanocrystals. However, the Raman spectra (Figure 5c) of the hydrothermal products synthesized at different reaction duration show that, at a shorter reaction time (less than 8 h), the hydrothermal products contain a mixture of CZTS, Cu_2SnS_3 and Cu_3SnS_4. Pure phase CZTS nanocrystals are only obtained at reaction duration of 24 h. The Raman spectra also show that, the intensity of CZTS peak at 337 cm^{-1} increases and the peak at 327 cm^{-1} which belongs to Cu_3SnS_4 decreases as the reaction time is prolonged [26]. The red shift of the peak at 298 to 287 cm^{-1} denotes the complete transformation of Cu_2SnS_3 to CZTS at 24 h hydrothermal reaction. Since no peak corresponding to ZnS is observed in the entire Raman spectra, it suggests that CZTS compound in the hydrothermal reaction might be formed through diffusion of Zn ion to the ternary Cu_xSnS_y (x = 2,3, y = 3,4) compound.

The atomic ratios of [Cu]/([Zn]+[Sn]) and [Zn]/[Sn] of the synthesized hydrothermal products obtained at different reaction duration are shown in Table 2. The much higher content of copper in the sample obtained prior to the hydrothermal reaction and the nearly two-fold of Cu relative to S is consistent with the observation of $Cu_{2-x}S$ product by the XRD measurement as discussed above. As the reaction time is prolonged from 0.5 h to 24 h, the [Cu]/([Zn]+[Sn]) ratio is reduced from 1/0.82 to 1/1.05, while the [Zn]/[Sn] ratio shows a little change from 1/0.93 to 1/0.99. The nearly stoichiometric composition (1.97/1.04/1.03/3.96) of CZTS is obtained at a reaction time of 24 h. Since no ZnS is detected in the samples synthesized at 0.5 and 2 h, we believe that the content of Cu_2SnS_3 impurity in these hydrothermal products is very low. The high content of Zn and Sn compound at 0.5 h and 2 h also suggests that CZTS compound is formed rapidly in the hydrothermal reaction.

Table 2: Quantitative elemental analysis of CZTS nanocrystals synthesized at different reaction duration.

Ratio	0 h	0.5 h	2 h	8 h	24 h
Cu/Zn/Sn/S	5.0/0.1/0.1/2.8	2.1/0.9/0.8/4.1	2.1/1.0/0.9/4.0	2.1/1.0/1.0/3.9	2.0/1.0/1.0/4.0
[Cu]/([Zn+Sn])	1/0.04	1/0.82	1/0.90	1/0.97	1/1.05
[Zn]/[Sn]	—	1/0.93	1/0.92	1/0.96	1/0.99

The TEM images of the hydrothermal products collected at different reaction duration are shown in Figure 6. Figure 6a illustrates that, prior to the hydrothermal process, the precipitate obtained from the precursor solution is consisting of microspheres with size around 20–250 nm. The HRTEM indicates that the microparticle is the result of aggregation of numerous oval-like nanocrystals with size ranging from 10–30 nm. The HRTEM image of the material (inset of Figure 6b) shows the lattice fringe of a nanocrystal with an interplanar spacing of 1.87 Å, which is in good agreement with the (886) plane of monoclinic structure of Cu_7S_4. Besides that, the lattice fringe of nanocrystal with an interplanar spacing of 1.97 Å which can be ascribed to (220) plane of cubic structure of $Cu_{1.8}S$ was also found as illustrated in the inset of Figure 6c. These finding are consisting with the above shown XRD pattern. Figure 6d and 6e show that when the hydrothermal reaction is proceeded for 0.5 h, the dominant products are nanocrystals with irregular size of about 2–5 nm. The interplanar spacing of the crystals is 3.125 Å, which belongs to the (112) plane of CZTS. This result further confirms the rapid formation of CZTS compound in the hydrothermal reaction. Figure 6f shows that after hydrothermal reaction for 2 h, the agglomeration starts to break into small particles with size ranging from 3–20 nm. As the reaction time is prolonged to 8 h (Figure 6g), nanocrystals with size in the range of 5–10 nm appear in the product, and meanwhile the large agglomerates disappear. Upon gradual evolution of the CZTS nanostructures, nanoparticles with uniform distribution are obtained after reaction duration of 24 h (Figure 6h).

Formation mechanism

It is normally assumed that metal cations in a hydrothermal reaction are firstly associated with TGA in the precursor solution to form metal-TGA complexes prior to the hydrothermal reaction [22,23]. However, the formation of Cu_7S_4 and $Cu_{1.8}S$ compounds in our case suggests that Cu^{2+} is reduced to Cu^+ by interaction with the –SH (thiol) group of TGA (oxidation of TGA to dithiodiglycolate) [27]. The XRD pattern of the precipitate collected from the precursor solution without TGA prior to hydrothermal reaction reveals that CuS (JCPDS 6-0464) instead of $Cu_{2-x}S$ ($x = 0$–0.2) is formed (Figure 7). This confirms the reduction role played by TGA in the hydrothermal reaction system.

We believe that the initially formed $Cu_{2-x}S$ nanocrystals in the precursor solution prior to hydrothermal reaction act as nuclei for the formation of kesterite CZTS. The formed Cu_7S_4 and $Cu_{1.8}S$ material has a monoclinic and cubic crystal structure, respectively as confirmed by XRD measurement shown in Figure 5a. At relatively high reaction temperature, the copper ions in $Cu_{2-x}S$ have a relatively high mobility which can accommodate an exchange with other metal ions at a low energy cost [28]. In addition, the crystal structure of $Cu_{1.8}S$ has a cubic close packing (ccp) array of sulfur ions which is similar to the arrangement of sulfur in kesterite CZTS crystal framework. Hence, the interdiffusion of cations such as Zn^{2+} and Sn^{4+} to $Cu_{2-x}S$ crystal to form CZTS compound is feasible because there is little lattice distortion in such process [29]. Thus, the typical reaction condition (220 °C and above) is
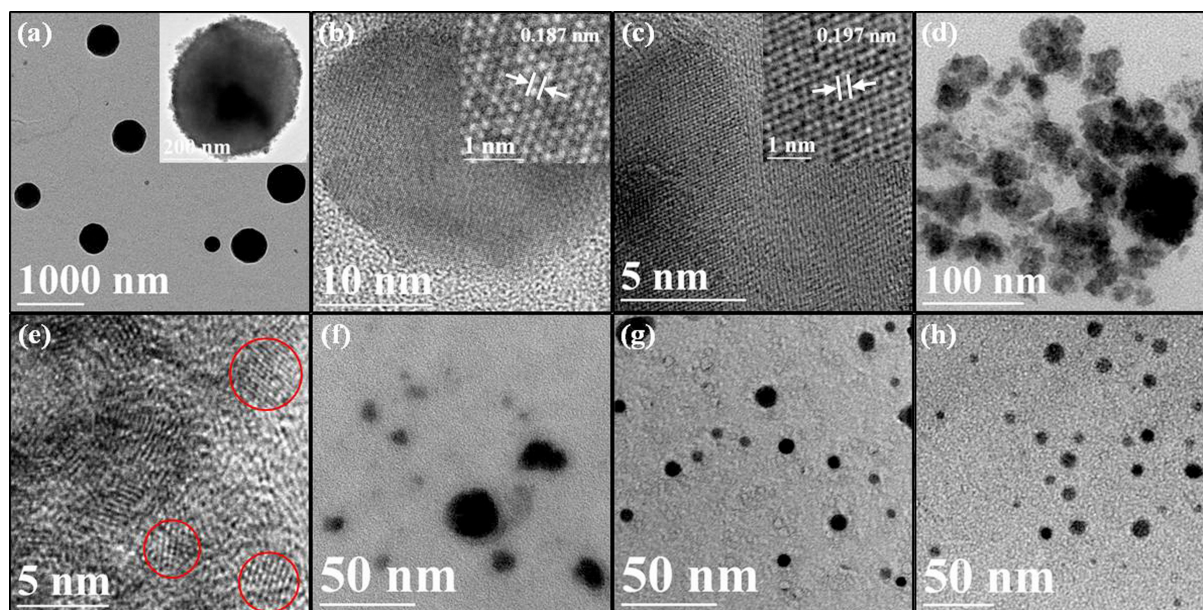

Figure 6: TEM images of (a, b, c) Cu_7S_4 and $Cu_{1.8}S$ nanocrystals collected prior to hydrothermal reaction and CZTS nanocrystals synthesized at different reaction duration: (d, e) 0.5 h, (f) 2 h, (g) 8 h, and (h) 24 h respectively.
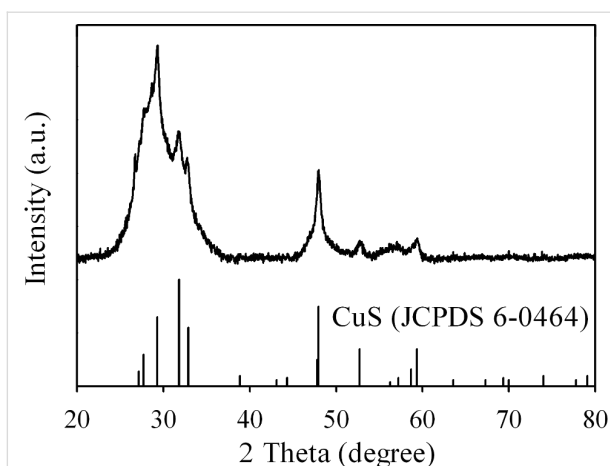
Figure 7: XRD pattern of the precipitate collected from the precursor solution without TGA prior to hydrothermal reaction.

believed to facilitate the chemical transformation from $Cu_{2-x}S$ to CZTS. Since no other binary products such as SnS_2 and ZnS are discovered in the entire hydrothermal process, and only Cu_2SnS_3 and Cu_3SnS_4 are detected in the Raman spectra, we believe Sn^{4+} cations are firstly incorporated into the crystal lattice of $Cu_{2-x}S$ and replaced parts of Cu^+ ion, followed by the rapid doping of Zn^{2+} to form CZTS compound in the hydrothermal process. The formation of CZTS compound as confirmed by TEM at the very short reaction time (0.5 h) suggests the fast diffusion rate of Zn and Sn ions to the lattice of $Cu_{2-x}S$ nuclei crystals in the hydrothermal process. Moreover, when the reaction duration is extended to 8 h, the Zn/Sn ratio is increased to 1/1.04 which matches well with the theoretical value of 1:1 in CZTS. With the proceeding of the reaction, the primary CZTS crystal nucleus grows to nanoparticles with different sizes. Based on Ostwald ripening process, the small crystal nucleus will grow up to form larger crystals because the large one has lower surface free energy [30]. TGA molecules which are adsorbed on the nanocrystals surface may restrict the growth of CZTS crystals and slow down the growth process, leading to the formation of monodisperse CZTS nanocrystals. Based on the above analysis, a schematics showing the formation mechanism for CZTS compound in the hydrothermal reaction is shown in Figure 8.

The UV–visible spectra of the hydrothermal samples synthesized at different reaction time are shown in Figure 9. It is found that the onset for light absorption of the material gradually shifts to longer wavelengths with the elongation of the reaction duration. The calculation of the band gap of the materials which is determined by extrapolation of the plot of $(Ah\nu)^2$ vs $h\nu$ (Inset of Figure 9) where A = absorbance, h = Planck's constant, and ν = frequency, shows that the hydrothermal products at reaction time of 0.5, 2, 8, and 24 h have band gap of 1.92, 1.76, 1.63 and 1.51 eV respectively. The decrement of the band gap value is due to the improvement of CZTS purity because impurities such as Cu_2SnS_3 and Cu_3SnS_4 have larger band gap than CZTS [31,32].
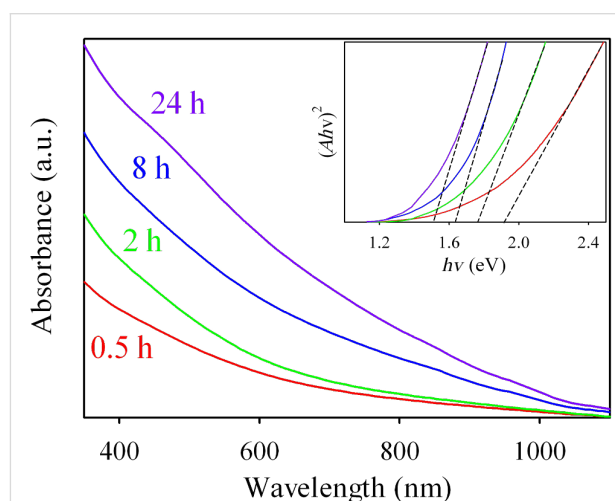
Figure 9: UV–visible absorption spectra of the CZTS nanocrystals synthesized at different reaction duration and the inset image shows the $(Ah\nu)^2$ vs $h\nu$ plots with corresponding fitting of the samples.

Conclusion

High quality, pure kesterite phase CZTS nanocrystals with uniform size distribution have been successfully synthesized by a facile one-step hydrothermal route based on a precursor solution containing thioglycolic acid (TGA) as surfactant. The role of TGA in the hydrothermal reaction is clarified and a formation mechanism of CZTS compound in the hydrothermal reaction is proposed. It is believed that the formation of CZTS is

Figure 8: Schematic illustrations of the formation process for kesterite CZTS nanoparticles.

initiated by the formation of $Cu_{2-x}S$ nanocrystals as a result of reduction of Cu^{2+} by TGA to become Cu^+. This is followed by the rapid diffusion of cations Sn^{4+} and Zn^{2+} to the crystal framework of $Cu_{2-x}S$ to form CZTS. The good optical properties and suitable band gap of 1.51 eV of the synthesized CZTS nanocrystals indicate the promise of this material for application in low cost thin film solar cells.

Acknowledgements

References

1. Kulendran, A.; Bell, J.; Wang, H. Size control of Cu2ZnSnS4 (CZTS) nanocrystals in the colloidal medium synthesis. In *Fourth International Conference on Smart Materials and Nanotechnology in Engineering,* Gold Coast, Australia, July 10–12, 2013; Epaarachchi, J. A.; Lau, A. K.-t.; Leng, J., Eds.; SPIE: Gold Coast, Australia, 2013; 87931A. doi:10.1117/12.2026592
2. Wang, H. *Int. J. Photoenergy* **2011,** *2011,* 801292. doi:10.1155/2011/801292
3. Scragg, J. J.; Dale, P. J.; Peter, L. M.; Zoppi, G.; Forbes, I. *Phys. Status Solidi B* **2008,** *245,* 1772–1778. doi:10.1002/pssb.200879539
4. Tiong, V. T.; Hreid, T.; Will, G.; Bell, J. M.; Wang, H. *Sci. Adv. Mater.,* in press. doi:10.1166/sam.2014.1824
5. Guo, Q.; Hillhouse, H. W.; Agrawal, R. *J. Am. Chem. Soc.* **2009,** *131,* 11672–11673. doi:10.1021/ja904981r
6. Zhou, H.; Hsu, W.-C.; Duan, H.-S.; Bob, B.; Yang, W.; Song, T.-B.; Hsu, C.-J.; Yang, Y. *Energy Environ. Sci.* **2013,** *6,* 2822–2838. doi:10.1039/c3ee41627e
7. Cao, Y.; Xiao, Y.; Jung, J.-Y.; Um, H.-D.; Jee, S.-W.; Choi, H. M.; Bang, J. H.; Lee, J.-H. *ACS Appl. Mater. Interfaces* **2013,** *5,* 479–484. doi:10.1021/am302522c
8. Todorov, T. K.; Tang, J.; Bag, S.; Gunawan, O.; Gokmen, T.; Zhu, Y.; Mitzi, D. B. *Adv. Energy Mater.* **2013,** *3,* 34–38. doi:10.1002/aenm.201200348
9. Todorov, T. K.; Reuter, K. B.; Mitzi, D. B. *Adv. Mater.* **2010,** *22,* E156–E159. doi:10.1002/adma.200904155
10. Jiang, H.; Dai, P.; Feng, Z.; Fan, W.; Zhan, J. *J. Mater. Chem.* **2012,** *22,* 7502–7506. doi:10.1039/c2jm16870g
11. Liu, W. C.; Guo, B. L.; Wu, X. S.; Zhang, F. M.; Mak, C. L.; Wong, K. H. *J. Mater. Chem. A* **2013,** *1,* 3182–3186. doi:10.1039/c3ta00357d
12. Wang, C.; Cheng, C.; Cao, Y.; Fang, W.; Zhao, L.; Xu, X. *Jpn. J. Appl. Phys.* **2011,** *50,* 065003. doi:10.1143/JJAP.50.065003
13. Zhou, Y.-L.; Zhou, W.-H.; Li, M.; Du, Y.-F.; Wu, S. N. *J. Phys. Chem. C* **2011,** *115,* 19632–19639. doi:10.1021/jp206728b
14. Tian, Q.; Xu, X.; Han, L.; Tang, M.; Zou, R.; Chen, Z.; Yu, M.; Yang, J.; Hu, J. *CrystEngComm* **2012,** *14,* 3847–3850. doi:10.1039/c2ce06552e
15. Cao, M.; Shen, Y. *J. Cryst. Growth* **2011,** *318,* 1117–1120. doi:10.1016/j.jcrysgro.2010.10.071
16. Zhou, Y.-L.; Zhou, W.-H.; Du, Y.-F.; Li, M.; Wu, S.-X. *Mater. Lett.* **2011,** *65,* 1535–1537. doi:10.1016/j.matlet.2011.03.013
17. Liu, M.; Wang, H.; Yan, C.; Will, G.; Bell, J. *Appl. Phys. Lett.* **2011,** *98,* 133113. doi:10.1063/1.3573799
18. Tiong, V. T.; Zhang, Y.; Bell, J. M.; Wang, H. *CrystEngComm* **2014,** in press. doi:10.1039/c3ce42606h
19. Cheng, A. J.; Manno, M.; Khare, A.; Leighton, C.; Campbell, S. A.; Aydil, E. S. *J. Vac. Sci. Technol., A* **2011,** *29,* 051203–051211. doi:10.1116/1.3625249
20. Fernandes, P. A.; Salomé, P. M. P.; da Cunha, A. F. *J. Alloys Compd.* **2011,** *509,* 7600–7606. doi:10.1016/j.jallcom.2011.04.097
21. Riha, S. C.; Parkinson, B. A.; Prieto, A. L. *J. Am. Chem. Soc.* **2009,** *131,* 12054–12055. doi:10.1021/ja9044168
22. Yang, D.; Zhao, J.; Liu, H.; Zheng, Z.; Adebajo, M. O.; Wang, H.; Liu, X.; Zhang, H.; Zhao, J.-c.; Bell, J.; Zhu, H. *Chem.–Eur. J.* **2013,** *19,* 5113–5119. doi:10.1002/chem.201202719
23. Zhu, H.; Yang, D.; Zhang, H. *Mater. Lett.* **2006,** *60,* 2686–2689. doi:10.1016/j.matlet.2006.01.065
24. Salavati-Niasari, M.; Davar, F.; Seyghalkar, H.; Esmaeili, E.; Mir, N. *CrystEngComm* **2011,** *13,* 2948–2954. doi:10.1039/c0ce00343c
25. Biswas, S.; Kar, S.; Chaudhuri, S. *Appl. Surf. Sci.* **2007,** *253,* 9259–9266. doi:10.1016/j.apsusc.2007.05.053
26. Su, Z.; Sun, K.; Han, Z.; Liu, F.; Lai, Y.; Li, J.; Liu, Y. *J. Mater. Chem.* **2012,** *22,* 16346–16352. doi:10.1039/c2jm31669b
27. Mishra, R.; Mukhopadhyay, S.; Banerjee, R. *Dalton Trans.* **2010,** *39,* 2692–2696. doi:10.1039/b918582h
28. Li, M.; Zhou, W.-H.; Guo, J.; Zhou, Y.-L.; Hou, Z.-L.; Jiao, J.; Zhou, Z.-J.; Du, Z.-L.; Wu, S.-X. *J. Phys. Chem. C* **2012,** *116,* 26507–26516. doi:10.1021/jp307346k
29. Regulacio, M. D.; Ye, C.; Lim, S. H.; Bosman, M.; Ye, E.; Chen, S.; Xu, Q.-H.; Han, M.-Y. *Chem.–Eur. J.* **2012,** *18,* 3127–3131. doi:10.1002/chem.201103635
30. Roosen, A. R.; Carter, W. C. *Physica A* **1998,** *261,* 232–247. doi:10.1016/S0378-4371(98)00377-X
31. Kuku, T. A.; Fakolujo, O. A. *Sol. Energy Mater.* **1987,** *16,* 199–204. doi:10.1016/0165-1633(87)90019-0
32. Fernandes, P. A.; Salomé, P. M. P.; da Cunha, A. F. *J. Phys. D: Appl. Phys.* **2010,** *43,* 215403. doi:10.1088/0022-3727/43/21/215403

Encapsulation of nanoparticles into single-crystal ZnO nanorods and microrods

Jinzhang Liu[*], Marco Notarianni, Llew Rintoul and Nunzio Motta

Abstract

One-dimensional single crystal incorporating functional nanoparticles of other materials could be an interesting platform for various applications. We studied the encapsulation of nanoparticles into single-crystal ZnO nanorods by exploiting the crystal growth of ZnO in aqueous solution. Two types of nanodiamonds with mean diameters of 10 nm and 40 nm, respectively, and polymer nanobeads with size of 200 nm have been used to study the encapsulation process. It was found that by regrowing these ZnO nanorods with nanoparticles attached to their surfaces, a full encapsulation of nanoparticles into nanorods can be achieved. We demonstrate that our low-temperature aqueous solution growth of ZnO nanorods do not affect or cause degradation of the nanoparticles of either inorganic or organic materials. This new growth method opens the way to a plethora of applications combining the properties of single crystal host and encapsulated nanoparticles. We perform micro-photoluminescence measurement on a single ZnO nanorod containing luminescent nanodiamonds and the spectrum has a different shape from that of naked nanodiamonds, revealing the cavity effect of ZnO nanorod.

Introduction

Anisotropic growth of compound semiconductors with wurtzite crystal structure normally leads to the formation of one-dimensional (1D) structures. A typical example is ZnO that, in its wurtzite form, has the fastest growth rate over the <0001> face and has been extensively studied in terms of synthesis methods and applications. ZnO is a multifunctional material with semiconducting, photonic, and piezoelectric properties. Potential applications of ZnO 1D nanostructures include gas sensor [1],

transistor [2], light-emitting device [3], optical waveguide [4], nanolaser [5], and piezoelectric power generator [6], etc. Since the first report of ZnO nanobelts in 2001 [7], methods for growing ZnO 1D nanostructures have been well developed, including high-temperature vapour-phase growth [8], low-temperature aqueous solution growth [9], and electrochemical deposition [10]. The aqueous solution growth is the least expensive one, and is scalable for production.

Single-crystal nanowires/nanorods of wide-bandgap semiconductors are ideal candidates for nanophotonic applications. The 1D geometry, dislocation-free single-crystalline nature, high index of refraction and atomically smooth surface, allow for sufficient end-facet reflectivity and photon confinement in a volume of just a few cubic wavelengths of material. Since the first report of a ZnO nanowire laser, much effort has been placed in nanophotonic research based on small-sized semiconducting nanocrystals with 1D or 2D structures. To study the photon–matter interaction within those crystals, the luminescence of the cavity material has been conventionally used as a light source. Under excitation, ZnO emits UV light at about 380 nm ascribed to its wide band gap ($E_g \approx 3.4$ eV). With crystal defects such as oxygen vacancies, ZnO show visible photoluminescence under UV light excitation. Though ZnO micro/nanorods can be both light emitters and optical cavities, the drawback is that their luminescence is not tunable in terms of wavelength and efficiency. For laser applications, the visible emission of ZnO micro/nanocavities has a broad range which can be used to observe a series of optical resonances [11,12], while lasing in this range cannot be achieved. Within the narrow excitonic emission range, UV lasing from ZnO micro/nanorods has been realized [5,13], however this requires that the resonant positions sit within the narrow UV emission range. Thus the options for lasing wavelength and resonant mode orders are limited. There is a large variety of nanoparticles that have various luminescent properties and potential applications. Luminescent nanoparticles including semiconductor quantum dots, nanodiamonds (NDs) with nitrogen-vacancy (NV) centres, and dye-doped polymer nanobeads, etc., have wide applications based on their luminescent properties. Luminescent NDs can be used for magnetic sensing [14]; dye-doped polymer nanobeads can act as laser gain media [15], depending on the selection of dye molecules. Semiconductor quantum dots can be used as laser gain media as well as for quantum communications when confined within an optical cavity. The coupling of luminescent nanoparticles emission to artificial optical cavities such as 2D photonic crystals [16] and micro-spheres [17] has been studied. Single crystal nanorods as dielectric cavities have superior features in terms of their small size and excellent cavity properties. Therefore by encapsulating luminescent nanoparticles into transparent single-crystal nanorods, it is possible to develop an interesting platform for novel photonic applications.

ZnO nano/microrods are particularly interesting because they are not only optical cavities but also components for developing UV light-emitting diodes (LEDs). If luminescent quantum dots or dye-doped polymer nanobeads can be encapsulated into a ZnO nano/microrod that is integrated into a LED, the UV emission of ZnO can act as an excitation source to stimulate the visible emissions of embedded nanoparticles, providing the way to develop small-size lasers. So far, nanoparticles-filled polymers or glass fibres have been reported [18,19]. No reports exist on integrating nanoparticles into single-crystal nanorods. By sealing functional nanoparticles, such as luminescent, magnetic, and plasmonic metal materials, etc., into single crystal nanorods, we believe that many applications can be explored. Herein, we report the encapsulation of nanoparticles into ZnO nanorods by exploiting the growth habit of ZnO. A low-temperature aqueous solution growth method is used to grow ZnO nanorods. It is worth mentioning that the low-temperature growth (<100 °C) does not produce any thermal damage to the encapsulated nanoparticles, and this is important in particular for organic nanomaterials.

Results and Discussion
Encapsulation of nanodiamonds
We firstly used small size NDs (10 nm size), which are non-luminescent and purchased as nanopowder, to study the encapsulation of small nanoparticles into ZnO nano/microrods, as shown in Figure 1. Two groups of samples, ZnO nanorods and microrods, used to study the embedment of NDs, are depicted in Figure 1a–c and Figure 1d–f, respectively. Figure 1a and Figure 1d show that NDs are attached to both the top and side facets of nano/microrods. The thin nanorods in Figure 1a and relatively thick microrods in Figure 1d were grown from two nutrient solutions with different chemical concentrations of 15 mM and 30 mM, respectively. The side-view image in Figure 1b shows that NDs were embedded in the nanorods after a second growth process (20 mM, 4 h). Regrowth of the nanorod along the axial direction leads to a new section with smooth surface. By measuring the length of newly-grown section, we can estimate that the second growth process results in 1.7 times increase of the length. Nevertheless, the growth over the side facets was too slow to completely bury the surface-attached NDs. The close-view image in Figure 1c shows that the incomplete encapsulation of NDs leads to holes in the nanorod surface. For ZnO microrods in Figure 1d, regrowth along the axial direction is much slower than that of the much thinner nanorods, concluded by comparing Figure 1b and Figure 1e. Note that experimental conditions for the second growth of the two samples are identical. On the other hand, for thick microrods the growth over the side facets was less suppressed as can be seen in Figure 1e, where most of the nanoparticles were completely encapsulated into the nanorods, leaving some big ND clusters partially exposed. All the surface attached NDs can be completely encapsulated into ZnO microrods if longer regrowth time (8 h) is allowed, as seen in Figure 1f. The encapsulation of 10 nm size NDs into ZnO nano/microrods indicates that luminescent quantum dots can be hosted by a ZnO nano/microrod cavity, in order to develop
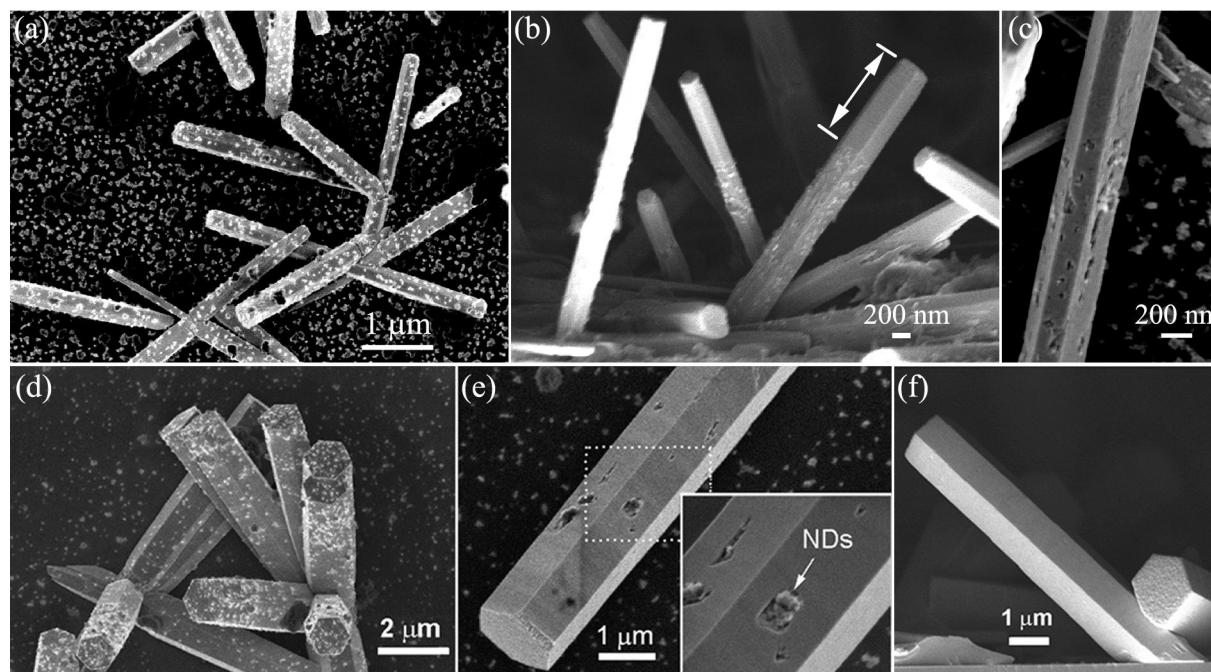
Figure 1: FE-SEM images showing the encapsulation of 10-nm-diameter NDs into ZnO nanorods and microrods. (a) Thin nanorods with NDs attached to their surfaces. (b) After a second growth process of ZnO nanorods. (c) A close-view of the nanorod, showing the embedment of NDs into the rod and the newly-grown section with smooth surface. (d) Relatively thick microrods with NDs in their surfaces. (e) After a second growth process, most of the NDs were encapsulated into the microrod, leaving some NDs clusters partially exposed. (f) NDs were completely encapsulated into the nanorod, given long regrowth time.

advanced photonic devices such as lasers and color-tunable light emitting devices. In our experiment NDs from isopropanol solution were dispersed onto both ZnO nano/microrods and a Si substrate. If a lithography technique is employed to grow ordered ZnO nanorods onto a lattice-constant-matched substrate, nanoparticles on the substrate can be avoided and the size of nanorod cavity can be well controlled in respect of light wavelength and optical cavity effect.

Figure 2 demonstrates the encapsulation of 40 nm diameter NDs, which contain NV luminescent centres, into ZnO nanorods. We dispersed NDs from the suspension twice onto ZnO nanorods in order to increase the areal density of nanoparticles. It can be seen in Figure 2a that some NDs even agglomerate. As nanoparticles were heavily loaded onto ZnO nanorods, regrowth of ZnO can only occur over the limited bare surface. However, it is surprising to see that these surface-attached NDs were completely encapsulated into nanorods after a regrowth process (20 mM, 6 h), as evidenced by the top-view image in Figure 2b and the side-view image in Figure 1c. Among the nanorods, few show incomplete encapsulation of agglomerated NDs. as can be seen in Figure 2d. We cut the Si substrate to take side-view images. Some nanorods were fractured at the edge of the cracked substrate. The cross-sections of fractured nanorods in Figure 2e and 2f clearly show NDs completely

encapsulated into the nanorods. Also, from Figure 2e we can measure that the thickness of newly-grown ZnO layer over the side facets is about 120 nm. For nanoparticles of inorganic materials, the size below 100 nm can be easily achieved. However for polymer materials it might be not easy to prepare small nanoparticles with size below 100 nm. Hence it is worth studying the encapsulation of relatively large nanoparticles into ZnO nanorods. The advantage of polymer nanobeads is that they can be multi-functional by hosting luminescent dye molecules or magnetic nanoparticles. As the growth rate over the side facets of a ZnO nanorod is much slower than that over the top facet, it would be more challenging to encapsulate large nanoparticles with size beyond the 100 nm regime into ZnO nanorod.

Encapsulation of polymer nanobeads

We used polystyrene nanobeads (diameter 200 nm) to study the encapsulation of large nanoparticles into ZnO nanorods. After dropping nanobeads aqueous suspension onto ZnO nanorods arrays and blow-drying, nanobeads were found sparsely scattered over the nanorods surfaces as seen in Figure 3a. Nanobeads attached to the top facet can be entirely encapsulated into the nanorod after a regrowth process due to the fast axial growth rate. However, those attached to the side surface were partially embedded into the nanorods after a second
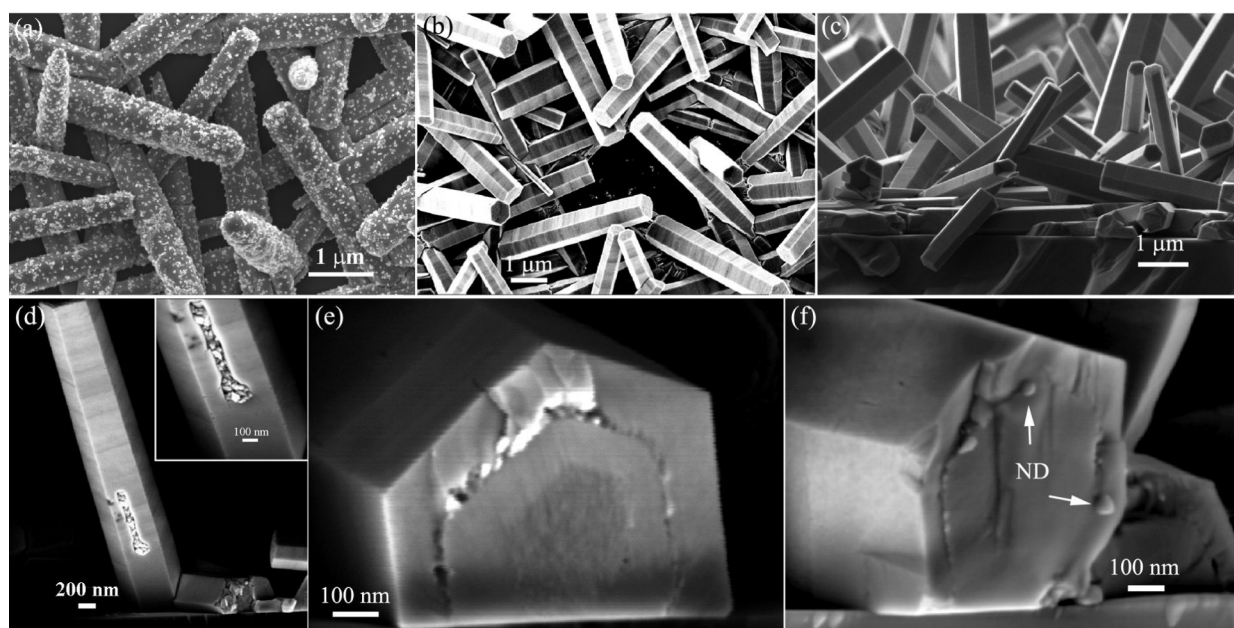
Figure 2: FE-SEM images showing the encapsulation of 40-nm-diameter NDs into ZnO nanorods. (a) ZnO nanorods covered with NDs. (b and c) Top- and side-view images of the nanorods after a second growth process, showing the complete encapsulation of NDs into the nanorods. (d) A nanorod shows the incomplete encapsulation of agglomerated NDs. (e and f) Cross-section images of fractured nanorods containing NDs, showing NDs inside the crystal.
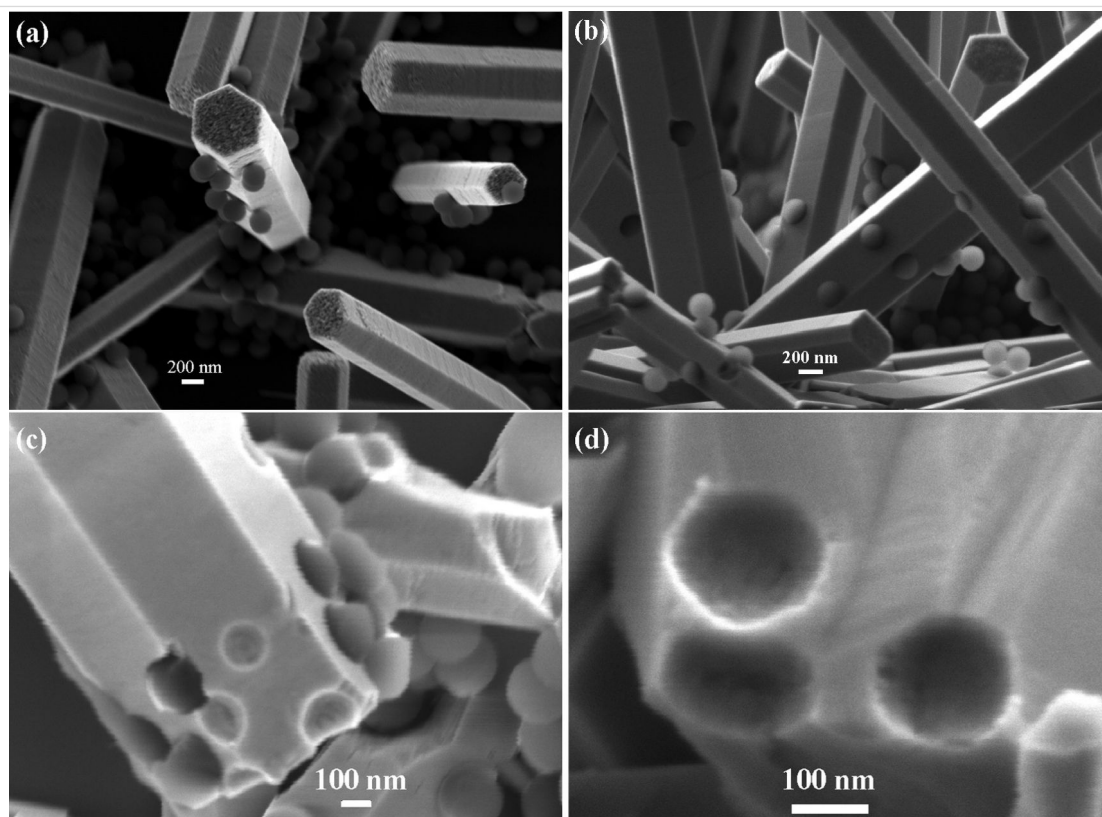
Figure 3: FE-SEM images showing the embedment of 200-nm-diameter polymer nanobeads in ZnO nanorods. (a) ZnO nanorods with polymer nanobeads attached to their surfaces. (b) Nanobeads were embedded in nanorods after a second growth process. These nanobeads were about half-volume exposed. (c) Intentionally fractured nanorods. (d) Close-view of the vacant sites where the nanobeads were broken off.

growth from solution (20 mM, 5 h), as seen in Figure 3b. We intentionally broke these nanorods by crushing them against a piece of bare Si for SEM imaging, as shown in Figure 3c and 3d. The close-view image in Figure 3c shows that the nanobeads were about half-volume embedded in the nanorod. Considering the nanobead radius of 100 nm, we can deduce that the thickness of newly-grown ZnO over the side facet is about 100 nm, which is consistent with the thickness of newly-grown layer revealed by Figure 2c. Some nanobeads embedded into the nanorod were detached when the nanorods were mechanically fractured. This exposes the bowl-shaped pits where the nanobeads once were. A close-view image of these voids in Figure 3d shows that their inner surface is rather smooth, which means the embedded nanobeads are tightly surrounded by ZnO. We believe that no chemical bonds were formed at the interface between nanobeads and ZnO, and the interaction is van der Waals force.

The polymer nanobeads can be embedded deeper or even completely incorporated into ZnO crystal, depending on how much the nanorod is regrown. Figure 4a shows the nanorod after a regrowth process of 8 h. Such a long regrowth process leads to an overgrowth thickness more than 120 nm but less than 200 nm, leading to a deep embedding of nanobeads into the ZnO nanorod. In Figure 4b, the nanobeads were embedded even deeper after a 12 h regrowth (thickness above 200 nm) of the nanorod. The deeply embedded nanobeads leave holes in the nanorod surface of about 100 nm across, much smaller than the nanobeads (200 nm). It is conceivable that the holes will gradually fill in and finally close if the nanorod continues to grow. Figure 4c shows a nanorod in which some nanobeads are slightly exposed and one is almost encapsulated into the nanorod bulk as indicated by an arrow. In the aqueous solution most of the Zn^{2+} ions are condensed into ZnO within 4 h, and the chemicals are exhausted if the growth duration exceeds
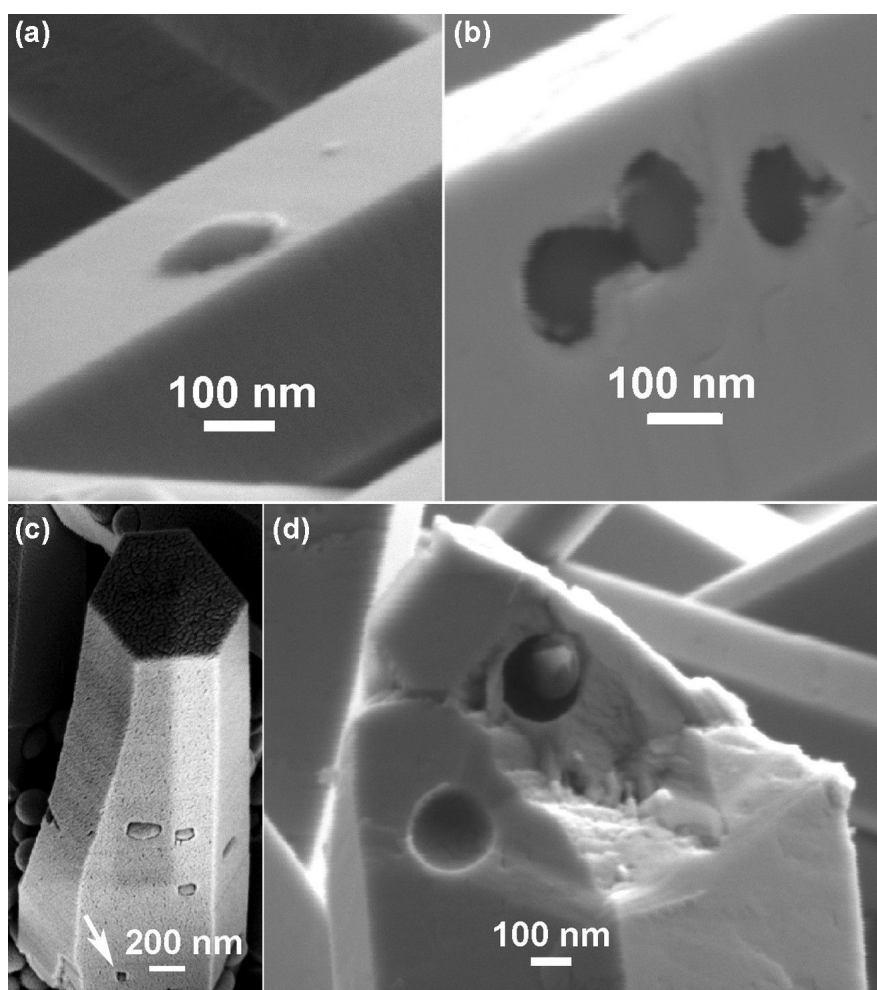
Figure 4: FE-SEM Images showing the encapsulation of nanobeads into ZnO nano/microrods after different regrowth processes. (a) Most part of the nanobead is embedded into a nanorod. (b) Nanobeads are deeper embedded into a nanorods, leaving holes in the surface. (c) A thick microrod showing that the embedded nanobeads are slightly exposed. (d) A fractured microrod showing a completely encapsulated nanobead inside.

12 h. Hence the 200 nm diameter nanobeads cannot be completely sealed into the nanorods by simply prolonging the growth time. To further thicken the nanorods, we used a three-step growth process. The nanorods after the first growth step were used to support nanobeads. After the second growth for 4 h, which is insufficient to completely encapsulate the nanobeads into ZnO nanorods, the sample was transferred to a fresh nutrient solution for the third-step growth for 4h. The fractured nanorod in Figure 4d reveals a nanobead entirely encapsulated into the nanorod.

Growth mechanism

The growth of ZnO in aqueous solution can be described as an epitaxial growth process. The precursors $Zn(NO_3)_2$ and HMTA in water lead to chemical reactions are as follows [20]:

$$(CH_2)_6N_4 + 6H_2O \rightarrow 4NH_3 + 6HCHO \qquad (1)$$

$$NH_3 + H_2O \rightarrow NH_4^+ + OH^- \qquad (2)$$

$$Zn^{2+} + 2OH^- \rightarrow Zn(OH)_2 \qquad (3)$$

$$Zn(OH)_2 \rightarrow ZnO + H_2O \qquad (4)$$
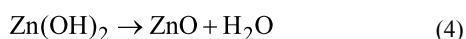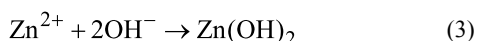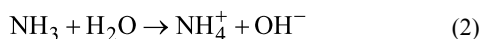
Hence, Zn^{2+} and OH^- are the growth species contributing to the growth of ZnO. When the ZnO nanorod is in the nutrient solution, the growth species deposited onto the surface contribute to the stack of atomic layers, making the nanorod grow thicker and longer while maintaining the single-crystal feature and hexagonal shape (Figure S1, Supporting Information File 1). This growth process can be described as solution homoepitaxy

[21,22]. By crushing ZnO nano/microrods containing NDs onto a bare Si, we were able to expose NDs in the fracture section. The smooth and continuous surface around those exposed NDs or tiny cavities with NDs off further reveals the single-crystal character of the rod after two-step growth process (Figure S2, Supporting Information File 1). Figure 5a illustrates the encapsulation of a nanoparticle into a growing crystal. Initially the nanoparticle attaches to the crystal surface. With atomic layers stacking and spreading over the surface, the nanoparticle is embedded in newly-grown crystal. Step by step, the crystal grows around the nanoparticle enclosing it into a perfectly matching cavity. When the overgrowth is nearly completed a hole above the nanoparticle could still be present. The epitaxial growth continues and the hole gradually shrinks and finally closes, sealing the nanoparticle in crystal. Figure 5b is a 3D view of the encapsulation process. The top (0001) facet of ZnO nanorod is known to have the fastest growth rate, hence nanoparticles at the top face can be quickly encapsulated. Complete encapsulation of nanoparticles attached to the side facets into the nanorod can be achieved if the newly-grown layer thickness is beyond the nanoparticle size.

Micro-photoluminescence of a single ZnO nanorod containing luminescent nanodiamonds

The 40 nm size NDs with NV luminescent centers exhibit red photoluminescence (PL) when excited by a green laser. The results of micro-PL measurements on a single ZnO nanorod containing luminescent NDs, a ZnO nanorod with NDs attached to its surface, and naked NDs dispersed from solution on a steel substrate are shown in Figure 6a. The insets show two fractured ZnO nanorods lying on Si substrates. One nanorod has
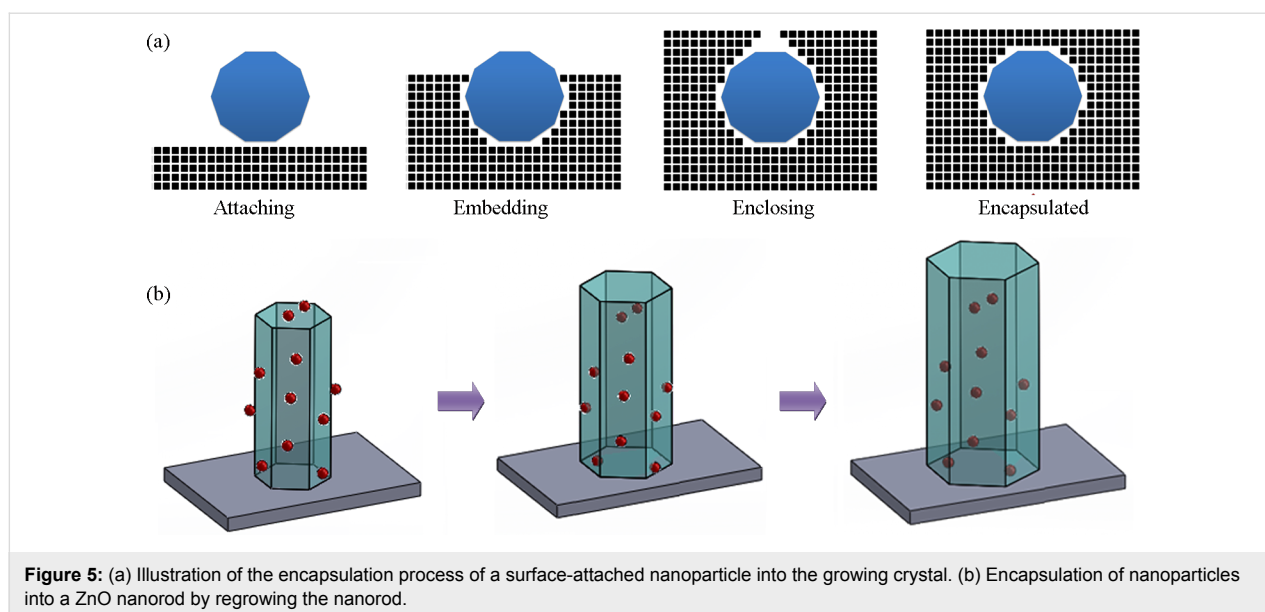
Figure 5: (a) Illustration of the encapsulation process of a surface-attached nanoparticle into the growing crystal. (b) Encapsulation of nanoparticles into a ZnO nanorod by regrowing the nanorod.

Figure 6: (a) Micro-PL spectra taken from a single ZnO nanorod containing NDs, a nanorod with NDs in the surface, and cluster of naked NDs, respectively. The insets show typical SEM images of two fractured ZnO nanorods lying on bare Si. One nanorod contains NDs and the other one has NDs attached to its surface. (b) Micro-PL spectra of a single ZnO microrod containing NDs and naked NDs. The inset shows an optical photograph taken during the PL measurement. The relatively thick rod marked by a cross was targeted for PL measurement. (c) Illustrations for light propagations when the emission from a ND interacts with the rod cavity.

NDs embedded inside and the other one has naked NDs attached to its surface. The three PL spectra, with peak maximum normalized, have two small characteristic peaks of the NV defect at 576 and 638 nm, corresponding to charge states of NV^0 and NV^-, respectively. The PL spectrum of naked NDs shows peak position of emission band at 705 nm. However, for those NDs in contact with a ZnO nanorod, either embedded or in the surface, their PL emission peak is blue-shifted to 686 nm. The laser energy is insufficient to produce PL of ZnO, ruling out the influence of ZnO luminescence in causing the shift of NDs emission. In Figure 6b, the PL spectrum of NDs in a thick ZnO microrod shows a different shape compared to that of naked NDs. The inset in Figure 6b is an optical microscope image, in which the relatively thick rod marked by a cross was the target for collecting PL spectrum. The diameter of this rod is estimated to be 1.5–2.0 µm, whereas those in Figure 6a are 0.6–1.0 µm. In micro-PL measurement, the laser beam with a spot size of about 1 µm was perpendicular to the nanorod and NDs inside or attached to the nanorod were excited to produce red luminescence. ZnO nanorod is transparent to visible light and emissions from NDs can transmit into ZnO nano/microrod to undergo multiple reflections. ZnO is a birefringent crystal with a refractive index of about 2.0 in the visible range, indicating the total refraction angle of light ray in ZnO is about 30 °C. Due to the waveguide effect partial photons would prop-

agate along the nanorod axis direction. Hence inside the nanorod light rays refracted to top upper facet have contribution to the PL signal (Figure 6c). Light rays with different polarizations have different transmittance when refracted from ZnO to air. The blue-shift of emission band of NDs inside or in the surface of a ZnO nanorod could be attributed to the optical cavity effect of ZnO nanorod. One possible light propagation path is a close loop in the rod cross-section, as show in the right hand in Figure 6c. That means, the nanorod is treated as a 2D cavity and the light ray strikes at the center of boundary at 60° incident angle to circulate in a hexagon loop, leading to whispering-gallery mode (WGM) resonances when the length of loop is an integer multiple of light wavelength. Normally, the larger the cavity size, the higher the resonance quality [23,24]. In the PL spectrum, the resonant peaks would broaden and peaks will be more separated with reducing the nanorod diameter. In Figure 6b, the PL spectrum of a relatively thick ZnO microrod containing NDs shows not only the blue-shift of the luminescence band but also the suppressed intensity of the band central region. The shoulder peak at 660 nm is pronounced, which can be explained by the resonant cavity-induced enhancement. The thickness of this microrod is estimated to be 1.5–2.0 µm, which is more suitable to produce discernible WGMs compared to those thinner nanorods with diameters smaller than 1 µm. Light emission from NDs is coupled to the

microrod cavity and WGM resonances behind the PL spectrum leads to enhancement of luminescence at positions aside the emission band peak, making the PL peak shift and the band shoulders prominent. Fabry–Pérot type resonances originated from photons bouncing between two opposite side facets of the nano/microrod cannot be observed due to the short inter-distance. If vertical ZnO nano/microrods containing luminescent nanoparticles are illuminated by an excitation laser at the top, we believe that much stronger PL signal can be collected due to the waveguide effect and Fabry–Pérot type resonances or even lasing can be achieved.

Conclusion

In summary, we have demonstrated the encapsulation of nanoparticles into single crystal ZnO nanorods by exploiting crystal growth. Nanodiamonds and polymer nanobeads are used as examples to study this process for nanoparticles with different sizes and shapes into ZnO nanorods grown in aqueous solution at low temperature. Our two-step aqueous epitaxial growth process results in the full encapsulation of 10 nm and 40 nm nanodiamonds. The same two-step process results only in a partial embedment of 200 nm diameter polymer nanobeads. Complete encapsulation of these relatively larger nanobeads into ZnO nanorods can be achieved by a further epitaxial growth of ZnO via a three-step process using the same solution method. Our study indicates that in principle any kinds of nanoparticles, both inorganic and organic, can be incorporated into ZnO nanorods. The epitaxial growth over ZnO surface leads to the encapsulation of nanoparticles into the crystal while maintaining the single crystal feature. We believe that nanoparticles can be encapsulated into not only ZnO, but also other functional crystals grown by the epitaxy process. Micro-PL measurements on a single ZnO nanorod containing luminescent NDs demonstrates that the light emission from NDs can be coupled to the nanorod cavity, resulting in shift of the PL emission peak and change of the PL spectrum shape.

This low temperature process opens the way to the encapsulation of nanoparticles made of polymers and even biomaterials, which would degrade at high temperature, creating a new platform for nano-devices, nano-detectors, and applications in nano-medicine.

Experimental

ZnO nanorods were grown at 90 °C onto Si substrates in an aqueous solution containing zinc nitrate and hexamethylenetetramine (HMTA) with molar ratio of 1:1. A piece of bare Si was put face-down floating on top of the nutrient solution surface. The strategy to encapsulate nanoparticles into ZnO nanorods is through a multi-step growth process. First, ZnO nanorods are grown onto the substrate; second, nanoparticles are attached to the surface of nanorods; Third, the nanorods are grown again in the solution to incorporate the nanoparticles. The growth duration was set 4 h for the first-step growth, but different concentrations of zinc nitrate and HMTA in the solution were used to control the nanorod thickness. To grow thin nanorods, 15 mM Zn^{2+} in the solution was used. Thick nanorods were grown in the 30 mM solution. After growth, the sample was rinsed with DI water and dried. Afterwards, nanoparticle suspension was dropped onto the substrate covered with nanorods, and then rinsed. This leads to the attachment of nanoparticles onto the nanorods surfaces by van der Waals force. The sample was dried at 50 °C, followed by a second growth of ZnO nanorods in the nutrient solution containing 20 mM Zn^{2+}. The regrowth duration was 4–12 h, and different nanoparticles were used: two types of diamond nanoparticles with average diameters of 10 nm and 40 nm, respectively, and polymer nanobeads with mean size of 200 nm. Nanopowder of NDs with mean size of 10 nm (Aldrich Sigma) was dispersed into isopropanol (0.2 mg/mL) to prepare a suspension. An aqueous suspension of 40 nm diameter NDs (0.1 mg/mL) with NV luminescent centres was purchased from Adamas Nanotech. Polystyrene nanobeads (200 nm size) dispersed in water (0.5 mg/mL) were purchased from Polyscience Inc. Field-emission scanning electron microscopy (FE-SEM, Zeiss Sigma) was employed to study the morphologies of ZnO nanorods and embedded nanoparticles. For micro-PL measurement, ZnO nanorod arrays were crushed against a bare Si, to produce fractured nanorods lying on the surface. A micro-Raman/PL spectrometer (Renishaw inVia) with 532 nm laser was employed to study the PL of single ZnO nanorod containing NDs.

Supporting Information

Supporting Information File 1
Additional figures.
[http://www.beilstein-journals.org/bjnano/content/supplementary/2190-4286-5-56-S1.pdf]

Acknowledgements

References

1. Ahn, M.-W.; Park, K.-S.; Heo, J.-H.; Park, J.-G.; Kim, D.-W.; Choi, K. J.; Lee, J.-H.; Hong, S.-H. *Appl. Phys. Lett.* **2008,** *93,* 263103. doi:10.1063/1.3046726

2. Goldberger, J.; Sirbuly, D. J.; Law, M.; Yang, P. *J. Phys. Chem. B* **2005,** *109,* 9–14. doi:10.1021/jp0452599
3. Lai, E.; Kim, W.; Yang, P. *Nano Res.* **2008,** *1,* 123–128. doi:10.1007/s12274-008-8017-4
4. Voss, T.; Svacha, G. T.; Mazur, E. *Nano Lett.* **2007,** *7,* 3675–3680. doi:10.1021/nl071958w
5. Huang, M. H.; Mao, S.; Feick, H.; Yan, H.; Wu, Y.; King, H.; Weber, E.; Russo, R.; Yang, P. *Science* **2001,** *292,* 1897–1899. doi:10.1126/science.1060367
6. Wang, Z. L.; Song, J. *Science* **2006,** *312,* 242–246. doi:10.1126/science.1124005
7. Pan, Z. W.; Dai, Z. R.; Wang, Z. L. *Science* **2001,** *291,* 1947–1949. doi:10.1126/science.1058120
8. Huang, M. H.; Wu, Y.; Feick, H.; Tran, N.; Weber, E.; Yang, P. *Adv. Mater.* **2001,** *13,* 113–116. doi:10.1002/1521-4095(200101)13:2<113::AID-ADMA113>3.0.CO;2-H
9. Huang, C.-H.; Whang, W.-T. *Mater. Chem. Phys.* **2003,** *82,* 705–710. doi:10.1016/S0254-0584(03)00331-6
10. Xu, L.; Guo, Y.; Liao, Q.; Zhang, J.; Xu, D. *J. Phys. Chem. B* **2005,** *109,* 13519–13522. doi:10.1021/jp051007b
11. Liu, J.; Lee, S.; Ahn, Y. H.; Park, J.-Y.; Koh, K. H.; Park, K. H. *Appl. Phys. Lett.* **2008,** *92,* 263102. doi:10.1063/1.2952763
12. Dai, G.; Zhang, Y.; Liu, R.; Wan, Q.; Zhang, Q.; Pan, A.; Zou, B. *J. Appl. Phys.* **2011,** *110,* 033101. doi:10.1063/1.3610521
13. Chu, S.; Wang, G.; Zhou, W.; Lin, Y.; Chernyak, L.; Zhao, J.; Kong, J.; Li, L.; Ren, J.; Liu, J. *Nat. Nanotechnol.* **2011,** *6,* 506–510. doi:10.1038/nnano.2011.97
14. Taylor, J. M.; Cappellaro, P.; Childress, L.; Jiang, L.; Budker, D.; Hemmer, P. R.; Yacoby, A.; Walsworth, R.; Lukin, M. D. *Nat. Phys.* **2008,** *4,* 810–816. doi:10.1038/nphys1075
15. Cerdán, L.; Enciso, E.; Martín, V.; Bañuelos, J.; López-Arbeloa, I.; Costela, A.; García-Moreno, I. *Nat. Photonics* **2012,** *6,* 621–626. doi:10.1038/nphoton.2012.201
16. Brossard, F. S. F.; Xu, X. L.; Williams, D. A.; Hadjipanayi, M.; Hugues, M.; Hopkinson, M.; Wang, X.; Taylor, R. A. *Appl. Phys. Lett.* **2010,** *97,* 111101. doi:10.1063/1.3487937
17. Jia, R.; Jiang, D.-S.; Tan, P.-H.; Sun, B.-Q. *Appl. Phys. Lett.* **2001,** *79,* 153–155. doi:10.1063/1.1380732
18. Henderson, M. R.; Gibson, B. C.; Ebendorff-Heidepriem, H.; Kuan, K.; Afshar, S.; Orwa, J. O.; Aharsonovich, I.; Tomljenovic-Hanic, S.; Greentree, A. D.; Prawer, S.; Monro, T. M. *Adv. Mater.* **2011,** *23,* 2806–2810. doi:10.1002/adma.201100151
19. Yu, H. C. Y.; Argyros, A.; Barton, G.; van Eijkelenborg, M. A.; Barbe, C.; Finnie, K.; Kong, L.; Ladouceur, F.; McNiven, S. *Opt. Express* **2007,** *15,* 9989–9994. doi:10.1364/OE.15.009989
20. Li, Q.; Kumar, V.; Li, Y.; Zhang, H.; Marks, T. J.; Chang, R. P. H. *Chem. Mater.* **2005,** *17,* 1001–1006. doi:10.1021/cm048144q
21. Lincot, D. *MRS Bull.* **2010,** *35,* 778–789. doi:10.1557/mrs2010.507
22. Kozhummal, R.; Yang, Y.; Güder, F.; Hartel, A.; Lu, X.; Küçükbayrak, U. M.; Mateo-Alonso, A.; Elwenspoek, M.; Zacharias, M. *ACS Nano* **2012,** *6,* 7133–7140. doi:10.1021/nn302188q
23. Nobis, T.; Grundmann, M. *Phys. Rev. A* **2005,** *72,* 063806. doi:10.1103/PhysRevA.72.063806
24. Liu, J.; Ngo, Q. M.; Park, K. H.; Kim, S.; Ahn, Y. H.; Park, J.-Y.; Koh, K. H.; Lee, S. *Appl. Phys. Lett.* **2009,** *15,* 221105. doi:10.1063/1.3268806

Resonance of graphene nanoribbons doped with nitrogen and boron: a molecular dynamics study

Ye Wei[1,2], Haifei Zhan[2], Kang Xia[2], Wendong Zhang[1], Shengbo Sang[*1] and Yuantong Gu[*2]

Full Research Paper

Address:
[1]MicroNano System Research Center, Key Lab of Advanced Transducers and Intelligent Control System of the Ministry of Education & College of Information Engineering, Taiyuan University of Technology, Taiyuan 030024, Shanxi, China and [2]School of Chemistry, Physics and mechanical Engineering, Queensland University of Technology, Brisbane, QLD 4109, Australia

Email:
Shengbo Sang[*] - sangshengbo@tyut.edu.cn; Yuantong Gu[*] - yuantong.gu@qut.edu.au

* Corresponding author

Abstract

Based on its enticing properties, graphene has been envisioned with applications in the area of electronics, photonics, sensors, bio-applications and others. To facilitate various applications, doping has been frequently used to manipulate the properties of graphene. Despite a number of studies conducted on doped graphene regarding its electrical and chemical properties, the impact of doping on the mechanical properties of graphene has been rarely discussed. A systematic study of the vibrational properties of graphene doped with nitrogen and boron is performed by means of a molecular dynamics simulation. The influence from different density or species of dopants has been assessed. It is found that the impacts on the quality factor, Q, resulting from different densities of dopants vary greatly, while the influence on the resonance frequency is insignificant. The reduction of the resonance frequency caused by doping with boron only is larger than the reduction caused by doping with both boron and nitrogen. This study gives a fundamental understanding of the resonance of graphene with different dopants, which may benefit their application as resonators.

Introduction

Graphene has drawn intensive interest since its discovery in 2005 [1]. It has been reported to have supreme stiffness (Young's modulus ≈ 1 TPa), very high electron mobility, electrical and thermal conductivity, optical absorption as well as many other excellent properties [2,3]. These properties of graphene open up huge potential applications in the area of electronics, photonics, composite materials, energy generation and storage, sensors, and biomedicine or bio-applications [3-5]. A great effort has been devoted to modify the properties of graphene to facilitate these promising applications,

which leads to a variety of graphene derivatives or hybrid structures.

Doping as one of the common approaches to manipulate the properties of nanomaterials has received wide applications in the synthesis of graphene derivatives. There are two typical doping schemes. One is the so-called electrical doping, which does not change the lattice structure or chemical composition of the graphene, such as the absorption of a gas or a metal (e.g., Ti, Fe, Pt). The other is chemical doping, which introduces substitutional atoms to graphene, e.g., nitrogen (N) [6], boron (B), sulphur (S) and silicon (Si) [7]. By either electrical or chemical doping, one can significantly alter the electronic and quantum transport properties of graphene. Such doped graphene is envisioned with exciting applications as high-performance FET devices [8], and metal-free electrocatalyst for oxygen reduction fuel cells [9]. In addition to doping, various graphene derivatives have also been synthesised through chemical functionalization with hydroxy and methyl groups or hydrogen [10], the decoration with quantum dots [11], noble metal nanoparticles (NPs) [12], or complex biomolecular structures [13,14]. A number of works have been conducted to investigate the properties of graphene derivatives, which however usually focus on their electrical or chemical properties, leaving their mechanical properties being rarely discussed. For instance, based on the Raman spectroscopy, the interactions between metal NPs (such as Au, Ag, Pt and Pd) and graphene were examined [15,16]. The structural and electrical properties of Pt, Fe, and Al NPs adsorbed on monovacancy-defective graphene were explored by density functional theory (DFT) calculations [17,18]. To accommodate different applications of graphene derivatives, a comprehensive understanding of their mechanical properties is crucial. For instance, graphene is proposed to build the ultimate of two dimensional nanoelectromechanical systems (as a resonator) owing to its ultrasensitive detection of mass, force and pressure [19].

Therefore, in this paper, we will discuss extensively on the vibration properties of graphene nanoribbons (GNRs) with different dopants. The study will be carried out by large-scale molecular dynamics (MD) simulations. Both perfect and defective (with initial vacancies) GNRs doped with boron and nitrogen will be considered.

Numerical implementation

Based on large-scale molecular dynamics (MD) simulations, a series of vibrational studies of the GNRs with different dopants have been conducted. The testing samples with a uniform sample size of about 2×10 nm^2 and armchair edges along the length direction were either doped with B or both B and N atoms. According to previous experimental work [20-22],

different densities of dopants have been adopted to build the testing models. Three groups of samples have been tested based on three different GNRs, e.g., a perfect GNR, a defective GNR with two vacancies, and a defective GNR with four vacancies. Each group contains two subgroups, one of which is only doped with boron and the other is doped with both boron and nitrogen (doping with only nitrogen has already been investigated in our earlier work [23], hence it will not be considered herein). The different dopants were randomly distributed in the GNR. Since the N–N single bond is chemically unstable due to the low bonding energy, such bonds will not exist in doped models. To ensure a reasonable comparison, the sample with a higher density of dopants contains all the dopant positions in the model with a lower doping percentage.

To describe the atomic interactions between carbon atoms, the commonly utilised reactive empirical bond order (REBO) potential [24] was employed, which gives a good representation for the binding energies and elastic properties of carbon nanotubes and graphene [25]. In general, the REBO potential is given as

$$E_i = \frac{1}{2} \sum_i \sum_{j \neq i} \left[E_{ij}^{\text{REBO}} + E_{ij}^{\text{LJ}} + \sum_{k \neq i,j} \sum_{l \neq i,j,k} E_{kijl}^{\text{TORSION}} \right], \quad (1)$$

where, E^{REBO} represents the short-distance C–C interaction, E^{LJ} depicts a longer-distance C–C interaction in the form of a typical Lennard-Jones (LJ) potential. The last term describes the dihedral-angle preferences in hydrocarbon configurations. For the other atomic interactions induced by the dopant atoms (i.e., C–B, C–N, and B–N), a typical Tersoff potential [26] was adopted. For each simulation, the conjugate gradient algorithm was firstly applied to relax the sample to a minimum energy state. Afterwards, the sample was equilibrated under a Nose–Hoover thermostat at 5 K. Finally, the graphene layer was actuated by applying a sinusoidal velocity excitation $v(z) = \lambda \cdot \sin(ky)$ along the z-axis, where λ is the actuation amplitude (here 0.6 Å), and $k = \pi/L$ (here L is the effective length of the graphene layer, which excludes the two fixed edges, see Figure 1). In the end, a microcanonical (*NVE*) ensemble was applied to simulate the free vibration of the system. The equations of moving atoms are integrated over time by using a Velocity Verlet algorithm [27]. In order to account for the spurious edge modes of the GNRs, a non-periodical boundary condition was applied along any direction during the whole simulation.

Results and Discussions

To acquire the impact from the dopants on the resonance properties of graphene, emphasis has been put on the quality factor,
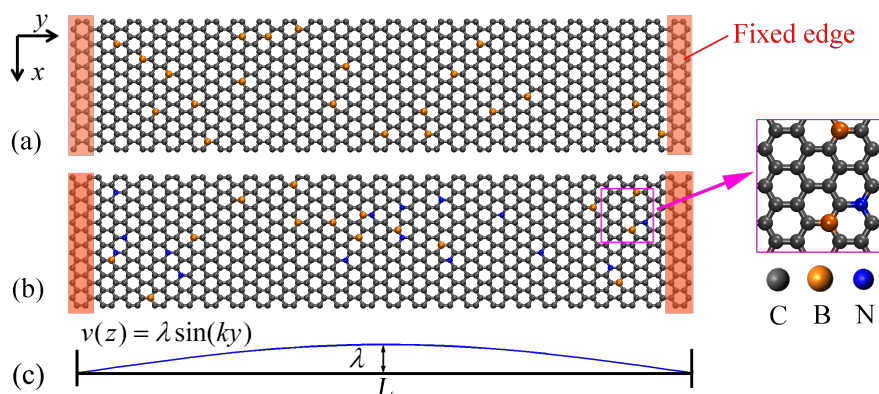
Figure 1: (a) A perfect GNR with 3% B-dopant. (b) A perfect GNR with 1.5% B- and 1.5% N-dopant. (c) Velocity excitation profile. The regions highlighted in red in (a) and (b) represent the fixed edges.

Q, and resonance frequency. These values are calculated following the commonly utilized estimation schemes by previous researchers [28,29]. That is, Q is defined as the ratio between the total system energy and the average energy loss in one radian at the resonant frequency [30], i.e., $Q = 2\pi E/\Delta E$, where E is the total energy of the vibrating system and ΔE is the energy dissipated by damping during one cycle of vibration. The value of Q is assumed as to be constant during vibration, which gives a relation between the maximum energy (E_n) and the initial maximum energy (E_0) as $E_n = E_0(1 - 2\pi/Q)^n$ after n vibration cycles [31]. Since an energy-preserving *NVE* ensemble is assumed during vibration and the simulation is under vacuum conditions, the damping will result from intrinsic loss only. Therefore, the loss of potential energy must be converted to kinetic energy. Thus, the change of the external energy over time will be tracked for the calculation of Q. The external energy is defined as the difference of the potential energy before and after the initial excitation is applied to the

testing sample [32]. Regarding the resonance frequency, a discrete Fourier transform will be applied [33]. For comparison, the vibration properties for the prefect GNR are firstly assessed. As shown in Figure 2a, the amplitude of the external energy decreases linearly with the increase of simulation time, with Q being estimated to be 4660. The corresponding frequency spectrum of the GNR is derived from fast Fourier transformation. As shown in Figure 2b, the natural frequency of the external energy is about 228 GHz. As the energy is a square function of the velocity, i.e., the natural frequency of the GNR is half of the external energy frequency, or 114 GHz.

Perfect GNRs with dopants
Influence of B-dopant
At the beginning, we consider the impact of B-dopants on the resonance properties of a perfect GNR. Six testing samples were established with a doping ratio ranging from 0.25% to 2.40%. Generally, it is found that the presence of different
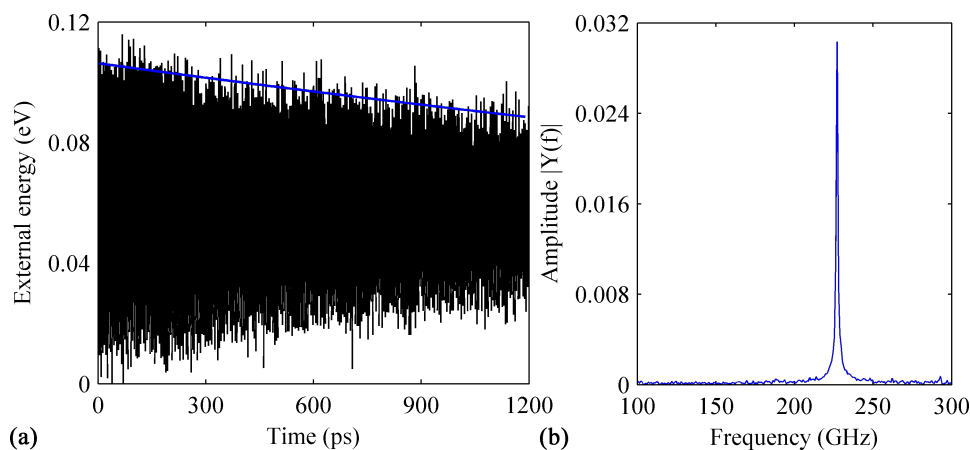
Figure 2: (a) Variation in time of the external energy obtained from a perfect GNR. (b) The corresponding frequency spectrum obtained.

densities of B-dopant reduces *Q* compared to that of pristine perfect GNR (shown in Figure 2a). In particular, the GNR with a B-dopant densities of 0.38%, 0.76%, 1.14% and 1.64% have a similar *Q* of around 2200, which means a reduction of more than 50%. The results obtained from the GNR with 0.76% B-dopant are illustrated in Figure 3a. Clearly, the amplitude of the external energy is found to decrease from about 0.10 to about 0.07 eV over the simulation time, which leads to Q ≈ 2260. From the corresponding frequency spectrum, the resonance frequency is estimated to be 107 GHz. Interestingly, the highest *Q* is found for the GNR with 1.89% B-dopant (Q ≈ 3070, about 34% reduction), followed by the GNR with 2.65% B-dopant (Q ≈ 2770). This phenomenon suggests that there is no correlation between the reduction of *Q* and the density of B-dopant (within the considered maximum density of 2.65%). Comparing with the results presented in Figure 2a, a much slower energy dissipation is found for the GNR with 1.89% B-dopant (see Figure 2b). We note that, although the GNR with a higher density of B-dopant might have a higher *Q*, the resonance frequency appears to have a consistent trend to decrease when the B-content is increased. It is concluded from all considered six cases that the reduction of *Q* does not necessarily increase with increasing density of dopants.
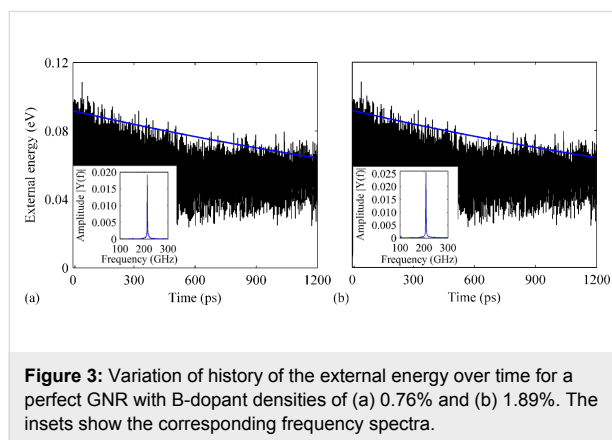
Figure 3: Variation of history of the external energy over time for a perfect GNR with B-dopant densities of (a) 0.76% and (b) 1.89%. The insets show the corresponding frequency spectra.

Influence of both B- and N-dopants

We then consider the GNR with both B- and N-dopants. Again, we consider six different cases, with the percentages of dopant atoms ranging from 0.26% to 2.78%, in which B and N share the same density, namely half of the total percentage. Strikingly, the GNR with 0.26% of B- and N-dopants appear to have an enhanced *Q*-factor of about 9050, which is twice of that observed from the pristine GNR. Except this case, the rest five samples exhibit apparent deteriorating vibration behavior.

Particularly, the profiles of the external energy of the GNRs with a density of 1.27% and 2.28% differ greatly from that of other cases, i.e., the amplitude does not show a consistent linear

decrease fashion. As shown in Figure 4a, the external energy is observed to experience a sharp dissipation from 0.10 to 0.06 eV within 150 ps of simulation time. Afterwards, it fluctuates around 0.06 eV with no obvious dissipation. From the frequency spectrum, the resonance frequency is estimated to be 106 GHz. For the GNRs with a density of 0.76%, 1.65% and 2.78%, a similar progression of the external energy is found. As shown in Figure 4b, the external energy of the GNR with 1.65% of dopants decreases quickly from 0.10 to 0.03 eV after 1200 ps of simulation time. A low *Q* of about 1610 is estimated with a corresponding natural frequency of 109 GHz. In all, although different densities of dopants influence the value of Q differently, the resonance frequency generally decreases with an increasing of the dopant density.
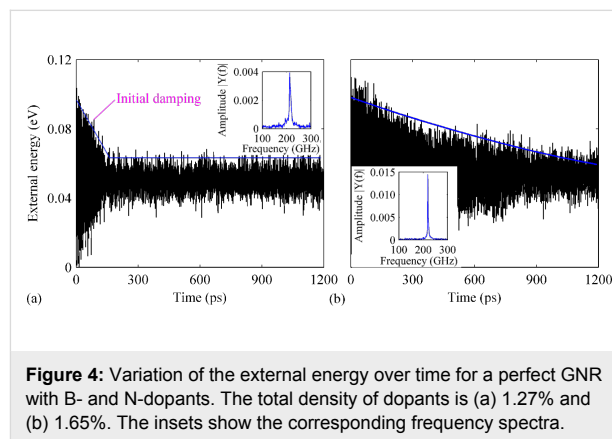
Figure 4: Variation of the external energy over time for a perfect GNR with B- and N-dopants. The total density of dopants is (a) 1.27% and (b) 1.65%. The insets show the corresponding frequency spectra.

Defective GNRs with two vacancies

Experimental results show that defects normally exist in GNRs. These defects can be grain boundaries, oxidations or vacancies [34,35]. Specifically, for GNRs with vacancies, researchers reported three different types of nitrogen doping, namely graphitic N, pyridine-like N and pyrrole-like N depending on their locations. Therefore, in the following, we consider the vibration properties of defective GNRs (with either two or four vacancies) with different dopants. We start from the GNR with two vacancies, discussions are given as below.

Influence of B-dopant

Similarly, seven different samples (including the pristine defective GNR) have been studied with a dopant density range of 0.38–2.40%. Random locations are adopted for the two vacancies as shown in the inset of Figure 5a. The MD results from the pristine defective GNR are depicted in Figure 5. Comparing with the results from the pristine perfect GNR (given in Figure 2a), the amplitude of the external energy shows an even smaller decrease pattern (from about 0.11 to 0.10 eV), which signifies a larger *Q* of about 8630. While an obvious decrease of the resonance frequency of about 4% is observed.
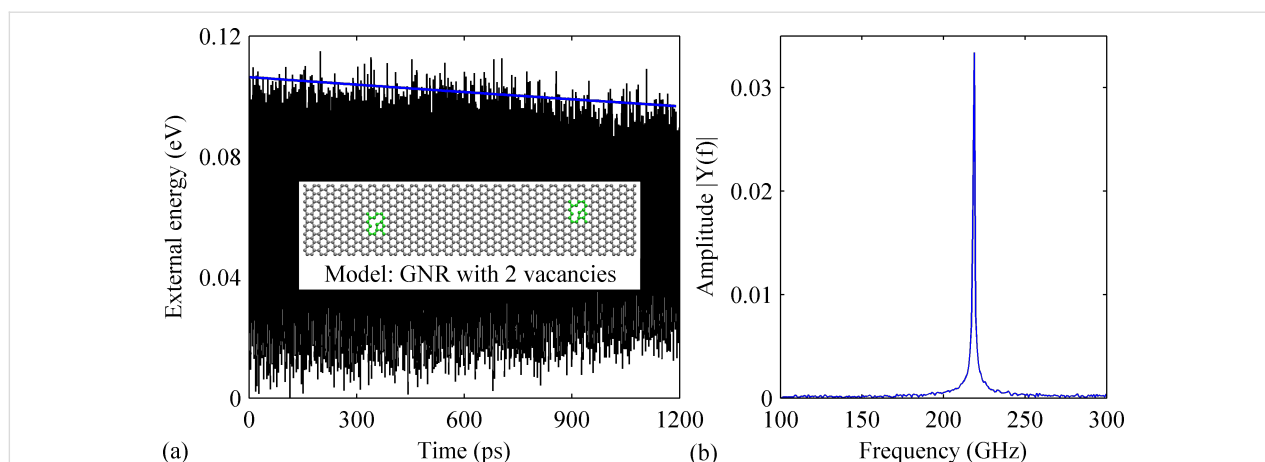
Figure 5: (a) Variation of the external energy over time obtained for a pristine GNR with two vacancies. The inset shows the corresponding model of the GNR. The regions highlighted in green represent the vacancies. (b) The corresponding frequency spectrum.

Consistent with the phenomena observed from perfect GNR with B-dopant (see above), the existence of B-dopant also induces an evident reduction to of Q. All doped cases except the one with 1.89% B-dopant show a greatly deteriorated Q with a reduction of over 70%. The smallest Q is found for the case containing 1.64% B-dopant. As illustrated in Figure 6a, the amplitude of the external energy decreases sharply from 0.10 to 0.07 eV within the 1200 ps simulation time. The value of Q is estimated as low as 1700, which is a reduction of over 80% compared to that of the pristine defective GNR. Besides, a relatively high Q is also found for the defective GNR with 1.89% B-dopant. As illustrated in Figure 6b, the amplitude of the external energy decreases slowly from 0.15 to 0.9 eV after 1200 ps and Q is calculated to be 6000. The fact the samples with higher densities of dopants exhibit higher Q further suggest that there is no correlation between the amount of dopants and the value of Q.

densities including 0.38%, 0.88%, 1.27%, 1.77%, 2.02% and 2.53% are considered. Overall, the influence from the different densities of dopants varies greatly. For the defective GNR with 0.38% B- and N-dopants, a very high Q of about 8300 is observed, while for the case with 0.88% dopants, an extremely low Q of about 1980 is detected. Figure 7a depicts the results obtained from the case with 0.38% dopants. A fast energy dissipation is observed, with the resonance frequency being estimated to be 109 GHz (the same as that obtained from the pristine defective GNR).
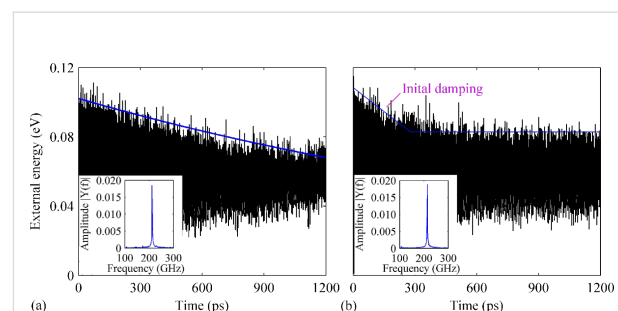
Figure 7: Variation of the external energy over time for the defective GNR (two vacancies) with both B- and N-dopants. The total dopant densities are (a) 0.89% and (b) 2.02%. The insets show the corresponding frequency spectra.

Figure 6: Variation of the external energy over time for a defective GNR (two vacancies) with B-dopant. The density of the dopant is (a) 1.64% and (b) 1.89%. The insets show the corresponding frequency spectra.

Influence of both B- and N-dopants

The influence of both B- and N-dopants on the resonance properties of the defective GNR are examined next. Different dopant

Different behaviors are also found for the other two samples with dopant densities of 1.77% and 2.02%. The results from the case with 2.02% dopants are given in Figure 7b. As clearly seen, the external energy exhibit a sharp initial damping from 0.11 to ca. 0.09 eV at the early stage of vibration (within 300 ps). Afterwards, it saturates around 0.09 eV. The corresponding resonance frequency is estimated to be 107 GHz.

Defective GNR with four vacancies
Influence of B-dopant

To further examine the influence of a combination of vacancies and dopants, we establish another GNR model with four randomly distributed vacancies (see the inset of Figure 8a). The simulation results obtained from the pristine case are presented in Figure 8. Compared to the GNR with two vacancies, a lower *Q* and a lower resonance frequency are observed, about 4080 and about 106 GHz, respectively.

Based on the above results, we then compare the resonance properties of the GNR (with four vacancies) with the presence of B-dopants (density ranges from 0.26% to 2.40%). Comparing with all previous cases, a relatively smaller degradation is found for *Q*. The smallest *Q*, which is about 2620, is observed in the case with 1.77% B-dopants, a 35% reduction comparing with that of the pristine GNR in Figure 8a. For densities of B-dopant density ranging from 0.26% to 1.90%, a similar variation over time of the external energy is observed. As shown in Figure 9a, the amplitude of the external energy for the case with 0.76% B-dopant decreases linearly from 0.10 to 0.08 eV after 1200 ps. A non-uniform linear decrease fashion of the external energy is also detected in the defective GNR with 2.40% B-dopant. Figure 9b shows a fast energy dissipation at the beginning of the vibration and the external energy saturates at around 0.06 eV. Besides of the evident impacts of the B-doping on *Q*, a continuous reduction of the resonance frequency is also observed with increasing B-dopant percentage.

Influence of both B- and N-dopants

In the end, we investigate the resonance properties of the GNR with four vacancies and B- and N-dopants. Considered dopant's density ranges from 0.26% to 2.40%. Interestingly, only the case with 0.76% of dopants is found to exhibit a decreased *Q*,
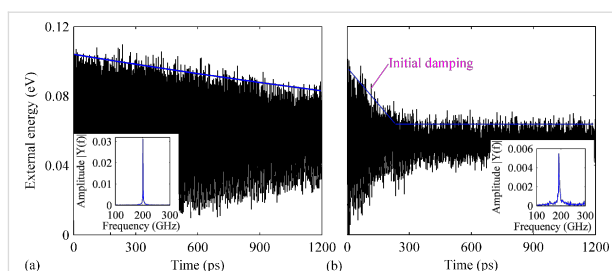
Figure 9: Variation over time of the external energy of the defective GNR with four vacancies and B-dopant densities of (a) 0.76% and (b) 2.40%. The insets show the corresponding frequency spectra.

which is around 3050 (Figure 10a). All other samples are found to have an enhanced *Q*. As seen in Figure 10b, the amplitude of the external energy of the case with 1.76% of dopants linearly decreases from 0.12 to 0.10 eV with the *Q* being estimated to be 4290 (a slight increase about 5% comparing with that of the pristine defective GNR shown in Figure 8a).
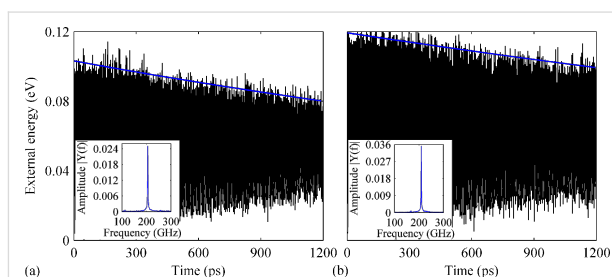
Figure 10: Variation over time of the external energy for the defective GNR (four vacancies) with both B- and N-dopants. The total densities of dopants are (a) 0.76% and (b) 1.76%. The insets show the corresponding frequency spectra.

The most significantly increased *Q* is observed for the case with 2.40% dopant density. As shown in Figure 11a, no obvious
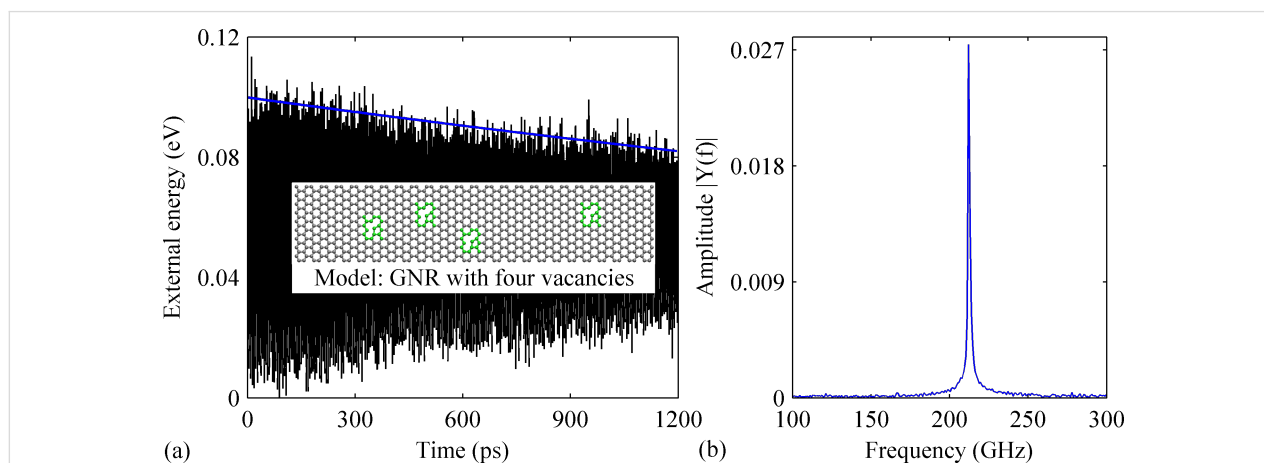
Figure 8: (a) Time history of the external energy obtained from pristine defective GNR with four vacancies. The inset shows the corresponding model of GNR with four vacancies. The regions highlighted in green represent the vacancies. (b) The corresponding frequency spectrum.

energy dissipation is found, which results in a *Q*-factor as high as 79020. The corresponding frequency spectrum reveals that there are two resonance modes existing. Close inspection of the atomic configurations of the sample shows that the GNR is vibrating along both lateral and length directions (see the insets in Figure 11a). It is evident that the vibration behavior is dominated by the vertical vibration, as indicated by the extremely small amplitude of the translational vibration comparing with that of the vertical vibration in Figure 11b. To further justify this observation, a smaller excitation amplitude (0.4 Å/ps) has been tested, for which we still find the co-existence of the vertical and translation vibration modes. A similar phenomenon is also observed for the case with a dopant density of 1.90%. It is concluded that for the GNR with four vacancies, a higher density of dopants will make the translational vibration mode much easier to be excited.

Figure 11: Results of the defective GNR (four vacancies) with 1.20% B- and 1.20% N-dopant. (a) Variation over time of the external energy. The inset shows the sample at the simulation time of 488 and 492 ps. (b) The corresponding frequency spectrum.
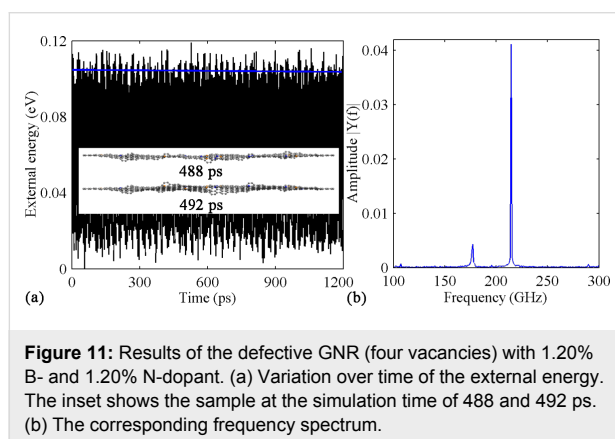
Before concluding, we compare the resonance frequencies and *Q*-factor among all testing samples. As seen in Figure 12a, the

resonance frequency usually decreases with the increase of the dopant percentages, which is evidently seen in the perfect GNR with B-dopants. The largest reduction of the resonance frequency is observed in a perfect GNR with 2.65% B-dopant, about 14% decrease. It is worth to mention that, the B- and N-doped defective GNR with four vacancies (dopant densities of 0.26% and 2.40%) even exhibit a larger resonance frequency than their pristine counterpart. Further, the reduction of the resonance frequency for the two groups of doped defective GNR with four vacancies is much smaller than that of other groups. These observations suggest that the vacancies will also exert significant influence to the resonance properties of GNR. It is observed from Figure 12 that, the doping with only boron induces a larger reduction of the resonance frequency of either perfect or defective GNR than doping with both boron and nitrogen. Figure 12b compares the *Q*-factor obtained from different samples. Note that, some cases exhibit a nonlinear profile for the external energy (e.g., Figure 4a, Figure 9b), for which a valid *Q* cannot be estimated. Thus, these cases are not compared, as well as the two cases with significantly enhanced *Q* (i.e., GNR with 1.8% and 2.4% of B- and N-dopant). In general, the impacts from different percentages of dopants vary greatly. As is seen, most of the tested samples show a decreased *Q*, while some cases show an enhanced *Q*. It is assumed that the locations of dopant atoms also exert great influence on the *Q*-factor, and future works are expected to unveil such influence.

Conclusion

Based on the MD simulations, we investigated the impacts of different dopants (only boron and boron with nitrogen) on the resonance properties of graphene nanoribbons (GNRs). Both perfect and defective (with either two or four randomly located
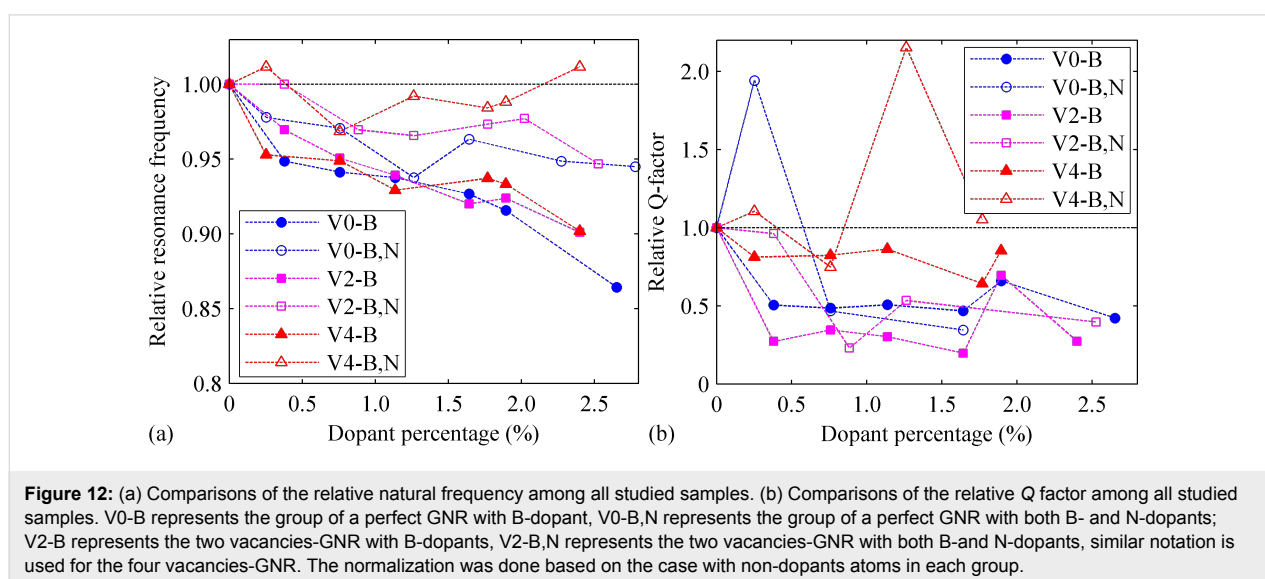

Figure 12: (a) Comparisons of the relative natural frequency among all studied samples. (b) Comparisons of the relative *Q* factor among all studied samples. V0-B represents the group of a perfect GNR with B-dopant, V0-B,N represents the group of a perfect GNR with both B- and N-dopants; V2-B represents the two vacancies-GNR with B-dopants, V2-B,N represents the two vacancies-GNR with both B-and N-dopants, similar notation is used for the four vacancies-GNR. The normalization was done based on the case with non-dopants atoms in each group.

vacancies) GNRs have been adopted as the samples, and the dopant densities were chosen below 3%. Major findings include: (a) Generally, the presence of dopants will lead to a degradation of the Q-factor and the resonance frequency of the GNR. (b) The impacts of doping on the *Q*-factor of perfect and defective GNR vary greatly, and there is no apparent correlation between the reduction of *Q* and the density of the dopant. (c) Compared with the influence on the *Q*-factor, the influences exerted on the resonance frequency are insignificant, i.e., the majority of the reduction is between 2–10%. (d) The reduction of resonance frequency of perfect and defective GNRs is larger when they are doped with boron only than when they are doped with both born and nitrogen. This study provides a comprehensive study of the impacts of different dopants on the resonance properties of graphene. The simulation techniques presented herein should also be applicable to graphene with other dopant elements (e.g., sulfur or silicon).

Acknowledgements

References

1. Novoselov, K. S.; Geim, A. K.; Morozov, S. V.; Jiang, D.; Zhang, Y.; Dubonos, S. V.; Crigorieva, I. V.; Firsov, A. A. *Science* **2004,** *306,* 666–669. doi:10.1126/science.1102896
2. Geim, A. K.; Novoselov, K. S. *Nat. Mater.* **2007,** *6,* 183–191. doi:10.1038/nmat1849
3. Novoselov, K. S.; Fal'ko, V. I.; Colombo, L.; Gellert, P. R.; Schwab, M. G.; Kim, K. *Nature* **2012,** *490,* 192–200. doi:10.1038/nature11458
4. Kuila, T.; Bose, S.; Khanra, P.; Mishra, A. K.; Kim, N. H.; Lee, J. H. *Biosens. Bioelectron.* **2011,** *26,* 4637–4648. doi:10.1016/j.bios.2011.05.039
5. Feng, L.; Liu, Z. *Nanomedicine* **2011,** *6,* 317–324. doi:10.2217/nnm.10.158
6. Zhao, L.; He, R.; Rim, K. T.; Schiros, T.; Kim, K. S.; Zhou, H.; Guitérrez, C.; Chockalingam, S. P.; Arguello, C. J.; Pálová, L.; Nordlund, D.; Hybertsen, M. S.; Reichman, D. R.; Heinz, T. F.; Kim, P.; Pinczuk, A.; Flynn, G. W.; Pasupathy, A. N. *Science* **2011,** *333,* 999–1003. doi:10.1126/science.1208759
7. Zou, Y.; Li, F.; Zhu, Z. H.; Zhao, M. W.; Xu, X. G.; Su, X. Y. *Eur. Phys. J. B* **2011,** *81,* 475–479. doi:10.1140/epjb/e2011-20225-8
8. Wei, D.; Liu, Y.; Wang, Y.; Zhang, H.; Huang, L.; Yu, G. *Nano Lett.* **2009,** *9,* 1752–1758. doi:10.1021/nl803279t
9. Qu, L.; Liu, Y.; Baek, J.-B.; Dai, L. *ACS Nano* **2010,** *4,* 1321–1326. doi:10.1021/nn901850u
10. López-Bezanilla, A.; Triozon, F.; Roche, S. *Nano Lett.* **2009,** *9,* 2537–2541. doi:10.1021/nl900561x
11. Cao, A.; Liu, Z.; Chu, S.; Wu, M.; Ye, Z.; Cai, Z.; Chang, Y.; Wang, S.; Gong, Q.; Liu, Y. *Adv. Mater.* **2010,** *22,* 103–106. doi:10.1002/adma.200901920
12. He, H.; Gao, C. *Sci. China: Chem.* **2011,** *54,* 397–404. doi:10.1007/s11426-010-4191-9
13. Guo, C. X.; Ng, S. R.; Khoo, S. Y.; Zheng, X.; Chen, P.; Li, C. M. *ACS Nano* **2012,** *6,* 6944–6951. doi:10.1021/nn301974u
14. Premkumar, T.; Geckeler, K. E. *Prog. Polym. Sci.* **2012,** *37,* 515–529. doi:10.1016/j.progpolymsci.2011.08.003
15. Jeon, K.-J.; Lee, Z. *Chem. Commun.* **2011,** *47,* 3610–3612. doi:10.1039/c0cc05167e
16. Subrahmanyam, K. S.; Manna, A. K.; Pati, S. K.; Rao, C. N. R. *Chem. Phys. Lett.* **2010,** *497,* 70–75. doi:10.1016/j.cplett.2010.07.091
17. Lim, D.-H.; Negreira, A. S.; Wilcox, J. *J. Phys. Chem. C* **2011,** *115,* 8961–8970. doi:10.1021/jp2012914
18. Lim, D.-H.; Wilcox, J. *J. Phys. Chem. C* **2011,** *115,* 22742–22747. doi:10.1021/jp205244m
19. Bunch, J. S.; van der Zande, A. M.; Verbridge, S. S.; Frank, I. W.; Tanenbaum, D. M.; Parpia, J. M.; Craighead, H. G.; Mceuen, P. L. *Science* **2007,** *315,* 490–493. doi:10.1126/science.1136836
20. Wang, Y.; Shao, Y.; Matson, D. W.; Li, J.; Lin, Y. *ACS Nano* **2010,** *4,* 1790–1798. doi:10.1021/nn100315s
21. Wei, D.; Liu, Y.; Zhang, H.; Huang, L.; Wu, B.; Chen, J.; Yu, G. *J. Am. Chem. Soc.* **2009,** *131,* 11147–11154. doi:10.1021/ja903092k
22. Deng, D.; Pan, X.; Yu, L.; Cui, Y.; Jiang, Y.; Qi, J.; Li, W.-X.; Fu, Q.; Ma, X.; Xue, Q.; Sun, G.; Bao, X. *Chem. Mater.* **2011,** *23,* 1188–1193. doi:10.1021/cm102666r
23. Zhan, H.; Wei, Y.; Gu, Y. *Appl. Mech. Mater.* **2014,** *553,* 3–9. doi:10.4028/www.scientific.net/AMM.553.3
24. Brenner, D. W.; Shenderova, O. A.; Harrison, J. A.; Stuart, S. J.; Ni, B.; Sinnott, S. B. *J. Phys.: Condens. Matter* **2002,** *14,* 783. doi:10.1088/0953-8984/14/4/312
25. Zhang, Y. Y.; Wang, C. M.; Cheng, Y.; Xiang, Y. *Carbon* **2011,** *49,* 4511–4517. doi:10.1016/j.carbon.2011.06.058
26. Tersoff, J. *Phys. Rev. B* **1988,** *37,* 6991. doi:10.1103/PhysRevB.37.6991
27. Verlet, L. *Phys. Rev.* **1967,** *159,* 98. doi:10.1103/PhysRev.159.98
28. Kim, S. Y.; Park, H. S. *Nano Lett.* **2009,** *9,* 969–974. doi:10.1021/nl802853e
29. Zhan, H.; Gu, Y.; Park, H. S. *Nanoscale* **2012,** *4,* 6779–6785. doi:10.1039/c2nr31545a
30. Bao, M. H. *Analysis and design principles of MEMS devices;* Elsevier Science B. V.: Amsterdam, The Netherlands, 2005.
31. Jiang, H.; Yu, M.-F.; Liu, B.; Huang, Y. *Phys. Rev. Lett.* **2004,** *93,* 185501. doi:10.1103/PhysRevLett.93.185501
32. Kim, S. Y.; Park, H. S. *Phys. Rev. Lett.* **2008,** *101,* 215502. doi:10.1103/PhysRevLett.101.215502
33. Brigham, E.; Morrow, R. E. *IEEE Spectrum* **1967,** *4,* 63–70. doi:10.1109/MSPEC.1967.5217220
34. Lahiri, J.; Lin, Y.; Bozkurt, P.; Oleynik, I. I.; Batzill, M. *Nat. Nanotechnol.* **2010,** *5,* 326–329. doi:10.1038/nnano.2010.53
35. Wang, X.; Li, X.; Zhang, L.; Yoon, Y.; Weber, P. K.; Wang, H.; Guo, J.; Dai, H. *Science* **2009,** *324,* 768–771. doi:10.1126/science.1170335

Highly NO$_2$ sensitive caesium doped graphene oxide conductometric sensors

Carlo Piloto[1], Marco Notarianni[1], Mahnaz Shafiei[1], Elena Taran[2], Dilini Galpaya[1], Cheng Yan[1] and Nunzio Motta[*1]

Full Research Paper

Address:
[1]Institute for Future Environments and School of Chemistry, Physics, and Mechanical Engineering, Queensland University of Technology, Brisbane, QLD 4001, Australia and [2]The University of Queensland, Australian Institute for Bioengineering and Nanotechnology, Australian National Fabrication Facility - QLD Node, Brisbane, QLD 4072, Australia

Email:
Nunzio Motta[*] - n.motta@qut.edu.au

* Corresponding author

Abstract

Here we report on the synthesis of caesium doped graphene oxide (GO-Cs) and its application to the development of a novel NO$_2$ gas sensor. The GO, synthesized by oxidation of graphite through chemical treatment, was doped with Cs by thermal solid-state reaction. The samples, dispersed in DI water by sonication, have been drop-casted on standard interdigitated Pt electrodes. The response of both pristine and Cs doped GO to NO$_2$ at room temperature is studied by varying the gas concentration. The developed GO-Cs sensor shows a higher response to NO$_2$ than the pristine GO based sensor due to the oxygen functional groups. The detection limit measured with GO-Cs sensor is ≈90 ppb.

Introduction

Graphene is a single layer of carbon atoms arranged in a honeycomb lattice [1,2]. Intrinsic low noise structure, large specific surface area and extraordinary mobility of carriers are the unique properties that make graphene-based materials excellent candidates for a wide variety of electrical applications [3]. One of the most promising applications is chemical sensing with detection limit down to ppb level [4-11]. Such ultrahigh sensitivity can play a crucial role in applications including health care, gas alarms, safety and environmental monitoring [12].

Theoretical [13,14] and experimental [15-19] studies have revealed that functionalization of graphene can improve significantly its gas sensing performance [20]. The presence of dopants or defects in the graphene lattice can increase the

adsorption energy, i.e., the gas molecules can absorb more strongly on the doped or defective graphene than the pristine graphene resulting in an enhancement of the sensitivity or selectivity.

Recently, graphene oxide (GO), a graphene layer decorated with oxygen functional groups, has been subject to extensive research [8,21-24], as the synthesis of GO is the first step to easily obtain functionalized graphene [25]. GO can be synthesized from colloidal suspensions of graphite derivatives [26-29], e.g., graphite oxide, a method significantly cheaper and scalable than most of the common processes to make pristine graphene sheets, like chemical vapour deposition, epitaxial growth or mechanical exfoliation [30-33].

By dispersion and sonication of graphite oxide in aqueous solution or organic solvent, a colloidal suspension of GO sheets is produced. The density of oxygen functional groups can be easily controlled [28,34-38] making this process a good candidate for graphene functionalization. The oxygen groups of the resulting GO lead to the disruption of the graphitic structure, thus making the material electrically too much insulating for resistive gas sensing applications. However, the partial removal of oxygen groups, leading to reduced GO can be achieved by chemical [38,39], thermal [40,41] or ultraviolet-assisted process [42]. The conductivity and gas sensing performance of the reduced GO is comparable or superior to that of the pristine graphene [43], due to the oxygen defects that act as low energy adsorption sites.

To further enhance its gas sensing properties, reduced GO can be doped with alkali metals [18], similarly to what has been done in other carbon materials, to tune up the electronic properties for sensing applications [44].

Different research groups have reported high gas sensing performance of conductometric devices based on GO [25,35,45], reduced GO (rGO) [15,23,24,29,46,47] and functionalized rGO [18,48-50]. Prezioso et al. [25] have measured the NO$_2$ sensing performance of GO drop casted on standard interdigitated Pt electrodes. They reported a very low detection limit (20 ppb), which is attributed to the high quality of their GO samples (large and highly oxidized flakes). Robinson et al. [46] demonstrated that by increasing the level of reduction it is possible to improve the response time and $1/f$ noise. It has also been proven by Yuan et al. [50] that reducing the thickness of the sensing layer below 5 nm results in a significant enhancement of the sensitivity [50]; although other authors claim that very thin layers would result in a not uniform conducting path [18]. The decoration of rGO with Pd nanoparticles using sputtering or by alternating current dielectrophoresis has shown an

improvement in the sensitivity to NO by a factor of 5 (down to 2 ppb at room temperature) [15] as well as selectivity to hydrogen [18].

Increasing air pollution and global warming raised the demand for highly sensitive and portable NO$_2$ gas sensors. To this purpose, metal oxide materials have been investigated reaching the lowest detection threshold of 0.1 ppm [51]. The high operating temperature of these devices, in the range of 200–400 °C, is a serious drawback that makes their utilization difficult in the field, where power consumption is a critical parameter. Carbon-based materials, such as graphene and chemically derived graphene, offer high sensitivity to cost ratio even when operating at room temperature [52].

In this article, we report for the first time the fabrication, characterization and gas sensing performance of a caesium-doped GO (GO-Cs) based conductometric sensor. Due to the reported catalytic activity of Cs, we believe that the sensing performance of the GO can be improved significantly [53]. Both pristine GO and Cs doped GO sensors have been tested towards different concentrations of NO$_2$ gas at room temperature. The detection limit measured with GO-Cs sensor is ≈90 ppb.

Experimental
Device fabrication
GO materials were prepared by oxidation of graphite flakes following the method reported by Marcano et al. [54]. Commercially available graphite flake was purchased from Sigma-Aldrich. All other chemical used, (99.99% H$_2$SO$_4$, 85% H$_3$PO$_4$, 35% HCl, 30% H$_2$O$_2$, KMnO$_4$) in this study were analytical grade and supplied by Sigma-Aldrich. Analytical grade ethanol, acetone and diethyl ether were used as solvents.

The graphite mixed with KMnO$_4$ (ratio of 1:6) was combined with a mixture of H$_2$SO$_4$:H$_3$PO$_4$ (540:60 mL) acids. The reaction was stirred at 50 °C for 12 h. Subsequently, the resulting mixture, cooled at room temperature, was poured onto ice with 3 mL of 30% H$_2$O$_2$ and sifted through a 250 μm sieve. The filtrate was centrifuged at 4000 rpm for 30 min. The obtained material was washed with DI water, HCl and ethanol. After each wash, the mixture was sieved and centrifuged for 30 min at 4000 rpm. The final precipitate was coagulated with diehyl ether. Coagulated solid was dissolved in DI water and sonicated for 1 h. The resulting GO aqueous dispersion was cooled down for 24 h followed in a de-freezer and subsequently for 72 h in a freezer dryer at −51 °C under vacuum.

In order to synthesize GO doped with caesium (GO-Cs), the GO was diluted in water and mixed with Cs$_2$CO$_3$, following the method suggested by Liu et al. [55]. The obtained solution was

stirred at room temperature for 30 min and sieved with a polyvinylidene fluoride membrane (0.2 μm). The precipitate was then added to water (30 mL) and filtered. The process was repeated twice to obtain dark solid GO-Cs.

Finally, the gas sensors were fabricated by drop casting of the prepared GO and GO-Cs materials onto 2×2 mm^2 transducers and then they were placed in oven at 60 °C for 12 h. The transducers consisted of Pt interdigitated electrodes (IDT) (200 μm separation) deposited on 0.25 mm thick alumina substrates.

Material characterisations

The structure and the composition of the synthesized GO and GO-Cs were analysed by field emission scanning electron microscopy (FESEM), X-ray photoelectron spectroscopy (XPS), atomic force microscopy (AFM), Raman spectroscopy and Kelvin probe force microscopy (KPFM).

XPS data were acquired using a Kratos Axis ULTRA X-ray photoelectron spectrometer incorporating a 165 mm hemispherical electron energy analyser. The incident radiation was monochromatic Al Kα X-rays (1486.6 eV) at 225 W (15 kV, 15 mA). Survey (wide) scans were taken at analyser pass energy of 160 eV and multiplex (narrow) high resolution scans at 20 eV. Survey scans were carried out over 1200–0 eV binding energy range with 1.0 eV steps and a dwell time of 100 ms.

Narrow high-resolution scans were run with 0.05 eV steps and 250 ms dwell time. Base pressure in the analysis chamber was kept at 1.0×10^{-9} Torr and during sample analysis 1.0×10^{-8} Torr. Peak fitting of the high-resolution data was also carried out using the CasaXPS software.

Raman spectroscopy was performed by using an ''inVia Renishaw Raman microscope'' with λ = 532 nm operated at 35 mW, with a 1 μm spot size, to investigate bond changes and defects in the material.

The KPFM was performed with a commercial AFM (Cypher-Asylum Research) equipped with an air temperature controller (ATC). The ATC flows temperature regulated, HEPA (High-Efficiency Particulate Absorption) filtered air through the Cypher enclosure. Closed-loop temperature control isolates the AFM from room temperature variations, minimizing thermal drift for imaging. During measurements the temperature was kept constant at 26 °C.

For all KPFM data shown here, we used conductive (Pt coated) AFM probes (NSG03 model from NT-MDT) with a nominal resonant frequency between 50 and 150 kHz. The GO and GO-Cs samples were deposited on gold-coated mica substrates from a liquid suspension (5 μg/mL). The Kelvin voltage was maintained with an integral gain of 4, no proportional gain, and an AC-voltage applied to the tip of 3 V.

Gas sensing measurements

The GO and GO-Cs sensors response to NO_2 was evaluated using a high precision multi-channel gas testing system, including a 1100 cc volume test chamber capable of testing four sensors in parallel, 8 high precision mass flow controllers (MKS 1479A) to regulate the gas mixture, 8 channel MFC processing unit (MKS 647C), a picoammeter (Keithley 6487) and a climatic chamber to control the temperature. The measurements were performed at room temperature with a mixture of synthetic air and NO_2 gas in different concentrations (up to a maximum of 12.2 ppm of NO_2 balanced in synthetic air). The right concentration of NO_2 gas in air was obtained by adjusting the respective flow rates via the MFCs, while maintaining a total constant flow rate of 200 SCCM (mL/min). The response upon gas exposure was evaluated by measuring the sensors resistance variation with bias voltage of 3 V.

Results and Discussion
Material characterisations

The morphology of the synthesized graphite oxide powder was investigated by FESEM (Figure 1). It is evident that the thin and aggregated flakes are stacked to each other with lateral sizes ranging from several hundred nanometers to several microns.

AFM images (Figure 2a and 2c) confirm that most of GO and GO-Cs flakes are approx. 1 nm thick, corresponding to one monolayer, with a lateral size in the range of hundred nanometers [56,57]. The thickness of each GO layer is usually higher than the pristine graphene sheet because of the orthogonally bonded oxygen groups coming out from the surface [28,57,58].

Electrical characterizations were carried out with KPFM providing a potential map of the samples with a resolution of few mV. Figure 2b and 2d show a comparison of pristine GO and GO-Cs KPFM signals.

The measurements collected from several samples and on different flakes show a net difference in the potential map of GO (see Figure 2b) and GO-Cs flakes (see Figure 2d), with a drop of the average potential on a flake from 30 ± 3 mV in the GO to 19 ± 3 mV in the GO-Cs. We attribute this drop to the chemical reduction of the GO caused by the Cs_2CO_3 that tends to decrease the work function as observed by [55,59-61]. This result suggests that doped GO may have good performance as a gas sensing material.
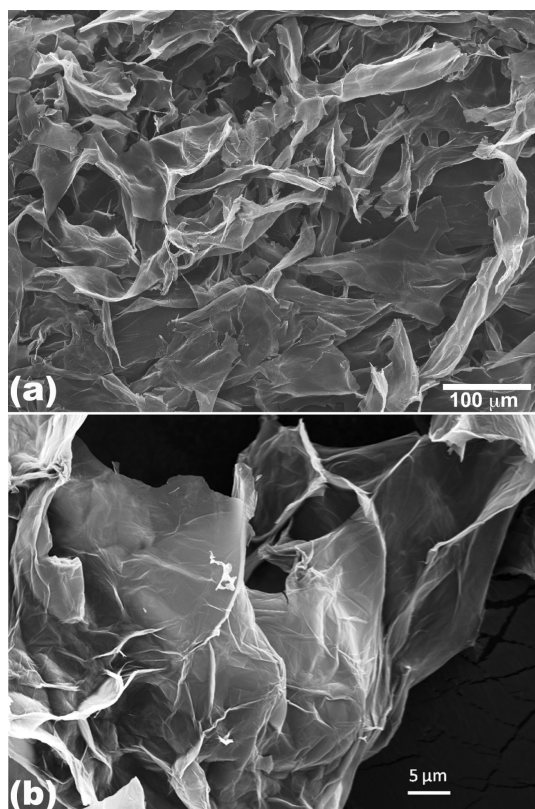
Figure 1: (a) Low magnification and (b) high magnification SEM images of graphite oxide flakes.

XPS survey analysis of the GO (Figure 3a, blue line) confirms that the GO does not contain any contaminants and is largely oxidised with an oxygen content of ≈32%. A reduction of the oxygen content down to ≈24% is observed in the GO-Cs (Figure 3a, red line) survey spectrum, which confirm the presence of ≈5% Cs. In the high resolution XPS spectra of the C peaks (Figure 3b and 3c), we identify the C–C contribution as the peak at 285.3 eV binding energy, while the C–O, C=O and COOH groups are assigned to binding energies of 287.5, 288.4 and 289.1 eV, respectively [62,63]. Figure 3b and 3c show that the intensity of the C–O band in the GO-Cs decreases compared to the C–O band of the GO, confirming a reduction mechanism occurring in the GO due to the Cs_2O_3. Also the COOH peak decreases appreciably in the GO-Cs because of the substitution occurring between –COOH (that are usually at the periphery in the GO flakes), with –COOCs groups [55]. During the reaction, Cs^+ is in fact expected to replace the H^+ ions in COOH groups due to its higher reactivity. This is confirmed by the position of the Cs 3d5/2 peak at 724.1 eV (high resolution data, not shown), corresponding to the value of Cs bound to a carboxylic group [55]. It is worth also to notice the effect of the doping on the Fermi level, causing a 1 eV shift towards lower binding energy of all C peaks in the XPS spectra of GO-Cs (Figure 3c). The edge functionalization with the introduction of Cs^+ does not cause much change in the carbon skeletons of the graphene oxide as observed by Liu et al. [55] and confirmed by our Raman spectra of GO and GO-Cs (Figure 4), where no appre-
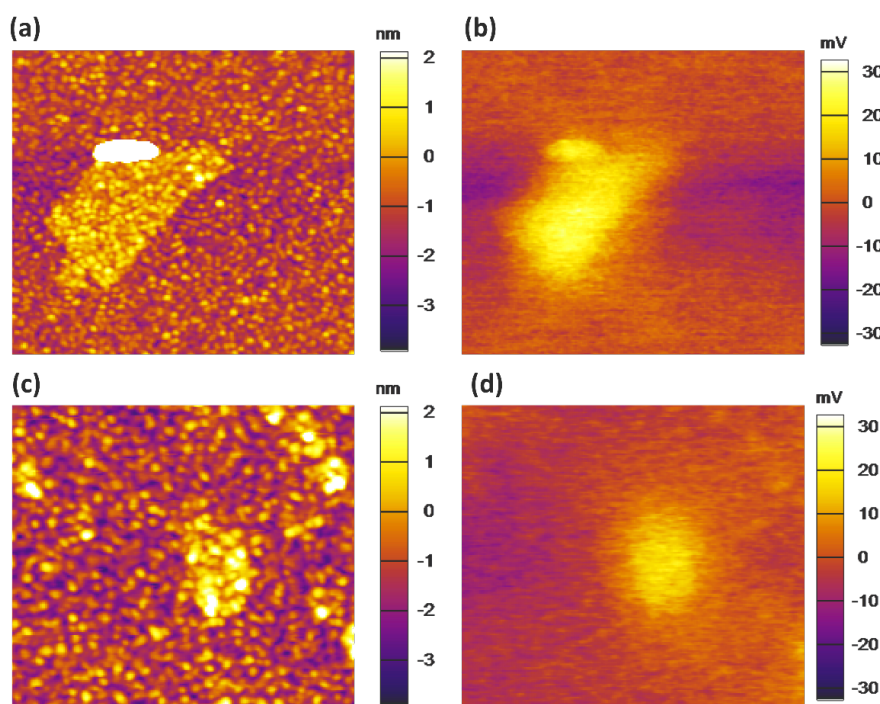
Figure 2: AFM and KPFM images of (a) and (b) a GO flake (2 × 2 μm); (c) and (d) a GO-Cs flake (1.4 × 1.4 μm).
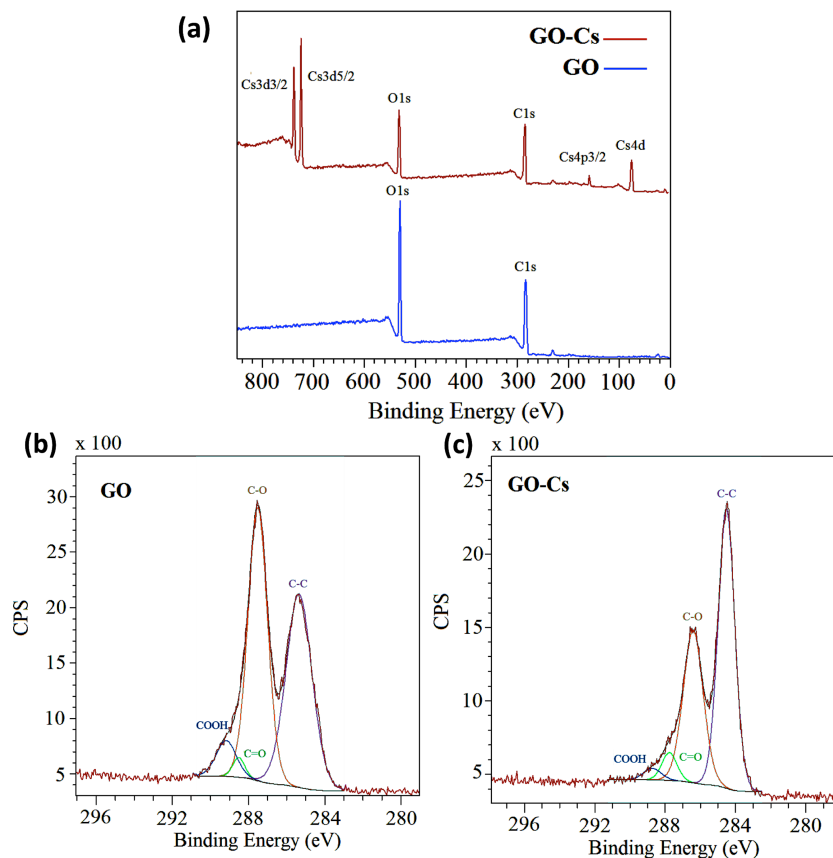
Figure 3: (a) XPS survey spectrum of GO (blue line) and GO-Cs (red line); High resolution XPS C1s spectra of (b) GO and (c) GO-Cs. The ≈1 eV shift towards lower binding energy of the peaks in (c) is due to the shift of the Fermi level caused by the doping.
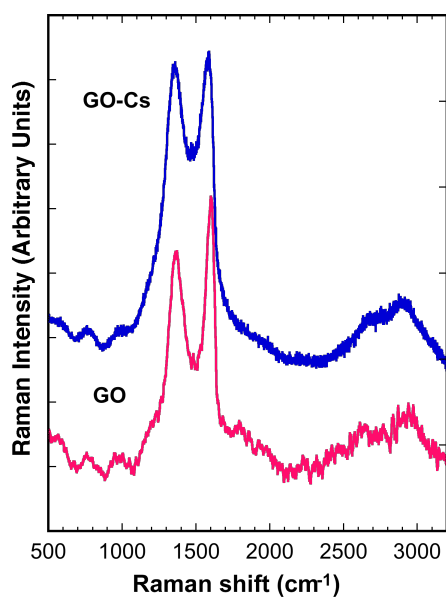
Figure 4: Raman spectra of GO-Cs and GO, displaying intense D and G peaks at ≈1380 and ≈1600 cm⁻¹, respectively. The increase of the D peak, which is the signature of defects in graphene and GO, is clearly linked to the presence of Cs in GO-Cs.

ciable shift is found in the D and G peaks. The 2D peak does not change as well, while the shape is compatible with the presence of several layers in the GO flakes. However a net increase in the D peak at 1360 cm⁻¹ of the GO-Cs sample is a signature of the increased number of defects due to the presence of Cs^+.

Gas sensing performance

The GO-Cs and pure GO sensors were tested towards different concentrations of NO_2 gas balanced in synthetic air at room temperature. The sensors response (R) was calculated according to the equation:

$$R(\%) = 100 \times \frac{(R_{air} - R_{gas})}{R_{air}} = 100 \times \frac{\Delta R}{R_{air}}$$

where R_{air} is the sensing film resistance under synthetic air only and R_{gas} is the film resistance during NO_2 exposure.

As expected, the GO film showed a much higher resistivity than the GO-Cs film in the presence of air (10^{13} Ω vs 10^{10} Ω). The lower baseline resistance can be attributed to the reduction of oxygen groups in GO-Cs film as confirmed by XPS analysis

(Figure 3). Being the value close to the resolution capability of our source meter (10 fA), the measurements of the GO film was affected by electrical noise.

We studied the response at room temperature towards different concentrations of NO_2, ranging from 0.090 to 12.2 ppm. Both sensors exhibited a reduction in resistivity upon exposure to the gas, in agreement with the theory developed by Tang and Cao [14]: a negative charge is transferred to the NO_2 molecules, mostly in correspondence of oxygen functional group, resulting in a p-type behaviour, which was also observed by Prezioso et al. [25]. For NO_2 concentrations higher than 3 ppm both GO and GO-Cs exhibited a significant response, while at low concentrations the GO-Cs performed better. The GO-Cs sensor exhibited a significant response to NO_2, down to concentrations as low as ≈91 ppb, while GO sensor did not show any response to concentrations below 3 ppm. This sensitivity enhancement could be attributed to defects introduced into the GO-Cs films during the doping process. Figure 5 shows the plot of the GO and GO-Cs sensors response as a function of NO_2 concentration. Both responses are approximately linear and proportional to the gas concentration. Since NO_2 is an oxidative gas with strong electron-withdrawing ability, the decrease in resistance confirms the p-type semiconductor behaviour of the sensors, like the one observed for carbon nanotubes [64]. For GO-Cs sensor a relative increase in the response (R_{GO-Cs}) of 0.7, 1, 2, 4.4, 10, 24 and 40% was recorded for 0.18, 0.36, 0.73, 1.5, 3, 6.1 and 12.2 ppm NO_2, respectively. Even at very low gas concentrations, a slope of about 3% ppm can be observed (inset of Figure 5), confirming that the as-prepared GO-Cs sample is highly sensitive to NO_2. On the contrary, no appreciable response has been recorded for GO sensor in the presence of concentrations below 3 ppm, while a relative increase in the response (R_{GO}) of 18, 41, 65% was recorded for 3, 6.1 and 12.2 ppm NO_2, respectively. Table 1 summarises the response of the GO and GO-Cs sensors for comparison.

Table 1: Comparison of the GO and GO-Cs response towards NO_2 with different concentrations.

NO_2 [ppm]	R_{GO} [%]	R_{GO-Cs} [%]
0.18	—	0.7
0.36	—	1
0.73	—	2
1.5	—	4.4
3	18	10
6.1	41	24
12.2	65	39.6

We observed that the resistance of both sensors kept on decreasing even after 20 min exposure to NO_2, reaching very slowly the saturation state. From deep saturation, the film required a very long time exposure to dry air to recover its original value. However, the significant variation of the resistance during the first phase of exposure can ensure a successful employment on the field of the sensing device. Therefore, we consider the exposure of approximately 4 min as an effective response time. This value has been chosen also in consideration of the time required to fill the volume of the gas chamber (1100 cc) with the target gas, which affects the dynamic response. The dynamic responses of GO and GO-Cs upon 4 min exposure to NO_2 concentrations decreasing from 12.2 to 1.5 ppm have been measured simultaneously.

As it can be seen from Figure 6a, the GO response is initially higher than GO-Cs, but decreases more rapidly. When exposed to 1.5 ppm, GO response is not anymore appreciable while a GO-Cs reaction is still evident. The noisier curves of GO is due to its higher resistivity value. Both sensors exhibit a long time to recover their initial value. Approximately 220 min are needed, although this value may be affected by the presence of residual NO_2 molecules present in the 1100 cc gas chamber. While GO sensor recovers faster, GO-Cs is not able to fully recover its initial baseline. The dynamic response of the GO-Cs sensor upon 4 min exposure to 0.091, 0.18, 0.36, 0.732 and 1.44 ppm NO_2 are shown in Figure 6b. The GO-Cs sensor reacts after few tens of seconds to the NO_2 even at very low concentrations, down to 180 ppb. In terms of recovery time, for concentrations below 1 ppm, few minute exposures to dry air is enough to restore the original resistivity value. For higher concentrations, the recovery is longer, suggesting that the amount of Cs doping can be optimized to make a balance

Figure 5: Response of the GO and GO-Cs based sensors as a function of NO_2 concentration. The inset shows the response at very low concentrations.
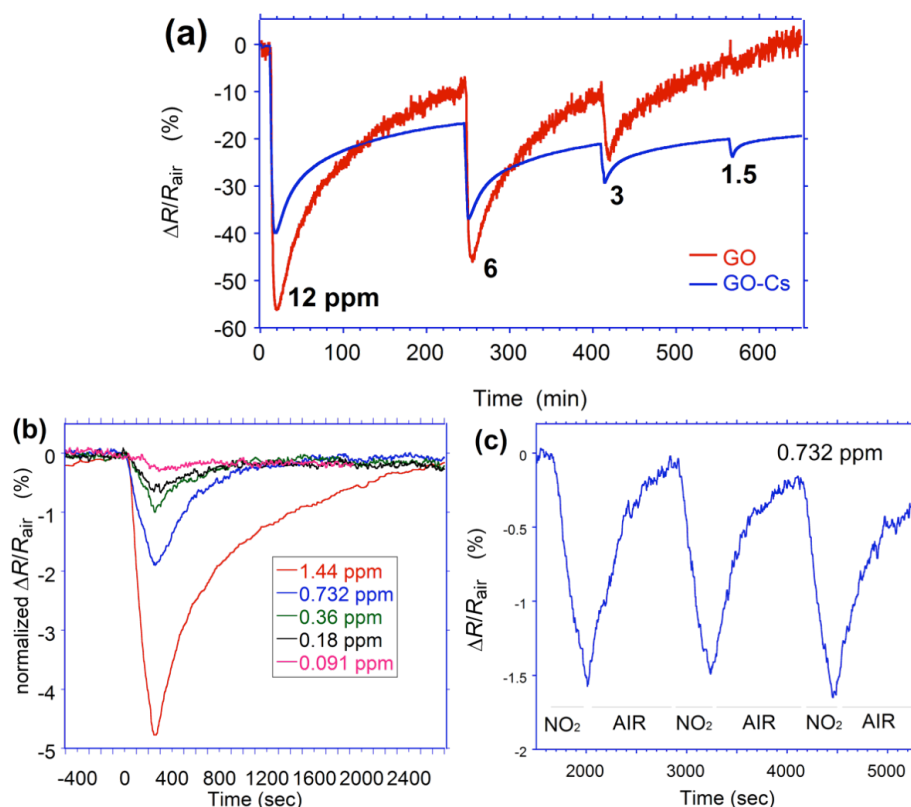
Figure 6: Response of (a) GO-Cs and GO based sensors towards NO$_2$ with concentrations higher than 1 ppm; (b) GO-Cs based gas sensor after exposure to different concentrations of NO$_2$ ranging from 0.091 to 1.44 ppm and (c) GO-Cs based sensor during 3 successive cycles of exposure to 0.732 ppm NO$_2$ for 4 min and to dry air for 15 min.

between the sensitivity and recovery time. This is in agreement with what observed by other researchers [25,46]. As shown in Figure 6c, the GO-Cs sensor exhibits a good repeatability, even if a slight drift in the baseline is observed. This may be due to the presence of gas molecules not yet desorbed from the sensor surface. An average time of 540 s is needed to recover after 240 s exposure to 0.732 ppm of NO$_2$.

Conclusion

We successfully fabricated and studied for the first time an NO$_2$ sensor based on caesium-doped graphene oxide (GO-Cs). We demonstrated that caesium doping is an effective technique to reduce the GO, making it a promising material for gas sensing applications. XPS, Raman and KPFM results confirm the successful incorporation of Cs into the GO resulting in the reduction of oxygen groups. The developed GO-Cs based conductometric sensor exhibits a very low detection limit for NO$_2$ (down to ≈90 ppb) at room temperature. This can be attributed to the p-character of the GO film, due to the intercalation of Cs atoms leading to the reduction of oxygen groups. However, the sensor shows very long recovery, making GO-Cs a good candidate for applications requiring high sensitivities, but not fast response. Future works will focus on investigating

the effect of different species and concentration of dopants on improving the selectivity, response and recovery time.

structure Strategy to provide nano and microfabrication facilities for Australia's researchers.

References

1. Geim, A. K.; Novoselov, K. S. *Nat. Mater.* **2007,** *6,* 183–191. doi:10.1038/nmat1849
2. Castro Neto, A. H.; Guinea, F.; Peres, N. M. R.; Novoselov, K. S.; Geim, A. K. *Rev. Mod. Phys.* **2009,** *81,* 109–162. doi:10.1103/RevModPhys.81.109
3. Chang, H.; Wu, H. *Energy Environ. Sci.* **2013,** *6,* 3483–3507. doi:10.1039/c3ee42518e
4. Schedin, F.; Geim, A. K.; Morozov, S. V.; Hill, E. W.; Blake, P.; Katsnelson, M. I.; Novoselov, K. S. *Nat. Mater.* **2007,** *6,* 652–655. doi:10.1038/nmat1967
5. Basu, S.; Bhattacharyya, P. *Sens. Actuators, B* **2012,** *173,* 1–21. doi:10.1016/j.snb.2012.07.092
6. Qazi, M.; Koley, G. *Sensors* **2008,** *8,* 7144–7156. doi:10.3390/s8117144
7. Arsat, R.; Breedon, M.; Shafiei, M.; Spizziri, P. G.; Gilje, S.; Kaner, R. B.; Kalantar-zadeh, K.; Wlodarski, W. *Chem. Phys. Lett.* **2009,** *467,* 344–347. doi:10.1016/j.cplett.2008.11.039
8. Fowler, J. D.; Allen, M. J.; Tung, V. C.; Yang, Y.; Kaner, R. B.; Weiller, B. H. *ACS Nano* **2009,** *3,* 301–306. doi:10.1021/nn800593m
9. Al-Mashat, L.; Shin, K.; Kalantar-zadeh, K.; Plessis, J. D.; Han, S. H.; Kojima, R. W.; Kaner, R. B.; Li, D.; Gou, X.; Ippolito, S. J.; Wlodarski, W. *J. Phys. Chem. C* **2010,** *114,* 16168–16173. doi:10.1021/jp103134u
10. Siegal, M. P.; Yelton, W. G.; Overmyer, D. L.; Provencio, P. P. *Langmuir* **2004,** *20,* 1194–1198. doi:10.1021/la034460s
11. Shafiei, M.; Spizzirri, P. G.; Arsat, R.; Yu, J.; du Plessis, J.; Dubin, S.; Kaner, R. B.; Kalantar-zadeh, K.; Wlodarski, W. *J. Phys. Chem. C* **2010,** *114,* 13796–13801. doi:10.1021/jp104459s
12. Geim, A. K. *Science* **2009,** *324,* 1530–1534. doi:10.1126/science.1158877
13. Zhang, Y.-H.; Chen, Y.-B.; Zhou, K.-G.; Liu, C.-H.; Zeng, J.; Zhang, H.-L.; Peng, Y. *Nanotechnology* **2009,** *20,* 185504. doi:10.1088/0957-4484/20/18/185504
14. Tang, S.; Cao, Z. *J. Chem. Phys.* **2011,** *134,* 044710. doi:10.1063/1.3541249
15. Li, W.; Geng, X.; Guo, Y.; Rong, J.; Gong, Y.; Wu, L.; Zhang, X.; Li, P.; Xu, J.; Cheng, G.; Sun, M.; Liu, L. *ACS Nano* **2011,** *5,* 6955–6961. doi:10.1021/nn201433r
16. Wei, X.-L.; Chen, Y.-P.; Liu, W.-L.; Zhong, J.-X. *Phys. Lett. A* **2012,** *376,* 559–562. doi:10.1016/j.physleta.2011.10.055
17. Niu, F.; Liu, J.-M.; Tao, L.-M.; Wang, W.; Song, W.-G. *J. Mater. Chem. A* **2013,** *1,* 6130–6133. doi:10.1039/c3ta11070b
18. Pandey, P. A.; Wilson, N. R.; Covington, J. A. *Sens. Actuators, B* **2013,** *183,* 478–487. doi:10.1016/j.snb.2013.03.089
19. Dan, Y.; Lu, Y.; Kybert, N. J.; Luo, Z.; Johnson, A. T. C. *Nano Lett.* **2009,** *9,* 1472–1475. doi:10.1021/nl8033637
20. Novoselov, K. S. *Rev. Mod. Phys.* **2011,** *83,* 837–849. doi:10.1103/RevModPhys.83.837
21. Dreyer, D. R.; Park, S.; Bielawski, C. W.; Ruoff, R. S. *Chem. Soc. Rev.* **2010,** *39,* 228–240. doi:10.1039/b917103g
22. Zhu, Y.; Murali, S.; Cai, W.; Li, X.; Suk, J. W.; Potts, J. R.; Ruoff, R. S. *Adv. Mater.* **2010,** *22,* 3906–3924. doi:10.1002/adma.201001068
23. Lu, G.; Ocola, L. E.; Chen, J. *Appl. Phys. Lett.* **2009,** *94,* 083111. doi:10.1063/1.3086896
24. Jung, I.; Dikin, D.; Park, S.; Cai, W.; Mielke, S. L.; Ruoff, R. S. *J. Phys. Chem. C* **2008,** *112,* 20264–20268. doi:10.1021/jp807525d
25. Prezioso, S.; Perrozzi, F.; Giancaterini, L.; Cantalini, C.; Treossi, E.; Palermo, V.; Nardone, M.; Santucci, S.; Ottaviano, L. *J. Phys. Chem. C* **2013,** *117,* 10683–10690. doi:10.1021/jp3085759
26. Stankovich, S.; Dikin, D. A.; Dommett, G. H. B.; Kohlhaas, K. M.; Zimney, E. J.; Stach, E. A.; Piner, R. D.; Nguyen, S. T.; Ruoff, R. S. *Nature* **2006,** *442,* 282–286. doi:10.1038/nature04969
27. Gilje, S.; Han, S.; Wang, M.; Wang, K. L.; Kaner, R. B. *Nano Lett.* **2007,** *7,* 3394–3398. doi:10.1021/nl0717715
28. Stankovich, S.; Dikin, D. A.; Piner, R. D.; Kohlhaas, K. A.; Kleinhammes, A.; Jia, Y.; Wu, Y.; Nguyen, S. T.; Ruoff, R. S. *Carbon* **2007,** *45,* 1558–1565. doi:10.1016/j.carbon.2007.02.034
29. Gómez-Navarro, C.; Weitz, R. T.; Bittner, A. M.; Scolari, M.; Mews, A.; Burghard, M.; Kern, K. *Nano Lett.* **2007,** *7,* 3499–3503. doi:10.1021/nl072090c
30. Sutter, P. W.; Flege, J.-I.; Sutter, E. A. *Nat. Mater.* **2008,** *7,* 406–411. doi:10.1038/nmat2166
31. Novoselov, K. S.; Geim, A. K.; Morozov, S. V.; Jiang, D.; Zhang, Y.; Dubonos, S. V.; Grigorieva, I. V.; Firsov, A. A. *Science* **2004,** *306,* 666–669. doi:10.1126/science.1102896
32. Dato, A.; Radmilovic, V.; Lee, Z.; Phillips, J.; Frenklach, M. *Nano Lett.* **2008,** *8,* 2012–2016. doi:10.1021/nl8011566
33. Berger, C.; Song, Z.; Li, X.; Wu, X.; Brown, N.; Naud, C.; Mayou, D.; Li, T.; Hass, J.; Marchenkov, A. N.; Conrad, E. H.; First, P. N.; de Heer, W. A. *Science* **2006,** *312,* 1191–1196. doi:10.1126/science.1125925
34. Park, S.; Ruoff, R. S. *Nat. Nanotechnol.* **2009,** *4,* 217–224. doi:10.1038/nnano.2009.58
35. Parades, J. I.; Villar-Rodil, S.; Martínez-Alonso, A.; Tascón, J. M. D. *Langmuir* **2008,** *24,* 10560–10564. doi:10.1021/la801744a
36. Park, S.; Lee, K.-S.; Bozoklu, G.; Cai, W.; Nguyen, S. T.; Ruoff, R. S. *ACS Nano* **2008,** *2,* 572–578. doi:10.1021/nn700349a
37. Stankovich, S.; Piner, R. D.; Chen, X.; Wu, N.; Nguyen, S. T.; Ruoff, R. S. *J. Mater. Chem.* **2006,** *16,* 155–158. doi:10.1039/b512799h
38. Stankovich, S.; Piner, R. D.; Nguyen, S. T.; Ruoff, R. S. *Carbon* **2006,** *44,* 3342–3347. doi:10.1016/j.carbon.2006.06.004
39. Tung, V. C.; Allen, M. J.; Yang, Y.; Kaner, R. B. *Nat. Nanotechnol.* **2009,** *4,* 25–29. doi:10.1038/nnano.2008.329
40. McAllister, M. J.; Li, J.-L.; Adamson, D. H.; Schniepp, H. C.; Abdala, A. A.; Liu, J.; Herrera-Alonso, M.; Milius, D. L.; Car, R.; Prud'homme, R. K.; Aksay, I. A. *Chem. Mater.* **2007,** *19,* 4396–4404. doi:10.1021/cm0630800
41. Schniepp, H. C.; Li, J.-L.; McAllister, M. J.; Sai, H.; Herrera-Alonso, M.; Adamson, D. H.; Prud'homme, R. K.; Car, R.; Saville, D. A.; Aksay, I. A. *J. Phys. Chem. B* **2006,** *110,* 8535–8539. doi:10.1021/jp060936f
42. Williams, G.; Seger, B.; Kamat, P. V. *ACS Nano* **2008,** *2,* 1487–1491. doi:10.1021/nn800251f
43. Pei, S.; Cheng, H.-M. *Carbon* **2012,** *50,* 3210–3228. doi:10.1016/j.carbon.2011.11.010
44. Zhao, J.; Han, J.; Lu, J. P. *Phys. Rev. B* **2002,** *65,* 193401. doi:10.1103/PhysRevB.65.193401
45. Yu, M.-R.; Wu, R.-J.; Suyambrakasam, G.; Joly, J.; Chavali, M. *Adv. Sci. Lett.* **2012,** *16,* 53–57. doi:10.1166/asl.2012.4264
46. Robinson, J. T.; Perkins, F. K.; Snow, E. S.; Wei, Z.; Sheehan, P. E. *Nano Lett.* **2008,** *8,* 3137–3140. doi:10.1021/nl8013007
47. Lipatov, A.; Varezhnikov, A.; Wilson, P.; Sysoev, V.; Kolmakov, A.; Sinitskii, A. *Nanoscale* **2013,** *5,* 5426–5434. doi:10.1039/c3nr00747b

48. Hu, N.; Wang, Y.; Chai, J.; Gao, R.; Yang, Z.; Kong, E. S.-W.;
Zhang, Y. *Sens. Actuators, B* **2012,** *163,* 107–114.
doi:10.1016/j.snb.2012.01.016

49. Dua, V.; Surwade, S. P.; Ammu, S.; Agnihotra, S. R.; Jain, S.;
Roberts, K. E.; Park, S.; Ruoff, R. S.; Manohar, S. K.
Angew. Chem., Int. Ed. **2010,** *49,* 2154–2157.
doi:10.1002/anie.200905089

50. Yuan, W.; Liu, A.; Huang, L.; Li, C.; Shi, G. *Adv. Mater.* **2013,** *25,*
766–771. doi:10.1002/adma.201203172

51. Tricoli, A.; Righettoni, M.; Teleki, A. *Angew. Chem., Int. Ed.* **2010,** *49,*
7632–7659. doi:10.1002/anie.200903801

52. Llobet, E. *Sens. Actuators, B* **2013,** *179,* 32–45.
doi:10.1016/j.snb.2012.11.014

53. Thomas, B.; Benoy, S.; Radha, K. K. *Sens. Actuators, B* **2008,** *133,*
404–413. doi:10.1016/j.snb.2008.02.050

54. Marcano, D. C.; Kosynkin, D. V.; Berlin, J. M.; Sinitskii, A.; Sun, Z.;
Slesarev, A.; Alemany, L. B.; Lu, W.; Tour, J. M. *ACS Nano* **2010,** *4,*
4806–4814. doi:10.1021/nn1006368

55. Liu, J.; Xue, Y.; Gao, Y.; Yu, D.; Durstock, M.; Dai, L. *Adv. Mater.* **2012,**
24, 2228–2233. doi:10.1002/adma.201104945

56. Chen, D.; Feng, H.; Li, J. *Chem. Rev.* **2012,** *112,* 6027–6053.
doi:10.1021/cr300115g

57. Glover, A. J.; Adamson, D. H.; Schniepp, H. C. *J. Phys. Chem. C* **2012,**
116, 20080–20085. doi:10.1021/jp305717v

58. Mkhoyan, K. A.; Contryman, A. W.; Silcox, J.; Stewart, D. A.; Eda, G.;
Mattevi, C.; Miller, S.; Chhowalla, M. *Nano Lett.* **2009,** *9,* 1058–1063.
doi:10.1021/nl8034256

59. Liscio, A.; Veronese, G. P.; Treossi, E.; Suriano, F.; Rossella, F.;
Bellani, V.; Rizzoli, R.; Samori, P.; Palermo, V. *J. Mater. Chem.* **2011,**
21, 2924–2931. doi:10.1039/c0jm02940h

60. Palermo, V.; Palma, M.; Samori, P. *Adv. Mater.* **2006,** *18,* 145–164.
doi:10.1002/adma.200501394

61. Jaafar, M.; López-Polín, G.; Gómez-Navarro, C.; Gómez-Herrero, J.
Appl. Phys. Lett. **2012,** *101,* 263109. doi:10.1063/1.4773357

62. Yang, D.; Velamakanni, A.; Bozoklu, G.; Park, S.; Stoller, M.;
Piner, R. D.; Stankovich, S.; Jung, I.; Field, D. A.; Ventrice, C. A., Jr.;
Ruoff, R. S. *Carbon* **2009,** *47,* 145–152.
doi:10.1016/j.carbon.2008.09.045

63. Ganguly, A.; Sharma, S.; Papakonstantinou, P.; Hamilton, J.
J. Phys. Chem. C **2011,** *115,* 17009–17019. doi:10.1021/jp203741y

64. Kong, J.; Franklin, N. R.; Zhou, C.; Chapline, M. G.; Peng, S.; Cho, K.;
Dai, H. *Science* **2000,** *287,* 622–625.
doi:10.1126/science.287.5453.622

Room temperature, ppb-level NO$_2$ gas sensing of multiple-networked ZnSe nanowire sensors under UV illumination

Sunghoon Park[1], Soohyun Kim[1], Wan In Lee[2], Kyoung-Kook Kim[3] and Chongmu Lee[*1]

Abstract

Reports of the gas sensing properties of ZnSe are few, presumably because of the decomposition and oxidation of ZnSe at high temperatures. In this study, ZnSe nanowires were synthesized by the thermal evaporation of ZnSe powders and the sensing performance of multiple-networked ZnSe nanowire sensors toward NO$_2$ gas was examined. The results showed that ZnSe might be a promising gas sensor material if it is used at room temperature. The response of the ZnSe nanowires to 50 ppb–5 ppm NO$_2$ at room temperature under dark and UV illumination conditions were 101–102% and 113–234%, respectively. The responses of the ZnSe nanowires to 5 ppm NO$_2$ increased from 102 to 234% with increasing UV illumination intensity from 0 to 1.2 mW/cm^2. The response of the ZnSe nanowires was stronger than or comparable to that of typical metal oxide semiconductors reported in the literature, which require higher NO$_2$ concentrations and operate at higher temperatures. The origin of the enhanced response of the ZnSe nanowires towards NO$_2$ under UV illumination is also discussed.

Introduction

ZnSe has been widely used in fabricating short-wave optoelectronic devices [1] including blue–green laser diodes [2], tunable mid-IR laser diodes for remote sensing [3], white-light LEDs [4], continuous wave ZnSe-based laser diodes [5] and UV photodetectors [6]. On the other hand, there are almost no reports on the gas sensing properties of ZnSe. This might be due

to the decomposition and oxidation of ZnSe at temperatures above 200 °C [7] and a lack of good sensing performance at room temperature.

In recent years, one-dimensionally (1D) nanostructured, metal oxide semiconductor sensors have been studied extensively

because of the associated higher sensitivity due to the high surface-to-volume ratios as compared to thin film gas sensors [8-13]. Most metal oxides exhibit some sensitivity to many gases at high temperatures because gas sensitivity tends to increase with increasing temperature. On the other hand, the development of highly sensitive and selective sensors at room temperature is still a challenge. Several techniques including the doping [12,14,15] or surface functionalization [16-18] of metal catalysts, core–shell structure formation [19-21] and UV irradiation [22-24] have been developed to improve the sensing performance, detection limit and selectivity of 1D nanostructure sensors at room temperature. Among these techniques, the UV illumination method was used in the present study to enhance the sensing performance of ZnSe, 1D nanostructure-based sensors at room temperature. In this study, multiple-networked ZnSe nanowire sensors were fabricated and examined for their room-temperature, NO_2-gas sensing properties under UV illumination. Unlike individual 1D nanostructure sensors, multiple-networked 1D-nanostructured sensors have the benefits of low sensor fabrication cost (because there is no need for precise techniques to connect the nanostructures), as well as outstanding sensing performance.

Results and Discussion
Analysis of the structure of ZnSe nanowires

Figure 1a shows a SEM image of the ZnSe, 1D nanostructures. The 1D nanostructures exhibited a wire- or fiber-like morphology with widths ranging from 30 to 100 nm and lengths ranging up to ≈300 μm. Figure 1b shows the corresponding XRD pattern of the ZnSe nanowires. The XRD pattern of the ZnSe nanowires showed six sharp reflection peaks assigned to wurtzite-structured ZnSe with lattice constants of $a = 0.3996$ nm and $c = 0.6626$ nm (JCPDS No. 89-2940), suggesting that the nanowires were crystalline.

The low-magnification TEM image in Figure 2a revealed a typical ZnSe nanowire with an extremely uniform diameter of approximately 80 nm. The HRTEM image in Figure 2b confirmed that the core region of the nanowire was perfectly crystalline, whereas the edge region showed twinning along the axis of the nanowire. Fringes with spacings of 0.346 and 0.331 nm corresponding to the interplanar distances of the {100} and {002} lattice planes, respectively, were clearly observed in the core region. The corresponding selected area in the electron diffraction pattern (Figure 2c) exhibited two types of reflection spots assigned to wurtzite-structured ZnSe: a round reflection from the core region and an elongated reflection from the edge region.

The corresponding selected area electron diffraction pattern (Figure 2c) exhibited two types of reflection spots assigned to
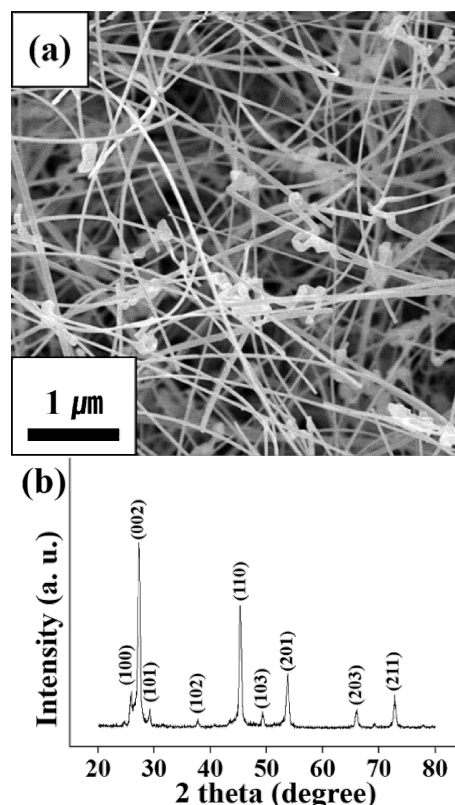
Figure 1: (a) SEM image of ZnSe nanowires. (b) XRD pattern of the ZnSe nanowires.

wurtzite-structured ZnSe: round one from the core region and elongated one from the edge region.

Performance of nanowire gas sensors

Figure 3a and Figure 3b show the dynamic response of the ZnSe nanowires towards NO_2 gas at room temperature in the dark and under UV illumination, respectively. The maximum resistance was reached immediately upon exposure to NO_2 and recovered completely to the initial value after the removal of NO_2. The resistance increased with increasing NO_2 concentration. The resistance showed good reversibility during the introduction and exhaust cycles of NO_2. The ZnSe nanowires showed responses to 50 ppb–5 ppm NO_2 ranging from ≈101% to ≈102% and from ≈113% to ≈234% in the dark and under UV (365 nm) illumination, respectively. In other words, UV (365 nm) irradiation increased the response of the ZnSe nanowires to 50 ppb–5 ppm NO_2 by 1.1–2.3 times.

Figure 4a–c show the responses, response times and recovery times of the ZnSe nanowires towards NO_2 gas at room temperature in the dark and under UV illumination, respectively. This information was determined from that of Figure 3a and Figure 3b. The ZnSe nanowires showed a sufficiently strong
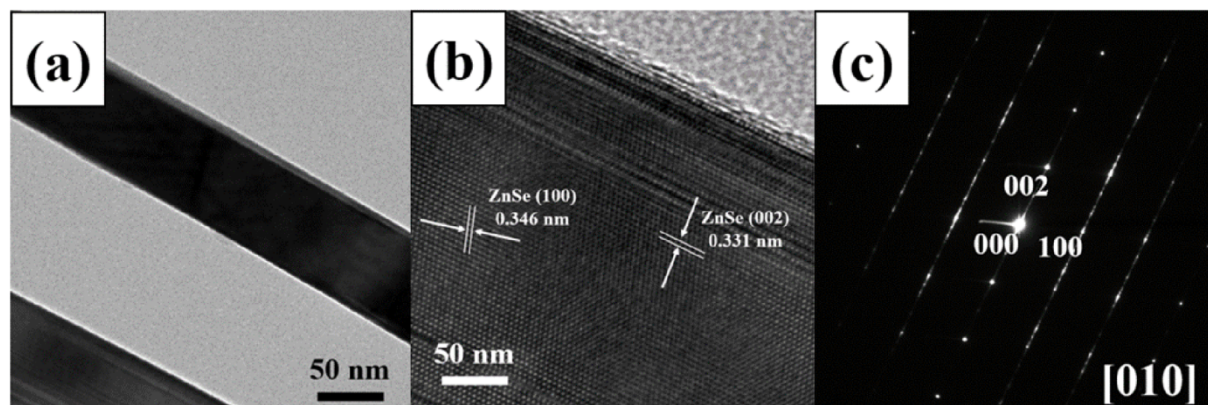
Figure 2: (a) Low-magnification TEM image of a typical ZnSe nanowire, (b) high-resolution TEM image of a typical ZnSe nanowire and (c) corresponding SAED pattern.
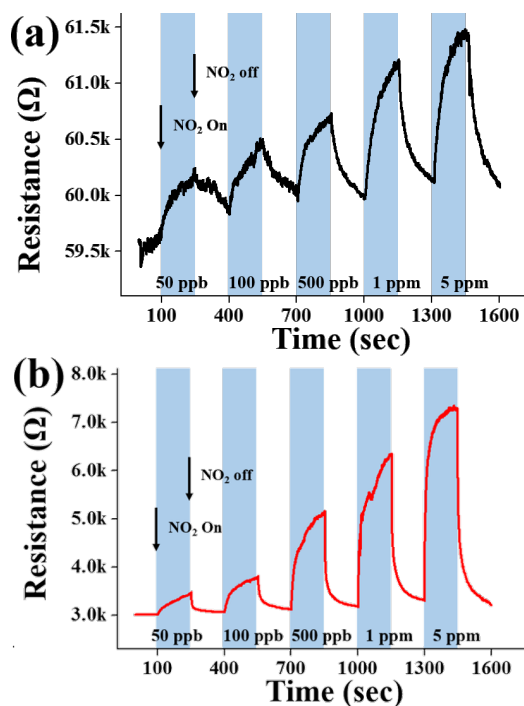
Figure 3: Electrical responses of the gas sensors fabricated from ZnSe nanowires to 50 ppb, 100 ppb, 500 ppb, 1 ppm and 5 ppm NO_2 gas at room temperature (a) in the dark and (b) under UV (365 nm) illumination at 1.2 mW/cm^2.

response to NO_2 gas, even at 50 ppb. The response of the ZnSe nanowires to NO_2 gas tended to increase more rapidly with increasing NO_2 concentrations under UV illumination than in the dark. Regarding the sensing time, both the response times and recovery times were shorter under UV illumination than in the dark. In particular, recovery times were more than 35 s shorter under UV illumination than in the dark at a NO_2 gas concentration range from 50 ppb to 5 ppm. Figure 4a–c show

the dependence of the response, response time and recovery times of the ZnSe nanowires to 5 ppm NO_2 gas at room temperature on the illumination intensity of UV light used to illuminate the gas sensors. The response of the nanowires was 102% in the dark. The responses of the nanowires increased from ≈102 to ≈234% with increasing UV illumination intensity from 0 to 1.2 mW/cm^2 (Figure 4a). Figure 5a shows a strong dependence of the electrical response of the ZnSe nanowires on the UV illumination intensity towards 5 ppm NO_2 gas at room temperature. The response increased rapidly with increasing UV illumination intensity. On the other hand, Figure 5a and Figure 5b show that both the response time and recovery time of the ZnSe nanowires at room temperature towards 5 ppm NO_2 gas tend to decrease with the UV illumination intensity. These high responses at room temperature highlight the strong influence of UV irradiation on the response of the nanosensor to NO_2 gas.

Table 1 compares the responses of the ZnSe nanowires towards NO_2 synthesized in this study with those of metal oxide semiconductor, 1D nanostructures reported in the literature. The response of the ZnSe nanowires to NO_2 gas with a lower concentration obtained at room temperature in the dark in this study was stronger than or comparable to those of typical metal oxide, 1D nanostructures, such as ZnO, SnO_2, In_2O_3, and MoO_3 at higher temperatures and higher NO_2 concentrations [25-30]. This suggests that the ZnSe nanowires are also a promising candidate as a NO_2 gas sensor material.

Conclusion

ZnSe nanowires exhibited responses towards 50 ppb–5 ppm NO_2 ranging from ≈101% to ≈102% and from ≈113% to ≈234% at room temperature in the dark and under UV (365 nm) illumination, respectively. These responses of ZnSe nanowires

Figure 4: (a) Response, (b) response times and (c) recovery times of the multiple-networked ZnSe nanowire gas sensor to NO₂ gas in the dark and under 365 nm UV illumination at 1.2 mW/cm².

Figure 5: (a) Electrical response and (b) response and recovery times of ZnSe nanowire gas sensors under UV (365 nm) illumination for different UV illumination intensities.
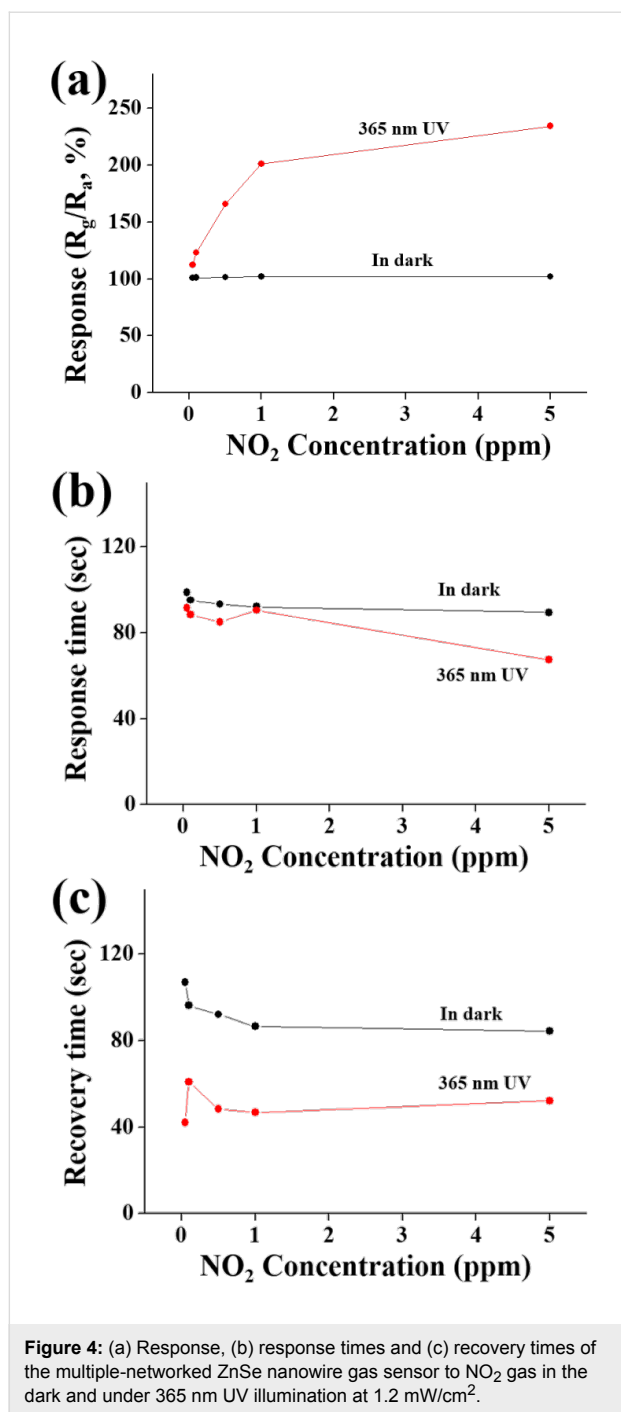
were stronger than or comparable to those of typical metal oxide semiconductors reported in the literature, such as ZnO, SnO_2, In_2O_3, and MoO_3, at higher temperatures and higher NO_2 concentrations. The ZnSe nanowire sensors cannot be used at high temperatures, such as 300 °C, because of the oxidation of ZnSe, but their sensing performance could be enhanced when used at room temperature under UV illumination. The response of the ZnSe nanowires increased from 0 to ≈234% with increasing UV illumination intensity from 0 to 1.2 mW/cm² and
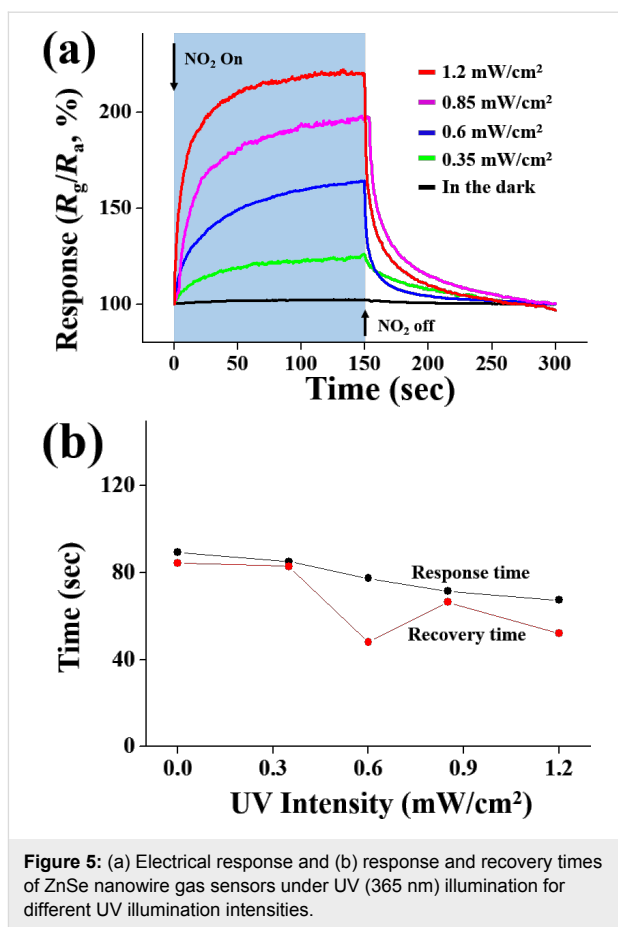
the response time and recovery time of the ZnSe nanowires tended to decrease with increasing UV illumination intensity from 0 to 1.2 mW/cm². The results show that ZnSe nanowires are also a promising nanomaterial for the fabrication of NO_2 gas sensors when used at room temperature. In addition, the enhanced response of the ZnSe nanowires under UV illumination to NO_2 gas might be due to (1) modulation of the depletion layer width and (2) the UV-activated adsorption, and desorption of NO_2 species.

Experimental
Synthesis of ZnSe nanowires

Similar to that previously described [31], ZnSe nanowires were synthesized on 3 nm-thick gold (Au) layer-coated, *c*-plane sapphire ($Al_2O_3(0001)$) substrates by the thermal evaporation of ZnSe powders. A quartz tube was mounted inside a horizontal tube furnace. The quartz tube consisted of two temperature zones: zone A at 850 °C and zone B at 700 °C. An alumina boat loaded with pure ZnSe powder was located in zone A, whereas the Au-coated Al_2O_3 substrate was placed in zone B. The nitrogen (N_2) gas flow rate and chamber pressure were 100 cm³/min and 1 Torr, respectively. The synthesis process time was 1 h.

Table 1: Responses of various nanomaterial gas sensors to NO_2 gas.

Nanomaterial	Temperature (°C)	NO_2 Conc. (ppm)	Response (%)	Ref.
ZnSe NWs (dark)	25	0.05	101	Present work
ZnSe NWs (UV)	25	0.05	113	Present work
ZnO nanorods	300	0.1	35	[24]
ZnO fibers	100	0.4	50	[25]
SnO_2 NWs	300	10	1.01	[26]
SnO_2 nanobelts	300	10	1.9	[27]
In_2O_3 NWs (multi-NW)	200	0.5	2.1	[28]
In_2O_3 NWs (single-NW)	200	0.5	2.6	[28]
MoO_3 lamellae	225	10	118	[29]

Characterization of the structure of the nanowires

The morphology and structure of the collected nanowire samples were examined by scanning electron microscopy (SEM, Hitachi S-4200) and transmission electron microscopy (TEM, Philips CM-200), respectively. The crystallographic structures of the samples were determined by glancing angle X-ray diffraction (XRD, Philips X'pert MRD diffractometer) using Cu Kα radiation ($\lambda = 0.15406$ nm) at a scan rate of 4°/min, and a 0.5° glancing angle with a rotating detector.

Preparation of sensors and gas sensing tests

ZnSe nanowire samples were dispersed ultrasonically in a mixture of deionized water (5 mL) and isopropyl alcohol (5 mL), and dried at 90 °C for 30 min. A slurry droplet containing the nanowires (10 µL) was placed onto the SiO_2-coated Si substrates equipped with a pair of interdigitated (IDE) Ni (≈200 nm)/Au (≈50 nm) electrodes with a gap of 20 µm. The flow-through technique was used to test the gas sensing properties. All measurements were performed in a temperature-stabilized, sealed chamber with a constant flow rate of 200 cm^3/min at 25 °C under 50% RH. The NO_2 concentration was controlled by mixing NO_2 gas with synthetic air at different ratios. The detailed procedures for the sensor fabrication and sensing test are reported elsewhere [32]. The electrical resistance of the gas sensors was determined in the dark and under UV light ($\lambda = 365$ nm) illumination at intensities ranging from 0.35 to 1.2 mW/cm^2 by measuring the electric current between the Ni/Au IDEs at 1 V and at room temperature. The response was defined as $(R_g/R_a) \times 100\%$ for NO_2 gas, where R_g and R_a are the electrical resistances of the sensors in the target gas and air, respectively.

Acknowledgements

References

1. Park, S.; An, S.; Ko, H.; Lee, C. *Mater. Chem. Phys.* **2014,** *143,* 735–739. doi:10.1016/j.matchemphys.2013.10.007
2. Ma, R.; Bando, Y. *Chem. Phys. Lett.* **2003,** *374,* 358–361. doi:10.1016/S0009-2614(03)00776-0
3. Mirov, S. B.; Fedorov, V. V.; Graham, K.; Moskalev, I. S.; Badikov, V. V.; Panyutin, V. *Opt. Lett.* **2002,** *27,* 909–911. doi:10.1364/OL.27.000909
4. Katayama, K.; Matsubara, H.; Nakanishi, F.; Nakamura, T.; Doi, H.; Saegusa, A.; Mitsui, T.; Matsuoka, T.; Irikusa, M.; Takebe, T.; Nishine, S.; Shirakawa, T. *J. Cryst. Growth* **2000,** *214,* 1064–1070. doi:10.1016/S0022-0248(00)00275-X
5. Okuyama, H. *Trans. Inst. Electron., Inf. Commun. Eng., Sect. E* **2000,** *E83-C,* 536–545.
6. Chang, S. J.; Su, Y. K.; Chen, W. R.; Chen, J. F.; Lan, W. H.; Lin, W. J.; Cherng, Y. T.; Liu, C. H.; Liaw, U. H. *IEEE Photonics Technol. Lett.* **2002,** *14,* 188–190. doi:10.1109/68.980508
7. Dow Chemical Corporate Website - The Dow Chemical Company. http://www.dow.com/assets/attachments/business/gt/infrared_materials /cvd_zinc_selenide/tds/cvd_zinc_selenide.pdf (accessed Oct 8, 2014).
8. Kim, H.; Jin, C.; An, S.; Lee, C. *Ceram. Int.* **2012,** *38,* 3563–3567. doi:10.1016/j.ceramint.2011.12.072
9. Kolmakov, A.; Zhang, Y.; Cheng, G.; Moskovits, M. *Adv. Mater.* **2003,** *15,* 997–1000. doi:10.1002/adma.200304889
10. Liu, Y.; Koep, E.; Liu, M. *Chem. Mater.* **2005,** *17,* 3997–4000. doi:10.1021/cm050451o
11. Law, M.; Kind, H.; Messer, B.; Kim, F.; Yang, P. *Angew. Chem.* **2002,** *114,* 2511–2514. doi:10.1002/1521-3757(20020703)114:13<2511::AID-ANGE2511>3.0. CO;2-N
12. Lin, Y.-H.; Huang, M.-W.; Liu, C.-K.; Chen, J.-R.; Wu, J.-M.; Shih, H.-C. *J. Electrochem. Soc.* **2009,** *156,* K196–K199. doi:10.1149/1.3223984
13. Kim, H. S.; Jin, C. H.; Park, S. H.; Kim, S. I.; Lee, C. *Sens. Actuators, B* **2012,** *161,* 594–599. doi:10.1016/j.snb.2011.11.006
14. Ramgir, N. S.; Mulla, I. S.; Vijayamohanan, K. P. *Sens. Actuators, B* **2005,** *107,* 708–715. doi:10.1016/j.snb.2004.12.073
15. Wan, Q.; Wang, T. H. *Chem. Commun.* **2005,** *1,* 3841–3843. doi:10.1039/b504094a
16. Kolmakov, A.; Klenov, D. O.; Lilach, Y.; Stemmer, S.; Moskovits, M. *Nano Lett.* **2005,** *5,* 667–673. doi:10.1021/nl050082v

17. Kuang, Q.; Lao, C.-S.; Li, Z.; Liu, Y.-Z.; Xie, Z.-X.; Zheng, L.-S.; Wang, Z. L. *J. Phys. Chem. C* **2008,** *112,* 11539–11544. doi:10.1021/jp802880c

18. Wright, J. S.; Lim, W.; Gila, B. P.; Pearton, S. J.; Johnson, J. L.; Ural, A.; Ren, F. *Sens. Actuators, B* **2009,** *140,* 196–199. doi:10.1016/j.snb.2009.04.009

19. Tamaki, J.; Shimanoe, K.; Yamada, Y.; Yamamoto, Y.; Miura, N.; Yamazoe, N. *Sens. Actuators, B* **1998,** *49,* 121–125. doi:10.1016/S0925-4005(98)00144-0

20. Park, S.; Ko, H.; Kim, S.; Lee, C. *ACS Appl. Mater. Interfaces* **2014,** *6,* 9595–9596. doi:10.1021/am501975v

21. Jin, C.; Park, S.; Kim, H.; Lee, C. *Sens. Actuators, B* **2012,** *161,* 223–228. doi:10.1016/j.snb.2011.10.023

22. Comini, E.; Cristalli, A.; Faglia, G.; Sberveglieri, G. *Sens. Actuators, B* **2000,** *65,* 260–263. doi:10.1016/S0925-4005(99)00350-0

23. Gong, J.; Li, Y.; Chai, X.; Hu, Z.; Deng, Y. *J. Phys. Chem. C* **2010,** *114,* 1293–1298. doi:10.1021/jp906043k

24. Lu, G.; Xu, J.; Sun, J.; Yu, Y.; Zhang, Y.; Liu, F. *Sens. Actuators, B* **2012,** *162,* 82–88. doi:10.1016/j.snb.2011.12.039

25. Park, S. H.; An, S. Y.; Ko, H. S.; Jin, C. H.; Lee, C. *ACS Appl. Mater. Interfaces* **2012,** *4,* 3650–3656. doi:10.1021/am300741r

26. Baratto, C.; Sberveglieri, G.; Onischuk, A.; Caruso, B.; di Stasio, S. *Sens. Actuators, B* **2004,** *100,* 261–265. doi:10.1016/j.snb.2003.12.045

27. Kim, H.; An, S.; Jin, C.; Lee, C. *Curr. Appl. Phys.* **2012,** *12,* 1125–1130. doi:10.1016/j.cap.2012.02.006

28. Law, M.; Kind, H.; Messer, B.; Kim, F.; Yang, P. *Angew. Chem., Int. Ed.* **2002,** *41,* 2405–2408. doi:10.1002/1521-3773(20020703)41:13<2405::AID-ANIE2405>3.0.CO;2-3

29. Moon, S. E.; Kim, E.-K.; Lee, H.-Y.; Lee, J.-W.; Park, J.; Park, S.-J.; Kwak, J.-H.; Park, K.-H.; Kim, J.; Jo, G.-H.; Lee, T.-H. *J. Korean Phys. Soc.* **2009,** *54,* 830–834. doi:10.3938/jkps.54.830

30. Rahmani, M. B.; Keshmiri, S. H.; Yu, J.; Sadek, A. Z.; Al-Mashat, L.; Moafi, A.; Latham, K.; Li, Y. X.; Wlodarski, W.; Kalantar-zadeh, K. *Sens. Actuators, B* **2010,** *145,* 13–19. doi:10.1016/j.snb.2009.11.007

31. Lee, C.; Jin, C.; Kim, H.; Kim, H. W. *Curr. Appl. Phys.* **2010,** *10,* 1017–1021. doi:10.1016/j.cap.2009.12.032

32. Oh, E.; Choi, H.-Y.; Jung, S.-H.; Cho, S.; Kim, J. C.; Lee, K.-H.; Kang, S.-W.; Kim, J.; Yun, J.-Y.; Jeong, S.-H. *Sens. Actuators, B* **2009,** *141,* 239–243. doi:10.1016/j.snb.2009.06.031

License and Terms

Characterization of 10,12-pentacosadiynoic acid Langmuir–Blodgett monolayers and their use in metal–insulator–metal tunnel devices

Saumya Sharma, Mohamad Khawaja, Manoj K. Ram, D. Yogi Goswami and Elias Stefanakos[*]

Abstract

The characterization of Langmuir–Blodgett thin films of 10,12-pentacosadiynoic acid (PDA) and their use in metal–insulator–metal (MIM) devices were studied. The Langmuir monolayer behavior of the PDA film was studied at the air/water interface using surface tension–area isotherms of polymeric and monomeric PDA. Langmuir–Blodgett (LB, vertical deposition) and Langmuir–Schaefer (LS, horizontal deposition) techniques were used to deposit the PDA film on various substrates (glass, quartz, silicon, and nickel-coated film on glass). The electrochemical, electrical and optical properties of the LB and LS PDA films were studied using cyclic voltammetry, current–voltage characteristics (I–V), and UV–vis and FTIR spectroscopies. Atomic force microscopy measurements were performed in order to analyze the surface morphology and roughness of the films. A MIM tunnel diode was fabricated using a PDA monolayer assembly as the insulating barrier, which was sandwiched between two nickel layers. The precise control of the thickness of the insulating monolayers proved critical for electron tunneling to take place in the MIM structure. The current–voltage characteristics of the MIM diode revealed tunneling behavior in the fabricated Ni–PDA LB film–Ni structures.

Introduction

Electronic device fabrication often requires thin film deposition processes which require precise control of the material thickness while maintaining conformity of the layer deposited on a solid substrates. The Langmuir–Blodgett (LB) deposition technique is particularly useful for the transfer of organized monolayers onto a substrate with a fine control of the deposition

thickness [1-4]. The technique makes use of the amphiphilic nature of molecules dispersed in water (or another subphase) and later transferred onto a substrate. The production of Langmuir–Schaefer (LS) films involves horizontally dipping the substrate into the liquid subphase, whereas in LB deposition, the substrate is perpendicularly lowered into the liquid subphase.

The use of ω-tricosanoic acid-based LB films in metal–insulator–metal (MIM) diodes with a Ag–LB monolayer–Mg structure was studied by Geddes et al [5]. Mochizuki et al. also explored the use of the LB technique in MIM tunnel diodes by deposition of conductive LB films of bis(ethylenedioxy)tetra-thiafulvalene which served as a top electrode [6]. Iwamoto reported on the electrical properties of MIM junctions using polyimide LB films over a range of temperatures [7]. Kaneko et al. reported the use of polydiacetylene thin films in MIM and metal–insulator–semiconductor structures. They measured the thermionic emission through MIM diodes with polydiacetylene LB multilayers [8]. Ram et al. also fabricated MIM structures with polyemeraldine LB films sandwiched between silver and ITO glass plates, which resulted in devices which showed non-linear rectification [9].

In this research, LB films of various fatty acids (with amide or alkyl groups) were used for the fabrication of MIM structures. Initially, a high failure rate was observed with short-circuited MIM devices, which was attributed to pinhole defects or damage to underlying insulating monolayers occurring during the top contact deposition. Pinhole defects can be minimized if individual molecules are bonded together to form a cross-linked structure. The selection of the insulating material is very important: it should be amphiphilic, compatible with the LB technique and polymerizable. Such cross-linking can make the film more compact, thereby reducing the intermolecular distance and making the film more resistant to physical damage during the top contact sputtering. Recently, Langmuir monolayer films of 10,12-pentacosadiynoic acid (PDA) were studied as reported in the literature [8,10,11]. A set of experiments were performed regarding the photo-polymerization of PDA monomers using in situ UV light exposure in the LB trough as well as after deposition of the Langmuir monolayer. This resulted in reduced pinhole defects in the film. In this context, monolayers of PDA were analyzed to check the transfer consistency of PDA onto the substrate for the deposition of LB and LS films. After material and film characterization, these LB layers were characterized for suitability for small signal rectification in MIM tunnel diodes.

The Langmuir monolayer behavior of PDA was studied at the air–water interface to find the ideal surface tension for a close-packed film at the water surface. This was followed by deposi-

tion of the film on silicon, indium tin oxide (ITO) glass, quartz and nickel substrates for optical spectroscopy, cyclic voltammetry and electrical measurements [12-15]. The optical and electrochemical properties of the films were investigated using FTIR and cyclic voltammetric studies, respectively. The electrochemical analysis of PDA has proved useful in understanding the chemical activity, such as the oxidation–reduction reactions, as well as their reversibility. Cyclic voltammetry was performed on PDA films deposited onto ITO-coated glass substrates in order to gain qualitative information about the electrochemical processes or for insight into electron transfer rates and the kinetic and thermodynamic behavior of the PDA. Such an analysis can potentially aid in the identification of suitable applications of such materials [16]. The Ni–PDA film–Ni structure was studied in order to understand the tunneling behavior in MIM structures.

Experimental
Overview of the deposition of PDA, LS films
Langmuir monolayers and LB films: For these experiments, PDA was obtained from Sigma-Aldrich in the form of 10,12-pentacosadiynoic acid (≥97.0%, HPLC grade). A 0.2 mg/mL solution of the surfactant PDA was prepared in chloroform (>99.8%, Sigma-Aldrich). Figure 1 shows the molecular structure and UV-polymerized structure of the PDA molecule. The pH value of the water subphase was found to be 6.8. Surface tension–area isotherms were obtained using the KSV NIMA Langmuir–Blodgett Trough system for samples with varying volume and concentration of PDA dissolved in chloroform. The surface tension was measured using a paper Wilhelmy plate suspended in the water in the LB trough. The deposition conditions were regulated using surface tension and compression feedback control. This resulted in the formation of a closely packed film at the air–water interface accomplished by monitoring the change in surface tension with respect to the position of the barriers in the trough. The surface tension–area isotherm of the Langmuir monolayer changes with the variation in the volume of the water-dispersed PDA solution. The Langmuir monolayer formation is dependent on the concentration of the solution and also on the volume of the solution dispersed on the water surface. Several experiments were performed with varying volumes (6, 7, 8 and 10 mL) of a 0.2 mg/mL PDA solution in order to obtain the best monolayer configuration.

The quality of the monolayer can be determined by monitoring the surface tension and transfer ratio calculated for each dipping experiment. The transfer ratio, which is defined as the ratio between the decrease in the monolayer area at the water surface during the deposition stage and the area of the substrate, was close to 1 for all experiments. After analysis and repetition of the isotherm as shown in Figure 2, a surface tension of
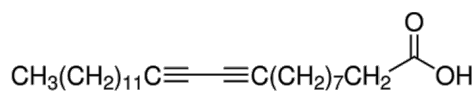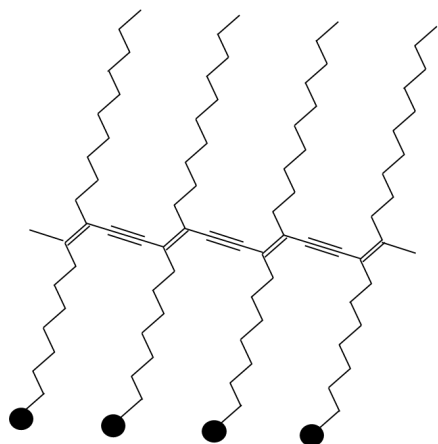
Figure 1: Chemical formula of 10,12-pentacosadiynoic acid is shown in (a). Cross-linking among adjacent monomers is shown in (b).

25 mN/m was selected as the best film configuration for transferring the Langmuir monolayer onto the substrate. The surface tension (and indirectly the film integrity) was efficiently controlled using the KSV NIMA LB Trough controller. For polymerization purposes, the monolayers were exposed to 245 nm UV radiation for 15 min using a UV bench lamp [17].

Optical characterization: A Jasco FTIR 4600 was used to perform IR spectroscopy on the PDA film in transmission mode. IR transparent Si was used as a substrate for the purpose of these measurements.

Electrochemical characterization: The electrochemical investigation was performed in a cell containing three electrodes. An ITO coated glass substrate with LS/LB films of PDA was used as the working electrode, a platinum wire was used as the counter electrode, and Ag/AgCl as the reference electrode in a 0.01 M HCl electrolyte solution. The electrochemical measurements were made using a Voltalab PGZ301 system.

MIM diode: In this experiment, 50 nm of Ni was sputtered onto a silicon wafer with a passivating surface layer of silicon dioxide at a deposition pressure of 3 mTorr. The LB films of 20 and 30 PDA monolayers were deposited onto this Ni-coated
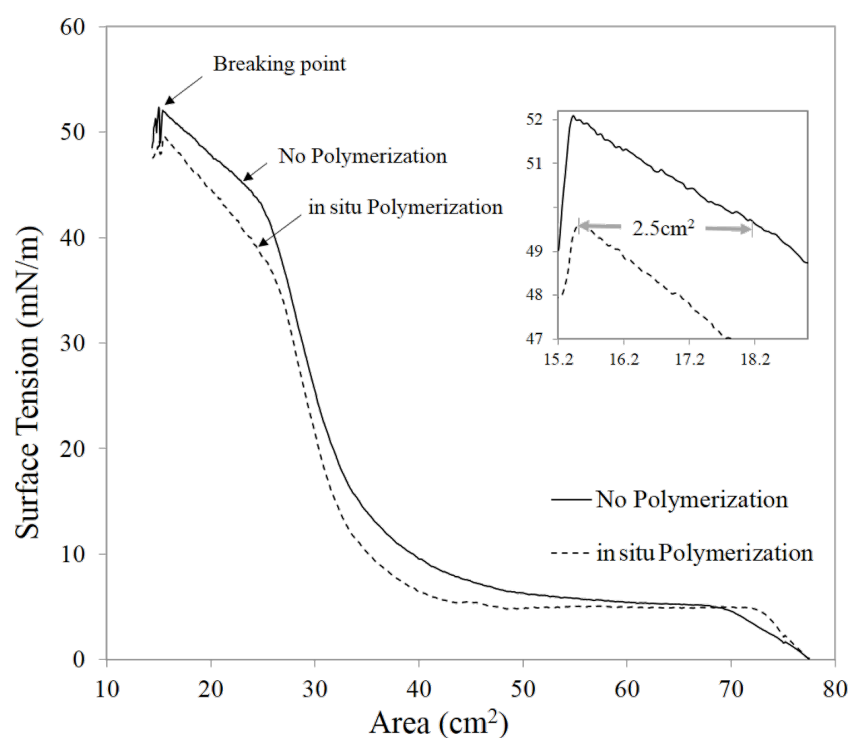
Figure 2: The surface tension–area isotherm of the PDA monolayer with and without in situ polarization in the trough. The inset shows that the in situ polymerization of the PDA film reduces the film surface area by 2.5 cm^2 (making it 15% more compact), which is close to the maximum confinement before the breaking point.

substrate using the LB deposition technique [10,18,19]. The Langmuir monolayer was exposed to 254 nm UV radiation to allow cross-linking of the monomers. A confined Ni top contact was sputtered onto the PDA layers with the aid of a shadow mask. To avoid physical damage to the PDA layers, the RF power during sputtering was kept at only 30 W to sustain enough plasma to allow sputtering of Ni atoms. Current–voltage characteristics of the Ni–PDA–Ni assembly were measured using a micromanipulator setup with Dumet (Cu–Fe) probe tips. The 4145B Semiconductor Parameter Analyzer was used to record the *I–V* measurements.

Results and Discussion

In order to analyze the monolayer configuration at the air–water interface of the Langmuir–Blodgett trough, the change in surface tension with respect to film compression was studied. Figure 2 shows the pressure–area isotherm of the PDA Langmuir monolayer with and without in situ polymerization in the trough at the air–water interface. The UV-exposed Langmuir monolayer shows a more compressed area for the same volume of PDA solution dispersed in water. The compactness of the film after in situ polymerization at the surface of the water was improved by 2.5 cm^2, which is ≈15% of the total surface area of the compressed monolayer. The surface area of the compact film right before the breaking point was recorded as 16.6 cm^2.

Figure 3 shows the infrared spectra of the 20 monolayer PDA sample. The deposition was performed on an infrared-transparent silicon substrate to characterize the material with respect to its absorption peaks. The analysis was carried out on the basis of the difference between the infrared spectra of a UV-irradiated sample compared to that of the PDA without UV exposure. The peak observed at 1700 cm^{-1} in Figure 3 shows the presence of C=O vibration frequencies. The peaks around 2600–2800 cm^{-1} are attributed to C–H stretching vibrations. There were no C=C peaks observed around ≈700 cm^{-1} in films without UV exposure. However, a distinct C=C peak was seen in the 650–750 cm^{-1} range for UV-irradiated samples, as can be seen in the inset in Figure 3 [20,21].

Figure 4 shows the cyclic voltammogram of the 20 monolayer PDA LB film on ITO coated glass substrates at various scan rates (5, 10, 25, 50, 100, 150 mV/s) in a 0.01 M HCl electrolyte. The PDA shows half-redox characteristics in the CV studies suggesting it is a pseudo-redox material. The redox peak of the PDA LB film shows a distinct shift with an increase in the scan rate from 5 to 150 mV/s. This peak can be attributed to the cross-linking of the vinyl group caused by the UV polymerization during the formation of the Langmuir layer (shown in Figure 1). The vinyl group of the PDA-polymerized molecules exhibits redox properties when interacting with the HCl molecules in the electrolyte. However, even though it is difficult to calculate the diffusion coefficient, the voltammogram is indicative of the presence of the polymerized vinyl group in the Langmuir monolayer. The PDA molecule (10,12-pentacosadiynoic acid) has π bonds which make it electrochemically active in addition to carboxylic acid. The electrolyte interacts with the π bond formation resulting in the pseudo-redox behavior recorded around −150 to 50 mV as a function of scan rate. The redox properties are not intrinsic to the film, but rather, they can be
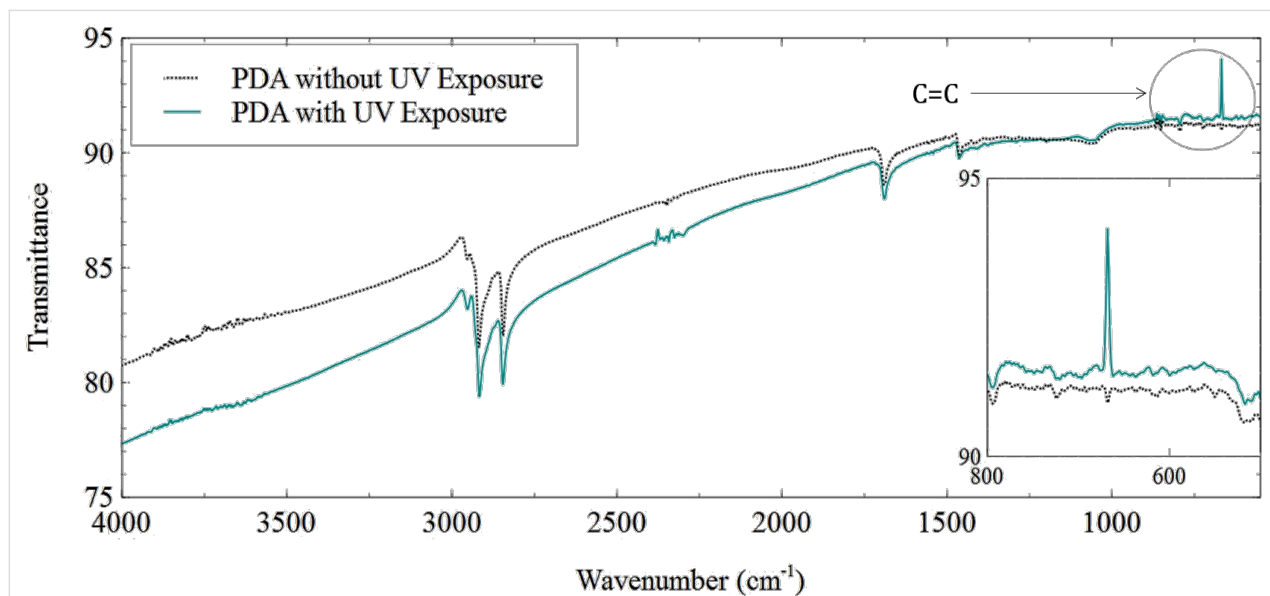
Figure 3: Infrared spectrum of a 20 monolayer PDA sample with and without UV exposure. The inset shows a magnified view of the C=C bending vibrations around 650–750 cm^{-1}.
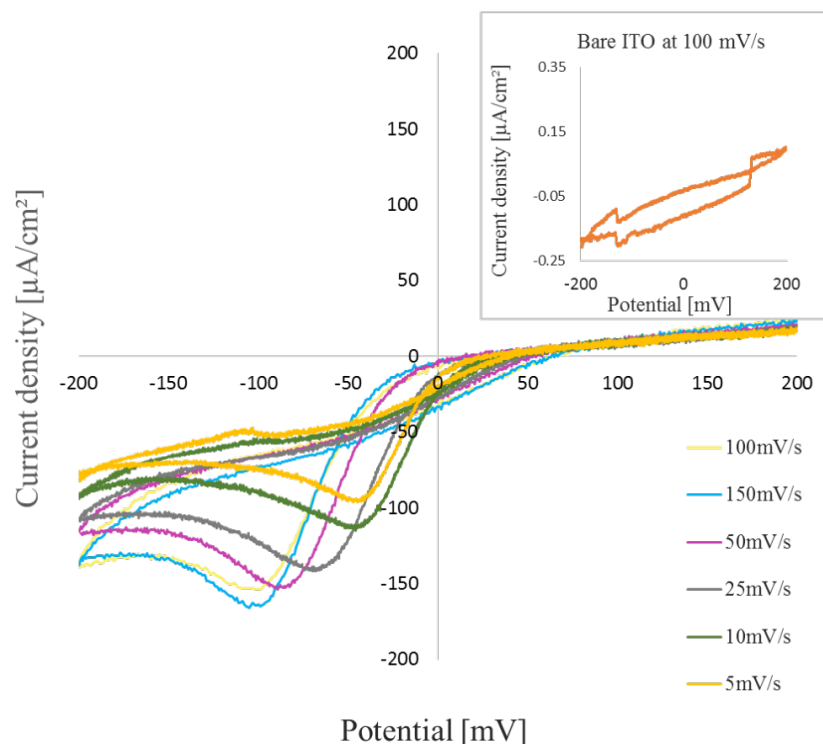
Figure 4: Cyclic voltammetry results with varying scan rates for a 20 monolayer PDA sample in 0.01 M HCl electrolyte. The inset shows the current density vs potential measurements for a bare ITO sample in the same measurement setup.

attributed to the reaction between the film and the electrolyte. However, this data clearly indicates that polymerized PDA has electrochemical redox properties. In spite of the π bond conjugation, which provides high carrier mobility, there is still a very low concentration of carriers, as can be seen by the insulating behavior of the material [22,23].

Figure 5 shows the relation of the current density to the (scan rate)$^{1/2}$, which was clearly not linear, as would be the case for a redox system.

The roughness of the deposited monolayers was analyzed using atomic force microscopy (AFM) as shown in Figure 6. Special Bruker AFM tips (0.01–0.025 Ohm·cm, Sb-doped Si) were utilized to scan the film morphology. An average roughness, R_a, of 34.2 Å was measured for 30 layers of PDA. However, this AFM characterization could only provide information about the surface morphology and not the film thickness. The surface roughness of the underlying nickel film was recorded as 18 ± 1 Å [24].

Discussion of the MIM structure: Initially, due to the extreme thinness of the PDA monolayers, it was difficult to avoid pinholes, and most MIM devices failed for this reason. After
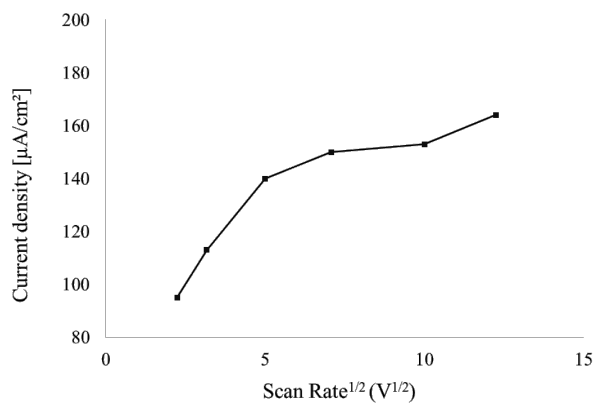
Figure 5: Current density vs voltage scan rate for a 20 monolayer PDA sample on an ITO substrate measured in 0.01 M HCl electrolyte.

polymerization of 30 monolayers of PDA Langmuir–Blodgett films, seven out of eight fabricated diodes failed. Figure 7 shows possible fabrication challenges during the production of insulating LB films for MIM devices. A major fabrication challenge was successfully overcome by reducing the RF power during sputtering to as low as 30 W. Higher RF power settings during sputtering of the top contact can potentially cause physical damage to the thin PDA film assembly, resulting in short-

Figure 6: AFM micrograph of 30 monolayer of PDA deposited using the Langmuir–Blodgett technique showing a surface roughness of 34.2 Å. The roughness of the underlying Ni-coated silicon substrate was 18 Å.
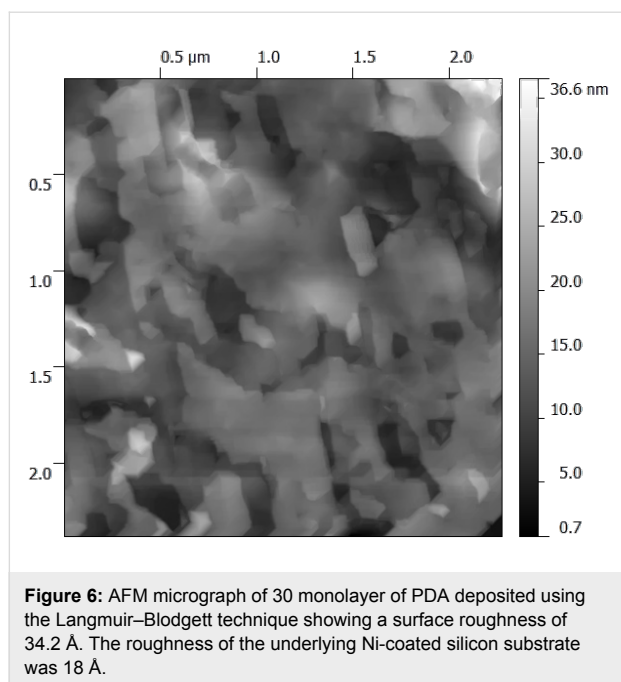
circuited MIM devices. Reduction of the RF power during the Ni top contact sputter runs greatly lowered the rate of failed devices, causing less physical damage and avoiding any significant field effect on the PDA film.

Probing on a delicate thin film device was another challenge. A liquid-metal drop directly on the polymeric film did not allow sufficient repeatability of *I–V* measurements. Such a mercury–polymer contact can cause an accumulation of charge on the surface of the mercury drop, thereby causing a change in

the effective potential at the interface [4]. To avoid this, Ni contact pads were sputtered to allow probe tip positioning outside of the active area of the device without the need for a liquid top contact. After such optimization, the *I–V* characteristics of the Ni–PDA–Ni MIM configuration could be successfully measured using the 4145B Semiconductor Parameter Analyzer and micromanipulator setup to control the probe tips.

The rectification ratio, *RR*, calculated at a bias voltage of 200 mV was as high as ≈110 at ±200 mV. This was calculated as a ratio of currents for an equal voltage deviation around the bias voltage (V_b) as $RR = I_f$ (at V_b +200 mV)/I_r (at V_b −200 mV).

Figure 8 shows the *I–V* characteristics for 20 to 30 monolayers of PDA in a Ni–PDA–Ni tunnel junction configuration, with an earlier turn-on voltage for 20 monolayer of PDA compared to that for 30 monolayer of PDA.

Conclusion

The Langmuir–Blodgett film deposition technique was successfully used to deposit highly conformal and less defect-prone PDA monomolecular layers on a solid substrate. A comparison between a UV cross-linked PDA monolayer and one without UV exposure was carried out with the help of infrared spectroscopy, cyclic voltammogram and AFM imaging. An insulating layer of PDA deposited using this technique was used as the thin, insulating layer in a metal–insulator–metal tunnel junction. The top contact deposition and probing procedures were optimized for MIM diode measurements to reduce damage on the underlying PDA monolayer assembly. UV-induced poly-

Figure 7: A schematic representation of the challenges in MIM device fabrication using LB monolayers. Typical LB monolayer on a Ni substrate (a); physical damage during top contact deposition (b); probe piercing through underlying metal and insulating layers (c); second liquid-metal contact for easier probing (d).
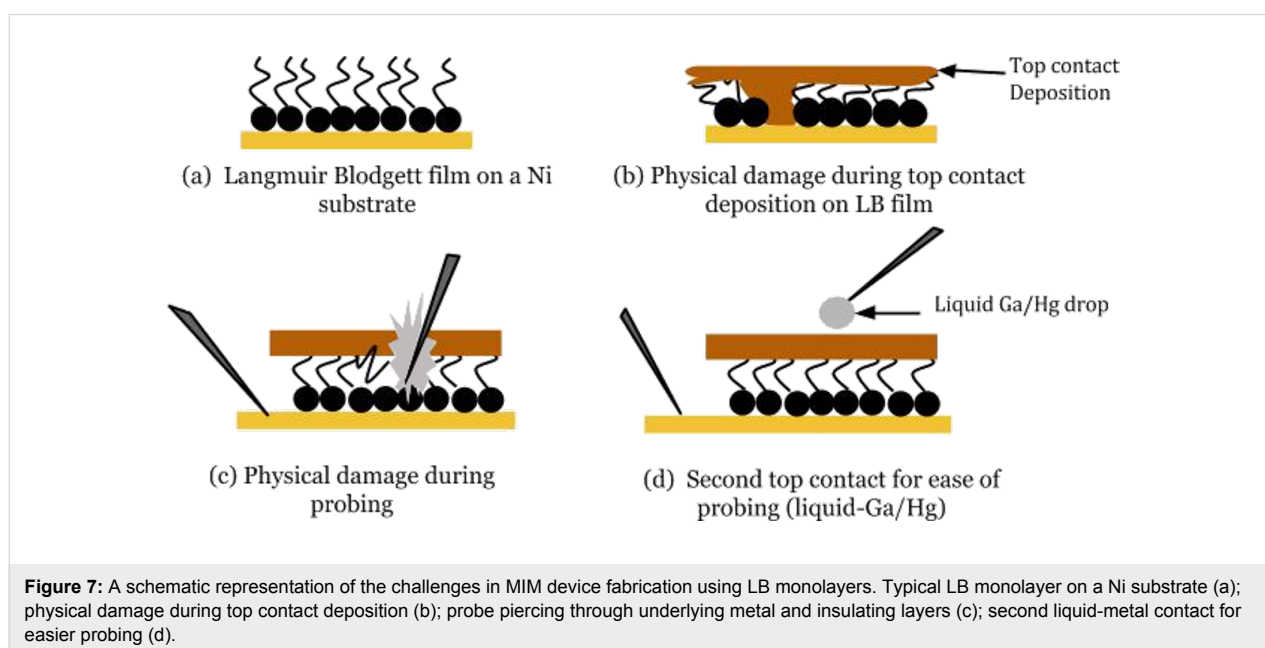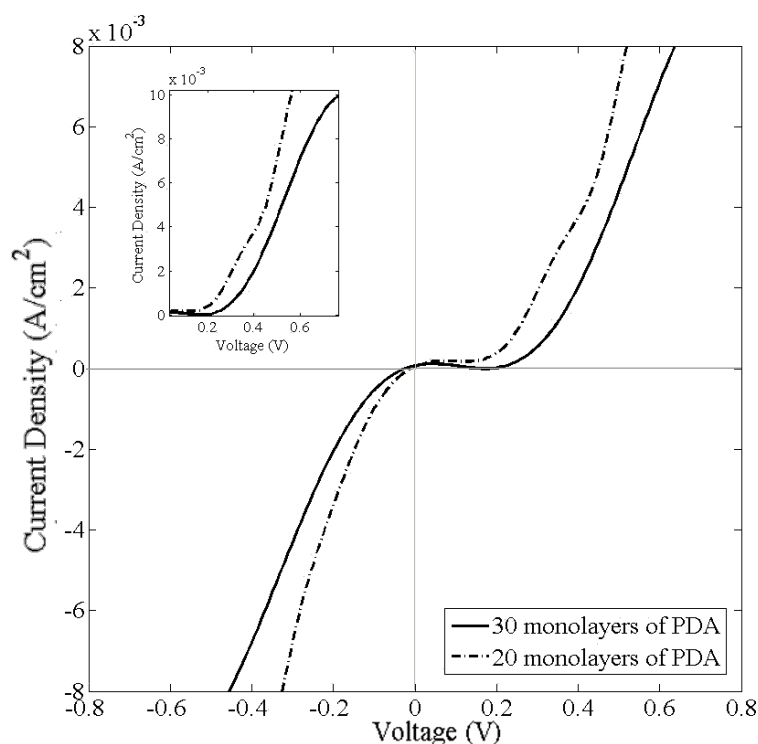
Figure 8: Current density–voltage characteristics for Ni–20 and 30 PDA monolayers–Ni junctions.

merization of PDA introduced intermolecular cross-linking in this layer. A confined Ni top contact was sputtered through a shadow mask at low RF power over the underlying Langmuir–Blodgett film assembly and the *I–V* characteristics of the MIM diode were successfully measured. A rectification ratio of ≈110 at ±200 mV was obtained for a bias voltage of 200 mV.

References

1. Roberts, G. *Langmuir-Blodgett Films;* Springer US: 1990.

2. Decher, G. *Langmuir-Blodgett Films: An Introduction;* Cambridge University Press: Cambridge, UK, 1996.

3. Ulman, A. *An Introduction to Ultrathin Organic Films: From Langmuir-Blodgett to Self-Assembly;* Academic Press, 1991.

4. Hussain, S. A.; Deb, S.; Bhattacharjee, D. *J. Sc. Dev. Env. Res.* **2005,** *4,* 25–33.

5. Geddes, N. J.; Parker, W. G.; Sambles, J. R.; Couch, N. R. Electrical Characterisation of Thin Insulating Langmuir Blodgett Films Incorporated in Metal-Insulator-Metal Structures. In *Physics, Fabrication, and Applications of Multilayered Structures;* Dhez, P.; Weisbuch, C., Eds.; Springer US, 1988; pp 377 ff. doi:10.1007/978-1-4757-0091-6_44

6. Mochizuki, K.; Ohnuki, H.; Ikegami, K.; Imakubo, T.; Izumi, M. *Phys. Procedia* **2011,** *14,* 134–138. doi:10.1016/j.phpro.2011.05.026

7. Iwamoto, M. *IEEE Trans. Electr. Insul.* **1990,** *25,* 541–548. doi:10.1109/14.55729

8. Kaneko, F.; Shibata, M.; Inaba, Y.; Kobayashi, S. *Thin Solid Films* **1989,** *179,* 121–127. doi:10.1016/0040-6090(89)90173-9

9. Ram, M. K.; Gowri, R.; Malhotra, B. D. *J. Appl. Polym. Sci.* **1997,** *63,* 141–145. doi:10.1002/(SICI)1097-4628(19970110)63:2<141::AID-APP1>3.0.CO;2-V

10. Leger, A.; Klein, J.; Belin, M.; Defourneau, D. *Thin Solid Films* **1971,** *8,* R51–R54. doi:10.1016/0040-6090(71)90089-7

11. McHale, G.; Newton, M. I.; Neal, D. B. *Vacuum* **1994,** *45,* 897–900. doi:10.1016/0042-207X(94)90130-9

12. Cemel, A.; Fort, T., Jr..; Lando, J. B. *J. Polym. Sci., Part A-1: Polym. Chem.* **1972,** *10,* 2061–2083. doi:10.1002/pol.1972.150100716

13. Fukuda, K.; Shibasaki, Y.; Nakahara, H. *Thin Solid Films* **1988,** *160,* 43–52. doi:10.1016/0040-6090(88)90045-4

14. Blumstein, A.; Billmeyer, F. W. *J. Polym. Sci., Part A-2: Polym. Phys.* **1966,** *4,* 465–474. doi:10.1002/pol.1966.160040315

15. Ogawa, K. *J. Phys. Chem.* **1989,** 5305–5310. doi:10.1021/j100350a052

16. Diao, P.; Jiang, D.; Cui, X.; Gu, D.; Tong, R.; Zhong, B. *J. Electroanal. Chem.* **1999,** *464,* 61–67. doi:10.1016/S0022-0728(98)00470-7

17. Ogawa, K. *Polym. Int.* **1992,** *28,* 25–33. doi:10.1002/pi.4990280106

18. Yoo, S.-Y.; Jung, S.-B.; Park, J. C.; Kwon, Y.-S. In *Proceedings of the IEEE International Conference on Properties and Applications of Dielectric Materials,* Seoul, Korea, May 25–30, 1997; pp 685–688. doi:10.1109/ICPADM.1997.616528

19. Kaneko, F.; Shibata, M.; Kobayashi, S. Electrical properties of MIS diodes with insulating Langmuir-Blodgett thin films. In *Conference on Electrical Insulation and Dielectric Phenomena, 1988. Annual Report,* Ottawa, Ontario, Oct 16–20, 1988; IEEE; pp 220–226. doi:10.1109/CEIDP.1988.26336

20. Mino, N.; Tamura, H.; Ogawa, K. *Langmuir* **1992,** *8,* 594–598. doi:10.1021/la00038a047

21. Saito, A.; Urai, Y.; Itoh, K. *Langmuir* **1996,** *12,* 3938–3944. doi:10.1021/la951503z

22. Kew, S. J.; Hall, E. A. H. *Analyst* **2007,** *132,* 801–810. doi:10.1039/b704921h

23. Riande, E.; Diaz-Calleja, R. *Electrical Properties of Polymers;* CRC Press: New York, 2004. doi:10.1201/9781420030471

24. Meyer, E.; Howald, L.; Overney, R. M.; Heinzelmann, H.; Frommer, J.; Güntherodt, H.-J.; Wagner, T.; Schier, H.; Roth, S. *Nature* **1991,** *349,* 398–400. doi:10.1038/349398a0

License and Terms

Gas sensing properties of nanocrystalline diamond at room temperature

Marina Davydova[*1], Pavel Kulha[2], Alexandr Laposa[2], Karel Hruska[1], Pavel Demo[1] and Alexander Kromka[1]

Abstract

This study describes an integrated NH_3 sensor based on a hydrogenated nanocrystalline diamond (NCD)-sensitive layer coated on an interdigitated electrode structure. The gas sensing properties of the sensor structure were examined using a reducing gas (NH_3) at room temperature and were found to be dependent on the electrode arrangement. A pronounced response of the sensor, which was comprised of dense electrode arrays (of 50 μm separation distance), was observed. The sensor functionality was explained by the surface transfer doping effect. Moreover, the three-dimensional model of the current density distribution of the hydrogenated NCD describes the transient flow of electrons between interdigitated electrodes and the hydrogenated NCD surface, that is, the formation of a closed current loop.

Introduction

Air pollution is one of the main environmental-health related threats. Increasing amounts of noxious pollutants are emitted into the atmosphere, resulting in damage to human health and the environment. There is great interest in using sensing devices to improve the environmental and safety regulations of toxic gases in particular within buildings, underground structures, and airports.

Semiconducting solid-state gas sensors can be considered as the most promising, portable, miniaturized gas sensors because of their minimal power requirements. However, most of these sensors show poor selectivity, and the main drawbacks are slow sensor response times and recovery speeds. Even if the response time for the detection of reactive gases is rapid (e.g., within the range of seconds), in many cases, the recovery times at room

temperature can be from several hours up to several days. Only thermal annealing of the sensor reduces the sensor recovery speed [1,2].

Recently, much attention has been given to solid-state integrating-type (i.e., accumulating- or dosimeter-type) gas sensing devices, which are able to overcome the aforementioned drawbacks [3-7]. To date, various publications have focused on conductometric integrating gas sensors, which are able to avoid several problems of conventional gas sensors. Nevertheless, the proper choice of the sensing material plays an essential role [3,4].

Diamond is a promising sensor material and can be deposited on the existing sensor elements. Undoped diamond is an extremely good insulator and upon the formation of a covalent bond with hydrogen, exhibits semiconducting properties [8]. This conductivity arises from free positive charge carriers (holes) in the sub-surface region and is highly sensitive to surrounding gases and/or liquids. Our previous works have shown that interdigitated electrodes (IDEs) capped with nanostructured, hydrogen-terminated, nanocrystalline diamond (NCD) were very sensitive and selective, especially towards phosgene gas [9,10]. In addition, we observed that the sensor sensitivity was strongly dependent on the total surface area.

In this study, we demonstrate a gas sensor based on hydrogen (H)-terminated NCD with an integrating measurement principle. The influence of the surface area (adjusted by nucleation time) and the electrode arrangement on the sensitivity of the NCD sensor is discussed. Finally, a simulation of the distribution of the current density of H-terminated NCD is presented.

Results and Discussion
Hot plasma microwave PECVD system

Microwave plasma chemical vapor deposition is a well-established process for the fast growth of high quality diamond. In the present study, the hot plasma system with an ellipsoidal, cavity-like reactor was used to grow diamond films under the following conditions: sample temperature, 450 °C; power, 1 kW; gas pressure, 30 mbar; hydrogen and methane flow rates, 300 and 3 sccm (i.e., 1% dilution), respectively; and deposition time, 5 h.

Figure 1a shows the SEM image of the surface morphology of the sensor substrate (Si/SiO_2 + IDEs with a separation of 200 µm) coated with the NCD layer using a 40 min nucleation time. This top view depicts the presence of an amorphous carbon shell at the diamond grains (film) and a visible development of diamond nanocrystal faceting. Moreover, the NCD primarily grew on the IDEs as was previously found [9].

The gas-sensing properties of the hydrogenated NCD sensor with a sparse electrode arrangement of 200 µm were tested against a sequence of NH_3 pulses (Figure 1b).

These results demonstrated that the hydrogenated diamond sensor exhibited a clear response to each sequence of NH_3, and this behavior indicated that the H-terminated NCD sensor demonstrated an integrator-type gas response.

Figure 2a shows an SEM image of the surface morphology of the sensor substrate (Si/SiO_2 + IDEs with a separation of 50 µm) coated with the NCD layer after 40 min of nucleation time. The coating exhibited a continuous diamond layer with diamond grains up to 80 nm in size.
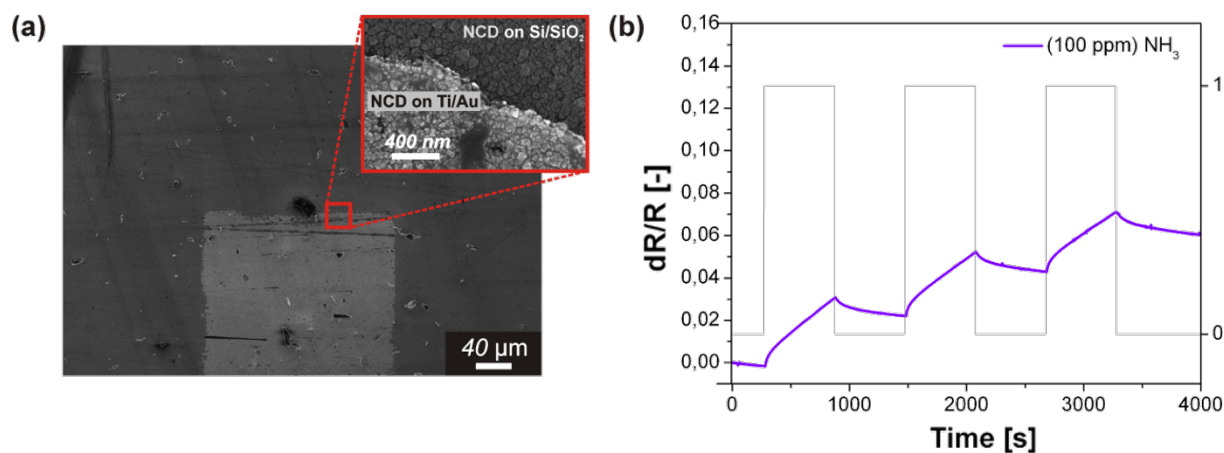
Figure 1: (a) SEM surface morphology of an NCD-coated sensor substrate with IDEs with separation of 200 µm and a nucleation time of 40 min, and (b) corresponding plot of the sensor response vs time.
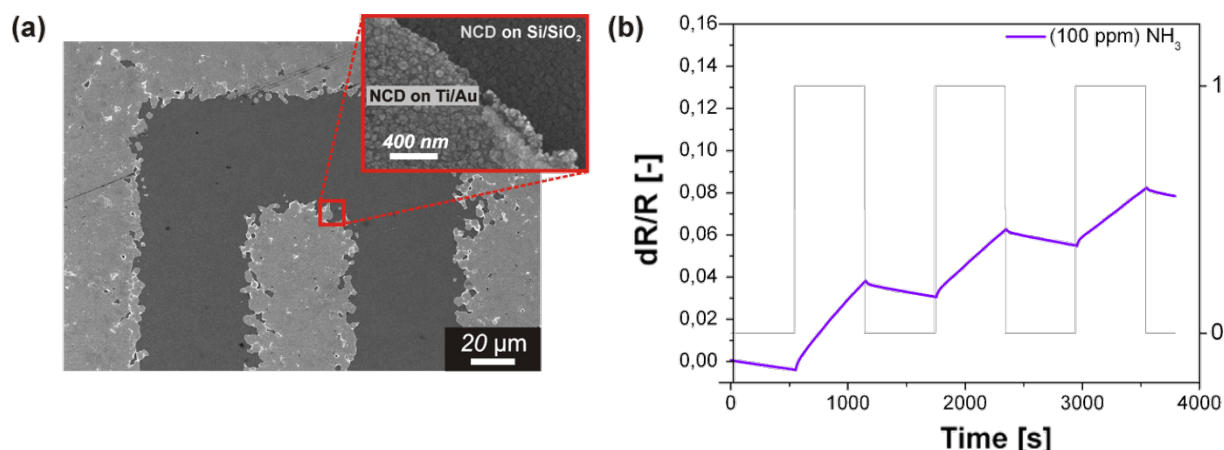
Figure 2: (a) SEM surface morphology of an NCD-coated sensor substrate with IDEs with separation of 50 μm and a nucleation time of 40 min, and (b) corresponding plot of the sensor response vs time.

The gas-sensing properties of the hydrogenated NCD sensor with a dense electrode arrangement of 50 μm was also tested against a sequence of NH_3 pulses (Figure 2b). It is evident that after being exposed to NH_3 at room temperature, the sensor response is slightly higher than that of the sensor with sparse electrode arrays (i.e., 200 μm; Figure 1b).

Figure 3a shows an SEM image of a sample that was nucleated for 2 min. A homogenous and continuous NCD film is observed. Figure 3b shows the plot of the sensor response as a function of time for a pulsed sequence of 100 ppm NH_3. The sensor displayed a significantly more rapid sensor response compared with the previous sensor (Figure 2b) for the same NH_3 exposure. Again, clear evidence of the integrator property was observed.

Overall, the hydrogenated diamond sensors exhibited a response to each sequence of NH_3. These behaviors indicated that the H-terminated NCD sensors were able to accumulate NH_3 gas in its water adsorbate layer, which confirms the integrator-type gas sensor property. Moreover, the NCD sensor with the most dense electrode arrangement of 50 μm and a nucleation time of 2 min (Figure 3) exhibited the highest response toward NH_3 gas. A similar behavior was observed by Beer et al., wherein the resistance at room temperature decreased or increased due to the electrolytic dissociation of the gases in the H-terminated diamond layer [3].

Cold plasma microwave PECVD system

In the following experiments, the fully-integrated sensor device on a micro-hotplate was used. In contrast to hot plasma, where
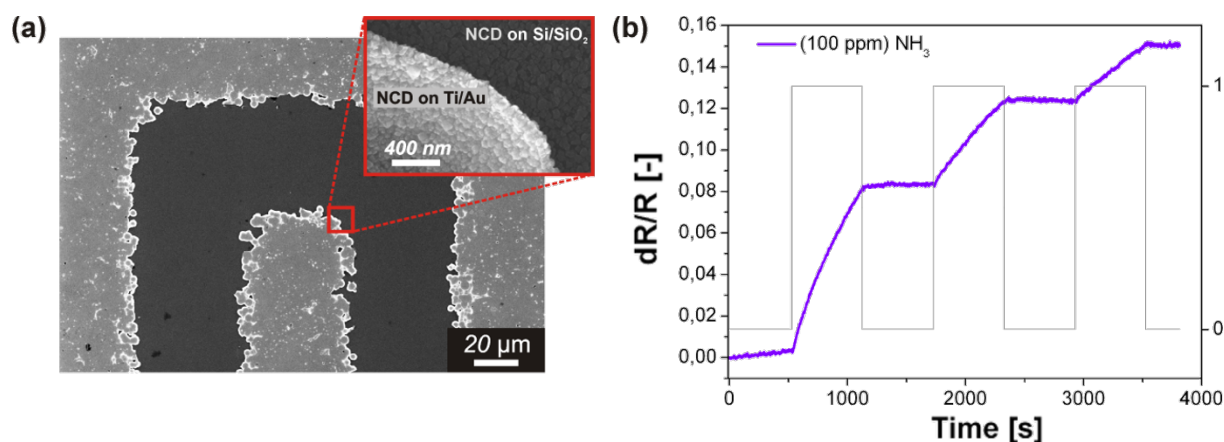
Figure 3: (a) SEM surface morphology of an NCD-coated sensor substrate with IDEs with separation of 50 μm and a nucleation time of 2 min, and (b) corresponding plot of the sensor response vs time.

the plasma is localized close to the substrate surface (i.e., a distance of 1–2 mm), which may cause the substrate to overheat, a linear antenna, microwave plasma, CVD system (i.e., cold plasma) was used to avoid this drawback. The main advantage of a cold plasma system is the minimization of overheating of the substrate surface due to the longer distance between the substrate and the linear antenna (i.e., 7–10 cm) [11]. An NCD film was grown from hydrogen-rich gas mixtures of methane and carbon dioxide. A microwave pulse of 2 kW was used for each antenna side. A total gas pressure of 0.1 mbar was used and the substrate temperature was kept at 450 °C. Figure 4 shows the surface morphologies of fully-integrated sensor substrates coated with hydrogenated NCD films. Unfortunately, the SEM images also show that for the different nucleation times of 1 and 5 min, almost no differences were observed between the diamond morphologies. Both sensor substrates demonstrated a relatively smooth and continuous diamond film consisting of ultra-small grains (i.e., <50 nm).

Figure 5 presents the room temperature response of fully-integrated sensor substrates (with 15 μm separation between IDEs) covered with H-terminated NCD with 1 and 5 min diamond nucleation times.

As illustrated in Figure 5, exposure of the sensor elements to 100 ppm of ammonia gas led to increased impedances from 4.4 to 5.4 MΩ and from 3.9 to 5.4 MΩ for the samples nucleated for 1 min and 5 min, respectively. It should be noted that a variation (shift) in the starting impedance value was observed. The starting impedance varied by nearly an order of magnitude in some cases. The origin for this difference can be attributed to several factors, for example, low quality ohmic contacts or memory effects of the surface state of NCD. It was concluded that technological optimization is still required for achieving better reproducibility and device reliability.
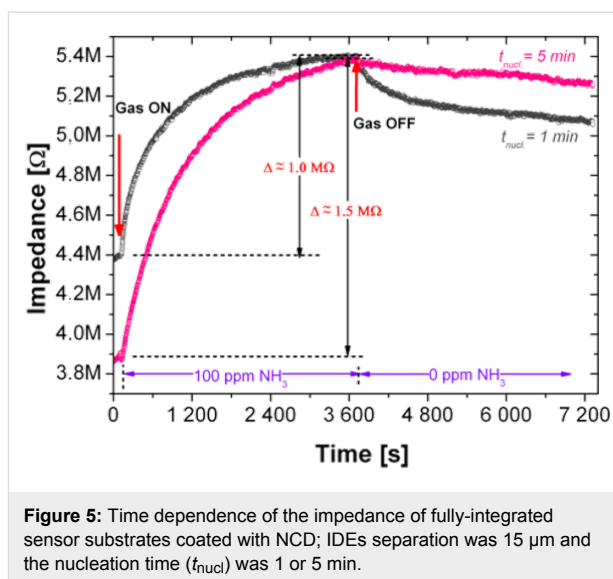
Figure 5: Time dependence of the impedance of fully-integrated sensor substrates coated with NCD; IDEs separation was 15 μm and the nucleation time (t_{nucl}) was 1 or 5 min.

The Raman spectrum of the structures (Figure 6) is characterized by two strong contributions: the peak characteristic for diamond centered at 1330 cm^{-1} (D-peak) and the broad band at approximately 1590 cm^{-1} attributed to the non-diamond phase (G-peak or sp^2-bonded carbon atoms) [12].

To determine the distribution of the electric field and the current density in the vicinity of the IDEs, a three-dimensional (3D) model was simulated. The results are shown in Figure 7.

The simulation of the current flow of the hydrogenated NCD was performed using the electrical solver MemPZR in the software package (Coventor, Raleigh, NC, USA). The insulating SiO$_2$ substrate with Au IDEs (of 100 nm thickness) was covered by intrinsic diamond (i-diamond) at a thickness of 300 nm. The hydrogenated surface was modeled as an additional layer on top of the i-diamond at a thickness of 5 nm [8].
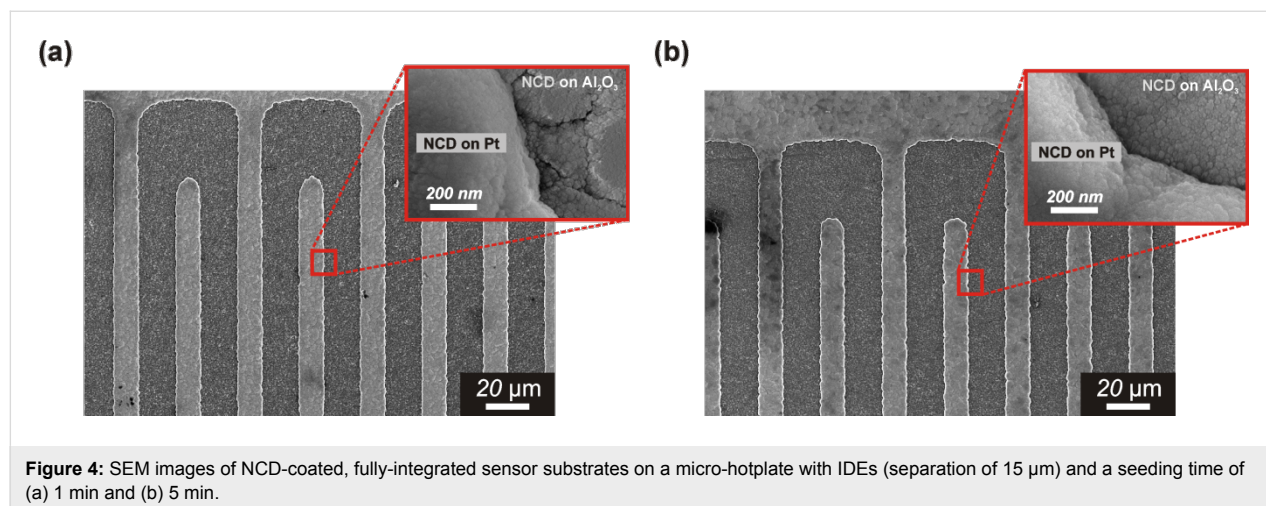
Figure 4: SEM images of NCD-coated, fully-integrated sensor substrates on a micro-hotplate with IDEs (separation of 15 μm) and a seeding time of (a) 1 min and (b) 5 min.

Figure 6: Raman spectrum of the NCD film. The sharp peak at 1330 cm^{-1} provides evidence of the diamond character of the deposited films.
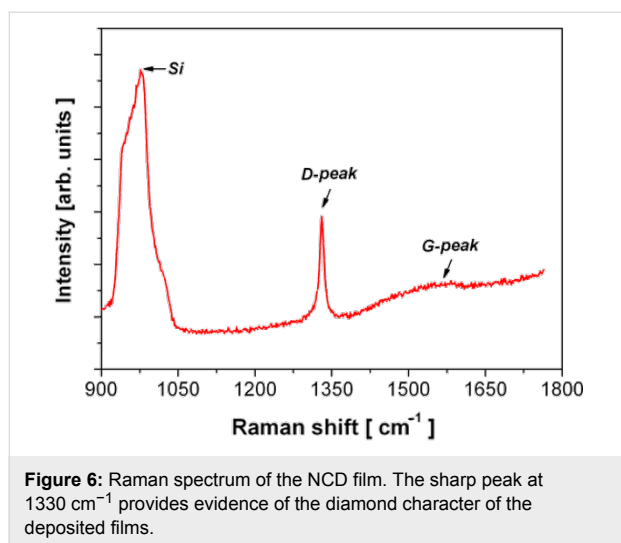
The model was discretized by a hexahedron parabolic mesh with over 19,000 elements. The interdigitated electrode arrangement was simplified to a single pair and the voltage boundary conditions were applied to the opposite sides of the metal electrodes/stripes (high voltage = 1 V, low voltage = 0 V). As demonstrated by the current density vectors in Figure 7, the simulation showed that current flowed from a high potential through the i-diamond to the H-diamond layer and then returned to the low potential. The maximum current density occurred on the surface area localized between the two conductive electrodes (Figure 7, cross-sectional view).

Moreover, the impedance measurements showed that the gap between the interdigitated electrodes is one of the most important geometric parameters of the sensor and should carefully be considered when enhancing the sensing response (Figure 3 and

Figure 5) [13]. Furthermore, clear evidence of the integrator property of H-terminated NCD sensors was also demonstrated by the staircase-like increase of the sensor resistance (sensor response).

In our previous work, the morphology (porosity) of the diamond film was adjusted via seeding and/or growth time [9]. In the present work, a similar procedure was employed to achieve different diamond morphologies (Figure 8). However, the present results significantly differ from a recent study. The deposited nanocrystalline diamond layers formed under various nucleation times (i.e., 1, 2, 5 and 40 min) were found to be similar at a microscopic resolution. This could be due to the use of high concentration, water-based, diamond powder suspensions. Even when a short nucleation time of 1 min was used, a continuous diamond layer was formed (Figure 4a). This variation is a sign that the nucleation process is not well-controlled enough to reliably grow films of various porosities. However, the impedance measurements indicated a higher sensitivity for the sample nucleated using a short nucleation time of 2 min (Figure 3 b). Additionally, the AFM measurements have shown

Figure 8: Schematic drawing of the sensor assemblies with diamond coatings: (a) continuous NCD film on IDEs with 200 μm electrode separation, (b) continuous NCD film on IDEs with 50 μm electrode separation, and (c) porous-like NCD film on IDEs with 50 μm electrode separation.

Figure 7: Current density profile for a single pair of IDEs covered by intrinsic diamond with a hydrogenated surface.

that at the nanoscale, the obtained diamond surface area was larger and was not well-resolvable by SEM measurements. The surface areas of the NCD films according to the samples presented in Figures 1, 2, and 3 were 1.20, 1.23, and 1.31 μm^2, respectively.

The origin of the variation in the surface conductivity on the gas type has been the subject of a number of studies [14-16]. Overall, when oxidizing or reducing gases appear in the atmosphere, the charge exchange between the diamond and the adsorbed molecules causes an increase or a decrease in the conductance. The mechanism of this variation is broadly interpreted by the established surface transfer doping mechanism of the H-terminated diamond [17,18]. First, by exposing the H-terminated diamond surface to ambient air, a thin layer of adsorbed water is formed at the H-terminated surface. Based on the surface transfer doping model, Helwig et al. explained the sensitivity of the H-terminated NCD to NO_2 and NH_3 gases [1]. In their setup, the IDE electrodes were deposited on the top of the monocrystalline diamond. A high concentration of H_3O^+ ions was observed after exposure of the H-terminated diamond surface to NO_2 gas because the electrons were transferred from the diamond sub-surface to the H_3O^+ species. Similarly, the increased surface conductivity of hydrogenated NCD upon exposure to phosgene gas was examined in one of our previous studies [2]. However, the exposure to NH_3 gas led to a considerably lower density of H_3O^+ ions, which subsequently led to a decreased surface conductivity. Our results are in agreement with these observations. Additionally, in our case, the IDE electrodes were built into the diamond film, and the simulation confirmed that a closed current loop was formed between the IDEs and the H-terminated NCD surface.

Conclusion

A nanocrystalline diamond film consisting of grains as small as 80 nm was used as the functional layer of a semiconductor gas sensor. Metallic electrodes were buried beneath the diamond film. This design protected them from harmful substances and the current flow localized at the grain boundaries. In this specific case, the H-terminated, diamond gas sensors behaved with an integrator-type gas response, that is, the sensor output signal was proportional to the integrated gas flow interacting with the diamond surface. The integrating properties were verified by cyclic measurements. The sensing characteristics of the H-terminated diamond layer towards NH_3 gas were found to be dependent on the electrode arrangement (i.e., width gap). The sensor with a gap width of 50 μm exhibited a response twice as high as that of a sensor with an IDE separation of 200 μm. Moreover, the 3D model of the current density distribution of the hydrogenated NCD indicated the formation of a closed current loop, that is, the transient flow of electrons between the

IDEs and the H-terminated diamond surface created a circular motion of the charge carriers. Additionally, the technological compatibility of the linear antenna plasma with a standard device confirmed that the functional NCD film can be deposited on its substrate without requiring other fabrication steps (e.g., lithography, masking, etc.). These results are promising for practical application in which small and simple H-NCD sensors can be used as gas sensors at room temperature.

Experimental

A schematic view of the sensor assembly is shown in Figure 8. Two different sensor designs were used with a variety of metal interdigitated electrodes. The first sensor was fabricated in-house by standard UV lithography, thermal evaporation and lift-off techniques. For each pattern, six IDE electrodes were prepared with a separation of 50 or 200 μm. The second sensor was a commercially available product and consisted of a built-in micro-heater, a platinum temperature sensor, and a pair of interdigitated electrodes of 15 μm width.

Based on our previous study where the morphology (i.e., the porosity) of a diamond film was controlled via the seeding and/or growth time [9], a similar procedure was used in this present study to achieve different diamond morphologies (Figure 8). The sensor layer was based on the sandwich structure of the intrinsic H-terminated NCD layer/metal IDE/insulating substrate. The NCD growth proceeded in two steps: first, seeding for 1, 2, 5 or 40 min, followed by treatment by with microwave plasma-enhanced chemical vapor deposition (PECVD). The diamond layers were grown either by focused microwave PECVD (Aixtron P6, named as "hot plasma") or pulsed-linear antenna microwave PECVD (Roth&Rau AK 400, named as "cold plasma") [11,19,20]. Next, the samples were exposed to a pure hydrogen plasma for 5 min in order to generate a p-type surface conductivity [8,16] and then cooled down to room temperature. The resulting morphology of each structured NCD film was characterized by scanning electron microscopy (SEM, Raith *e_*LiNE). The diamond character of the sensor element was confirmed by Raman spectroscopy (Renishaw, In Via Reflex Raman spectrometer, 442 nm excitation wavelength).

For both sensor designs, the impedance measurements were realized at a voltage of 1 V and a frequency of 3 kHz (LCR—HIOKI 3532-50). A custom LabView program was used which allowed the temperature and gas-flow rate to be automatically controlled by a computer. Prior to the conductivity measurements, the sample was mounted in a gas-flow apparatus, and the chamber was flushed with dry nitrogen gas (N_2) for 15 min to stabilize the output characteristics. Subsequently, the specific testing gas (NH_3) was injected into the chamber through the inlet port, and the change in the resistance

of the sensors (dR/R) was investigated as a function of exposure time. Ammonia (NH_3, quality N38, purity 99.98%) was diluted with nitrogen (N_2, quality N50, purity 99.999%) by mixing to the desired concentration. The sensor response was defined as a relative change in the resistance $dR = R - R_o$ upon exposure to a specific gas (NH_3) with respect to the resistance R_o (i.e., a change in the resistance dR/R) in the reference gas (N_2).

Supporting Information

Supporting Information File 1

Additional AFM and XRD experimental results.
[http://www.beilstein-journals.org/bjnano/content/supplementary/2190-4286-5-243-S1.pdf]

Acknowledgements

References

1. Helwig, A.; Müller, G.; Sberveglieri, G.; Eickhoff, M. *J. Sens.* **2009**, *2009,* No. 620720. doi:10.1155/2009/620720
2. Davydova, M.; Stuchlik, M.; Rezek, B.; Larsson, K.; Kromka, A. *Sens. Actuators, B* **2013**, *188,* 675–680. doi:10.1016/j.snb.2013.07.079
3. Beer, S.; Helwig, A.; Müller, G.; Garrido, J.; Stutzmann, M. *Sens. Actuators, B* **2013**, *181,* 894–903. doi:10.1016/j.snb.2013.02.072
4. Groß, A.; Beulertz, G.; Marr, I.; Kubinski, D. J.; Visser, J. H.; Moos, R. *Sensors* **2012**, *12,* 2831–2850. doi:10.3390/s120302831
5. Marr, I.; Groß, A.; Moos, R. *J. Sens. Sens. Syst.* **2014**, *3,* 29–46. doi:10.5194/jsss-3-29-2014
6. Roadman, M. J.; Scudlark, J.; Meisinger, J. J.; Ullman, W. J. *Atmos. Environ.* **2003**, *37,* 2317–2325. doi:10.1016/S1352-2310(03)00163-8
7. Geupel, A.; Schönauer, D.; Röder-Roith, U.; Kubinski, D. J.; Mulla, S.; Ballinger, T. H.; Chen, H.-Y.; Visser, J. H.; Moos, R. *Sens. Actuators, B* **2010**, *145,* 756–761. doi:10.1016/j.snb.2010.01.036
8. Hayashi, K.; Yamanaka, S.; Watanabe, H.; Sekiguchi, T.; Okushi, H.; Kajimura, K. *J. Appl. Phys.* **1997**, *81,* 744–753. doi:10.1063/1.364299
9. Kromka, A.; Davydova, M.; Rezek, B.; Vanecek, M.; Stuchlik, M.; Exnar, P.; Kalbac, M. *Diamond Relat. Mater.* **2010**, *19,* 196–200. doi:10.1016/j.diamond.2009.10.006
10. Davydova, M.; Stuchlik, M.; Rezek, B.; Kromka, A. *Vacuum* **2012**, *86,* 599–602. doi:10.1016/j.vacuum.2011.07.025
11. Kromka, A.; Babchenko, O.; Izak, T.; Hruska, K.; Rezek, B. *Vacuum* **2012**, *86,* 776–779. doi:10.1016/j.vacuum.2011.07.008
12. Pop-Georgievski, O.; Neykova, N.; Proks, V.; Houdkova, J.; Ukraintsev, E.; Zemek, J.; Kromka, A.; Rypáček, F. *Thin Solid Films* **2013**, *543,* 180–186. doi:10.1016/j.tsf.2012.11.128
13. Singh, K. V.; Bhura, D. K.; Nandamuri, G.; Whited, A. M.; Evans, D.; King, J.; Solanki, R. *Langmuir* **2011**, *27,* 13931–13939. doi:10.1021/la202546a
14. Helwig, A.; Müller, G.; Garrido, J. A.; Eickhoff, M. *Sens. Actuators, B* **2008**, *133,* 156–165. doi:10.1016/j.snb.2008.02.007
15. Ri, Gi, S.; Tashiro, K.; Tanaka, S.; Fujisawa, T.; Kimura, H.; Kurosu, T.; Iida, M. *Jpn. J. Appl. Phys.* **1999**, *38,* 3492. doi:10.1143/JJAP.38.3492
16. Wang, Q.; Qu, S. L.; Fu, S. Y.; Liu, W. J.; Li, J. J.; Gu, C. Z. *J. Appl. Phys.* **2007**, *102,* 103714. doi:10.1063/1.2817465
17. Maier, F.; Riedel, M.; Mantel, B.; Ristein, J.; Ley, L. *Phys. Rev. Lett.* **2000**, *85,* 3472–3475. doi:10.1103/PhysRevLett.85.3472
18. Chakrapani, V.; Angus, J. C.; Anderson, A. B.; Wolter, S. D.; Stoner, B. R.; Sumanasekera, G. U. *Science* **2007**, *318,* 1424–1430. doi:10.1126/science.1148841
19. Izak, T.; Sveshnikov, A.; Demo, P.; Kromka, A. *Phys. Status Solidi B* **2013**, *250,* 2753–2758. doi:10.1002/pssb.201300117
20. Neykova, N.; Kozak, H.; Ledinsky, M.; Kromka, A. *Vacuum* **2012**, *86,* 603–607. doi:10.1016/j.vacuum.2011.07.055

License and Terms

Low-cost plasmonic solar cells prepared by chemical spray pyrolysis

Erki Kärber[*1], Atanas Katerski[1], Ilona Oja Acik[1], Valdek Mikli[2], Arvo Mere[1], Ilmo Sildos[3] and Malle Krunks[1]

Abstract

Solar cells consisting of an extremely thin $In_2S_3/CuInS_2$ buffer/absorber layer uniformly covering planar ZnO were prepared entirely by chemical spray pyrolysis. Au nanoparticles (Au-NPs) were formed via thermal decomposition of a gold(III) chloride trihydrate ($HAuCl_4 \cdot 3H_2O$) precursor by spraying 2 mmol/L of the aqueous precursor solution onto a substrate held at 260 °C. Current–voltage scans and external quantum efficiency spectra were used to evaluate the solar cell performance. This work investigates the effect of the location of the Au-NP layer deposition (front side vs rear side) in the solar cell and the effect of varying the volume (2.5–10 mL) of the sprayed Au precursor solution. A 63% increase (from 4.6 to 7.5 mA/cm^2) of the short-circuit current density was observed when 2.5 mL of the precursor solution was deposited onto the rear side of the solar cell.

Introduction

The cost of solar cells scales with the complexity of the technology involved as well as the price and volume of the semiconductors used (but in particular, the absorber material). The use of very thin absorber layers in solar cells requires adoption of various light trapping techniques to take advantage of the smaller absorbing volume. The use of mesoporous TiO_2 or ZnO nanorods provides increased surface area of the absorber, while the introduction of metal nanoparticles allows photons to be captured via plasmonic effects [1-4]. This work attempts to utilize the advantages of the plasmon effect, while providing a technologically simple method for solar cell production.

Chemical spray pyrolysis (CSP) is a simple method to produce thin semiconductor oxide- and sulphide layers and metal

nanoparticles (NPs) via thermal decomposition of metal precursor salts. CuInS$_2$ (CIS) is a semiconductor material with a band gap of 1.5 eV that is often used as a photovoltaic absorber. Previously published, related work by our research group regarding CIS-based solar cells includes: the synthesis and properties of CIS [5,6], application of CIS in extremely thin absorber solar cells based on ZnO nanorods [7], the thermal decomposition of a HAuCl$_4$·3H$_2$O precursor solution for Au-NP formation [8], and CIS/Au-NP and Au-NP/CIS composite layers prepared by spraying on glass [9]. In the composite layers, the Au-NPs assist photon absorption in the CIS absorber in the wavelength region of 500–800 nm [9].

Increased photocurrent due to the plasmonic effects of NPs have been demonstrated, for example, for thin film Si solar cells [3], polymer cells [10,11], dye-sensitized cells [12,13] and for solar cells that use ultrathin inorganic absorber layers [14]. However, the use of an in-line spray method for the deposition of the solar cell, including the plasmonic NPs within the cell, has not yet been published.

In the present study, Au-NP layers are deposited by CSP at various stages of the solar cell preparation. This work investigates which locations within the solar cell are optimal for the deposition of Au-NPs in order to increase the photocurrent in the sprayed solar cell.

Experimental

Using commercially available, ITO-covered glass as a substrate, Au-NPs were deposited onto the ITO layer (ITO/Au-NP/ZnO/In$_2$S$_3$/CuInS$_2$) or on top of the absorber layer (ITO/ZnO/In$_2$S$_3$/CuInS$_2$/Au-NP). Details regarding the ITO/ZnO/In$_2$S$_3$/CuInS$_2$ solar cell preparation by spray pyrolysis can be found elsewhere [15].

For the deposition of the Au-NP layer, gold(III) tetrachloride trihydrate (HAuCl$_4$·3H$_2$O, 99.9%, Aldrich) was dissolved in deionized water at a concentration of 2 mmol/L and used as a precursor. The solution was pneumatically sprayed through air onto a substrate with a surface temperature of 260 °C. The solution volume was varied from 2.5 to 10 mL and the solution feeding rate was 1 mL/min.

Current–voltage scans of the solar cells were used to obtain the principal characteristics of the solar cells: voltage at open-circuit condition (V_{OC}), current density at short-circuit condition (J_{SC}), the fill factor (FF) and the conversion efficiency (η).

The total reflectance spectra of the solar cells were measured in the wavelength range of 300–1500 nm on a Jasco V-670 spectrophotometer equipped with an integrating sphere.

The external quantum efficiency (EQE) of the solar cells was measured in the range of 300–1000 nm on a Newport Oriel kit that contains a 300 W Xe lamp, high-resolution monochromator (Cornerstone 260), digital dual-channel lock-in detector (Merlin), and a calibrated silicon reference detector. The Xe lamp is a light source which simulates the conventional AM1.5 spectrum for testing solar cells. The dispersed light from the Xe lamp (incident on the solar cell as monochromatic light) was optically chopped at 30 Hz. EQE is defined as the number of collected charge carriers per incident photon. The EQE is a unitless characteristic (EQE < 1) given by:

$$EQE(\lambda) = \frac{hc}{q\lambda} \cdot \frac{J_{SC}(\lambda)}{P(\lambda)} \qquad (1)$$

where $J_{SC}(\lambda)$ (A·m^{-2}) is the spectrally resolved short-circuit current of the solar cell, $P(\lambda)$ (W·m^{-2}) is the calibrated light intensity incident on the solar cell, and hc/qλ is the energy (eV) of a photon as function of wavelength λ.

For visualization of the morphology of the cross-section of the solar cells, a Zeiss HR FESEM Ultra 55 scanning electron microscope (SEM) at operating voltage of 4 kV was used. The electron beam induced current (EBIC) mode of the SEM was used to map the local electronic activity of the solar cells.

Results and Discussion

A sketch of the solar cell is presented in Figure 1A for the design where the Au-NP layer follows the ITO layer and in Figure 1B for the configuration where the Au-NP layer follows the CuInS$_2$ layer. The corresponding external quantum efficiency (EQE) spectra of the solar cells are presented in Figure 2 and Figure 3, respectively.

In Figure 2, it can be observed that the EQE of the solar cell with the ITO/Au-NP/ZnO/In$_2$S$_3$/CuInS$_2$ configuration suffers losses in the region of 550–700 nm when compared to the reference solar cell without the Au-NP layer. The loss of EQE is attributed to the reflection of light from the Au-NP layer as evaluated from the reflectivity spectra of the cells (not shown).

Conversely, when the Au-NP layer is deposited on top of the CuInS$_2$ layer (ITO/ZnO/In$_2$S$_3$/CuInS$_2$/Au-NP), the EQE increases in the region of 600–850 nm (Figure 3A). When larger volumes of the Au-NP precursor solution are sprayed (up to 10 mL) onto the CuInS$_2$, a further relative increase in the EQE is evident (Figure 3B,C) as compared to the reference spectra.

From these results, one can observe that the region of relative absorption gain was red-shifted with respect to the Au-NP on
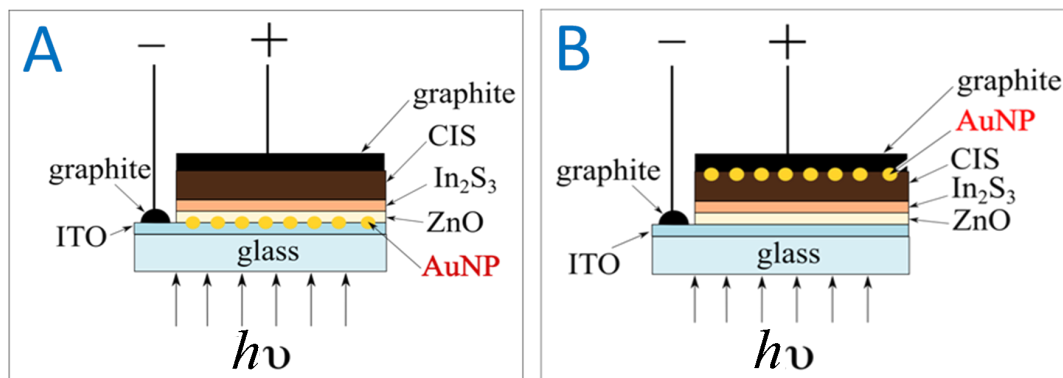
Figure 1: Sketch of the cross-section of the Au-NP/ZnO/In$_2$S$_3$/CuInS$_2$ solar cell (A), and of the ZnO/In$_2$S$_3$/CuInS$_2$/Au-NP solar cell (B), all layers prepared by chemical spray using ITO/glass substrates.
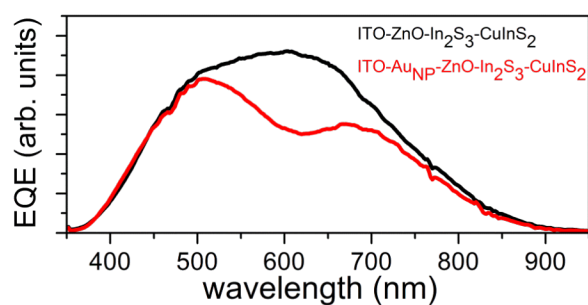
Figure 2: External quantum efficiency (EQE) of a plasmonic solar cell employing Au-NPs on top of an ITO layer. The EQE of the cells without the Au-NP layer is indicated with black lines. The volume of the solution of the Au-NP precursor was 2.5 mL.

Figure 3: Left: External quantum efficiency (EQE) of ITO/ZnO/In$_2$S$_3$/CuInS$_2$/Au-NP solar cells (red line) and EQE of the solar cells without the Au-NP layer (black lines). The volume of the Au-NP precursor solution was 2.5 mL (A), 5 mL (B) or 10 mL (C). Right: SEM images of the CuInS$_2$/Au-NP surface aligned with the corresponding EQE. Note that the EQE graphs have been normalized to emphasize the relative gain of the EQE. The overall EQE decreased when 5 mL or 10 mL of the Au-NP precursor solution was sprayed.

ITO configuration. The penetration depth of the optical radiation (in the region of 400–900 nm) remains roughly between 0.1 and 1 μm within the CuInS$_2$ absorber [16]. Since the thickness of the CuInS$_2$ is approximately 350 nm, a significant gain of absorption was not expected for wavelength regions with a low penetration depth. However, longer wavelengths penetrate deeper into the absorber (or are transmitted) and hence can fully utilize the presence the Au-NPs on the rear side of the absorber. In addition, Au is also an excellent reflector for wavelengths greater than 600 nm. Furthermore, an increase in the optical absorption can be expected in the red/infrared region for the sprayed CIS/Au-NP composite layers, as previously shown [9,17].

The increase in the EQE is attributed to the increased CuInS$_2$ coverage with Au-NPs when using a larger volume of the Au precursor solution [9]. The mean diameter of the individual spherical Au-NPs was between 20 and 60 nm for the 2.5–10 mL sprayed Au precursor solution, as evaluated from the SEM images (Figure 3). These values correspond well to those obtained in our previous study regarding Au-NPs produced by spray pyrolysis onto CuInS$_2$ using HAuCl$_4$ as a precursor [9]. However, Au-NP agglomerates of up to 200 nm can also be found, thus a size distribution of the of Au-NP agglomerates is also present. An increase in the particle size is likely to cause a red shift of the corresponding plasmon resonance, whereas a wide size distribution of Au-NPs and agglomerates is likely to cause a wide absorption band and a corresponding EQE gain due to the overlapping plasmon resonances [17]. To support this argument, details of the relative EQE gain (ΔEQE = EQE$_{CIS/AuNP}$ − EQE$_{CIS}$) in the wavelength region of

550–900 nm are presented in Figure 4. Here, for the solar cell that uses 10 mL of Au precursor solution (curve C), at least three separate bands emerge centered at around 650, 710 and 850 nm.

Figure 4: Spectra of the relative increase in ΔEQE for the ITO/ZnO/In$_2$S$_3$/CuInS$_2$/Au-NP solar cells when compared to the EQE of the solar cells without the Au-NP layer. The ΔEQE curves A, B and C corresponds to the EQE data presented in Figure 3A, B and C, respectively.
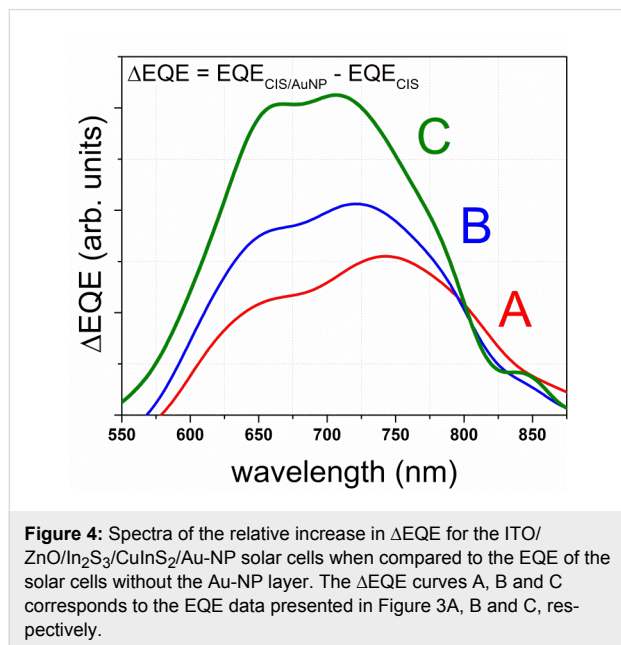
Thus, the increase in the EQE in the red/infrared region (Figure 3) is likely due to the gain in optical absorptance induced by the surface plasmon resonance effect. For this effect to occur, the scattering medium must have a lower refractive index than that of the absorbing medium. As required, the refractive index of Au is in the range 1.5–0.2 [18] and that of CuInS$_2$ is 3–2.6 [19] in the wavelength range of 400–900 nm.

It cannot be entirely excluded that charge transfer at the back contact region (graphite/gold/CuInS$_2$) was improved with respect to the reference (graphite/CIS). However, resonant absorption peaks in the red/infrared region would not be expected to emerge (Figure 4) in the case of the charge transfer argument.

For the solar cell prepared by spraying 2.5 mL of the Au precursor (Figure 3A) onto the CuInS$_2$, the V_{OC} of the respective solar cell decreases from 448 to 414 mV (−8%), the current density, J_{SC}, increases from 4.6 up to 7.5 mA/cm^2 (+63%) and the FF decreases from 56 to 49% (−13%), as summarized in Table 1. The conversion efficiency η is proportional to V_{OC}, and J_{SC} and FF and increase from 1.15 to 1.5% (+30%). Thus, the using of 2.5 mL of the precursor solution to deposit Au-NPs on the rear side of the solar cell is advantageous when compared to the deposition of Au-NPs onto the front of the cell. As an illustration, an SEM image and an EBIC image of the

cross-section of the solar cell using 2.5 mL of Au precursor sprayed onto the CuInS$_2$ is presented in Figure 5.

Table 1: Open-circuit voltage (V_{OC}), short-circuit current (J_{SC}), fill factor (FF) and light to electricity conversion efficiency (η) of ITO/ZnO/In$_2$S$_3$/CuInS$_2$/Au-NP solar cell, evaluated from current–voltage measurements. The volume of the precursor solution for Au-NP was 2.5 mL. The EQE of the cell is presented in Figure 3A, the SEM image and EBIC image are presented in Figure 5.

	V_{OC} (mV)	J_{SC} (mA/cm^2)	FF (%)	η (%)
ITO/ZnO/In$_2$S$_3$/CuInS$_2$	448	4.6	56	1.15
ITO/ZnO/In$_2$S$_3$/CuInS$_2$/Au$_{NP}$	414	7.5	49	1.5

Figure 5: SEM image and EBIC image of the cross-section of the ZnO/In$_2$S$_3$/CuInS$_2$/Au-NP solar cell prepared by spray pyrolysis on ITO/glass substrates. The Au-NP layer was deposited using 2.5 mL of the Au-precursor solution sprayed onto the CuInS$_2$ layer at 260 °C. The images were acquired simultaneously from the same location on the sample.
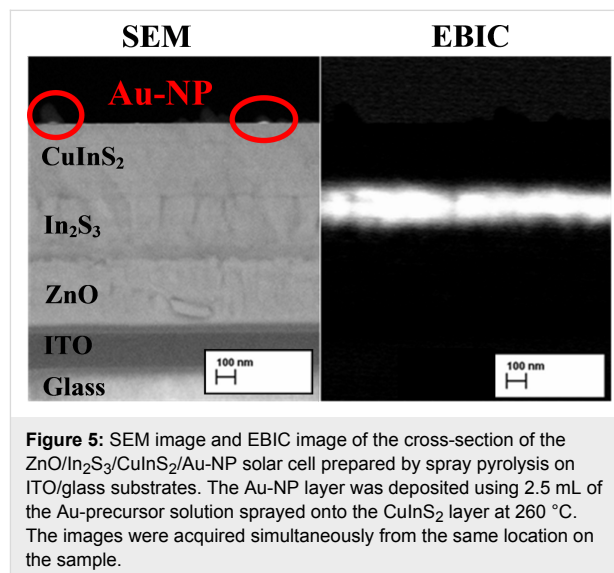
In contrast, when using larger volumes of Au-precursor solution (5 mL and 10 mL), the V_{OC}, J_{SC} and FF all decrease (not shown). It was assumed that the decrease is a secondary effect since the CuInS$_2$ layer will gradually dissolve/deteriorate when larger volumes of HAuCl$_4$ are deposited [9]. To avoid the dissolution of CuInS$_2$, deposition of presynthesized Au-NPs could be advantageous.

Conclusion

Chemical spray pyrolysis (CSP) was employed to deposit ZnO/In$_2$S$_3$/CuInS$_2$ solar cells that use an extremely thin CuInS$_2$ absorber layer and an ITO substrate. Au-NPs as constituents of the solar cells were produced by spraying chloroauric acid (HAuCl$_4$) onto the ITO or CuInS$_2$ layer. The external quantum efficiency (EQE) of the solar cell decreased due to increased reflection of light due to the Au plasmon resonance in the region of 550–700 nm when the Au-NP layer was deposited onto the ITO layer. Conversely, the EQE of the solar cell

increased when Au-NPs were deposited on top of the $CuInS_2$ absorber material when a small volume of the $HAuCl_4$ precursor was used. The increase in the EQE is due to increased absorption in region of 600–850 nm due to the Au-plasmon resonance. The increase in the absorption ability of the solar cell results in a relative increase of the conversion efficiency of the solar cells by 30% (from 1.15 to 1.5%) and a 63% increase (from 4.6 to 7.5 mA/cm^2) in the short-circuit current of the solar cell. We have experimentally demonstrated that the deposition of a Au-NP layer on top of the $CuInS_2$ absorber material can increase the absorption ability, the short-circuit current and the conversion efficiency of the $ZnO/In_2S_3/CuInS_2$ solar cell, all prepared by an in-line, simple CSP method.

Acknowledgements

References

1. Ferry, V. E.; Munday, J. N.; Atwater, H. A. *Adv. Mater.* **2010,** *22,* 4794–4808. doi:10.1002/adma.201000488
2. Sreekanth, K. V.; Sidharthan, R.; Murukeshan, V. M. *J. Appl. Phys.* **2011,** *110,* 033107. doi:10.1063/1.3622149
3. Ferry, V. E.; Verschuuren, M. A.; Li, H. B. T.; Verhagen, E.; Walters, R. J.; Schropp, R. E. I.; Atwater, H. A.; Polman, A. *Opt. Express* **2010,** *18,* A237–A245. doi:10.1364/OE.18.00A237
4. Catchpole, K. R.; Polman, A. *Opt. Express* **2008,** *16,* 21793. doi:10.1364/OE.16.021793
5. Oja Acik, I.; Otto, K.; Krunks, M.; Tõnsuaadu, K.; Mere, A. *J. Therm. Anal. Calorim.* **2013,** *113,* 1455–1465. doi:10.1007/s10973-013-3155-7
6. Kärber, E.; Katerski, A.; Oja Acik, I.; Mikli, V.; Mere, A.; Krunks, M. *Thin Solid Films* **2013,** *519,* 7180–7183. doi:10.1016/j.tsf.2010.12.185
7. Kärber, E.; Abass, A.; Khelifi, S.; Burgelman, M.; Katerski, A.; Krunks, M. *Sol. Energy* **2013,** *91,* 48–58. doi:10.1016/j.solener.2013.01.020
8. Otto, K.; Oja Acik, I.; Krunks, M.; Tõnsuaadu, K.; Mere, A. *J. Therm. Anal. Calorim.* **2014,** *118,* 1065–1072. doi:10.1007/s10973-014-3814-3
9. Katerski, A.; Kärber, E.; Oja Acik, I.; Dolgov, L.; Mere, A.; Sildos, I.; Mikli, V.; Krunks, M. *Nanoscale Res. Lett.* **2014,** *9,* 494. doi:10.1186/1556-276X-9-494
10. Kim, S.-S.; Na, S.-I.; Jo, J.; Kim, D.-Y.; Nah, Y.-C. *Appl. Phys. Lett.* **2008,** *93,* 073307. doi:10.1063/1.2967471
11. Yang, J.; You, J.; Chen, C.-C.; Hsu, W.-C.; Tan, H.-R.; Zhang, X. W.; Hong, Z.; Yang, Y. *ACS Nano* **2011,** *5,* 6210–6217. doi:10.1021/nn202144b
12. Brown, M. D.; Suteewong, T.; Kumar, R. S. S.; D'Innocenzo, V.; Petrozza, A.; Lee, M. M.; Wiesner, U.; Snaith, H. J. *Nano Lett.* **2011,** *11,* 438–445. doi:10.1021/nl1031106
13. Hou, W.; Pavaskar, P.; Liu, Z.; Theiss, J.; Aykol, M.; Cronin, S. B. *Energy Environ. Sci.* **2011,** *4,* 4650. doi:10.1039/c1ee02120f
14. Lim, C.-S.; Im, S. H.; Kim, H.; Chang, J. A.; Lee, Y. H.; Seok, S. I. *Phys. Chem. Chem. Phys.* **2012,** *14,* 3622. doi:10.1039/c2cp23650h
15. Krunks, M.; Kärber, E.; Katerski, A.; Otto, K.; Oja Acik, I.; Dedova, T.; Mere, A. *Sol. Energy Mater. Sol. Cells* **2010,** *94,* 1191–1195. doi:10.1016/j.solmat.2010.02.036
16. Thai, T. T.; Hung, P. P.; Son, V. T.; Bich, V. T. *Commun. Phys. (Hanoi, Viet Nam)* **2012,** *22,* 59–64. doi:10.15625/0868-3166/22/1/633
17. Repan, T.; Dolgov, L.; Katerski, A.; Oja Acik, I.; Kärber, E.; Mere, A.; Mikli, V.; Krunks, M.; Sildos, I. *Appl. Phys. A* **2014,** *117,* 455–458. doi:10.1007/s00339-014-8681-z
18. Rakić, A. D.; Djurišić, A. B.; Elazar, J. M.; Majewski, M. L. *Appl. Opt.* **1998,** *37,* 5271–5283. doi:10.1364/AO.37.005271
19. Alonso, M. I.; Wakita, K.; Pascual, J.; Garriga, M.; Yamamoto, N. *Phys. Rev. B* **2001,** *63,* 75203. doi:10.1103/PhysRevB.63.075203

Manganese oxide phases and morphologies: A study on calcination temperature and atmospheric dependence

Matthias Augustin[*1,2], Daniela Fenske[1], Ingo Bardenhagen[1], Anne Westphal[1], Martin Knipper[2], Thorsten Plaggenborg[2], Joanna Kolny-Olesiak[2] and Jürgen Parisi[2]

Full Research Paper

Address:
[1]Fraunhofer Institute for Manufacturing Technology and Advanced Materials, Wiener Str. 12, 28359 Bremen, Germany and [2]Department of Physics, Energy and Semiconductor Research Laboratory, Carl von Ossietzky University of Oldenburg, 26129 Oldenburg, Germany

Email:
Matthias Augustin[*] - matthias.augustin@ifam.fraunhofer.de

* Corresponding author

Abstract

Manganese oxides are one of the most important groups of materials in energy storage science. In order to fully leverage their application potential, precise control of their properties such as particle size, surface area and Mn^{x+} oxidation state is required. Here, Mn$_3$O$_4$ and Mn$_5$O$_8$ nanoparticles as well as mesoporous α-Mn$_2$O$_3$ particles were synthesized by calcination of Mn(II) glycolate nanoparticles obtained through an economical route based on a polyol synthesis. The preparation of the different manganese oxides via one route facilitates assigning actual structure–property relationships. The oxidation process related to the different MnO$_x$ species was observed by in situ X-ray diffraction (XRD) measurements showing time- and temperature-dependent phase transformations occurring during oxidation of the Mn(II) glycolate precursor to α-Mn$_2$O$_3$ via Mn$_3$O$_4$ and Mn$_5$O$_8$ in O$_2$ atmosphere. Detailed structural and morphological investigations using transmission electron microscopy (TEM) and powder XRD revealed the dependence of the lattice constants and particle sizes of the MnO$_x$ species on the calcination temperature and the presence of an oxidizing or neutral atmosphere. Furthermore, to demonstrate the application potential of the synthesized MnO$_x$ species, we studied their catalytic activity for the oxygen reduction reaction in aprotic media. Linear sweep voltammetry revealed the best performance for the mesoporous α-Mn$_2$O$_3$ species.

Introduction

Manganese oxides are a class of inexpensive compounds with a high potential for nanostructuring, which makes them attractive candidates for various applications, for example, as basis materials in supercapacitors and electrodes for Li-ion accumulators [1-3]. They exhibit high catalytic activity for different oxidation and reduction reactions due to the diversity in their Mn^{x+}

cation oxidation states as well as morphological characteristics [4,5]. Many manganese oxide phases consist of tunnel structures built from MnO_6 octahedra; these tunnels facilitate the access of reactants to the active reaction sites as well as the absorption of small molecules within the structure. The latter property is especially useful for application as molecular sieves and absorbents for the removal of toxic species from waste gases such as carbon monoxide and nitrogen oxide [6-8]. Additionally, manganese oxide structures exhibiting oxygen vacancies provide additional active sites for reduction and oxidation reaction intermediates, especially those involving oxygen. These properties are especially important for catalytic applications such as water oxidation [9-11] and the oxygen reduction and evolution reactions in metal/air battery systems [12-16]. Additionally, the advantages of manganese oxides can be enhanced by nanostructuring of the different species, which was recently shown by Zhang et al. [17]. In their report, better cyclability of Li-ion cells was obtained with anodes consisting of mesoporous Mn_2O_3 particles compared to Mn_2O_3 bulk powder electrodes [17].

Several nanoscale manganese oxide compounds can be prepared via calcination processes from suitable precursors [7,18-20]. Whereas many synthetic protocols yield manganese oxide species at the nanometer scale [21], for example, precipitation or the solvothermal route, these methods require long reaction times in the range of hours (up to 24 h) and subsequent drying processes of up to 2 days [22-27]. The synthesis via oxidation of manganese metal nanoparticles by gas condensation must be followed by annealing in O_2-containing atmospheres to obtain different manganese oxide species [28]. An advantage of the calcination route, on the other hand, is the conservation of the morphology and size of the precursor during this process, which is of special interest when considering the use of nanoscale precursor particles. Further advantages include a relatively short synthesis time of about 1 to 5 h and the fact that a single precursor can be used to obtain several different products. Additionally, the calcination procedure is the only way to obtain pure phase Mn_5O_8 [28-33].

Here, we present the synthesis of nanocrystalline Mn(II) glycolate by a polyol process and demonstrate its suitability as a precursor in the synthesis of different manganese oxides. The polyol process is a well-known route for the synthesis of metal glycolates, usually yielding disc-shaped particles with diameters and thicknesses in the range of 1 to 3 µm and 100 to 250 nm, respectively [19,29,34,35]. By applying milder reaction conditions (i.e., decreasing the synthesis temperature and increasing the reaction time), we obtained homogeneous, rectangular Mn(II) glycolate nanocrystals with diameters less than 25 nm. The preparation of nanoscale precursor particles

with uniform morphology is advantageous for the further synthesis of manganese oxides, because the control of the morphology and size of the particles is a major issue for their catalytic applications. The subsequent calcination process yielded Mn_3O_4 and Mn_5O_8 nanoparticles as well as mesoporous α-Mn_2O_3 particles with high surface areas of 300, 30 and 20 m^2/g, respectively. The nanostructures of the obtained MnO_x particles make them attractive candidates as highly active compounds in the field of catalysis and other applications in the field of energy storage. Furthermore, the synthesis presented in this study provides easy access to three different nanostructured MnO_x species via one calcination process. This is advantageous for the investigation of the properties of the manganese oxides, as it rules out any synthesis-caused effects. The temperature- as well as the time-dependent phase transformation processes occurring during the oxidation of Mn(II) glycolate to Mn_3O_4, Mn_5O_8 and α-Mn_2O_3 were studied by in situ XRD measurements. A detailed study of the structural parameters of the manganese oxide products obtained after calcination in a temperature range from 320 to 550 °C in Ar and O_2 atmosphere was performed using powder XRD.

Results and Discussion
Precursor synthesis

The polyol process reported by Liu et al. [19] was modified to yield the Mn(II) glycolate precursor for the thermal decomposition to the various manganese oxides. During the heating of the compound to 170 °C, a white precipitate appeared after 1 h, which was identified as manganese glycolate containing large impurities of the dehydrated educt Mn(II) acetate dihydrate and the product of a side reaction, manganese oxalate (MnC_2O_4, see Supporting Information File 1 for the powder XRD pattern of the product mixture). In order to obtain the pure Mn(II) glycolate precursor having homogeneous particle morphology, the reaction was continued at 170 °C until a white precipitate of pure Mn(II) glycolate appeared. This was verified by the X-ray diffraction pattern of the product after 7 h of synthesis as depicted in Figure 1. This product can be assigned to the trigonal brucite-type structure ($P\bar{3}m1$) reported for Mn(II) glycolate by other groups [19,29,35]. A mean Scherrer crystallite size of 17 ± 8 nm was calculated for the Mn(II) glycolate particles. The interlayer distance along the [001] direction was calculated to be 8.2 Å. This value corresponds to the lattice constant, *c*, and is consistent with reports by other groups who measured lattice constants of *c* = 8.3 Å and *c* = 8.27 Å for Mn and Co glycolate, respectively [34,35]. As Sun et al. [35] did not use tetraethylene glycolate (TEG) in their synthesis, it is proposed here that TEG anions are not part of the Mn(II) glycolate structure presented in this report, as *c* would be increased even beyond 8.2 Å in this case. Hence, it can be concluded that TEG acts only as a stabilizing ligand to the Mn(II) glycolate parti-

cles. This and the milder synthesis conditions applied are considered to be the reasons for the relatively small crystallite sizes, differing by one order of magnitude from the data presented to date in the literature [19,29,35]. Inorganic compounds with a brucite structure such as $Mg(OH)_2$, $Co(OH)_2$, $Ca(OH)_2$ and $Ni(OH)_2$, exhibit lattice constant *c* between 4.6 and 4.9 Å and *a* in the range from 3.1 to 3.6 Å. For Mn(II) glycolate, the Mn–Mn distance (corresponding to lattice constant *a*) was calculated to be 3.2 Å from the (110) reflection, which is also in accordance with the findings of Sun et al. [35] who proposed that the structure widening in the *c* direction is due to the long-chain alcoholate anions interconnecting the metal–oxygen sheets in the *ab* plane of the unit cell.
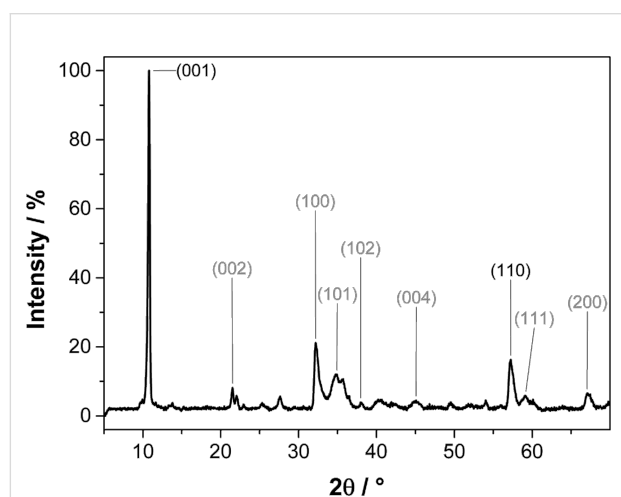
The morphology of the as-synthesized Mn(II) glycolate was investigated with SEM and TEM measurements. Figure 2a depicts SEM images of spherical Mn(II) glycolate particles with diameters up to 1 µm. These particles are hollow, which is deduced from the particles with broken outer shells (highlighted by white frames). Figure 2b shows a TEM image of one of these spherical particles, broken under the electron beam. A closer look reveals that the spheres are in fact agglomerates of rectangular Mn(II) glycolate nanoparticles with dimensions less than 15 nm (Figure 2c). The observed sizes of the particle are in good agreement with the calculated Scherrer crystallite sizes from the XRD pattern shown in Figure 1. The small dimensions of the particles make the synthesized Mn(II) glycolate a perfect precursor for the generation of manganese oxides by thermal decomposition processes.

The oxidation process to different MnO_x species

In order to investigate the temperature dependence of the oxidation process of Mn(II) glycolate, in situ X-ray diffractograms were recorded in the presence of O_2 while heating the precursor to 700 °C at a heating rate of 2 K/min (see Figure 3). The 2θ region of 17.6–23.8° was monitored during the measurement, as it contains the reflections of the species that are most likely to be generated during the oxidation process (21.5° (Mn(II) glycolate, □) [19], 18.0° (Mn_3O_4, *) [36], 18.1° and 21.6° (Mn_5O_8, +) [31], and 23.2° (α-Mn_2O_3, ○) [37]). The reflection of Mn(II) glycolate at 21.5° is observed until a temperature of about 185 °C is reached, where a sudden decrease of the intensity (including the background intensity) is observed in the diffraction patterns due to the loss of organic species from the sample. This loss derives from the decomposition of the organic ligands and anions by oxidation; this is

Figure 1: Powder XRD pattern of Mn(II) glycolate particles synthesized for 7 h; literature assignments [35] (black) and calculated reflection assignments (grey) are given for the brucite structure exhibiting lattice constants of *a* = *b* = 3.2 Å and *c* = 8.2 Å.
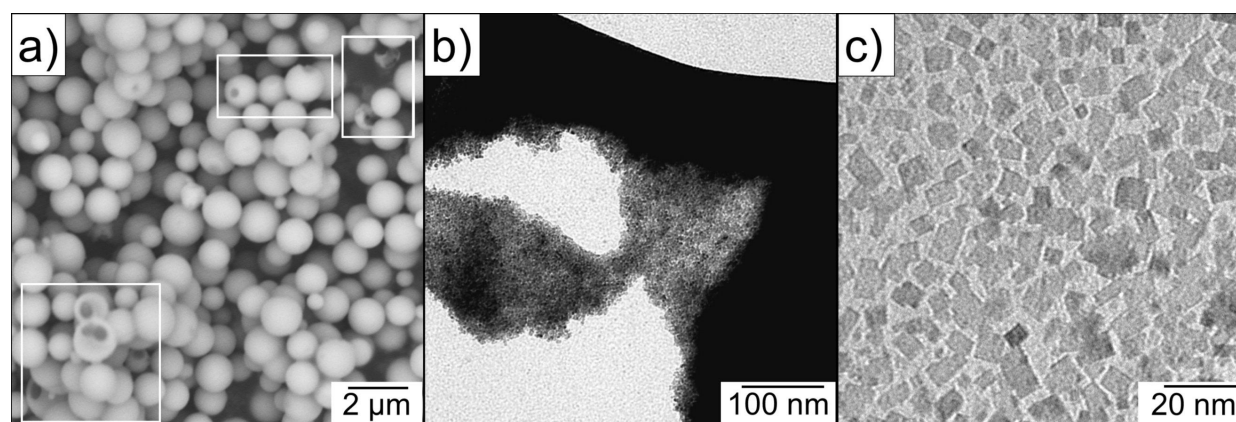
Figure 2: a) SEM and b) and c) TEM images of the Mn(II) glycolate particles. Particles with broken outer shells are highlighted by white frames in panel (a).

dependent on the temperature as well as on the partial pressure of oxygen. The Mn_3O_4 reflection at 18.0° immediately evolves at about 185 °C after the Mn(II) glycolate reflection has vanished. The appearance of the Mn_5O_8 reflection at 21.6° at about 350 °C is accompanied by the decreasing intensity of the Mn_3O_4 reflection at 18.0° as well as an increasing intensity of the Mn_5O_8 reflection at 18.1°, which is attributed to the slow oxidation of Mn_3O_4 to Mn_5O_8. The Mn_3O_4 reflection at 18.0° disappears at about 440 °C, indicating a completed oxidation process of Mn_3O_4 to Mn_5O_8. Both reflections assigned to Mn_5O_8 disappear at 550 °C after the appearance of the intense α-Mn_2O_3 reflection at 23.2° at a temperature of about 530 °C.

Hence, in O_2 atmosphere, Mn_3O_4 is obtained at temperatures between 185 and 400 °C, Mn_5O_8 between 400 and 550 °C and α-Mn_2O_3 above 530 °C. This oxidation of Mn_3O_4 to Mn_5O_8 (rather than to Mn_2O_3) was found by Feitknecht [30] to take place during the heating of Mn_3O_4 particles at temperatures between 250 and 550 °C in an atmosphere containing more than 5% O_2. Feitknecht attributed this Mn_3O_4/Mn_5O_8 phase transformation to a one-phase mechanism for Mn_3O_4 particles exhibiting BET surface areas of more than 10 m²/g. That is, the small particle diameters provide sufficient reaction sites for oxidation

of the surface of the particles. Feitknecht also reported similar reflection intensities for Mn_3O_4 and Mn_5O_8 with a linear decrease and increase, respectively, during the oxidation process. The subsequent reduction process of Mn_5O_8 to α-Mn_2O_3 was observed by several groups to take place even in oxygen-containing atmospheres at temperatures greater than 500 °C [26,32,37].

The Mn(II) glycolate particles were calcined for 2 h in Ar and O_2 atmospheres at different temperatures between 320 and 550 °C to investigate the dependence of the particle size, their morphology and the Mn^{x+} oxidation state in the resulting manganese oxide on the calcination temperature and atmosphere. The X-ray diffractograms of the resulting species as well as the reference patterns are shown in Figure 4; the crystalline phases observed in the XRD patterns are listed in Table 1.

The tetragonal Mn_3O_4 phase (ICDD 01-075-1560, $I4_1/amd$) is observed in the powder XRD patterns after calcination at temperatures between 320 and 450 °C in both atmospheres. It is, however, obtained as a pure phase only at temperatures up to 400 °C in Ar and up to 350 °C in O_2 (see also Table 1). The presence of Mn_3O_4 in O_2 atmosphere could also be observed in
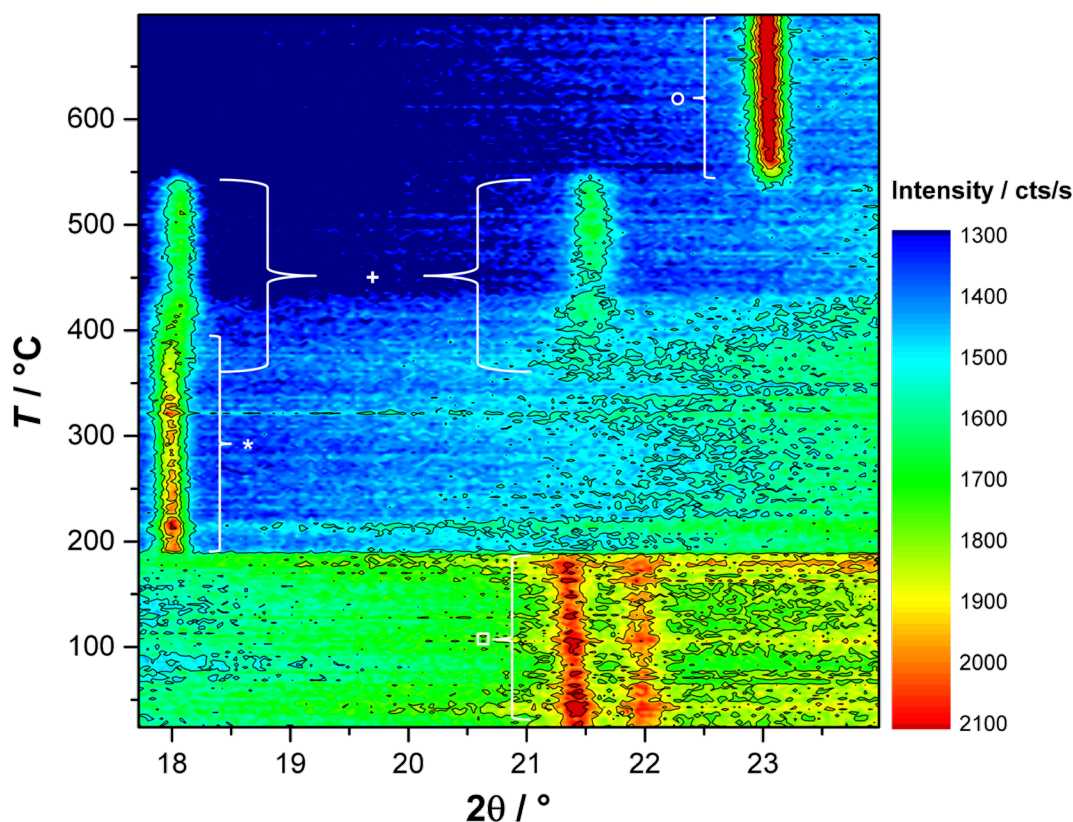
Figure 3: In situ XRD patterns recorded in a pure O_2 flow while heating the Mn(II) glycolate precursor to 700 °C at 2 K/min; reflexes denoted are: Mn(II) glycolate (□), Mn_3O_4 (⋅), Mn_5O_8 (+) and α-Mn_2O_3 (○).

Figure 4: Powder XRD patterns of the manganese oxide particles obtained after calcination of the Mn(II) glycolate for 2 h at different temperatures in an Ar (black) and an O$_2$ (red) flow of 50 NL/h. Reference patterns are depicted at the top for Mn$_3$O$_4$ (∙), Mn$_5$O$_8$ (+) and α-Mn$_2$O$_3$ (○), where the symbols indicate the respective low-angle reflections.
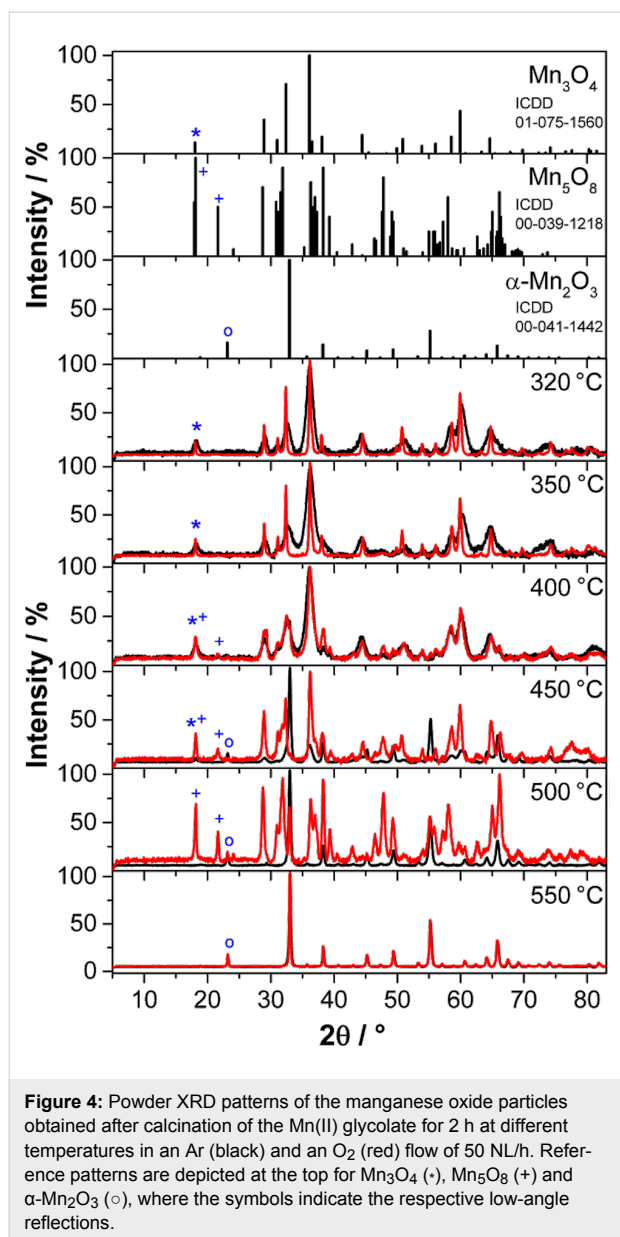
the in situ XRD measurements up to a temperature of 440 °C (see Figure 3). The lattice parameters and crystallite sizes of the pure Mn$_3$O$_4$ samples obtained by calcination in Ar as well as O$_2$ atmospheres at 320 °C and 350 °C listed in Table 1 are obviously independent of the calcination temperature, but dependent on the calcination atmosphere. The samples obtained in Ar exhibit crystallite sizes of less than a third compared to those obtained in O$_2$. Furthermore, the lattice constants of Mn$_3$O$_4$ produced in Ar are smaller at all temperatures than those obtained by calcination in O$_2$ atmosphere. This could be due to oxygen vacancies, as the oxygen for the oxidation to Mn$_3$O$_4$ in pure Ar is only supplied by the manganese glycolate precursor and cannot be obtained from the gas atmosphere. The presence of oxygen vacancies is also supported by the less pronounced

variation of the lattice constants of Mn$_3$O$_4$ obtained at 320 °C and 350 °C in O$_2$ atmospheres, leading to the assumption of completely occupied oxygen sites in the structure of the oxide.

Cubic α-Mn$_2$O$_3$ (ICDD 00-041-1442, $Ia\overline{3}$) is obtained in Ar after calcination at temperatures between 450 and 550 °C and at 500–550 °C in O$_2$. Pure-phase α-Mn$_2$O$_3$, however, is only obtained after calcination at temperatures of 500 and 550 °C in Ar and at 550 °C in O$_2$ atmospheres (see also Table 1). The presence of α-Mn$_2$O$_3$ after calcination at 500 °C in O$_2$ does not support the observations made in the in situ XRD measurements (compare to Figure 3), where a generation of α-Mn$_2$O$_3$ from Mn$_5$O$_8$ in an O$_2$ atmosphere was only detected at temperatures above 530 °C. However, this is probably due to an additional time dependence of the phase transformation of Mn$_5$O$_8$ to α-Mn$_2$O$_3$, which was also suggested by Dimesso et al. [28]. In their report the α-Mn$_2$O$_3$ phase was observed to be the minor species second to Mn$_5$O$_8$ after calcination at 400 °C in air for 1 h, but was found to be the major species after calcination for 5 h at the same temperature. The lattice constants of the pure α-Mn$_2$O$_3$ phase obtained after calcination in Ar and O$_2$, are obviously independent of the temperature and the calcination atmosphere (see Table 1). Therefore, in contrast to the observations made for Mn$_3$O$_4$, the absence of O$_2$ in the calcination atmosphere does not lead to an increase in the concentration of oxygen vacancies in the α-Mn$_2$O$_3$ structure, which would be high enough to significantly change the lattice constants. The values of the Scherrer-derived crystallite sizes, however, suggest a temperature dependence of the obtained α-Mn$_2$O$_3$ particle size in Ar atmosphere, which was not the case for the Mn$_3$O$_4$ particles. The Scherrer-derived size of the crystallites of the pure phase α-Mn$_2$O$_3$ obtained in an O$_2$ atmosphere at 550 °C is one third larger than that calculated for particles obtained in Ar at the same temperature. Hence, similar to the Mn$_3$O$_4$ phases described above, the presence of O$_2$ in the calcination atmosphere yields larger crystallites of the same product.

No pure phase of monoclinic Mn$_5$O$_8$ (ICDD 00-039-1218, $C2/m$) could be obtained by calcination at temperatures between 320 and 550 °C for 2 h in both atmospheres. However, after calcination in O$_2$ atmosphere, a small fraction of Mn$_5$O$_8$ can be detected in the products obtained at 400 and 450 °C, while it forms the majority of the product obtained after calcination at 500 °C. This is in good agreement with the in situ XRD patterns recorded in O$_2$ atmosphere, where Mn$_5$O$_8$ was generated at about 350 °C and decomposed at 550 °C (see Figure 3).

In order to obtain pure-phase Mn$_5$O$_8$ particles, a longer calcination time of 5 h at 400 °C in an O$_2$ atmosphere was chosen based on the time profile from the in situ XRD measurements (see Supporting Information File 1 for further details).

Table 1: Crystalline manganese oxide phases obtained after calcination for 2 h in an Ar flow and an O_2 flow (50 NL/h) at different temperatures; mean Scherrer crystallite sizes (from all assigned reflections) and lattice parameters (from the (101) and (004) reflections of Mn_3O_4 as well as the (400) reflection of α-Mn_2O_3) were calculated for samples yielding pure phases.

Temperature [°C]	Atmosphere	Crystalline phase(s)	Lattice parameters [Å]	Crystallite size [nm]
320	Ar	Mn_3O_4	a = 5.72 c = 9.38	11 ± 3
	O_2	Mn_3O_4	a = 5.75 c = 9.47	38 ± 11
350	Ar	Mn_3O_4	a = 5.69 c = 9.44	10 ± 3
	O_2	Mn_3O_4	a = 5.74 c = 9.47	35 ± 10
400	Ar	Mn_3O_4	a = 5.73 c = 9.39	9 ± 2
	O_2	Mn_3O_4, Mn_5O_8		
450	Ar	α-Mn_2O_3, Mn_3O_4		
	O_2	Mn_3O_4, Mn_5O_8		
500	Ar	α-Mn_2O_3	a = 9.41	27 ± 4
	O_2	Mn_5O_8, α-Mn_2O_3		
550	Ar	α-Mn_2O_3	a = 9.40	34 ± 5
	O_2	α-Mn_2O_3	a = 9.41	44 ± 12

The properties of the Mn_5O_8 sample were investigated in more detail and compared to those of the Mn_3O_4 and α-Mn_2O_3 samples obtained by calcination for 2 h in Ar at 350 °C and at 550 °C, respectively. These Mn_3O_4 and α-Mn_2O_3 samples were chosen as they exhibit the most interesting properties for possible catalytic applications due to their small particle sizes.

The X-ray diffraction pattern of pure Mn_5O_8 obtained by calcination in an O_2 atmosphere at 400 °C for 5 h is shown in Figure 5. The Scherrer-derived crystallite size of this species is 22 ± 5 nm, and the lattice parameters of the monoclinic unit cell (ICDD 00-039-1218) are a = 10.40 Å, b = 5.73 Å and c = 4.87 Å with β = 109.6°, which is in good agreement with the data from literature (a = 10.34 Å, b = 5.72 Å and c = 4.85 Å with β = 109.25°) [31].

The temperature- and gas atmosphere-dependent oxidation process of Mn(II) glycolate to the manganese oxide species observed in the XRD patterns (see Figure 3 and Figure 4) was also investigated by thermogravimetric analysis (TGA). TGA measurements were recorded while heating the Mn(II) glycolate samples up to 700 °C with a heating rate of 2 K/min in an Ar (black) and an O_2/Ar (1:2) (red) flow, respectively.

In both atmospheres a mass loss of 2.1% due to loss of water from the samples is detected up to a temperature of 150 °C. In Ar atmosphere, a further mass loss of 5.7% occurs up to 320 °C, which we attribute to the decomposition of the organic ligands
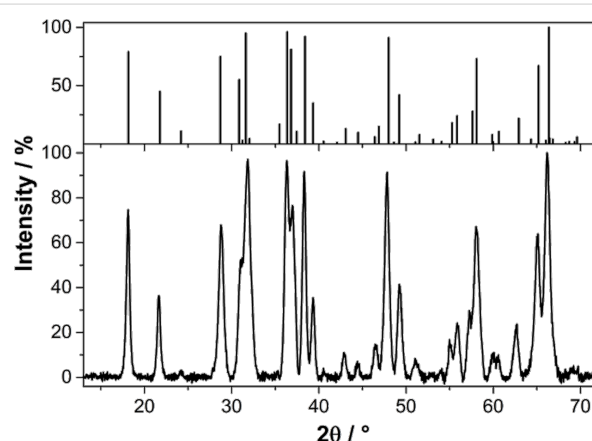
Figure 5: Powder XRD patterns of the Mn_5O_8 particles obtained by calcination of Mn(II) glycolate for 5 h at 400 °C in an O_2 flow of 50 NL/h; a reference pattern is given in the top panel (ICDD 00-039-1218).

(tetraethylene glycol and ethylene glycol), whose boiling points are in the temperature range of 150 °C to 320 °C. Subsequently, a mass loss of about 37% is detected up to 450 °C, which was also observed in TGA measurements of Ti(IV) glycolate by Jiang et al. [38] and was explained as a complete decomposition of the organic anions connecting the metal ions in that compound. Simultaneously, Mn(II) glycolate is oxidized to Mn_3O_4 and further to α-Mn_2O_3 between 185 °C to 450 °C, as was observed in the XRD measurements after calcination of the precursor for 2 h, as discussed above (see Figure 4). Although this oxidation process is accompanied by a decomposition of

the organic groups, XPS results showed the presence of approximately 25 atom % carbon in the α-Mn_2O_3 species obtained after calcination for 2 h at 550 °C in Ar atmosphere. This, however, will not have a significant effect on its application as an electrocatalyst, as the reference and substrate material for the catalysts consists of carbon.

The decomposition of the organic species of Mn(II) glycolate in combination with an immediate oxidation to Mn_3O_4 in O_2 atmosphere was observed at 185 °C in the in situ XRD measurement depicted in Figure 3. In the TGA measurement, however, a mass loss of 44% attributed to this process is detected between 150 and 250 °C. Hence, the observed mass loss includes the decomposition of organic species as well as the oxidation to Mn_3O_4. The temperature delay of the processes can be explained by considering the smaller O_2 partial pressure of the atmosphere used for the TGA measurement. As both processes take place simultaneously, a clear assignment of the weight loss cannot be made. In order to investigate the processes subsequent to the large mass loss in the O_2-containing atmosphere, a detailed view of the temperature region from 250 to 500 °C is shown in Figure 6b. Here, a mass increase of 0.54% is observed between 250 and 330 °C accompanied by a differential scanning calorimetry (DSC) signal of an exothermal phase transformation at 270 °C indicating a partial oxidation of Mn_3O_4 to Mn_5O_8. This is in good agreement with the development of the Mn_5O_8 phase observed at about 350 °C in the in situ XRD measurements (see Figure 3). The expected mass gain by complete oxidation to Mn_5O_8 of 5.59% is, however, much larger. Gillot et al. [27] proposed that heating rates between 1.2 and 2.5 K/min could lead to a direct oxidation of Mn_3O_4 to α-Mn_2O_3 even in O_2 atmosphere, which would result in an expected mass gain of 0.97%. As both the direct oxidation of Mn_3O_4 to α-Mn_2O_3 and the oxidation via Mn_5O_8 would result in larger mass increases than the one observed in the measurement (0.54%), it is suggested that the decomposition of the organic species is not complete at a temperature of 330 °C. However, the subsequent mass loss of 1.60% from 330 to 480 °C, a DSC signal of an exothermal phase transformation at 480 °C, and the XRD measurements presented in this report (see Figure 3 and Figure 4) indicate the presence of Mn_5O_8. This mass loss again is lower than the expected value of 2.03% for a complete conversion of Mn_5O_8 to α-Mn_2O_3, which indicates that less α-Mn_2O_3 is formed from Mn_5O_8 than expected. Hence, in an O_2/Ar atmosphere, α-Mn_2O_3 is generated partially from Mn_5O_8 and partially by direct oxidation from Mn_3O_4.

The increase and decrease in mass in the presence of gaseous O_2 was proposed to be due to slow seed crystal oxidation of Mn_3O_4 to Mn_5O_8 for particles with BET surfaces larger than

Figure 6: a) TGA measurements recorded while heating the Mn(II) glycolate precursor up to 700 °C at 2 K/min in an Ar (black) and an O_2/Ar (1:2) (red) flow of 40 NmL/min; b) detailed view of the temperature range between 250 and 500 °C of the TGA (red) and DSC (blue) measurements in O_2/Ar (1:2) flow indicating the oxidation of Mn_3O_4 to Mn_5O_8 and α-Mn_2O_3.
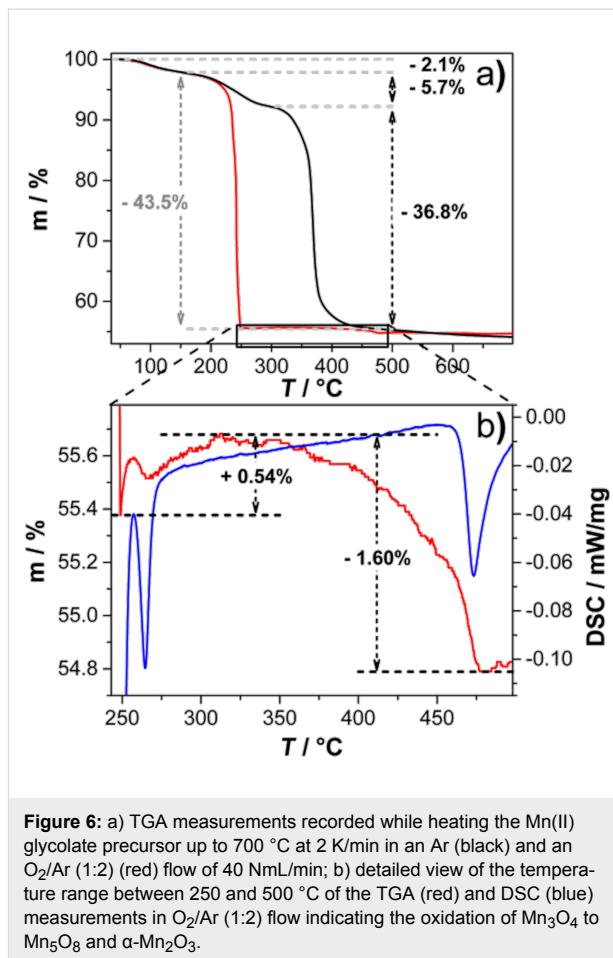
10 m^2/g and their subsequent transformation to α-Mn_2O_3 [29,30].

In order to characterize the size of the particles and the active surface areas, pure Mn_3O_4, Mn_5O_8 and α-Mn_2O_3 species obtained by calcination of the Mn(II) glycolate precursor at temperatures of 350, 400 and 550 °C were characterized by TEM and BET measurements. The TEM images of the Mn_3O_4 and Mn_5O_8 samples are shown in Figure 7a,b; the sizes of the particles observed in TEM are in good agreement with the Scherrer-derived crystallite sizes calculated from the XRD patterns (see Figure 4 for comparison). The Mn_3O_4 sample shown in Figure 7a consists of a network of nanoparticles with diameters less than 10 nm and voids between the particles of about the same size. The same is true for the Mn_5O_8 sample in Figure 7b, but here the nanoparticles with diameters of up to 30 nm are obviously packed more densely. We attribute this to the increased temperature and duration of the calcination process, as well as to the presence of O_2 in the atmosphere, which leads to larger particles, as previously discussed (see discussion for Figure 4). The α-Mn_2O_3 sample obtained by calcination in an Ar atmosphere (see Figure 7c,d), however,

contains splinter-like pieces in the μm range (approximately 1–2 μm in the given TEM image) with a high concentration of holes with diameters of up to 20 nm, rather than individual nanoparticles. This manner of porosity for α-Mn_2O_3 was also confirmed by N_2 adsorption–desorption measurements (see Figure 8). Mesoporosity in hexagonally shaped α-Mn_2O_3 particles and circular Mn_2O_3 discs obtained by calcination at temperatures above 600 °C was reported by several groups [17,37]. Ren et al. suggested that the mesopores are derived from a sequence of processes including Mn_5O_8 nanoparticle growth, rearrangement and merging during the transformation to α-Mn_2O_3 [37]. As the phase of Mn_5O_8 was not observed after calcination in Ar atmosphere, we propose that the presence of pores in the α-Mn_2O_3 particles reported here results from the analog growth, rearrangement and merging processes of the Mn_3O_4 nanoparticles.

The considerably smaller size of the crystallites obtained from the broadening of the XRD reflections of α-Mn_2O_3 is another argument for the porosity of these particles, as the pore walls in this case represent boundaries of the crystalline domains. Because these domains are regarded as Scherrer crystallites, we conclude that the obtained sizes are the mean distances between the pores as well as the minimum diameter of the α-Mn_2O_3 particles.

From the isotherms recorded during N_2 adsorption–desorption measurements (see Figure 8a) specific BET surface areas of 302, 30 and 20 m^2/g were calculated for the Mn_3O_4, Mn_5O_8 and α-Mn_2O_3 samples, respectively. The porosity of the α-Mn_2O_3 particles observed in the TEM images (see Figure 7c,d) is also supported by the N_2 adsorption–desorption isotherms, which exhibit hysteresis. As hysteresis is also

Figure 7: TEM images of the a) Mn_3O_4, b) Mn_5O_8, and c) and d) α-Mn_2O_3 samples.

Figure 8: a) N$_2$ adsorption–desorption isotherms (volume adsorbed versus relative pressure, P/P_0) and b) the corresponding pore size distributions of the (A) Mn$_3$O$_4$, (B) Mn$_5$O$_8$ and (C) α-Mn$_2$O$_3$ samples.

Figure 7c,d for comparison) and the lowest BET surface area of all the samples, these pores do not derive from voids in the nanoparticle network but rather from the mesoporosity of the splinter-like pieces. A surface area of approximately 20 m^2/g and pore diameters from 4 to 7 nm were also reported for Mn$_2$O$_3$ discs synthesized for the use as electrode material by Zhang et al. [17]. However, we believe a larger pore size to be advantageous for application as electrocatalysts, as electrochemical processes often produce solid products, which might easily clog pores in the micro- and meso-porous range.

The specific surface areas of Mn$_3$O$_4$ and Mn$_5$O$_8$ are in good agreement with the sizes of the particles observed in the TEM images and calculated from the XRD patterns, as smaller particles generally exhibit larger surface areas. However, the α-Mn$_2$O$_3$ particles, which are one order of magnitude larger, exhibit a high specific BET surface area comparable to that of the Mn$_5$O$_8$ nanoparticles. Two explanations for this large specific surface are proposed: the lower molar weight of α-Mn$_2$O$_3$ compared to Mn$_5$O$_8$ (resulting in a larger specific surface area), and the mesoporosity of the α-Mn$_2$O$_3$, which was already observed in the TEM images (see Figure 7c,d).

Electrocatalytic activities of the MnO$_x$ species

In order to investigate the electrocatalytic activity of the synthesized MnO$_x$ species for the oxygen reduction reaction (ORR), linear sweep measurements were carried out.

Figure 9 shows linear sweep measurements recorded at 50 mV/s comparing the activity of various 10% MnO$_x$/carbon electrodes to a pure carbon electrode as a reference material for the ORR in aprotic electrolyte. The ORR peak potentials as well as the apparent reaction rate constant, k_{app}^0, for the different electrode materials are summarized in Table 2. The reaction rate constant was calculated from:

$$j_0 = n \cdot F \cdot C_{O2} \cdot k_{app}^0, \qquad (1)$$

where j_0 is the cathodic exchange current density (obtained from the Tafel plots of the linear sweep measurements), $n = 1$ is the number of transferred electrons, F is the Faraday constant, and $C_{O2} = 2.1\cdot10^{-6}$ mol cm^{-3} is the oxygen solubility in DMSO [39].

The mean ORR peak potential of the carbon reference material given in Table 2 is observed at 2.58 V. The only MnO$_x$ species with a significant increase of the ORR potential of 100 mV with respect to the carbon as well as the other MnO$_x$/C electrodes is the mesoporous α-Mn$_2$O$_3$ catalyst. The obvious activity is

observed in the Mn$_3$O$_4$ and Mn$_5$O$_8$ nanoparticle isotherms (but not supported by observations made in the TEM images for these species, see Figure 7a,b), two different definitions of porosity can be applied for the different manganese oxide species. The pore size distributions depicted in Figure 8b show a pore diameter distribution between 3 and 20 nm with a mean pore diameter of 8.2 nm for the Mn$_3$O$_4$ sample. The porosity of the Mn$_3$O$_4$ nanoparticles can be explained by considering the voids between the particles in the network as the "pores" detected in the N$_2$ adsorption–desorption measurements. This assumption is in good agreement with the similar sizes of the voids and nanoparticles observed in the TEM image (compared with Figure 7a). The same "pore definition" can be applied to the Mn$_5$O$_8$ sample exhibiting pore sizes between 3 and 5 nm with a comparably small mean pore size of 4.2 nm, probably due to the dense network of the particles observed in the TEM image (compared to Figure 7b). The α-Mn$_2$O$_3$ sample does not contain nanoparticles, but exhibits a pore size distribution between 3 and 5 nm as well as 10 and 90 nm with a mean diameter of 32.6 nm. In accordance with the TEM images (see

Figure 9: Linear sweep voltammograms of pure carbon powder (grey), Mn_3O_4/C (black), Mn_5O_8/C (red) and α-Mn_2O_3/C (blue) electrodes; electrolyte: 1 M LiTFSI/DMSO, cathodic scan direction, v = 50 mV/s, ω = 200 rpm.
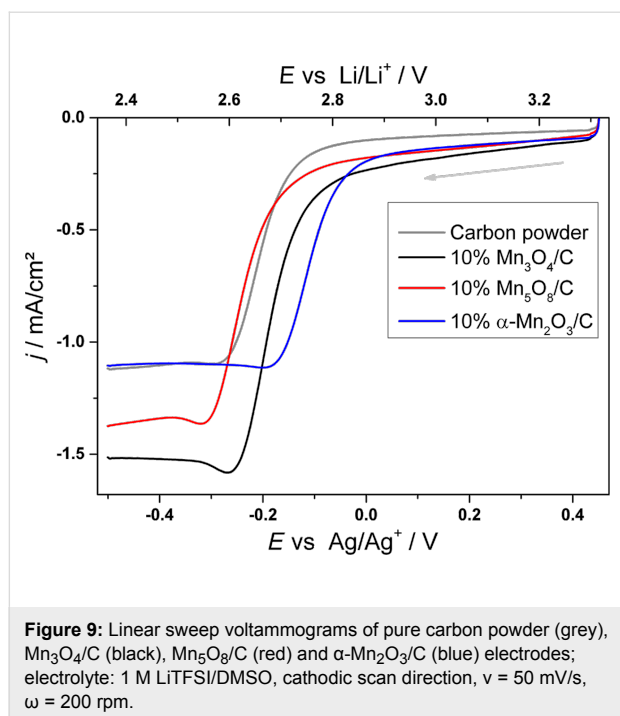
Table 2: ORR potentials and reaction rate constants obtained from the linear sweep measurements recorded at v = 50 mV/s.

	E_{peak} vs Li/Li$^+$ [V]	k^0_{app} [10^{-4} cm/s]
Carbon (C)	2.58 ± 0.02	1.2 ± 1.1
Mn_3O_4/C	2.58 ± 0.08	2.6 ± 1.3
Mn_5O_8/C	2.58 ± 0.07	2.7 ± 2.3
α-Mn_2O_3/C	2.68 ± 0.05	4.5 ± 2.5

reflected in the approximately four- and two-fold larger apparent ORR rate constant k^0_{app} compared to the carbon and the other MnO$_x$/C electrodes, respectively.

A detailed kinetic and mechanistic study on the electrocatalytic activities of the different MnO$_x$ species for the aprotic oxygen reduction reaction is reported elsewhere [40].

Conclusion

In summary, a polyol synthesis was presented yielding rectangular, Mn(II) glycolate nanoparticles with dimensions of 17 ± 8 nm. Particle sizes of less than 100 nm are reported here for the first time. We attribute this small size of the particles to the stabilizing tetraethylene glycol ligand used during the synthesis, as well as milder reaction conditions compared with other reports (i.e., a decreased temperature and a longer reaction time). In situ XRD measurements showed the sequence of time- and temperature-dependent phase transformations during oxidation of the Mn(II) glycolate precursor to α-Mn_2O_3 via Mn_3O_4 and Mn_5O_8 in O_2 atmosphere. Structural and morphological investigations revealed the dependence of the lattice constants and particle sizes of the MnO$_x$ species on the calcination temperatures in a range from 320 to 550 °C as well as on Ar and O_2 atmospheres. Based on the results of these measurements, several manganese oxide species were synthesized by calcination of Mn(II) glycolate particles in argon and oxygen atmosphere at different temperatures. The calcination process yielded Mn_3O_4 nanoparticles with dimensions of about 10 nm and a surface area of 302 m^2/g, Mn_5O_8 nanoparticles with diameters of 22 nm and a surface area of 30 m^2/g as well as mesoporous α-Mn_2O_3 particles with mean pore diameters of about 33 nm and a surface area of 20 m^2/g. The small dimensions of the particles and large surface areas of the manganese oxides presented here result from use of nanostructured precursor particles. Linear sweep measurements showed the activity of the mesoporous α-Mn_2O_3 species for the oxygen reduction reaction in aprotic media with respect to the observed potentials as well as an enhanced kinetic activity. The catalytic activity of different manganese oxides can be enhanced by a larger surface area, resulting from small particle dimensions or mesoporosity. This makes our synthesis a suitable process to obtain manganese oxides having properties of particular interest for electrochemical and chemical catalysis. Furthermore, the synthesis of manganese oxides via one route reported here is of additional interest, as it excludes any synthesis-caused effects on the products and allows investigation on the catalytic effect of similarly synthesized manganese oxides with different properties.

Experimental
Materials

Manganese(II) acetate tetrahydrate ($MnAc_2$, >99%, pure) and ethylene glycol (EG, >99.5%, p.a.) were purchased from Carl-Roth. Tetraethylene glycol (TEG, 99%) was delivered by Sigma-Aldrich. For the electrode preparation, a 10 wt % Nafion®/water solution was purchased from Sigma-Aldrich, analytical reagent-grade ethanol from Fisher Scientific, and Vulcan® XC72R carbon powder was obtained from Cabot. For electrochemical measurements, reagent-grade lithium bis(trifluoromethylsulfonyl)imide (LiTFSI) was purchased from Merck KGaA and dimethyl sulfoxide (DMSO, anhydrous, ≥99.9%) from Sigma-Aldrich. All chemicals were used without further purification.

Synthesis of Mn(II) glycolate

In a typical reaction, 1 mmol (0.246 g) $MnAc_2$ was mixed with 3 mmol (3 mL) TEG and added to 30 mL EG in a three-neck round-bottom flask. The solution was heated to 170 °C while stirring. Upon heating, the solution turned brown at a tempera-

ture of about 110 °C, and after further heating for about 1 h at 170 °C, a white precipitate appeared that disappeared again after 1 h. The solution was stirred for another 4 h at 170 °C until a white precipitate appeared again which indicated the formation of the Mn(II) glycolate particles. The product was stirred for another hour at 170 °C to complete the reaction and was subsequently cooled down to room temperature. The white powder was centrifuged and washed at least five times with ethanol to remove any impurities. Subsequently, the white product was dried under Ar flow.

Synthesis of Mn_3O_4, Mn_5O_8 and α-Mn_2O_3

The obtained Mn(II) glycolate powder was calcined in an Ar flow of 50 NL/h for 2 h at 350 °C and at 550 °C yielding Mn_3O_4 and α-Mn_2O_3, respectively. Mn_5O_8 was obtained by calcination of the precursor in an O_2 flow of 50 NL/h for 5 h at 400 °C.

Characterization methods

Transmission electron microscopy (TEM) was carried out with a Zeiss EM 902A microscope with an acceleration voltage of 80 kV. For high resolution TEM (HR-TEM) measurements a JEOL JEM2100F microscope with an acceleration voltage of 200 kV was used. The samples for TEM and HR-TEM measurements were prepared by depositing a drop of an ethanol emulsion of the powder on a carbon-coated copper grid and drying at room temperature.

Scanning electron microscopy (SEM) was carried out with an Oxford INCA system employing a PentaFET Precision INCA X-act detector integrated into the Hitchai S-3200N microscope. The sample was prepared by depositing an ethanol emulsion of the sample onto an Al substrate and drying at room temperature.

For X-ray diffraction (XRD), a PANalytical X'Pert Pro MPD diffractometer was used operating with Cu Kα radiation, Bragg-Brentano θ-2θ geometry and a goniometer radius of 240 mm. Samples for XRD measurements were prepared by placing the powder onto low-background silicon sample holders. Different atmospheres were used as mentioned in the text. The crystallite sizes of the samples were calculated from all assigned reflections via the Scherrer equation. The lattice parameters were obtained with the Bragg equation from assigned diffraction reflections.

In situ XRD measurements were performed in the same geometry using a high temperature chamber from Anton Paar (HTK 1200N). The temperature profile measurement was recorded while heating the powder sample from 25 to 700 °C with a heating rate of 2 K/min. The time profile measurement (shown in Supporting Information File 1) was conducted by heating the

powder sample from 25 to 400 °C with a heating rate of 18 K/min and subsequent constant heating at 400 °C for 350 min. The powder sample was placed on a corundum sample holder. During the measurement the thermal expansion was corrected automatically. The measurements were performed in an O_2 flow.

Thermogravimetric analysis (TGA) and differential scanning calorimetry (DSC) were carried out with a Netzsch STA 449 F3 Jupiter thermo-analysis system. The sample was deposited in an Al_2O_3 crucible and heated from 35 to 700 °C with a heating rate of 2 K/min in an $O_2(6.0)/Ar(5.0)$ (1:2) and an Ar(5.0) gas flow of 40 NmL/min.

The porosity of the manganese oxides was determined by N_2 adsorption–desorption measurements. Prior to the measurement, the material was kept for 18 h at 180 °C under vacuum to remove any residual gas and moisture from the sample. The adsorption–desorption isotherms were measured employing a Quantachrome Nova 2000E device at 77 K. The Brunauer–Emmet–Teller (BET) method was used to determine the complete inner surfaces S_0 and the Barrett–Joyner–Halenda (BJH) method for mesopore surface analysis as well as the determination of pore size distributions.

Electrode preparation

The catalyst/carbon ink for the powder electrodes was prepared by mixing and grinding 90 mg Vulcan® XC72R carbon powder with 10 mg of MnO_x catalyst. This active material was dispersed in ethanol and ultrasonicated for 20 min. As a binder material, 0.1 wt % Nafion/water solution was added to the catalyst/carbon paste and ultrasonicated for another 20 min. A 10 µL drop of the ink was applied on a glassy carbon disc ($d = 0.5$ cm) and dried for 12 h at 80 °C. The 10 wt % catalyst loading of the prepared electrodes equals 4.8 µg per electrode or 24.4 µg cm^{-2}.

Electrochemical measurements

For linear sweep voltammetry measurements, a Gamry Instruments Reference 600 Potentiostat was used. The measurements were carried out on a rotating disc electrode (RDE) in a glove box in Ar atmosphere at ambient temperature. For the electrochemical setup, glassy carbon (Pine Research Instrumentation, electrode model no. AFE3T050GC) and carbon/catalyst-coated glassy carbon discs (see above) served as working electrodes. A polished Ag wire and a Pt disc were used as reference and counter electrodes, respectively. 1 M LiTFSI/DMSO was used as the electrolyte, which was saturated with pure O_2 for 25 min before the start of the measurement. The linear sweep measurements were recorded at a scan rate of $v = 50$ mV/s and a rotational frequency of $ω = 200$ rpm.

Supporting Information

The supporting information features the powder XRD pattern of Mn(II) glycolate particles after 1 h of synthesis at 170 °C in addition to in situ XRD patterns of the time-dependent oxidation of Mn_3O_4 to Mn_5O_8 at 400 °C in O_2.

Supporting Information File 1

Additional XRD experimental data.
[http://www.beilstein-journals.org/bjnano/content/supplementary/2190-4286-6-6-S1.pdf]

References

1. Owens, B. B.; Passerini, S.; Smyrl, W. H. *Electrochim. Acta* **1999,** *45,* 215–224. doi:10.1016/S0013-4686(99)00205-4
2. Park, K.-W. *J. Mater. Chem. A* **2014,** *2,* 4292–4298. doi:10.1039/c3ta14223j
3. Xu, M.-W.; Niu, Y.-B.; Bao, S.-J.; Li, C. M. *J. Mater. Chem. A* **2014,** *2,* 3749–3755. doi:10.1039/c3ta14211f
4. Gil, A.; Gandía, L. M.; Korili, S. A. *Appl. Catal., A* **2004,** *274,* 229–235. doi:10.1016/j.apcata.2004.07.004
5. Mellan, T. A.; Maenetja, K. P.; Ngoepe, P. E.; Woodley, S. M.; Catlow, C. R. A.; Grau-Crespo, R. *J. Mater. Chem. A* **2013,** *1,* 14879–14887. doi:10.1039/c3ta13559d
6. Feng, Q.; Kanoh, H.; Ooi, K. *J. Mater. Chem.* **1999,** *9,* 319–333. doi:10.1039/a805369c
7. Kapteljn, F.; Singoredjo, L.; Andreini, A.; Moulijn, J. A. *Appl. Catal., B: Environ.* **1994,** *3,* 173–189. doi:10.1016/0926-3373(93)E0034-9
8. Xiao, J.; Wan, L.; Wang, X.; Kuang, Q.; Dong, S.; Xiao, F.; Wang, S. *J. Mater. Chem. A* **2014,** *2,* 3794–3800. doi:10.1039/c3ta14453d
9. Su, H.-Y.; Gorlin, Y.; Man, I. C.; Calle-Vallejo, F.; Nørskov, J. K.; Jaramillo, T. F.; Rossmeisl, J. *Phys. Chem. Chem. Phys.* **2012,** *14,* 14010–14022. doi:10.1039/c2cp40841d
10. Ramírez, A.; Friedrich, D.; Kunst, M.; Fiechter, S. *Chem. Phys. Lett.* **2013,** *568–569,* 157–160. doi:10.1016/j.cplett.2013.03.054
11. Najafpour, M. M.; Rahimi, F.; Amini, M.; Nayeri, S.; Bagherzadeh, M. *Dalton Trans.* **2012,** *41,* 11026–11031. doi:10.1039/c2dt30553d
12. Ogasawara, T.; Débart, A.; Holzapfel, M.; Novák, P.; Bruce, P. G. *J. Am. Chem. Soc.* **2006,** *128,* 1390–1393. doi:10.1021/ja056811q
13. Débart, A.; Bao, J.; Armstrong, G.; Bruce, P. G. *J. Power Sources* **2007,** *174,* 1177–1182. doi:10.1016/j.jpowsour.2007.06.180
14. Giordani, V.; Freunberger, S. A.; Bruce, P. G.; Tarascon, J.-M.; Larcher, D. *Electrochem. Solid-State Lett.* **2010,** *13,* A180–A183. doi:10.1149/1.3494045
15. Cheng, H.; Scott, K. *Appl. Catal., B: Environ.* **2011,** *108–109,* 140–151. doi:10.1016/j.apcatb.2011.08.021
16. Jung, K.-N.; Riaz, A.; Lee, S.-B.; Lim, T.-H.; Park, S.-J.; Song, R.-H.; Yoon, S.; Shin, K.-H.; Lee, J.-W. *J. Power Sources* **2013,** *244,* 328–335. doi:10.1016/j.jpowsour.2013.01.028
17. Zhang, Y.; Yan, Y.; Wang, X.; Li, G.; Deng, D.; Jiang, L.; Shu, C.; Wang, C. *Chem. – Eur. J.* **2014,** *22,* 6126–6130. doi:10.1002/chem.201304935
18. Lei, S.; Tang, K.; Fang, Z.; Liu, Q.; Zheng, H. *Mater. Lett.* **2006,** *60,* 53–56. doi:10.1016/j.matlet.2005.07.070
19. Liu, L.; Yang, Z.; Liang, H.; Yang, H.; Yang, Y. *Mater. Lett.* **2010,** *64,* 891–893. doi:10.1016/j.matlet.2010.01.054
20. Azzoni, C. B.; Mozzati, M. C.; Galinetto, P.; Paleari, A.; Massarotti, V.; Capsoni, D.; Bini, M. *Solid State Commun.* **1999,** *112,* 375–378. doi:10.1016/S0038-1098(99)00368-3
21. Cushing, B. L.; Kolesnichenko, V. L.; O'Connor, C. J. *Chem. Rev.* **2004,** *104,* 3893–3946. doi:10.1021/cr030027b
22. Gui, Z.; Fan, R.; Mo, W.; Chen, X.; Yang, L.; Hu, Y. *Mater. Res. Bull.* **2003,** *38,* 169–176. doi:10.1016/S0025-5408(02)00983-2
23. Javed, Q.; Feng-Ping, W.; Rafique, M. Y.; Toufiq, A. M.; Iqbal, M. Z. *Chin. Phys. B* **2012,** *21,* 117311–117317. doi:10.1088/1674-1056/21/11/117311
24. Yuan, Z.-Y.; Ren, T.-Z.; Du, G.; Su, B.-L. *Chem. Phys. Lett.* **2004,** *389,* 83–86. doi:10.1016/j.cplett.2004.03.064
25. Liu, L.; Yang, H.; Wei, J.; Yang, Y. *Mater. Lett.* **2011,** *65,* 694–697. doi:10.1016/j.matlet.2010.11.042
26. Dhaouadi, H.; Ghodbane, O.; Hosni, F.; Touati, F. *ISRN Spectrosc.* **2012,** *2012,* 1–8. doi:10.5402/2012/706398
27. Gillot, B.; El Guendouzi, M.; Laarj, M. *Mater. Chem. Phys.* **2001,** *70,* 54–60. doi:10.1016/S0254-0584(00)00473-9
28. Dimesso, L.; Heider, L.; Hahn, H. *Solid State Ionics* **1999,** *123,* 39–46. doi:10.1016/S0167-2738(99)00107-1
29. Larcher, D.; Sudant, G.; Patrice, R.; Tarascon, J. *Chem. Mater.* **2003,** *15,* 3543–3551. doi:10.1021/cm030048m
30. Feitknecht, W. *Pure Appl. Chem.* **1964,** *9,* 423–440. doi:10.1351/pac196409030423
31. Oswald, H. R.; Wampetich, M. J. *Helv. Chim. Acta* **1967,** *50,* 2023–2034. doi:10.1002/hlca.19670500736
32. Punnoose, A.; Magnone, H.; Seehra, M. S. *IEEE Trans. Magn.* **2001,** *37,* 2150–2152. doi:10.1109/20.951107
33. Thota, S.; Prasad, B.; Kumar, J. *Mater. Sci. Eng., B* **2010,** *167,* 153–160. doi:10.1016/j.mseb.2010.01.049
34. Chakroune, N.; Viau, G.; Ammar, S.; Jouini, N.; Gredin, P.; Vaulay, M. J.; Fiévet, F. *New J. Chem.* **2005,** *29,* 355–361. doi:10.1039/b411117f
35. Sun, Y.; Hu, X.; Luo, W.; Huang, Y. *J. Mater. Chem.* **2012,** *22,* 19190–19195. doi:10.1039/c2jm32036c
36. Aminoff, G. *Z. Kristallogr., Kristallgeom., Kristallphys., Kristallchem.* **1926,** *64,* 475–490.
37. Ren, T.-Z.; Yuan, Z.-Y.; Hu, W.; Zou, X. *Microporous Mesoporous Mater.* **2008,** *112,* 467–473. doi:10.1016/j.micromeso.2007.10.025
38. Jiang, X.; Wang, Y.; Herricks, T.; Xia, Y. *J. Mater. Chem.* **2004,** *14,* 695–703. doi:10.1039/b313938g
39. Sawyer, D. T.; Chiericato, G., Jr.; Angells, C. T.; Nanni, E. J., Jr.; Tsuchiya, T. *Anal. Chem.* **1982,** *54,* 1720–1724. doi:10.1021/ac00248a014
40. Augustin, M.; Yezerska, O.; Fenske, D.; Bardenhagen, I.; Westphal, A.; Knipper, M.; Plaggenborg, T.; Kolny-Olesiak, J.; Parisi, J. *Electrochim. Acta* **2014,** submitted.

Synthesis and applications of carbon nanomaterials for energy generation and storage

Marco Notarianni[1,2], Jinzhang Liu[3], Kristy Vernon[1] and Nunzio Motta[*1]

Abstract

The world is facing an energy crisis due to exponential population growth and limited availability of fossil fuels. Over the last 20 years, carbon, one of the most abundant materials found on earth, and its allotrope forms such as fullerenes, carbon nanotubes and graphene have been proposed as sources of energy generation and storage because of their extraordinary properties and ease of production. Various approaches for the synthesis and incorporation of carbon nanomaterials in organic photovoltaics and supercapacitors have been reviewed and discussed in this work, highlighting their benefits as compared to other materials commonly used in these devices. The use of fullerenes, carbon nanotubes and graphene in organic photovoltaics and supercapacitors is described in detail, explaining how their remarkable properties can enhance the efficiency of solar cells and energy storage in supercapacitors. Fullerenes, carbon nanotubes and graphene have all been included in solar cells with interesting results, although a number of problems are still to be overcome in order to achieve high efficiency and stability. However, the flexibility and the low cost of these materials provide the opportunity for many applications such as wearable and disposable electronics or mobile charging. The application of carbon nanotubes and graphene to supercapacitors is also discussed and reviewed in this work. Carbon nanotubes, in combination with graphene, can create a more porous film with extraordinary capacitive performance, paving the way to many practical applications from mobile phones to electric cars. In conclusion, we show that carbon nanomaterials, developed by inexpensive synthesis and process methods such as printing and roll-to-roll techniques, are ideal for the development of flexible devices for energy generation and storage – the key to the portable electronics of the future.

Review

The energy future: challenges and opportunities

The demand for energy in the 21st century is increasing due to the increase in the world's population and rapid technological advancement [1]. Today, the worldwide population is using about 17 trillion watts of power with around 4 trillion watts being consumed in the United States alone [2]. Energy experts are predicting that we will need an additional 30 trillion watts by 2050 due to the global population growth and worldwide economic development [3].

Solving this energy demand using more efficient or clean alternative energy sources will not only save the planet from harmful effects caused by pollution but could also reduce disparity and create a more peaceful world [4]. Energy is just one of the many problems that the world is facing but it is probably the most important to be addressed with urgency in order to also solve other offshoot problems. In one of his last talks, Richard E. Smalley, the 1996 Nobel Laureate in Chemistry for the discovery of the fullerene, presented a list named "Top Ten Problems of Humanity for the Next 50 Years" [5]. The list was presented in order of priority as:

1. Energy
2. Water
3. Food
4. Environment
5. Poverty
6. Terrorism and war
7. Disease
8. Education
9. Democracy
10. Population

The energy problem is on the top of the list because, according to Smalley, it directly influences the other problems and thus should be prioritized accordingly by governments worldwide. The first immediate solution to this problem would be to work on energy efficiency programs. With the implementation of such programs, it has been demonstrated that developed nations could already reduce energy consumption by 25% [6].

The majority (about 87%) of energy produced in 2013 was composed of fossil fuels such as oil, gas and coal, which represented the best choice of energy production at competitive costs in the 20th and 21st century (Figure 1) [7]. Unfortunately, It has been proven that fossil fuels have catastrophic consequences for human health [8] and global warming [9] and their reserves are progressively decreasing [10].

Despite the fact that technological advances are able to reduce the amount of kilograms of carbon emitted into the atmosphere as CO_2 per year per watt (Figure 2a), CO_2 emissions continue to increase due to the increase in worldwide energy consumption (Figure 2b) [11]. For example, to stabilize the concentration of CO_2 at 350 ppm (purple line in Figure 2b), ideally, we will need to reduce worldwide carbon emissions to zero by 2050 [12].

It has been estimated that in order to generate about 1/3 of the prospective energy needed by 2050, we should build around 10,000 nuclear plants over the next 36 years [12]! Apart from the costs of building these nuclear plants, nuclear energy has associated risks and hazards. Nuclear plants are in fact very expensive to build, maintain and protect from attack. Not to
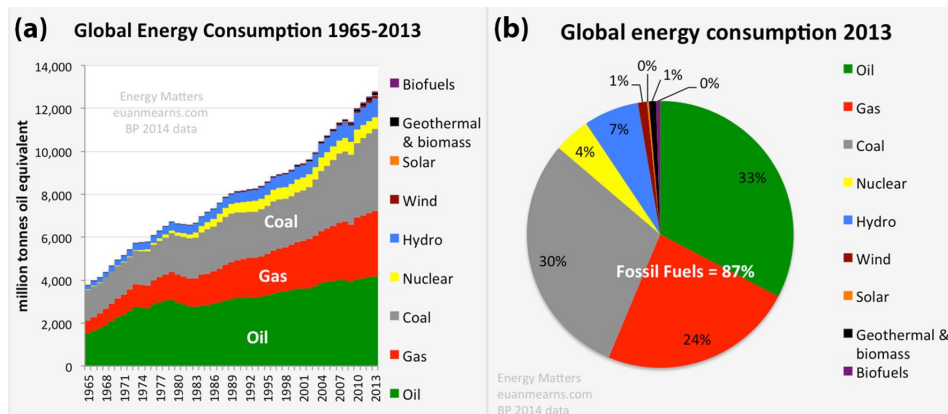
Figure 1: (a) Global energy consumption growth from 1965 to 2013. (b) The share of different energy sources for global energy consumption in 2013 [7].
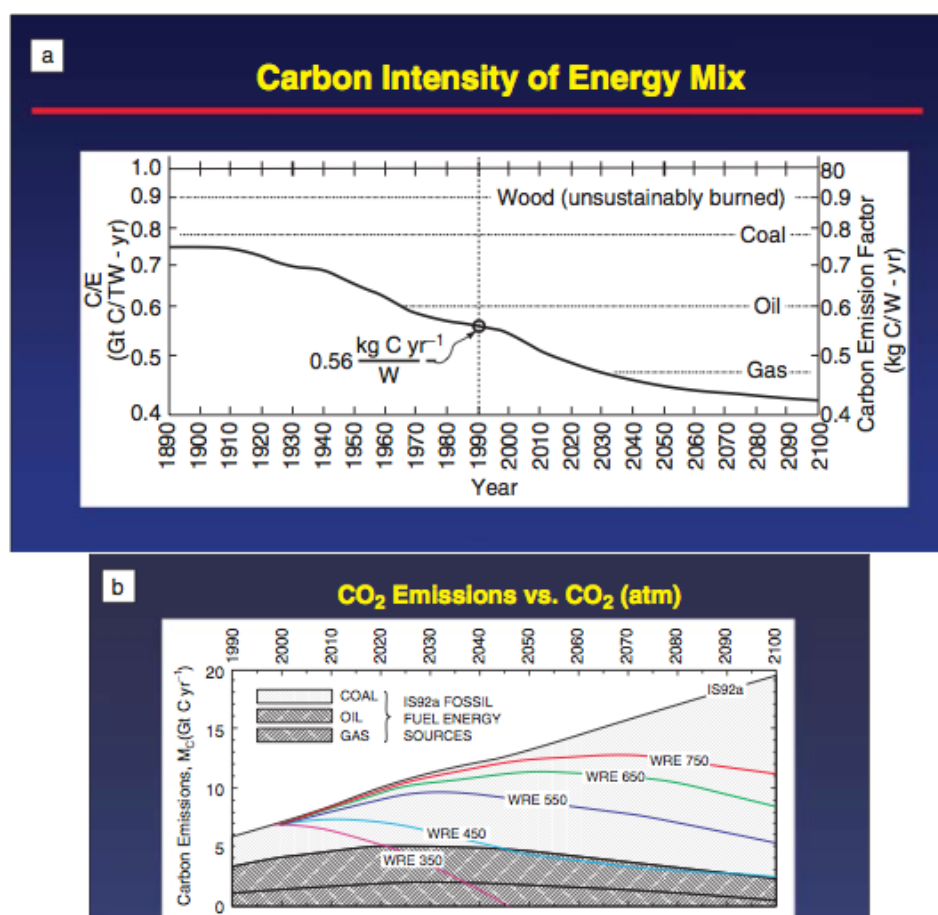
Figure 2: (a) Carbon concentration in the energy mixture from 1890–2100 (projected), i.e., kilograms of carbon emitted into the atmosphere as CO_2 per year per watt of power, produced from combined sources of fuel. The average in 1990 is shown as an open circle on the carbon intensity curve. Reprinted with permission from [11]. Copyright (1998) Nature Publishing Group. (b) CO_2 emissions versus CO_2 in the atmosphere, projected through 2100. Reprinted with permission from [12]. Copyright (2011) Cambridge University Press.

mention that the disposal of nuclear waste has still not been resolved, leaving problems for future generations to deal with [13].

Renewable energy represents the easiest way to produce clean and safe energy but included only 10% of the resources used in 2013 (Figure 1). Unfortunately, the cost of producing energy from renewable sources is still high. However, costs are decreasing, allowing these technologies to be considered in the near future when the price of fossil fuels increase due to their scarcity. Among all of the renewable energy resources available, including hydroelectricity, geothermal energy, wind energy, biomass and others, solar energy likely represents the best renewable resource. In fact, the biggest nuclear reactor that we can even imagine is the sun, which has provided energy to the earth for over 4 billion years and provides more energy in one hour than all of the energy consumed on our planet in an entire year. On Earth, we receive about 170,000 trillion watts of electromagnetic radiation. Therefore, covering 0.16% of the

land on earth with 10% efficient solar conversion systems would provide over 20 trillion watts of power [3]. However, apart from the costs of this technology at the moment ($0.20–0.50 per kW·h), building solar farms in remote areas is not without problems. In fact, the advantage of oil in the last century (and still today) is its transportability across oceans without the need to build expensive infrastructure. For example, the price per gallon of gas includes less than 10% of the transportation cost to the gas station [12]. On the other hand, the cost of building solar farms is very high when infrastructure is factored into the transport of the electricity from remote desert areas to the urban centers where 25% of energy is lost in the transportation [3]. Receiving incentives from the government to install photovoltaic systems on private property could be a viable solution to immediately benefit from the energy produced without the construction of additional infrastructure and without transportation losses. However, this could definitely create a sort of energy independence that is not favored by major energy corporations. The energy business is one of the

biggest in the world including companies such as Exxon Mobil (which was listed second in the United States in 2014 for publicly traded companies as having the greatest market capitalization) and Saudi Aramco (an oil state owned company), estimated from \$781 billion to \$7 trillion [14].

The other major problems of solar energy are that it is diffuse (170 W/m^2) and intermittent. This is why concentration and storage become two critical issues to solve in order to make this energy source cost competitive with fossil fuels. The challenge over the next few years will not just be to produce electricity in a safe and clean way but also how to store the energy produced using technologies more efficient and more environmentally friendly than chemical batteries [13]. Creating small-scale energy storage technologies combined with smart grid technologies could help to provide energy to individual households when immediately needed and with a high efficiency.

Nanotechnology could help to solve solar energy's obstacles and meet energy expectations without compromising the environment and human health by creating new devices that are able to generate, store and transport electricity in a clean and more efficient way and with smaller space requirements. Specifically, the use of nanostructured allotrope forms of carbon and derivatives such as fullerenes, carbon nanotubes (CNTs) and graphene have been widely investigated over the past 10 years for energy generation and storage. In particular, the possibility to include these nanostructured materials using lightweight flexible substrates, printable inks, low temperature and ambient pressure fabrication tools allows for a dramatic reduction in production costs [15].

Organic solar cell devices and electrochemical capacitors, also called supercapacitors, based on carbon nanostructures could allow for the fabrication of devices in the near future that could be more efficient and cheaper to produce than conventional silicon solar cells and chemical batteries [16,17]. The potential to produce these devices "in house" with simple tools such as printers, scissors and glue makes these technologies widely accessible, including in developing countries.

Carbon nanomaterials: properties and synthesis

Carbon, one of the most abundant materials found on earth, can be found in nature in its elemental form as graphite, diamond and coal. Its production is about 9 Gt/year for technological applications, constituting the highest production compared to all other elements [18]. Nanostructured allotrope forms of carbon have been intensively investigated in the past two decades because of their unique hybridization properties and sensitivity to perturbation during synthesis, allowing for fine manipulation of the material properties. In particular, carbon can be found in several different hybridization states, each having unique properties (Figure 3). In fact, the chemical, mechanical, thermal and electrical properties of the different allotrope forms are directly correlated to their structure and hybridization state, opening up the possibility to use the same material for a wide range of applications [19]. Herein, the synthesis and application of fullerenes, CNTs and graphene will be discussed for energy generation and storage.

Fullerenes

Fullerenes are allotropes of carbon, also called buckyballs because of their spherical structure. Fullerenes were predicted and theoretically studied before their experimental discovery by Japanese [20] and Russian [21] researchers in the 1970s, but it was only in the mid-1980s that H. Kroto, R. Smalley and R. Curl were able to detect the first fullerene molecule obtained by laser vaporization of carbon from a graphite target using mass spectroscopy [22]. The name fullerene (C$_{60}$) was dedicated to the architect Buckminster Fuller who was famous for designing and building geodesic domes [23]. The C$_{60}$ molecule is composed of hexagonal and pentagonal faces to form a spherical structure similar to a soccer ball with a diameter of ≈10 Å. This icosahedral symmetry was only first experimentally demonstrated in the 1990s by nuclear magnetic resonance [24].
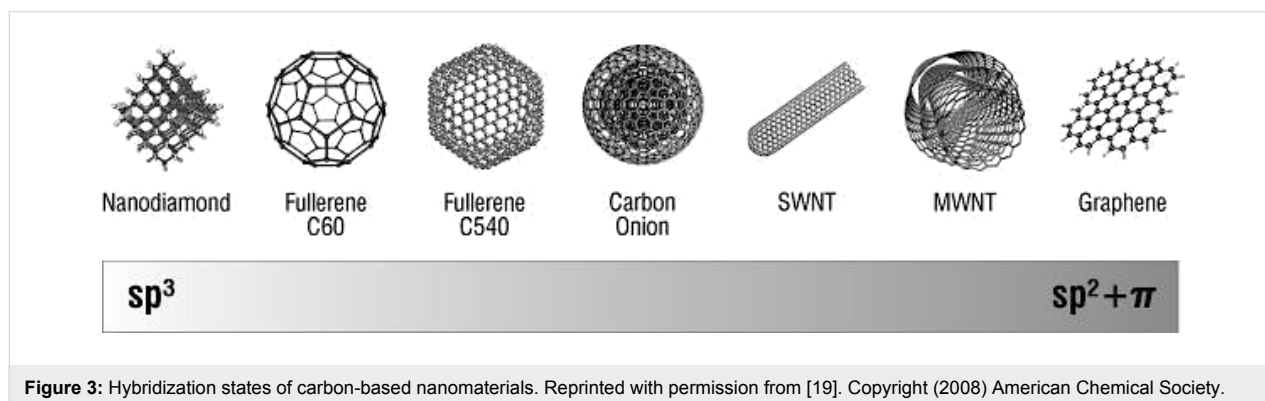
Figure 3: Hybridization states of carbon-based nanomaterials. Reprinted with permission from [19]. Copyright (2008) American Chemical Society.

The C_{60} was the first 0D allotrope of carbon discovered but it is not the only one. In fact, large quantities of C_{70}, C_{76}, C_{78}, C_{84} and even larger clusters, such as C_{240} and C_{330}, have also been synthetized and studied [25]. In particular, C_{70} can be seen as a C_{60} molecule with a belt of five hexagons around the equatorial plane and exhibits a more oval shape (Figure 4) [26].

Figure 4: Structure of the most significant fullerenes, C_{60} and the C_{70}. All fullerenes exhibit hexagonal and pentagonal rings of carbon atoms. Reprinted with permission from [26]. Copyright (2005) John Wiley and Sons.
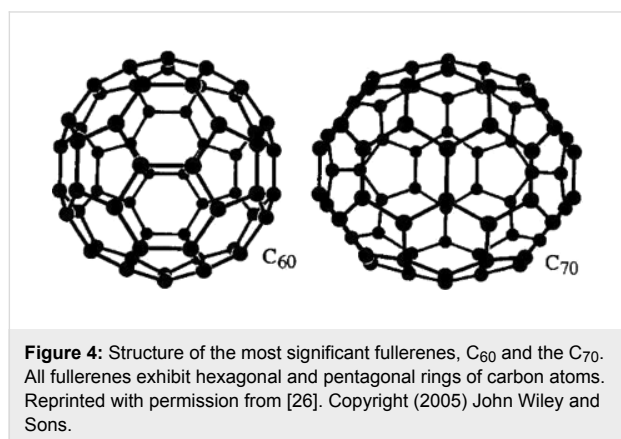
The main properties of C_{60} are [25]:

- Young's modulus, ≈14 GPa
- Electrical resistivity, ≈1014 Ω m
- Thermal conductivity, ≈0.4 W/mK
- Band gap, 1.7 eV

The other fullerene species show similar properties to C_{60}. Depending on the application, different fullerenes are chosen according to their slight differences in properties.

Historically, the first technique to synthesize fullerenes was based on laser ablation of graphite targets in a He gas; however, this does not produce large quantities of the material and is thus mostly used for research studies. The common method to produce large quantities (several grams per day) of fullerenes was first developed by Kratschmer et al. [27] and consisted of an AC arc discharge between high purity graphite rods in 100–200 Torr of helium (He) or Argon (Ar) gas. The temperature required for fullerene formation is about 2000 °C. At this temperature, the electrodes evaporate carbon, forming soot that contains fullerenes, which then condenses on the cool walls of a reactor made of stainless steel or Pyrex [28]. Typically the concentration of fullerenes found in the soot is about 15% (≈13% C_{60} and ≈2% C_{70}). Several setups have been proposed but the one proposed by Bezmelnitsyn et al. [29] is one of the most popular because of the large quantity of material produced. It uses 24 carbon strip, auto-loaded anodes that are subsequently consumed during the process. The cathode consists of a rotating carbon wheel, which passes over a scraper to remove the accumulated carbon powder (Figure 5). This method leads to a fullerene production of about 100–200 g/day.

Another method based on the combustion of benzene in an oxygen deficient environment has been proposed for the formation of C_{60} and C_{70} [30,31]. Benzene diluted with Ar is injected along the central axis of a combustion chamber and oxygen is fed at 12–40 Torr through a large diameter porous plate. The flame chamber is usually composed of a burner and a fuel injection system mounted in the bottom of the chamber. The chamber has viewing ports to monitor the process and to insert the plate where the final material is deposited (Figure 6) [31].

Chemical methods have also been proposed to synthetize fullerenes, but the production yield is so low that it is considered only for research purposes. For example, C_{60} can be produced by the pyrolysis hydrogenation of naphthalene, corannulene or others, but it requires high energy. Dehydrohalogenation of precursors can also be a valid chemical method to form C_{60} from a chloroaromatic compound, as shown for example in Figure 7 [32].

Figure 5: Schematic depiction of an auto-loading version of an arc-discharge apparatus used for fullerene production. Reprinted with permission from [29]. Copyright (1969) Royal Society of Chemistry.
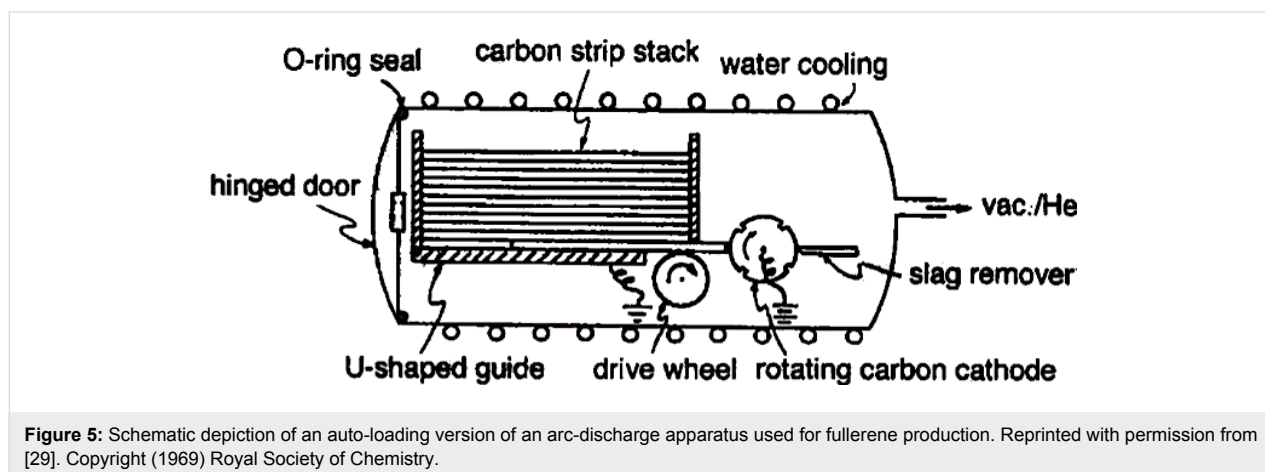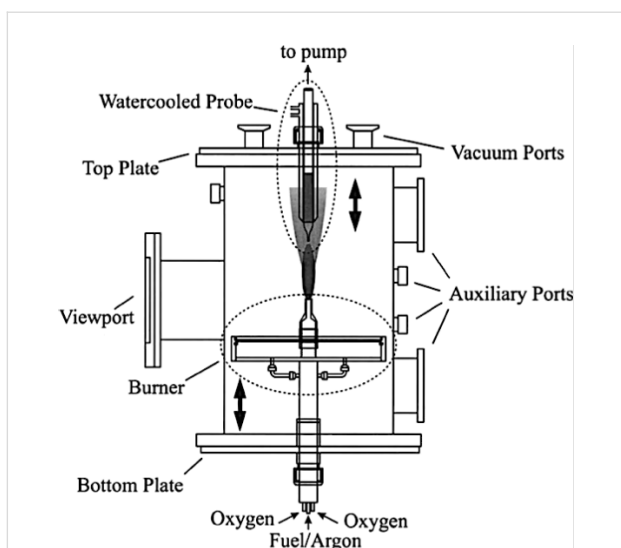
Figure 6: Diffusion flame chamber for fullerene production. Reprinted with permission from [31]. Copyright (2000) Elsevier Limited.

Fullerenes can also be modified by putting dopants inside the structure. Fullerenes with atoms enclosed inside are called "endohedral fullerenes". The endohedral fullerenes are divided into two categories: the endohedral metallofullerenes, where metal atoms (typically transitional metal atoms) are inserted into the structure during the synthesis [33]; and the endohedral nonmetal-doped fullerenes with noble gas such as helium, neon, argon and xenon inserted into the structure [34].

Another fullerene species is the exohedral fullerene or fullerene derivative, which are molecules created by bonding a fullerene with other chemical groups. A typical example of a fullerene derivative is the [6,6]-phenyl-C61-butyric acid methyl ester ($PC_{61}BM$), which is largely used in organic solar cells. Hummelen et al. [35] were the first group to synthesize $PC_{61}BM$ by reacting diazoalcane with a C_{60} to reach the [5,6]fulleroid ester and subsequent isomerization to the [6,6]methanofullerene by refluxing it with *o*-dichlorobenzene solution or with trifluoroacetic acid (Figure 8) [36].
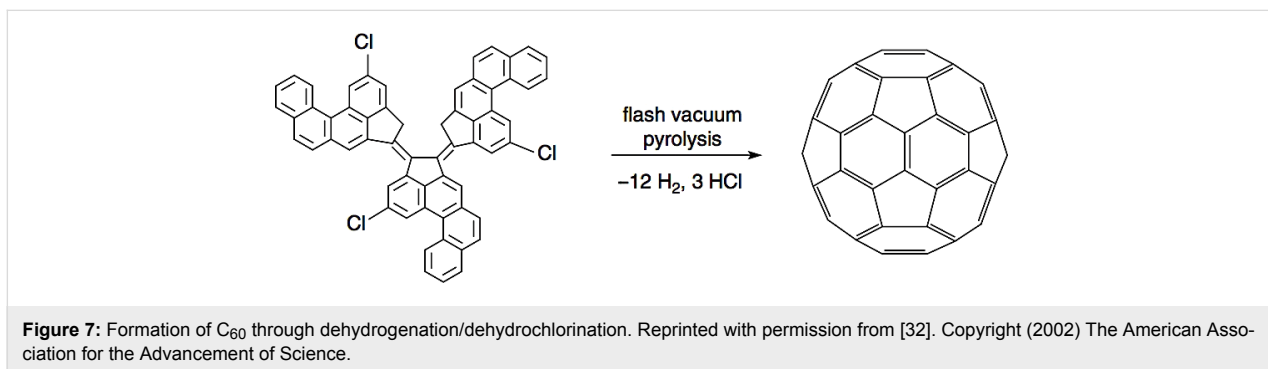
Figure 7: Formation of C_{60} through dehydrogenation/dehydrochlorination. Reprinted with permission from [32]. Copyright (2002) The American Association for the Advancement of Science.
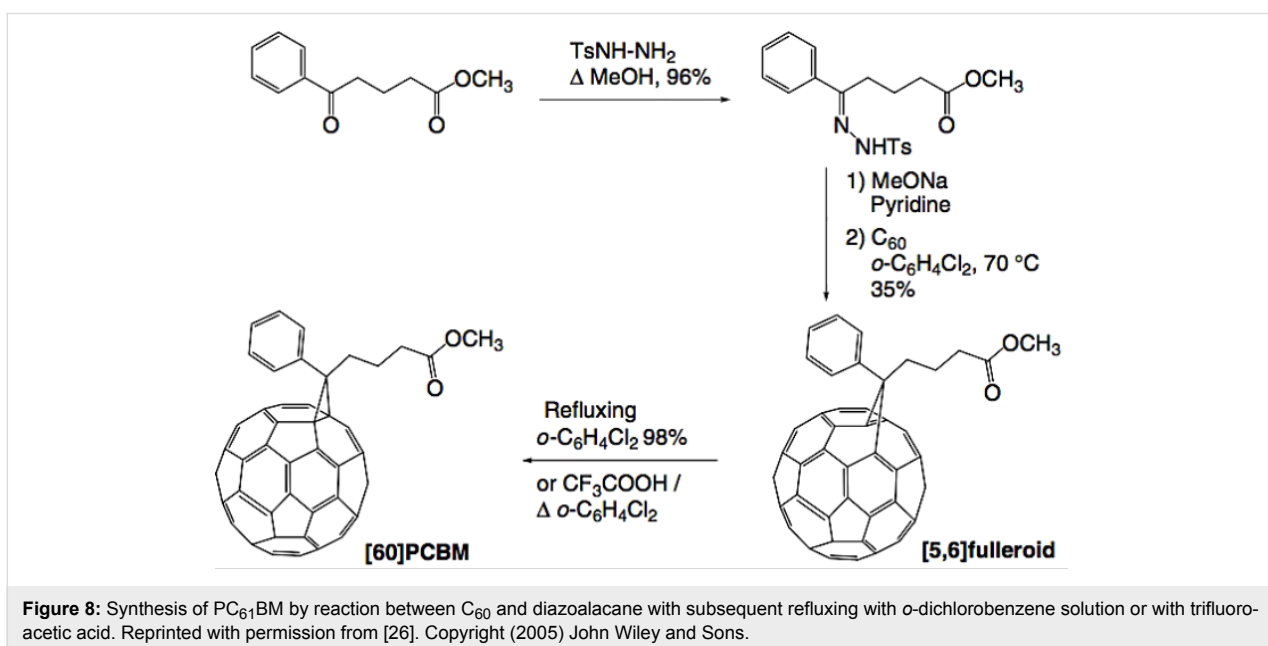
Figure 8: Synthesis of $PC_{61}BM$ by reaction between C_{60} and diazoalacane with subsequent refluxing with *o*-dichlorobenzene solution or with trifluoroacetic acid. Reprinted with permission from [26]. Copyright (2005) John Wiley and Sons.

Carbon nanotubes

Carbon nanotubes (CNTs), discovered by Ijima in 1991 [37], are another allotrope form of carbon with a cylindrical structure. The unique structure of CNTs results in many extraordinary properties. Since the discovery of CNTs, scientists have made great progress in the experimental and theoretical study of their mechanical, electrical and thermal properties. CNTs exhibit remarkable properties including:

- Tensile strength of at least 37 GPa and strain to failure of at least 6% [38,39]
- Young's modulus, ≈0.62–1.25 TPa [40]
- Electrical resistivity, ≈1 μΩ cm [41]
- Thermal conductivity, ≈3000 W/mK [42]

In addition to their extraordinary properties, the density of CNTs is around 1.33–1.4 g/cm^3 [40], which is half of the density of aluminium (2.7 g/cm^3), making them very attractive for lightweight applications.

CNTs are categorized as single-walled carbon nanotubes (SWNTs) and multiwall carbon nanotubes (MWNTs). SWNTs are single graphene sheets rolled up to form a tube, while the MWNTs consist of multiple rolled layers (concentric tubes) of graphene (Figure 9) [43].

The manner in which the graphene wraps is indicated by a chiral vector whose components along the base vectors are defined by indices (n, m). If $m = 0$ the SWNTs are called

Figure 9: Graphene and carbon nanotubes as a (a) single-walled carbon nanotube (SWCNT) and (b) multiwall carbon nanotube (MWCNT) structure [44].
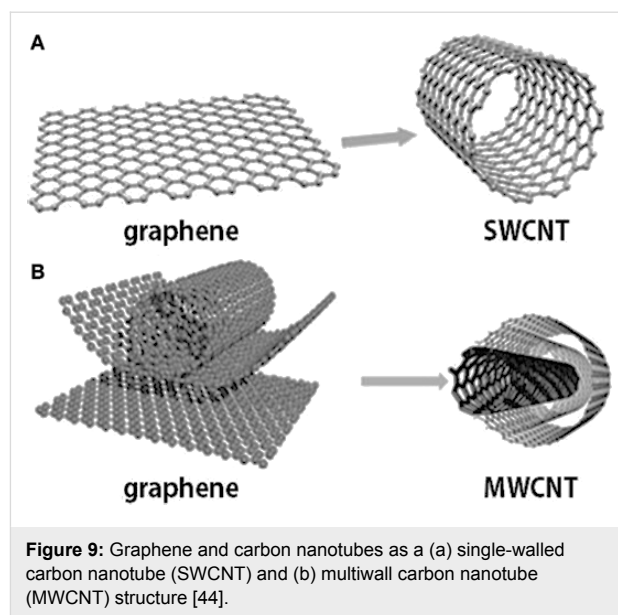
zigzag; if $n = m$, they are armchair, otherwise, they are chiral if $n \neq m$ (see Figure 10) [45].

The chiral vector, identified by the index (n, m), is very important because it strongly affects the electronic properties of the SWNTs. For a given (n, m) nanotube, if $n = m$, the nanotube is metallic; in all other cases, the nanotube is semiconducting with the remarkable situation that when $(n - m)$ is a multiple of 3, the nanotube has a very small band gap [45]. It was also observed that the energy gap scales inversely with the tube diameter [45].

Figure 10: Schematic models for SWCNTs with the nanotube axis normal to the chiral vector, which, in turn, is along: (a) the direction $\vartheta = 30°$ in an armchair (n, n) nanotube, (b) the direction $\vartheta = 0°$ in a zigzag $(n, 0)$ nanotube, and (c) a general ϑ-direction in a chiral (n, m) nanotube.
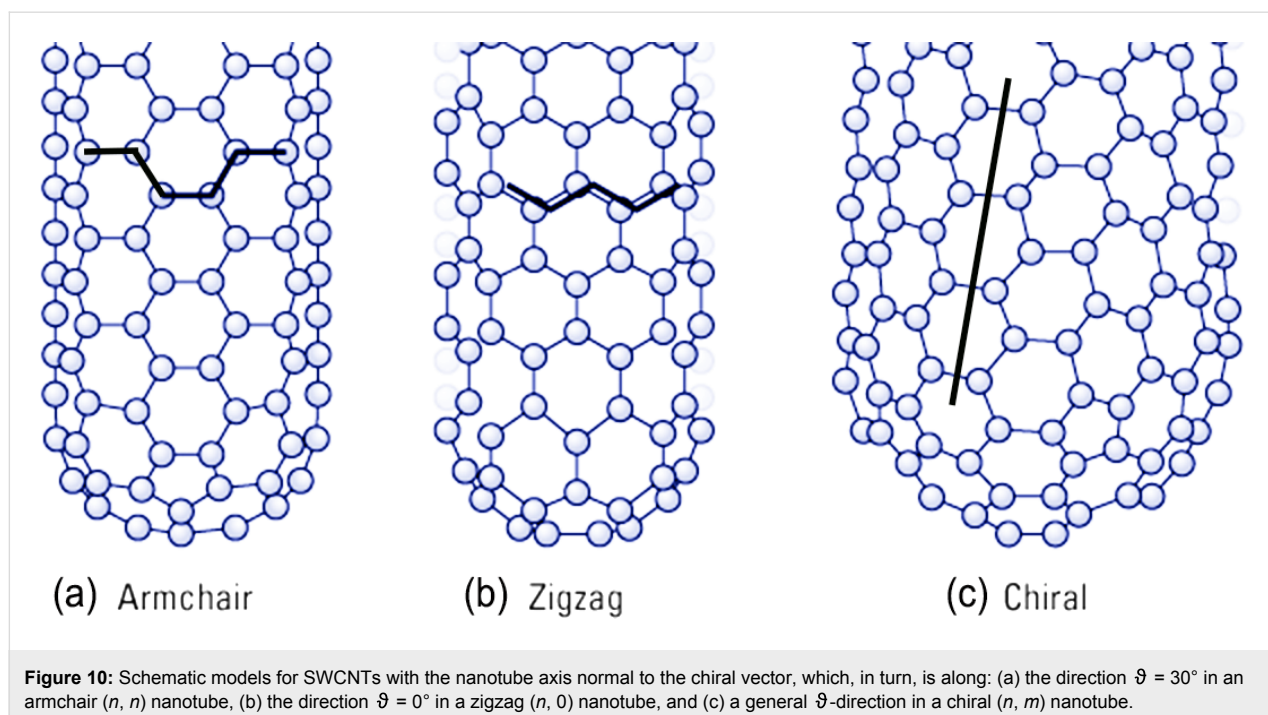
An important feature of the CNTs is that they have a high aspect ratio ($A = 10^{10}$), with $A = l/d$, where l is the length of the CNT that varies from 20 nm to 2 mm and d is the diameter of the CNT (typically 0.3–2 nm) [46].

There are three main methods to synthesize CNTs, each of which have advantages and disadvantages in terms of quality and length of the nanotubes produced, are [47] (Figure 11):

- Arc discharge: higher batch yield (≈1 g/day) as compared to CVD,
- Laser vaporization: higher batch yield (≈1–10 g/day) as compared to CVD, and
- Chemical vapor deposition (CVD): high quality, most common method with low batch yield (≈30 mg/day).

In the arc-discharge method, the carbon is evaporated by helium plasma ignited by high current passed through an opposing carbon anode and cathode. This method requires the use of a metal catalyst such as cobalt [48]. The nanotubes are typically bound together by strong van der Waals interactions and form tight bundles.

The second method, laser ablation, uses continuous wave [49] or pulsed [50] lasers to ablate a carbon target in a 1200 °C tube furnace. A laser beam evaporates a graphite sample containing 1% nickel and cobalt catalyst particles [51]. In the resulting vapor, the metal aggregates into carbon-saturated catalyst nanoparticles, which instigate the growth of CNTs [48]. These catalyst particles are necessary to produce SWNTs rather than MWNTs [52]. The relative amount of SWNTs, MWNTs, and

impurities produced by these methods is dependent on the exact reactor conditions. Impurities include fullerenes, metal catalyst particles encapsulated by graphitic polyhedrons, and amorphous carbon. The majority of impurities can be removed by purification processes based on nitric acid [53]. In both the arc discharge and laser ablation methods, bundles of MWNTs and SWNTs held together by van der Waals forces are generated by the condensation of carbon atoms generated from the evaporation of solid carbon sources.

The third method, chemical vapor deposition (CVD), involves the flow of a hydrocarbon gas over a catalyst in a tube furnace. The catalyst is typically transition metal nanoparticles on a support such as alumina. Materials grown on the catalyst are collected after cooling the furnace to room temperature. The key process parameters are the hydrocarbon and catalyst types, as well as the operating temperature [54]. The production of MWNTs typically involves ethylene or acetylene feedstock with an iron, nickel or cobalt catalyst and operating temperatures of 550–750 °C. SWNTs are produced by using methane or ethane feedstock, similar catalysts, and operating temperatures of 850–1000 °C [55]. Other CVD derivative methods are used that produce CNTs at a reduced growth temperature and increased batch yield. These methods are: plasma-enhanced CVD, where a gas such as C_2H_2, CH_4, C_2H_4, C_2H_6, or CO is supplied to the chamber and a discharge at high frequency is applied in the chamber [56]; laser-assisted thermal CVD, where a continuous wave CO_2 laser with medium power is applied perpendicular to a substrate, then pyrolyses sensitized mixtures of acetylene and $Fe(CO)_5$ vapor in a flow reactor [57]; and high-pressure catalytic decomposition of carbon monoxide
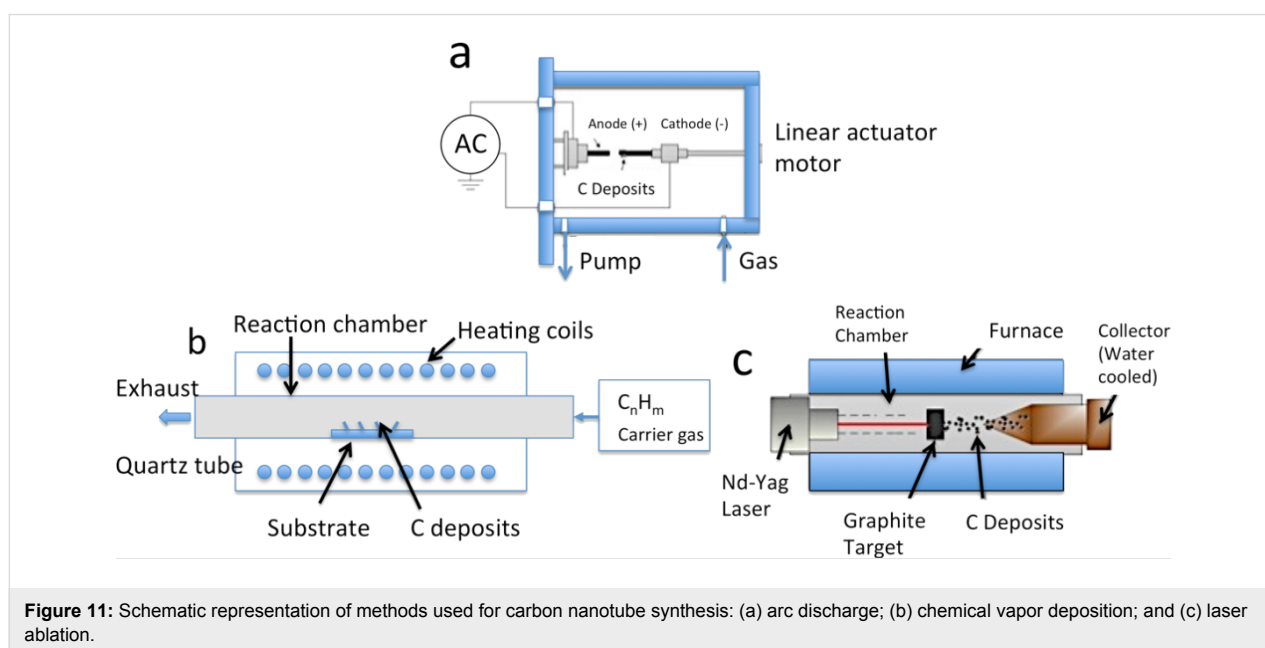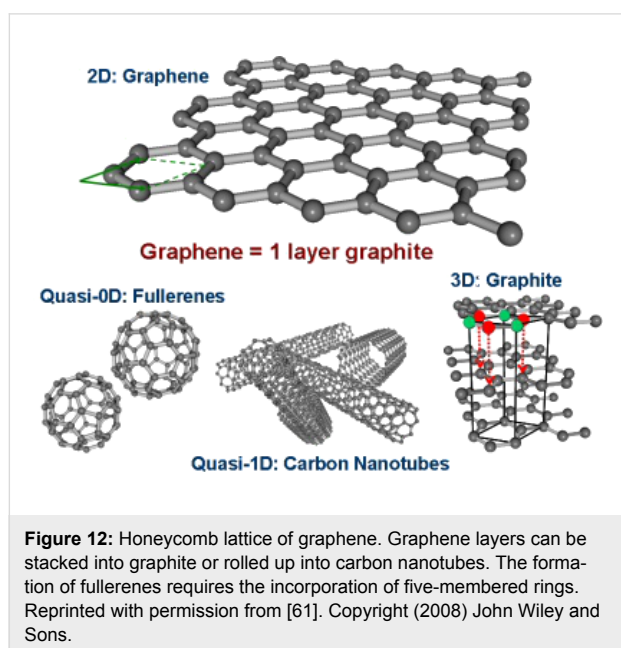

Figure 11: Schematic representation of methods used for carbon nanotube synthesis: (a) arc discharge; (b) chemical vapor deposition; and (c) laser ablation.

(HiPco), where carbon monoxide and catalyst particles generated from the decomposition of $Fe(CO)_5$ flow into a high pressure reactor (up to 10 atm) at temperatures from 800–1200 °C [58]. With the HiPco method, a large yield (>10 g/day) and narrow nanotubes can be produced [59].

Graphene

Despite their excellent electrical, mechanical and thermal properties, CNTs are not the only carbon nanomaterial that could play a major role in replacing conventional materials for energy generation and storage devices. In particular, the discovery of the electrical properties of graphene, another allotrope carbon, by Geim, Novoselov and co-workers [60] opened up the potential of this interesting material to being employed in real-world applications. In fact, graphene shows similar or even better mechanical, thermal and electrical properties than CNTs. Moreover, from an engineering point of view, the production and the usage of graphene could be easier when compared to CNTs. Fewer manufacturing parameters, such as chirality and the nature of the nanotubes (SWNTs vs MWNTs), need to be considered and a larger availability of synthesis processes makes it very attractive in the field of material science.

Graphene is the building block of other important allotropes because it can be stacked to form 3D structures (graphite), rolled to form 1D structures (nanotubes) and wrapped to form 0D structures (fullerenes) (Figure 12) [61]. It consists of a single atomic layer of carbon atoms bonded together in a honeycomb lattice formed by two sublattices, A and B. A single graphene layer has a thickness of 0.34 nm and a carbon–carbon distance of 0.142 nm [60].

Figure 12: Honeycomb lattice of graphene. Graphene layers can be stacked into graphite or rolled up into carbon nanotubes. The formation of fullerenes requires the incorporation of five-membered rings. Reprinted with permission from [61]. Copyright (2008) John Wiley and Sons.

The experimentally measured graphene properties are very close to the theoretically predicted limits: high intrinsic mobility at room temperature (250,000 $cm^2 V^{-1} s^{-1}$) [62,63], high Young's modulus ($\approx$1 TPa) with an intrinsic strength of 130 GPa [64,65], high thermal conductivity (over 3000 W m^{-1} K^{-1}) [66] and excellent optical transmittance ($\approx$97.7%) [67]. Additional graphene characteristics include: high theoretical specific surface area (2630 $m^2 g^{-1}$) [68], impermeability to gases [69], capability to carry high current densities (a million times higher than copper) [70], anomalous quantum Hall effect (QHE) that appears larger than in other materials [71,72], and zero band gap semiconducting properties with one type of electrons and one type of holes [73] that can also be tuned for different electronic applications [74,75].

Most of these extraordinary properties, in particular the electrical and electronic ones, are attributed to the unique band structure that this material has, which was first calculated in 1947 by P. R. Wallace [76]. The valence band, formed by bonding π states and the conduction band, formed by the antibonding $π^*$ states, are orthogonal and they touch only at six points (Dirac points indicated as K and K'). The graphene electron dispersion is linear but also very sensitive to external perturbations that can interact with the π-electron of the system (Figure 13) [77].

It should be mentioned that graphene is not the only 2D material today that offers great performance for a wide range of applications [78]. Boron nitride and molybdenum disulfide are examples of other 2D materials that offer the possibility to tune material and device characteristics for a specific application and can even be used in combination with graphene [79,80].

As mentioned previously, the synthesis processes available today to produce graphene can potentially achieve a better quality material with higher batch yield than CNTs, resulting in increased interest from industry in the development of this technology. There are more than ten processes available to synthesize graphene but only the following five can be reasonably considered in terms of quality and material scalability (Figure 14) [81]:

- Mechanical exfoliation
- Chemical exfoliation
- Chemical exfoliation via graphene oxide
- CVD
- Synthesis on SiC

Each of these methods has its advantages and disadvantages in terms of quality, yield production and applications, as summarized in Table 1. In particular, mechanical exfoliation most

Figure 14: Several methods for the mass production of graphene that allow a wide choice in terms of size, quality and price for any particular application. Reprinted with permission from [81]. Copyright (2012) Nature Publishing Group.
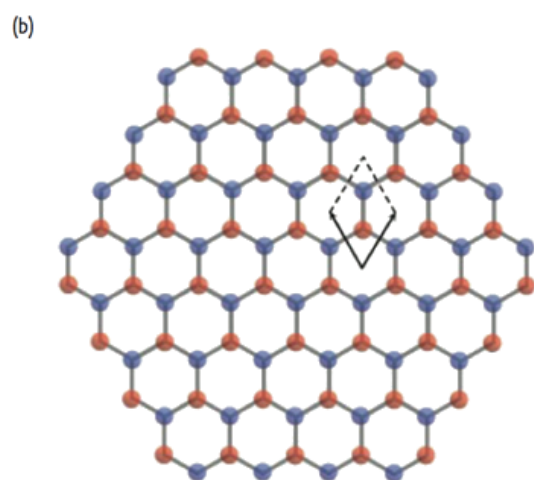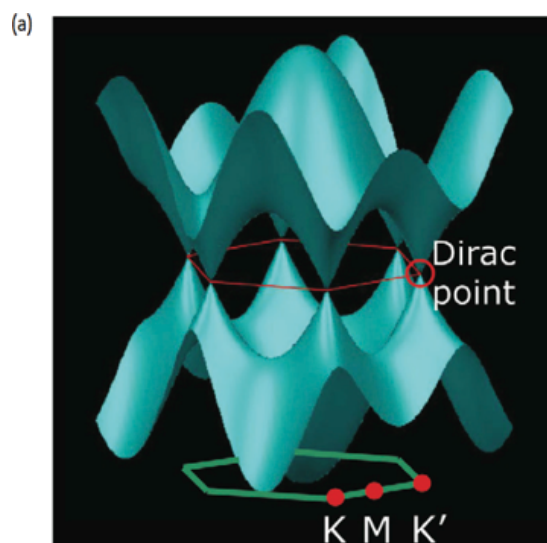
Figure 13: (a) Representation of the electronic band structure and Brillouin zone of graphene; (b) The two graphene sublattices (red and blue) and the unit cell [77].

likely produces the best samples in terms of charge carrier mobility but is probably the worst in terms of scalability. In contrast, CVD methods can produce pristine graphene sheets but only in limited quantities. Large quantities of graphene sheets have recently been obtained with CVD methods using catalytic metal substrates [82,83]. However, associated problems such as harsh conditions (high temperature and high vacuum), complexity of the process, difficulties in transferring to different substrates and high costs still must be resolved. Also, graphene flakes have irregular shapes that require a substrate to control the orientation for high-tech applications [77].

Table 1: Properties of graphene obtained by different methods (from [81]).

Method	Crystallite size (µm)	Sample size (mm)	Charge carrier mobility (ambient temperature) (cm^2 V^{-1} s^{-1})	Applications
Mechanical exfoliation	>1,000	>1	>2 × 10^5 and >10^6 (at low temperature)	Research
Chemical exfoliation	≤0.1	Infinite as a layer of overlapping flakes	100 (for a layer of overlapping flakes)	Coatings, paint/ink, composites, transparent conductive layers, energy storage, bioapplications
Chemical exfoliation via graphene oxide	≈100	Infinite as a layer of overlapping flakes	1 (for a layer of overlapping flakes)	Coatings, paint/ink, composites, transparent conductive layers, energy storage, bioapplications
CVD	1,000	≈1,000	10,000	Photonics, nanoelectronics, transparent conductive layers, sensors, bioapplications
SiC	50	100	10,000	High-efficiency transistors and other electronic devices

Other methods based on the chemical exfoliation of graphite and thermal or chemical reduction of graphene oxide can produce graphene on an industrial scale but unfortunately with structural defects that can affect the electronic and electrical properties [84,85].

These are the main problems that impede the production of high quality graphene on a large scale. However, a possible application timeline has already appeared in the literature indicating when possible electronic device prototypes could be expected in the future (Figure 15) [81].

Mechanical exfoliation. The mechanical exfoliation method was historically the first to be adopted by Geim, Novoselov and co-workers to isolate single layers of graphene [86]. With this method, bulk graphite can be exfoliated into individual graphene sheets by using Scotch tape and then transferred by pressing it onto a substrate, such as Si, SiO_2 or Ni [87]. Typically, highly ordered pyrolytic graphite (HOPG) is chosen in order to guarantee a product of high quality graphene crystallites. The main advantages of this method are the ability to complete this process at room temperature and with inexpensive equipment. However, in terms of scalability, it performs the worst and can thus only be considered for research purposes.

Chemical exfoliation. It is well known that the van der Waals forces that bond together the graphene sheets to form graphite are particularly weak and can be broken by external mechanical force. A common example of this can be seen with the usage of pencils or solid lubricants based on graphite.

Graphene can also be exfoliated from graphite by chemical methods, the process of which is very similar to the dispersion of polymers in particular solvents. This method can be ex-

plained by enthalpy and charge transfer between the graphene layers and the solvent molecules [88,89]. In particular, it was discovered that effective solvents are those with a surface energy similar to graphene ($\approx$0–50 mJ m^{-2}) [88]:

$$\frac{\Delta H_{\mathrm{mix}}}{V_{\mathrm{mix}}} \approx \frac{2}{T_{\mathrm{NS}}} \left(\sqrt{E_{\mathrm{S,S}}} - \sqrt{E_{\mathrm{S,G}}} \right)^2 \phi_{\mathrm{G}} \qquad (1)$$

where ΔH_{mix} is the enthalpy of the mixing, V_{mix} is the volume of the mixture, T_{NS} is the thickness of a graphene nanosheet, $E_{\mathrm{S,S}}$ and $E_{\mathrm{S,G}}$ are the surface energies of the solvent and graphene, and ϕ_{G} is the volume fraction of graphene dispersed in the solution. From Equation 1, it is clear that the enthalpy of the mixing is minimal when the two surface energies are close or equivalent meaning that the exfoliation will take place with mild sonication [88,90]. Furthermore, some solvents are more suitable because they match the graphene surface energy, such as *N,N*-dimethylformamide (DMF), benzyl benzoate, γ-butyrolactone (GBL), 1-methyl-2-pyrrolidinone (NMP), *N*-vinyl-2-pyrrolidone (NVP) and *N,N*-dimethylacetamide (DMA), while ethanol, acetone and water are considered poor solvents for exfoliation [91,92].

Other solvents, such as ionic liquids [93] and chlorosulfonic acid [94], have also been proposed for exfoliating graphite but the exfoliation mechanism has been explained differently. In fact, it has been demonstrated in these cases that there is a charge transfer between the solvent and the graphite layers allowing the exfoliation to take place. Therefore, the graphene sheets could be positively or negatively charged with varying donor and acceptor numbers depending on the solvents.

Surfactants and polymers can also contribute to graphite exfoliation if mixed with particular solvents such as water. Specifi-

Figure 15: Graphene-based display and electronic devices. Display applications are shown in green; electronic applications are shown in blue. Possible application timeline, based on projections of products requiring advanced materials such as graphene. Reprinted with permission from [81]. Copyright (2012) Nature Publishing Group.
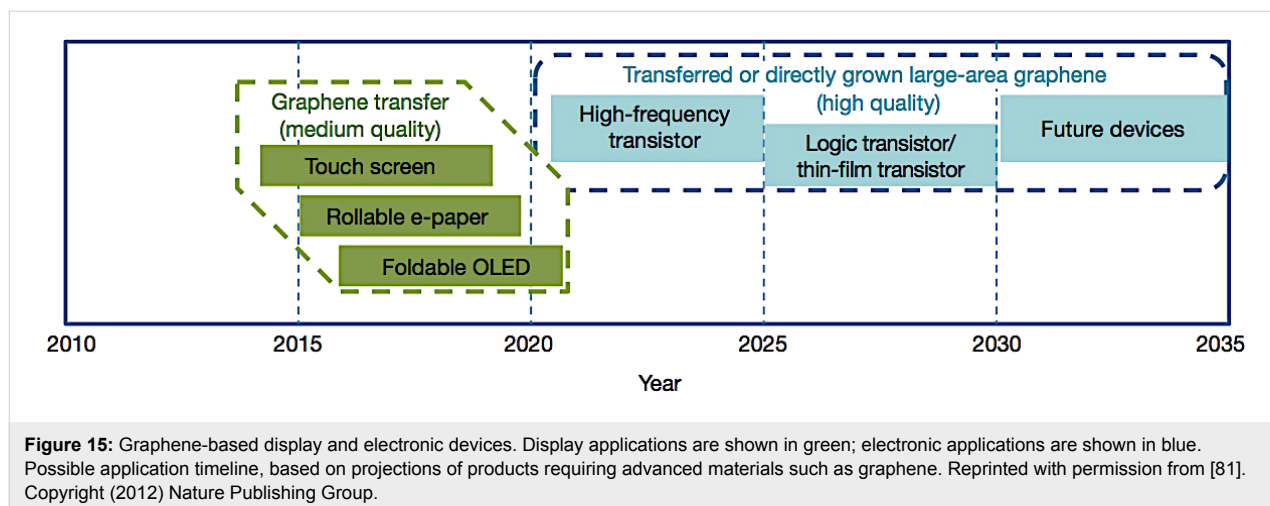
cally, they can change the wettability and prevent aggregation due to electrostatic repulsion [95].

The main problem with the liquid-phase exfoliation method is that it produces graphene for films that is not completely transparent (from 80% to 90%) with high sheet resistance (from 8 to 5 kΩ) [88,90]. The increased sheet resistance is due to damage caused by the sonication during exfoliation.

For these reasons, electrochemical exfoliation methods have recently been employed to produce better quality graphene with a faster process [96,97]. In the electrochemical exfoliation method, the graphite or HOPG is usually connected to an electrode (anode). The counter electrode (cathode) is usually a platinum (Pt) wire and the setup is usually placed in an acidic solution (Figure 16). The complete exfoliation takes place in 15–30 min with voltages varying from 4–10 V. The final graphene flakes produced are usually employed to make a thin film transparent electrode with a sheet resistance of 210 Ω/sq with 96% transparency [96] or to make thin film supercapacitors with capacitance values of over 1 mF/cm^2 [97].

Chemical or thermal reduction of graphene oxide. Graphene oxide (GO) is a semiconducting material originating from graphene research and can be considered a precursor of the graphene synthesis by chemical or thermal reduction [84,85,98,99]. It has recently attracted significant interest because of its potential as a precursor material for high yield production and functionalization of graphene sheets.

The main difference between GO and graphene is that GO consists of epoxy (C–O–C) trigonally bonded in sp^2/partially sp^3 configurations, hydroxyl groups (C=O) in sp^3 configuration displaced above or below the graphene plane, and of some carboxylic groups (–COOH) at the edges of the graphene plane (Figure 17) [100-102].

GO exhibits excellent mechanical, optical, thermal and electronic properties that are similar to graphene because of its specific 2D structure and the presence of various oxygenated functional groups. From an electronic point of view, the GO, as synthesized, is typically insulating and has a high sheet resistance around 10^{12} Ω/sq [103]. This intrinsic insulating nature is strongly related to the amount of C–O–C and C=O groups in this material. However, chemical and thermal treatments can help to reduce the GO in order to remove the oxygen groups with a resulting increase in the conductivity and a tuning of the intrinsic properties from insulating to semiconducting [104]. As compared with pristine graphene, GO presents enhanced chemical activity because of the presence of a large number of oxygen containing functional groups and structural defects.

GO can be chemically produced from graphite oxide (also obtained from graphite by treatment with strong oxidizers),
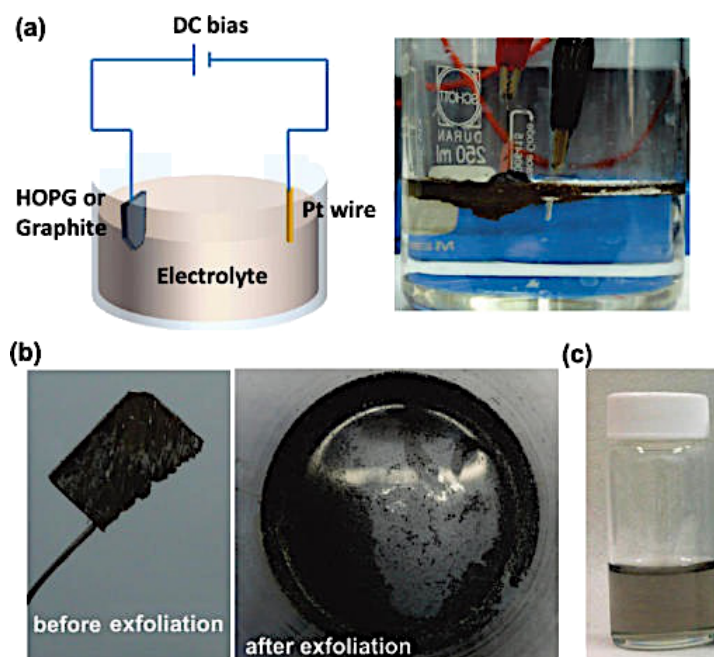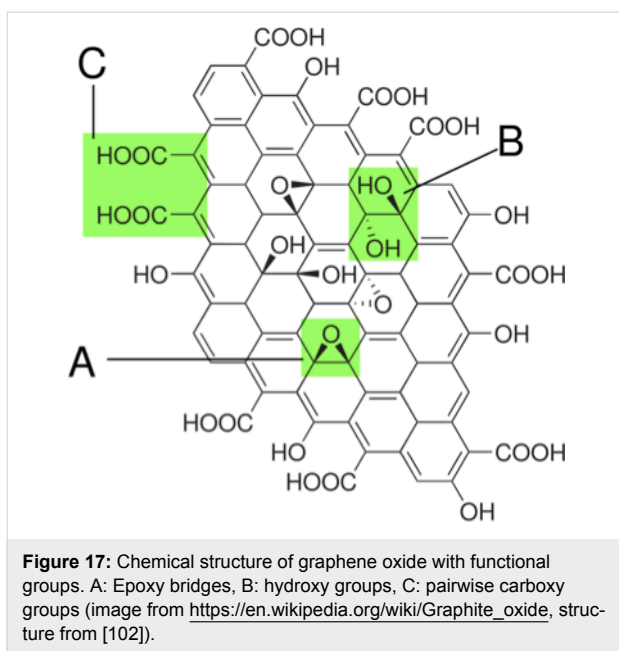

Figure 16: (a) Schematic illustration and photo of the electrochemical exfoliation process for graphite. (b) Photos of the graphite flakes before and after electrochemical exfoliation. (c) Photo of the dispersed graphene sheets in a DMF solution. Reprinted with permission from [96]. Copyright (2011) American Chemical Society.

Figure 17: Chemical structure of graphene oxide with functional groups. A: Epoxy bridges, B: hydroxy groups, C: pairwise carboxy groups (image from https://en.wikipedia.org/wiki/Graphite_oxide, structure from [102]).

the scientific community and is based on a mixture of sulfuric acid (H_2SO_4), sodium nitrate ($NaNO_3$), and potassium permanganate ($KMnO_4$) [106]. Recently, Hummers-modified methods have been proposed in order to produce a higher fraction of well-oxidized hydrophilic carbon material with a more regular structure where the basal plane of the graphite is less disrupted [107].

The attractive property of GO is that it can be thermally and chemically reduced to produce graphene, usually called reduced GO (rGO) [108,109]. The name rGO is given in order to differentiate it from the pristine graphene. In fact, residual, functional groups and defects break the conjugate structure, decreasing the carrier mobility and concentration. Current research in rGO is not only focused on removing the functional groups but also on recovering the network of the graphene lattice [110]. In fact, rGO results in a much lower conductivity when compared to pristine graphene because of large areas of defects as demonstrated by TEM images (Figure 18) [111].

which is a compound of carbon, oxygen, and hydrogen in variable ratios. The first to synthetize the graphite oxide was Benjamin C. Brodie in 1859 [105] by treating graphite with a mixture of potassium chlorate ($KClO_3$) and fuming nitric acid (HNO_3). Then, in 1957, Hummers and Offeman found a safer, quicker, and more efficient way, which is largely used today in

GO and rGO can be easily distinguished by standard optical observation [109]. rGO usually has an increased charge carrier concentration and mobility that results in improved light reflection when deposited onto a metallic substrate as compared to a GO film deposited on the same substrate. Additionally, when immersed in a solvent such as DMF, the GO solution develops a
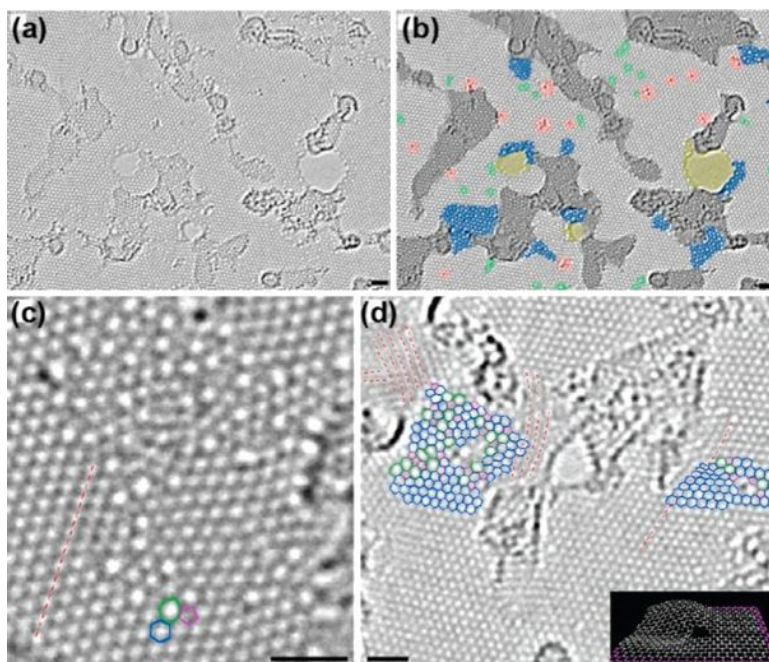
Figure 18: Atomic resolution, aberration-corrected TEM image of a single layer, H-plasma-reduced GO membrane. (a) Original image, (b) original image with false colored to highlight the various features; (c) atomic resolution TEM image of a nonperiodic defect configuration; and (d) partial assignment of the configurations in defect areas, where the inset shows a structural model clearly showing the strong local deformations associated with defects. All scale bars are 1 nm. Reprinted with permission from [111]. Copyright (2010) American Chemical Society.

brown color while rGO appears black. The microscopic character of GO flakes reveals a certain wrinkling of thin and aggregated flakes stacked onto each other. Their lateral size ranges from 100 nm to several µm [112] (Figure 19).
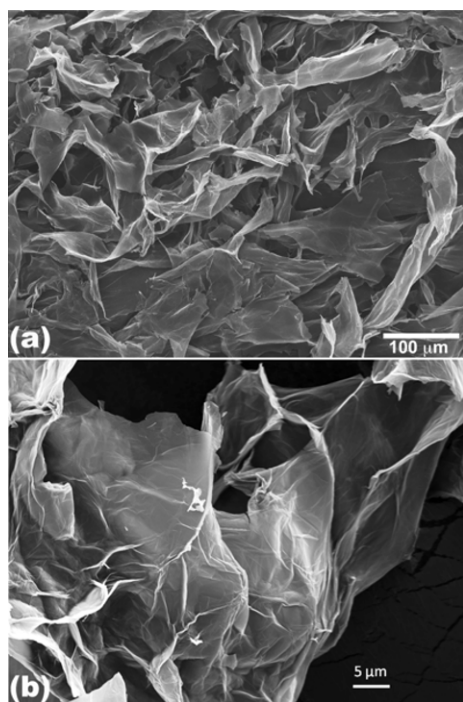
Figure 19: (a) Low magnification and (b) high magnification SEM images of graphite oxide flakes [112].

Before reduction, the C/O ratio is typically 4:1 to 2:1 [113,114] and can be reduced to 12:1 [115] or even to 246:1 [99], as was recently obtained. The C/O ratio is usually characterized by X-ray photoelectron spectroscopy (XPS) because of the possibility to easily identify all the species and their percentage values in the material (Figure 20) [116,117].

The thermal reduction of GO is usually carried out by annealing films or powders in the presence of inert or reducing gases or in vacuum. The annealing temperature certainly affects the properties of the rGO produced. In particular, it was found that the C/O ratio could increase from more than 7 to 13 if the temperature was increased from 500 to 750 °C [118]. The ratio of C/O is also directly connected to the conductivity. In fact, Pei and Cheng [109] demonstrated that the conductivity increased from 50 to 550 S/cm for annealing temperatures of 500 and 1100 °C, respectively. This result has been recently confirmed and explained in detail by Chambers et al. [119] and was found to be related to the loss of oxygen (Figure 21).

Wu et al. [120] used an arc discharge system (instead of a typical furnace) to exfoliate and reduce graphite. With this method, they were able to obtain graphene sheets with a conductivity of 2000 S/cm and a C/O ratio of ≈18 due to the arc discharge system that reached temperatures of over 2000 °C for a short time.

Not only the temperature but also the annealing atmosphere is very important to determine the quality of the resulting rGO.
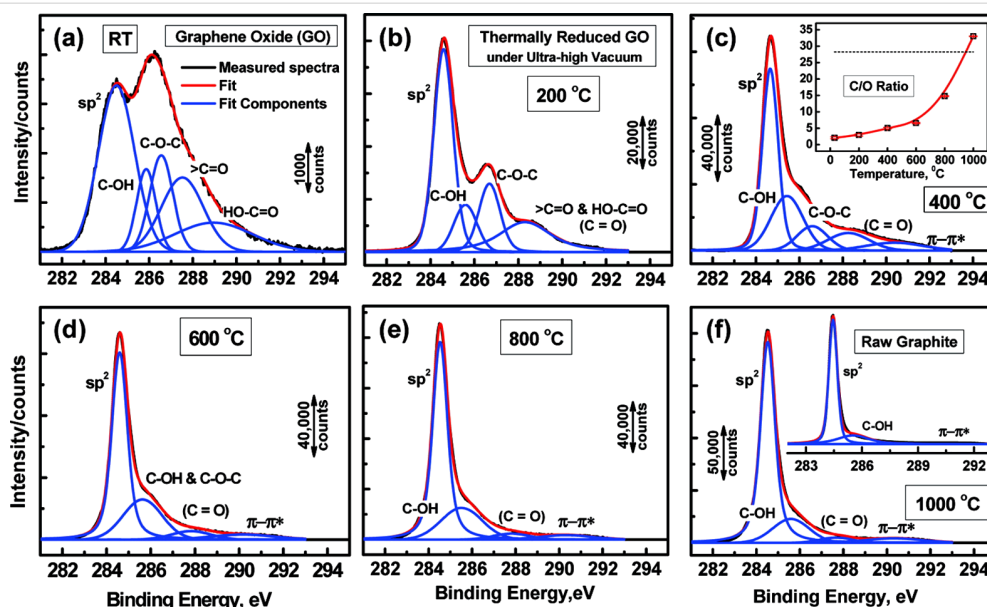
Figure 20: High resolution C 1s XPS spectra: deconvoluted peaks with increasing reduction temperature (T_r). (a) Room temperature; (b) 200 °C; (c) 400 °C, where the insert shows the C/O ratio as a function of *T*; (d) 600 °C; (e) 800 °C; and (f) 1000 °C, where the insert shows the C 1s spectra for the graphite precursor. Reprinted with permission from [116]. Copyright (2011) American Chemical Society.
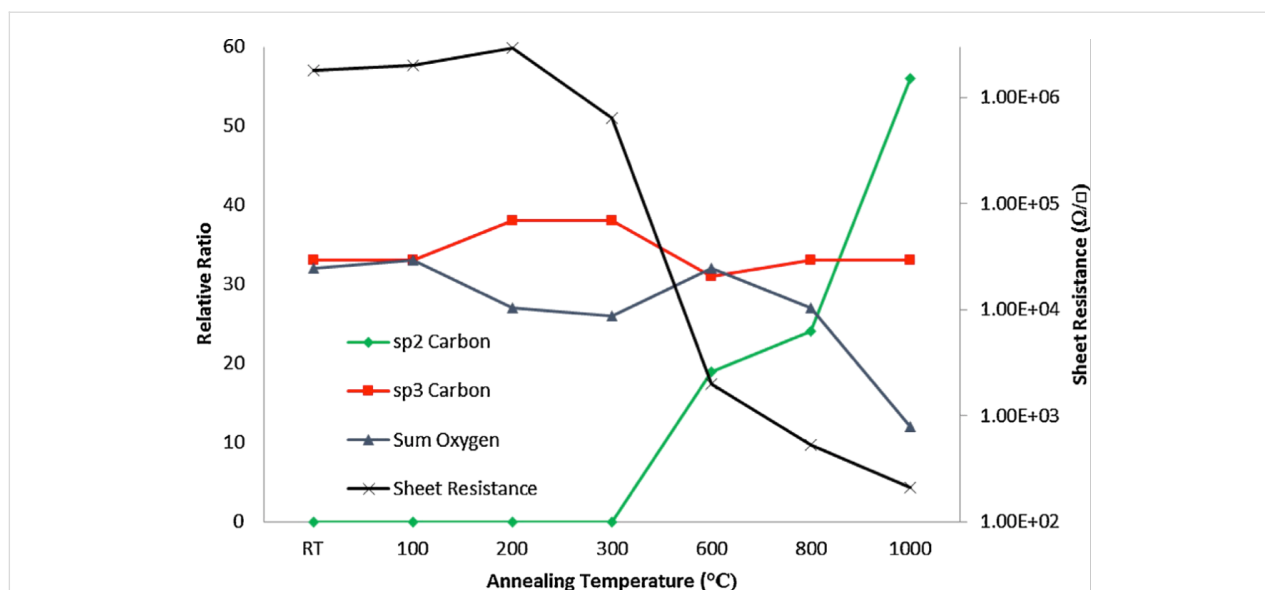
Figure 21: Plot of sheet resistance against annealing temperature with a comparison to key carbon and oxygen ratios. It should be noted that the sheet resistance has been plotted on a logarithmic scale. Reprinted with permission from [119]. Copyright (2015) Elsevier.

Becerril et al. [103] demonstrated that at 1000 °C, the quality of the vacuum was critical for high quality rGO because of the reaction with residual O_2 molecules. For this reason, the usage of reducing gases such as H_2 can help to decrease the required annealing temperature to 450 °C and still give a high C/O ratio of ≈15, as was demonstrate by Wu et al. [120]. Li et al. [121] instead used a mixture of ammonia and argon (2 Torr, NH_3/Ar (10% NH_3), 500 °C) to produce good quality, doped rGO.

The drawbacks of thermal reduction are the high energy consumption due to high temperature and time consumption, given that the GO must slowly reach higher temperatures in order to prevent explosion of the material. For these reasons, other heating approaches based on microwave irradiation [122] and photoirradiation have been considered due to the simplicity of these systems and the reduced exposure time [123].

A cheaper and easy way to reduce GO is by chemical reduction, which is usually done at room temperature or with low heating [109]. Among the many chemical reagents that could reduce GO, hydrazine and its derivatives are probably the most widely used by simple addition to an aqueous GO solution [124-127]. The C/O ratio can reach values above 10 and a conductivity of 99.6 S/cm [84,128]. Other compounds based on metal hybrids such as sodium hydride and sodium borohydride have also been used to specifically remove the C=O species. The main problem that occurred is that sodium borohydride, for example, does not reduce the epoxy and carboxylic groups well [129], and for this reason, it should be utilized after treating the GO with concentrated sulfuric acid at 180 °C. With this method, Gao et al. [99]

were able to obtain a C/O ratio of 8.6 and a conductivity of about 16.6 S/cm. Unfortunately, these values are still low when compared to the rGO obtained from the hydrazine derivative compounds.

Other reducing agents such as ascorbic acid ($C_6H_8O_6$) and hydroiodic (HI) acid have been recently proposed because of their potential to obtain higher quality rGO as compared with the product obtained from hydrazine derivative compounds. Fernández-Merino et al. [128] were able to obtain rGO with a C/O ratio of 12.5 and a conductivity of 77 S/cm with ascorbic acid while Moon et al. [130] obtained rGO with a C/O ratio of 15 and a conductivity of 300 S/cm with HI acid.

Derivative approaches of the chemical method have also been employed to reduce GO: photocatalyst reduction where the GO mixed with TiO_2 particles is exposed to ultraviolet (UV) irradiation [131]; electrochemical reduction with an inert electrode placed in an aqueous buffer solution containing GO where cyclic voltammetry scans are performed between certain voltage ranges [132]; solvothermal reduction where the sealed vial containing GO in a solvent can withstand high temperature and vapor pressure [133].

Much effort has been made by the research community to make the chemical or thermal reduction processes of GO effective; however, the final product is still lacking in terms of quality when compared to pristine graphene. It should be mentioned that mildly oxidized GO has been recently proposed because it could preserve the conjugated structure with few defects [134].

Chemical vapor deposition (CVD). The CVD method is commonly used to produce large-area uniform graphene films [77,135]. Similar to the CVD method used to grow CNTs, graphene can be grown from gases containing C on catalytic metal surfaces or by surface segregation of C dissolved in metals such as Fe [136], Ni [137], Co, Pt and Pd [138]. The pioneer who discovered single layer graphite on Pt was S. Hagstrom in 1965 [139], but the first to interpret it as a single layer was J. W. May in 1969 [140]. The CVD and surface segregation methods can also coexist causing the carbon atoms coming from the gas source to diffuse into the metal. The process is very difficult to control, and especially so in polycrystalline metals where the grain boundaries act as nucleation sites for multilayer growth [141]. For this reason, single crystal and atomically smooth metals are usually preferred to grow high quality, monolayer graphene. Also, the choice of the metal, catalytic substrate is very important to avoid the diffusion of the carbon atoms into the metal. For example, Cu surfaces are probably the best choice for a pure CVD process with the formation of a monolayer graphene because the diffusion of C atoms in Cu is very low (0.001 atom % at 1000 °C) [83,142]. The CVD process on Cu foils can be scaled using a roll-to-roll technique, allowing for a 30 inch graphene film for a transparent electrode (Figure 22a) [82]. However, even this method does not guarantee perfect graphene in terms of quality. In fact, the graphene produced is mostly polycrystalline with aperiodic heptagon/pentagon pairs [143] or overlapped bilayer regions [144] at the grain boundaries (Figure 22b). It has also been demonstrated that the presence of grain boundaries can reduce the mechani-

cal and electrical properties of the graphene (Figure 22c,d) [143,145].

To polish the commercial Cu foil, which is generally covered with a protective layer, the electrochemical method is commonly used, followed by treatment in a CVD system at 2 atm of H_2 for 7 h to reduce the defects. In this way, an ≈2.3 mm wide monolayer of graphene with mobility of ≈11,000 cm^2 V^{-1} s^{-1} was synthesized (Figure 23) [146].

Enclosure-like Cu structures have also been used by Ruoff's group to grow large single crystal graphene (≈0.5 mm) [147,148]. Specifically, the Cu was electrochemically polished and then rolled into a tube before being placed in the furnace. They demonstrated that, with this method, the Cu inner surface is smoother than the outer one, allowing the formation of millimeter-sized graphene (Figure 24).

Mohsin et al. [149] also showed that the Cu surface morphology is very important for graphene nucleation. In fact, by melting and resolidifying Cu substrates, they were able to obtain a piece of monolayer graphene grains with a size of about 1 mm due to the reduction in the Cu roughness from 166 to 8 nm after treatment (Figure 25).

Another approach, reported by Zhou et al. [150], is to anneal Cu foils in Ar to maintain the catalytically inactive Cu_2O layer and to extend the graphene growth to 48 h. With this method, they were able to achieve 5 mm wide, monolayer graphene with
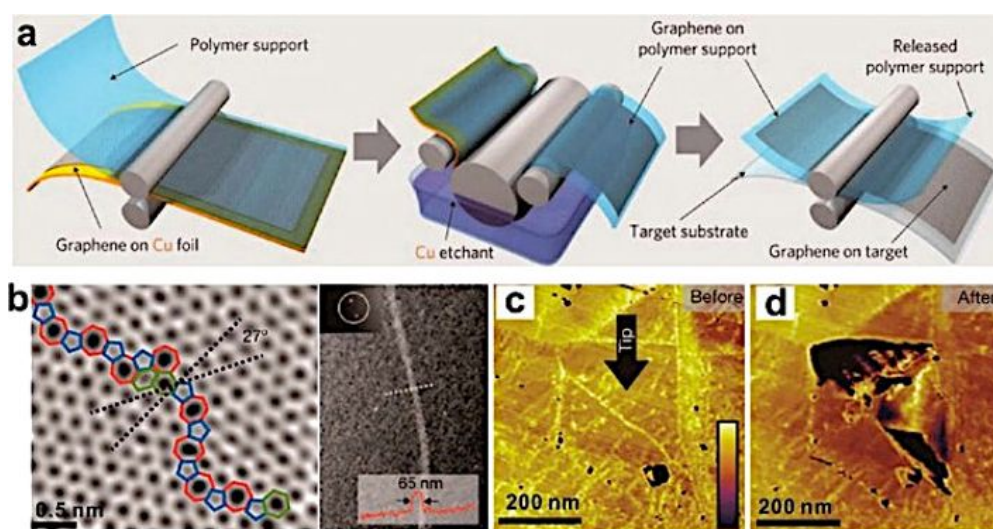
Figure 22: CVD graphene. (a) Schematic of the transfer of graphene produced on Cu using the roll-to-roll method. (b) Two types of graphene boundaries: aperiodic heptagon/pentagon pairs and overlapped bilayer regions. (c,d) Tears along the graphene grain boundaries after indentation. Reprinted with permission from [135]. Copyright (2014) American Chemical Society.
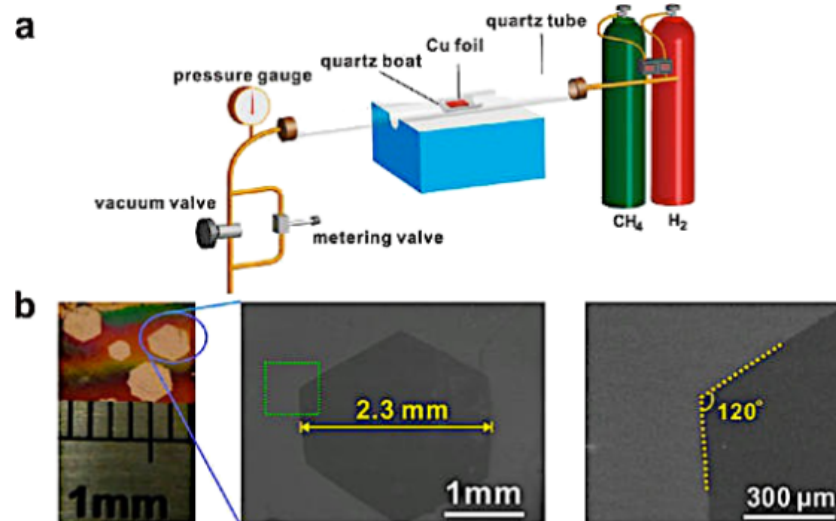
Figure 23: Millimeter-sized graphene grains produced on polished and annealed Cu foils. (a) Schematic of the controlled pressure CVD system. (b) Typical optical and scanning electron microscope (SEM) images of as-produced millimeter-sized graphene grains on pretreated Cu foils. Reprinted with permission from [135]. Copyright (2014) American Chemical Society.
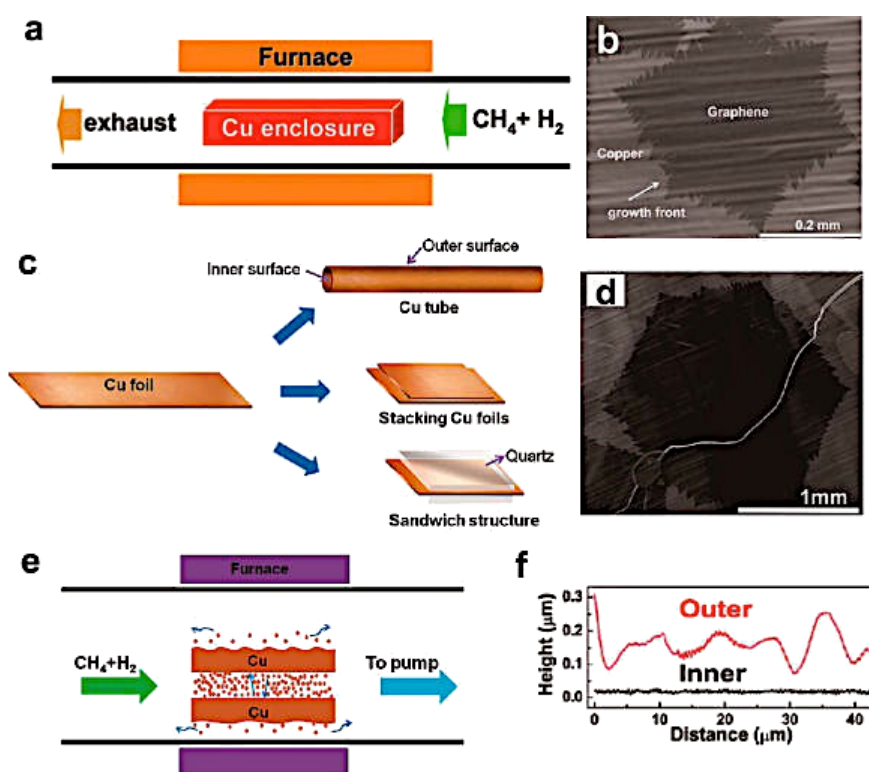
Figure 24: Millimeter-sized graphene grains produced on the inside of enclosure-like Cu structures. (a) Schematic of Cu enclosures for graphene growth. (b) An SEM image of graphene grains grown on the inner surface of a Cu enclosure. (c) Schematic of the Cu tube, stacked Cu foils, and Cu foil between two quartz slides. (d) Typical SEM image of one graphene grain grown on the inner surface of the tube-like Cu structure. (e) Reduction of loss of Cu by evaporation due to redeposition of Cu in a confined space. (f) Height profiles on the inner surface (the black curve) and the outer surface (the red curve) of a tube-like Cu structure after annealing. Reprinted with permission from [135]. Copyright (2014) American Chemical Society.

Figure 25: Millimeter-sized graphene grains made on resolidified Cu. (a) Schematic of the Cu resolidification process on a tungsten substrates (left) and an optical image of millimeter-sized hexagonal graphene grains grown on resolidified Cu (right). AFM topographical images of various copper surfaces: (b) as-received and (c) resolidified. Reprinted with permission from [135]. Copyright (2014) American Chemical Society.
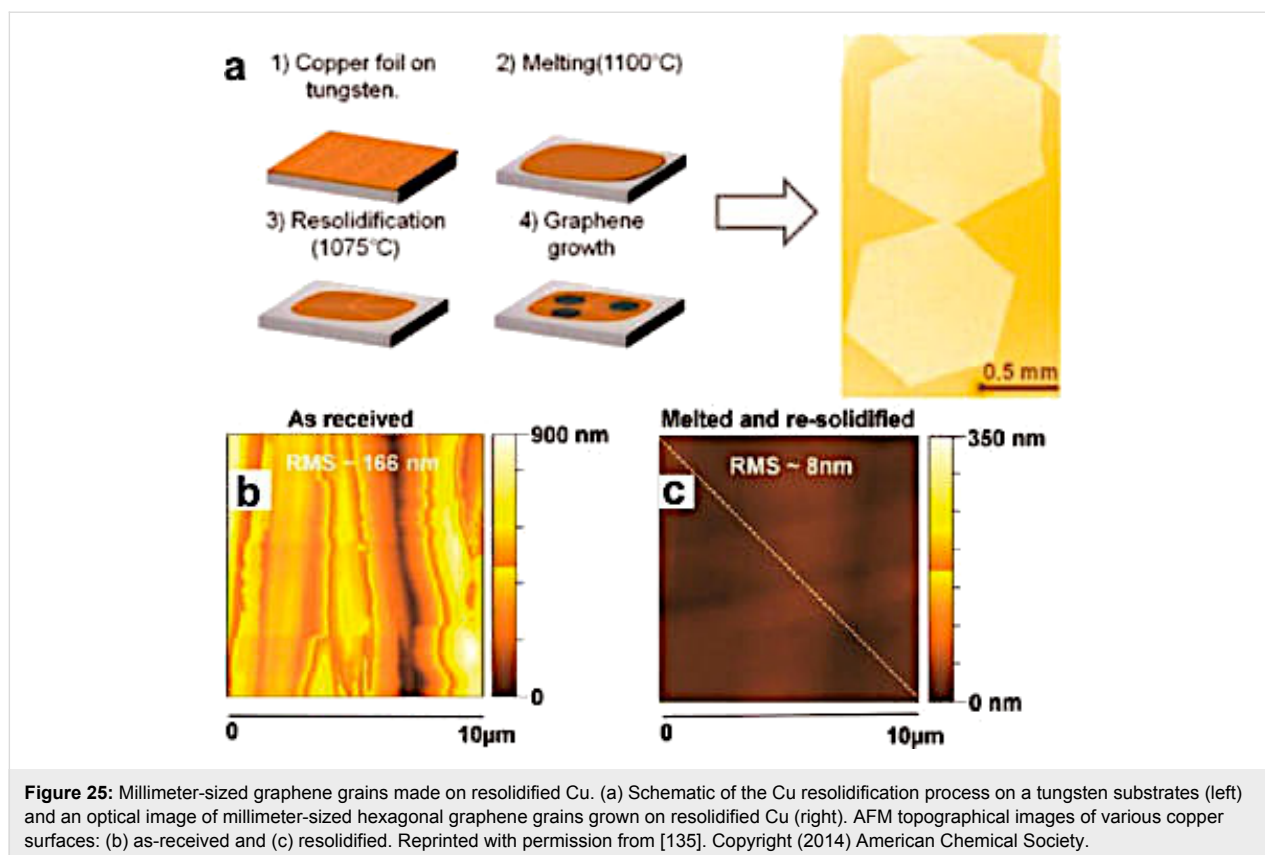
a high carrier mobility of 16,000 cm^2 V^{-1} s^{-1}. The groups of Luo and Ruoff then adopted a similar strategy and were able to produce centimeter-scale, single crystal graphene [151,152].

The drawbacks of the CVD process are: (1) it is expensive because a large amount of energy is required, (2) the transfer to dielectric (or other) substrates is not easy to achieve, and (3) controlling the crystallographic orientation is critical for many electronic applications. However, the breakthrough that would make this technology viable for large scale production would be to develop a low temperature CVD process (e.g., plasma-enhanced CVD) that could produce large area, high quality graphene on any type of substrate.

Epitaxial growth on SiC. Graphene growth on silicon carbide (SiC) has also been extensively explored as it results in wafer-scale growth. Additionally, SiC is an excellent substrate for many electronics applications, avoiding the need to transfer to another substrate. High-quality graphene with a controlled thickness and a specific crystallographic orientation can in fact be grown on commercially available, semiconducting or insulating SiC wafers. For these reasons, this process is very attractive for industrial applications because it can easily be integrated with conventional silicon technology.

SiC is a semiconducting material that can be found in 250 crystalline forms [153]. A large family of similar crystalline forms can be catalogued in particular structures called polytypes, which all present different physical properties.

All the polytypes show a similar local chemical environment for both the carbon and silicon species. Specifically, each C (or Si) atom is situated above the center of a triangle of Si (or C) atoms and underneath a Si (or C) atom belonging to the next layer in a tetrahedral co-ordination. The distance between neighboring silicon or carbon atom is ≈3.08 Å, while the distance between the C atom to each of the Si atoms (Si–C bond length) is ≈1.89 Å. A second type of building block also exists that is identical but rotated 180° with respect to the first (Figure 26) [154]. These units are periodically repeated in closed-packed layers, whose stacking sequence gives rise to the different polytypes.

The two major polytypes are α-SiC and β-SiC. The α-SiC exhibits a hexagonal crystal structure (similar to wurtzite) and is usually formed at temperatures above 1700 °C. β-SiC exhibits a cubic crystal structure with a stacking sequence of ABCABC along the (111) direction, which is typical of a zinc blende crystal structure (similar to diamond) and is formed at temperatures below 1700 °C. The α-SiC and the β-SiC can also be cata-

Figure 26: The characteristic tetrahedron building block of all SiC crystals. Four carbon atoms are covalently bonded with a silicon atom in the center or vice versa. Two types exist: one is rotated 180° around the *c*-axis with respect to the other as shown [154].
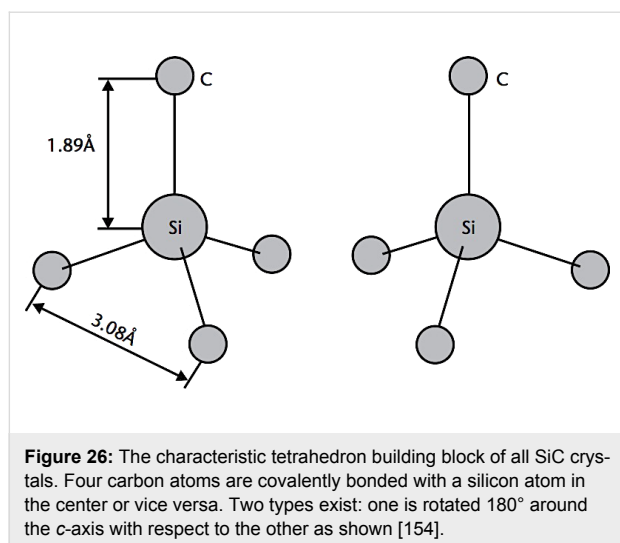
logued with the Ramsdell classification scheme where a number indicates the layer and a letter indicates the Bravais lattice type, such as cubic (C), hexagonal (H) or rhombohedral (R) [155].

For example the α-SiC can also be called 2H-, 4H- or 6H-SiC, depending on the unit cell, while β-SiC can also be called 3C-SiC because of the ABC stacking [156] (Figure 27).

The formation process of graphene on SiC is also called graphitization. It consists of the sublimation of Si atoms from the SiC surface caused by high temperatures with a consequent rearrangement of the carbon atoms on the surface to form a graphene lattice [157-159]. Graphene can be grown on both terminated C- or Si-faces, but Si allows for better control over

the number of graphene layers and gives a uniform coverage with an azimuthal orientation that is determined by the crystal structure [160].

Hexagonal polytypes of SiC (such as 6H and 4H) with orientation (0001) are preferred because of the lattice structure that matches the graphene lattice. However, 3C polytype structures have also been used on (111)-oriented surfaces in order to maintain a good match with the hexagonal lattice of graphene [161,162].

The SiC wafer is usually precleaned in ultrahigh vacuum (UHV) or in other environments with different techniques in order to increase the graphene quality during graphitization. The three most common techniques are: heating the sample ex situ while hydrogen etching for 30 min at 950 °C; preparing a silicon rich phase (3 × 3) in a Si flux and then heating the sample for 30 min at 1000 °C; or heating the sample at around 1000 °C under Si flux to remove the native oxide and to avoid silicon depletion of the surface [163].

Graphene growth occurs at temperatures of 1200–1350 °C in UHV [164,165] even though graphitic bonds start to appear at temperatures around 1000 °C [166]. Graphene can also be grown at temperatures of 1400–1600 °C in other environments such as inert gas atmosphere [167,168] or in an excess of Si in the gas phase [169] in order to reduce the sublimation rate with the positive pressure. The growth temperature is a very important parameter because it influences the number of graphene layers grown and it is directly related to the Si diffusion (Figure 28) [170].

Figure 27: Schematic representation of the stacking sequence of hexagonal SiC bilayers for 2H, 3C, 4H and 6H polytypes.
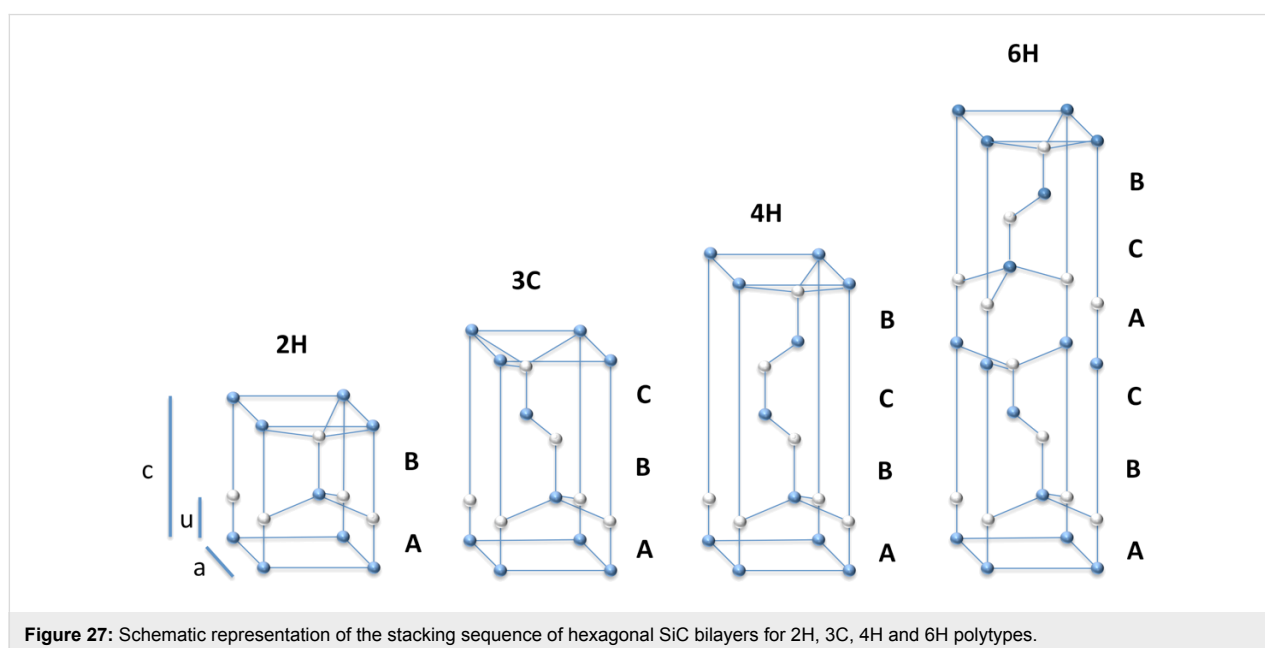
Figure 28: Number of graphene layers grown by annealing 3C-SiC for 10 h in UHV as a function of temperature. Reprinted with permission from [164]. Copyright (2014) Elsevier.

The graphene can also be grown on a C face. The advantages are the absence of a buffer layer and the possibility to easily grow multilayer graphene (MLG) in all directions on the SiC surface (Figure 29a) [171]. The different graphen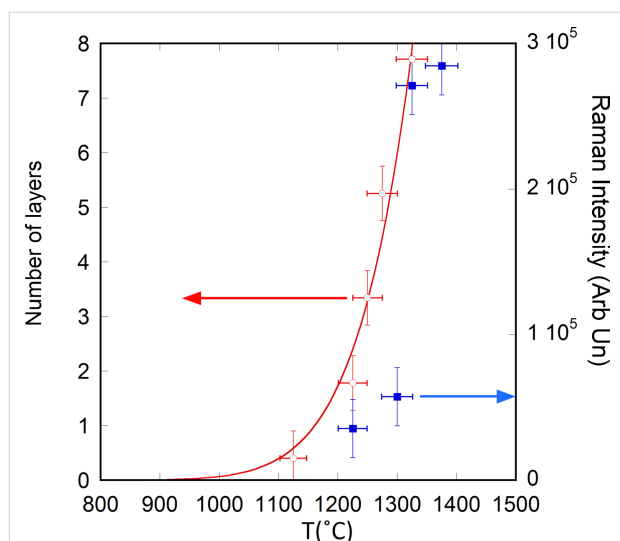e layers are not stacked in the same direction and are usually rotated about 23° with respect to each other (Figure 29b,c). It has been demonstrated that the rotationally stacked graphene has a van Hove singularity, which generates peaks in the density of the states. This property could be useful to tune the electronic properties of graphene.

One potential application of graphene grown on SiC is for high frequency transistors. Pioneering work was completed in 2006 by Berger et al. [172] by fabricating a field-effect transistor (FET). They were able to show the Dirac nature and the high mobility (25,000 cm^2 V^{-1} s^{-1}) of graphene grown on SiC. An IBM research group recently reached the 300 GHz cut-off frequency for a graphene-based FET grown on SiC. They showed the stable operation of an integrated circuit containing graphene (Figure 30) [173,174].

The two major drawbacks of this graphene synthesis process are the high cost of the SiC wafers and the high temperature involved that is not suitable for the Si technology [81]. The first drawback can been resolved by growing thin layers (100–300 nm) of SiC on top of Si substrates, but further development is required for uniform deposition on a large diameter wafer with a low roughness and elimination of the terraces in order to guarantee high-quality, monolayer graphene. The second drawback could be solved, as in the CVD process, by reducing the growth temperature by the use of PECVD equipment. Industry and research groups worldwide are intensely searching for a solution to this problem because it could contribute to the launch of graphene into the electronic market.

Organic photovoltaics

Over the past twenty years, organic photovoltaics have rapidly improved because of the potential to obtain a manufacturing process that is faster, less expensive and with higher production volume as compared to silicon technology [175-178]. Figure 31 shows the best solar cell efficiencies reported by the National
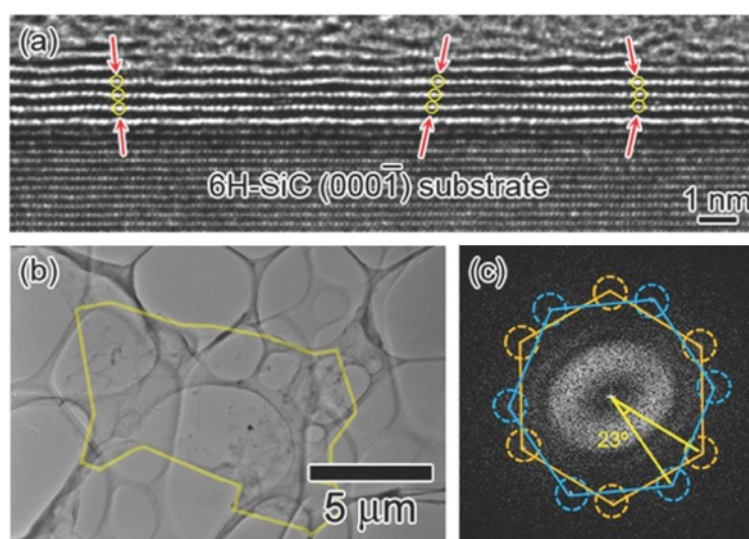
Figure 29: TEM images of MLG on the C-face. (a) A cross-sectional TEM image. (b) A low-magnification TEM image of graphene exfoliated from the SiC substrate. (c) FFT pattern from the area highlighted in (b). Reprinted with permission from [171]. Copyright (2012) Surface Science Society of Japan.
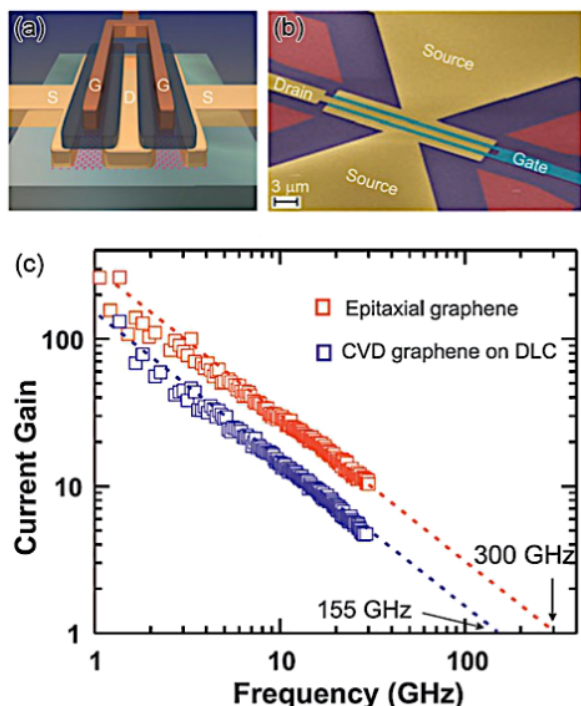
Figure 30: High frequency graphene transistor. (a) and (b) Structure of a graphene-based FET for an analogue radio frequency device. (c) Current gain as a function of frequency, showing a cut-off frequency of 300 GHz for epitaxial graphene on SiC. Reprinted with permission from [173]. Copyright (2012) MRS Bulletin.

Renewable Energy Laboratory (NREL) in the United States over the last 40 years. Of note is that the organic solar cell efficiencies increased from 4 to 12% (record established by Heliatek in 2013 for a tandem, organic solar cell) in just a little over ten years [179].

Three problems still must be solved in order to make this technology competitive with others already present on the market: the power conversion efficiency (PCE) [181], the device lifetime [182] and the large scale production [183].

Typically, an organic solar cell consists of two electrodes (one of which is transparent) and an active layer between them where the generation of free charge carriers occurs. A buffer layer is usually included between each electrode and the active layer in order to prevent charge recombination, which reduces the efficiency of the device. The active layer can be a double layer (one has a stronger affinity for electrons (donor) and the other has a stronger affinity for holes (acceptor)) or a bulk heterojunction (mixture of a donor and acceptor material in bulk). The bulk heterojunction (BHJ) provides a larger volume of paths for the transport of free carriers and more efficient charge separation in comparison to the other structures [184-186]. The first kind of BHJ architecture was originally proposed by Sariciftci et al. [187] and is based on an active blend of a conducting polymer (electron donor material) mixed with fullerene derivatives (electron acceptor material) [188].
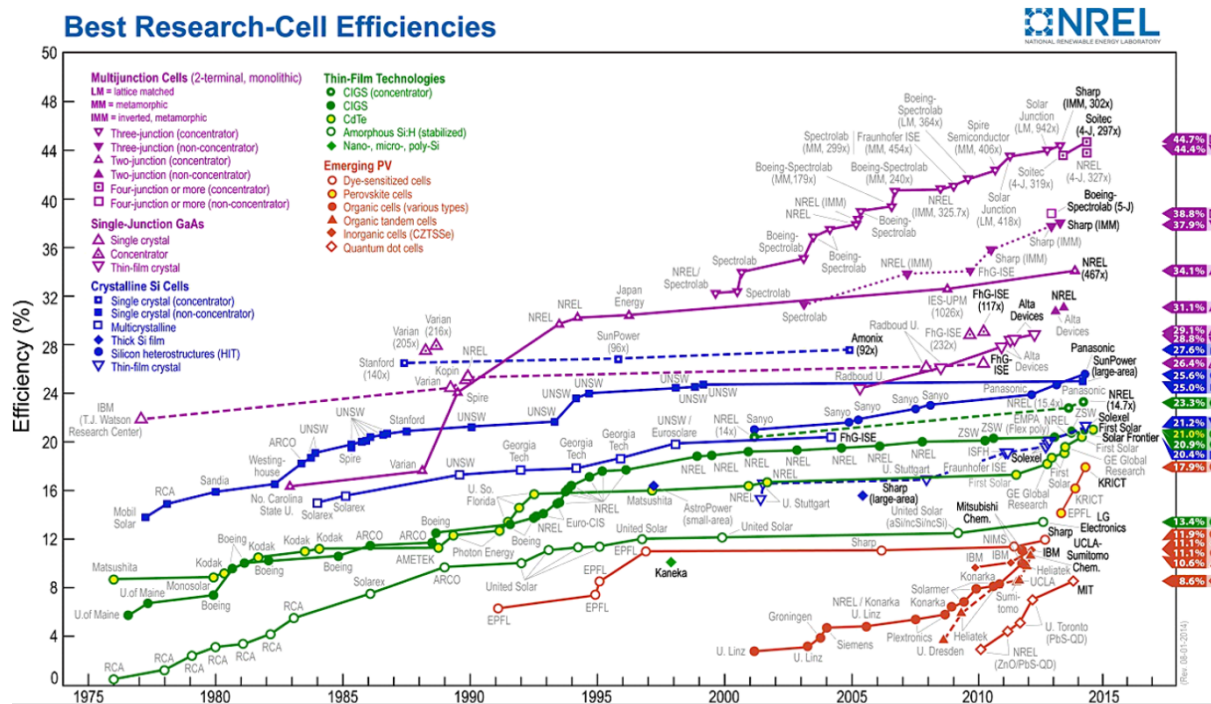
Figure 31: Record solar cell efficiencies, worldwide, as reported by NREL in 2014 [180].

The generation of a photocurrent due to light incident upon an organic solar cell device consists of three steps (Figure 32) [189,190]:

1. Photon absorption in the conducting polymer (donor material).
2. Creation of an exciton. An exciton is a bound state of an electron and a hole that are attracted to each other by the electrostatic Coulomb force. Its diffusion length is about 10 nm.
3. Exciton separation at the interface between the donor and the acceptor. Because of the built-in electric field at the interface, the electron is transferred to the acceptor and the hole to the donor (creation of the photocurrent).

One problem is the short lifetime of excitons generated by light. Considering that their recombination distance is between 4 and 20 nm [191,192], the morphology of the active layer is an important parameter for the performance of the device [193-195].

Fullerene derivatives in organic solar cells

The BHJ solar cells currently most studied are based on a fullerene derivative commonly called [6,6]-phenyl-C_{61}-butyric acid methyl ester ($PC_{61}BM$ or PCBM) as the acceptor material and the conducting polymer poly(3-hexylthiophene-2,5-diyl) (P3HT) as the donor material [196-198]. Both materials are commercially available and guarantee stable devices. In the regular structure, indium tin oxide (ITO) is typically used as the transparent conducting anode and poly(3,4-ethylenedioxythiophene)/poly(styrene sulfonate) (PEDOT/PSS) as the electron blocking layer. The blend of PCBM and P3HT form the active layer onto which a thin layer of lithium fluoride (LiF), used to block holes, and a layer of aluminium as cathode are coated respectively (Figure 33a) [199,200].
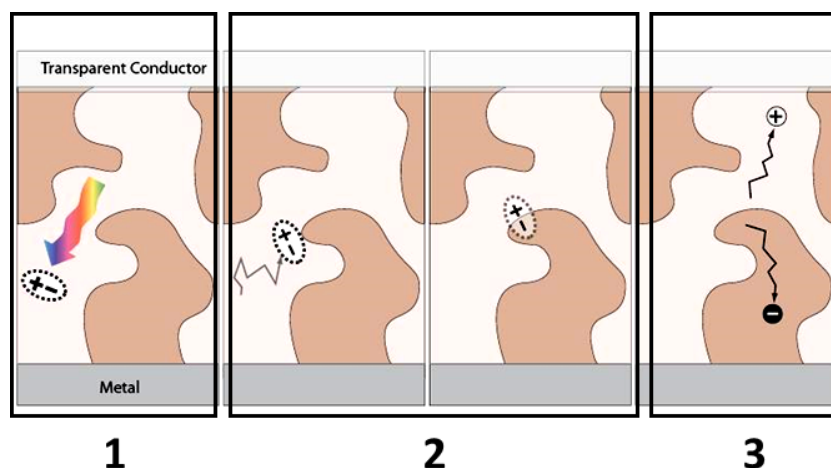
Figure 32: Photocurrent generation steps in an organic solar cell. Step 1: photon absorption in the conducting polymer (donor material). Step 2: creation of an exciton. Step 3: exciton separation at the interface of the heterojunction (interface between the donor and the acceptor).
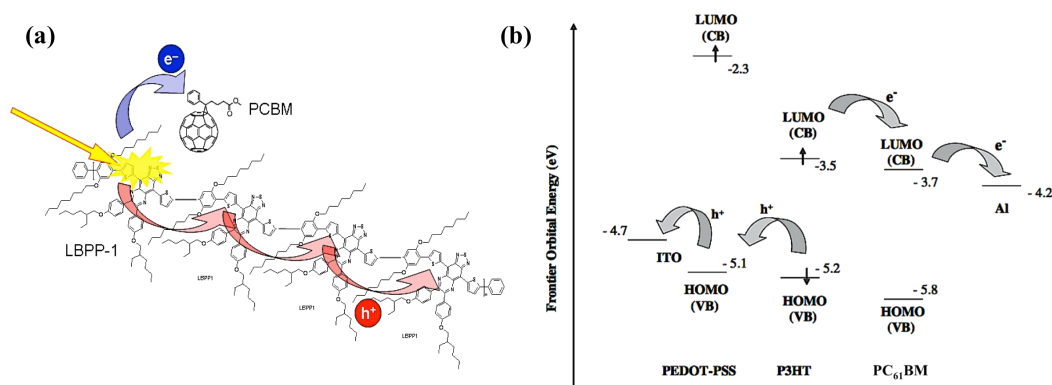
Figure 33: (a) Electron transfer from P3HT to PCBM after generation of the exciton at the interface of the two materials. (b) HOMO and LUMO levels of the different materials in an organic solar cell structure ITO/PEDOT–PSS/P3HT–PCBM/LiF/Al. Reprinted with permission from [26]. Copyright (2005) John Wiley and Sons.

The specific choice of these materials is due to the fact that the exciton separation at the acceptor/donor interface and the transport of the charges across the device is strongly affected by the energy band alignment. Figure 34a shows how, in a regular structure, the electrons and holes can easily move from the donor/acceptor interface to the respective electrodes because the energy values of the lowest unoccupied molecular orbital (LUMO) and the highest occupied molecular orbital (HOMO) of each material are very similar [26]. An organic solar cell device can also have a reversed structure by inserting a hole blocking layer between the transparent electrode and the active layer in order to collect electrons and an electron blocking layer on the metallic electrode in order to collect holes. Figure 34b shows a typical inverted structure composed of ITO as the cathode, zinc oxide (ZnO) as the hole blocking layer, $PC_{61}BM$/ P3HT as the active layer, PEDOT/PSS as the electron blocking layer and gold (Au) as the anode [201].

In order to characterize the performance of an organic solar cell, the electrical current (I) and the voltage potential (V) across the device are measured and plotted on the *y*- and *x*-axis, respectively, under a standard illumination. The current produced by a solar cell is the combination of the current of the solar cell diode (I_D) in the dark with the light-generated current (I_L) (Figure 35).

The total current calculated from the circuit in Figure 35 is [203]:

$$I = I_0 \left[\exp\left(\frac{qV}{nKT}\right) - 1 \right] - I_L \qquad (2)$$
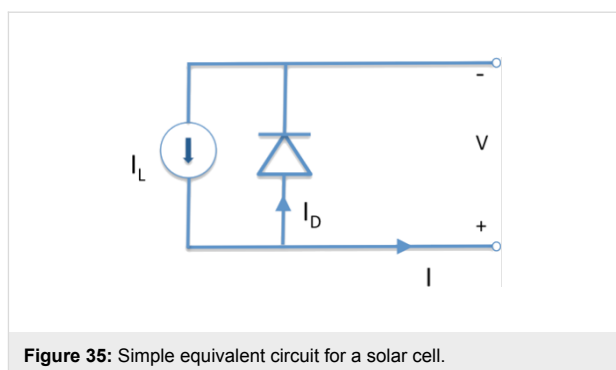
Figure 35: Simple equivalent circuit for a solar cell.

The *I–V* curve of a solar cell is the superposition of the *I–V* curve of the solar cell diode in the dark, described by the Shockley diode equation, with the light-generated current. The light has the effect of shifting the *I–V* curve down into the fourth quadrant so that power can be extracted (Figure 36).

Typical resistive effects are unfortunately present and they contribute to reduced performance of the device. The most common parasitic resistances are series resistance (R_S) and shunt resistance (R_{SH}). R_S and R_{SH} are included in a more complicated equivalent circuit model (Figure 37).

The efficiency, η, of a solar cell can be calculated from the *I–V* curves (as in Figure 36) [203]:

$$\eta = \frac{V_{oc} I_{sc} \text{FF}}{P_{in}} \qquad (3)$$

where V_{oc} is the open circuit voltage, I_{sc} the short circuit current, P_{in} is the input power and FF is the fill factor that indi-

Figure 34: (a) Schematic of a regular organic solar cell structure. (b) Schematic of an inverted organic solar cell structure. Reprinted with permission from [202]. Copyright (2014) Elsevier Limited.

polymer film and to form an intermixed layer. In particular, 1-(3-methoxycarbonyl)propyl-1-phenyl[6,6]methanofullerene or the $PC_{61}BM$ derivative is more soluble in organic solvents than pristine C_{60} [35]. Currently, many stable devices are prepared with a mixture of different conducting polymers and $PC_{61}BM$, achieving a stable PCE of about 4% [206].

Because $PC_{61}BM$ has small absorption peaks, other fullerene derivatives such as phenyl-C_{71}-butyric acid methyl ester ($PC_{71}BM$) have recently been used to provide better absorption in the visible spectra [207], boosting the PCE to values higher than 7% (Figure 38) [208].

Figure 36: *I–V* curves of a solar cell. I_L indicates the current under illumination. V_{oc} and I_{sc} represent the open circuit voltage and the short circuit current, respectively, while V_{mp} and I_{mp} indicate the maximum power point.
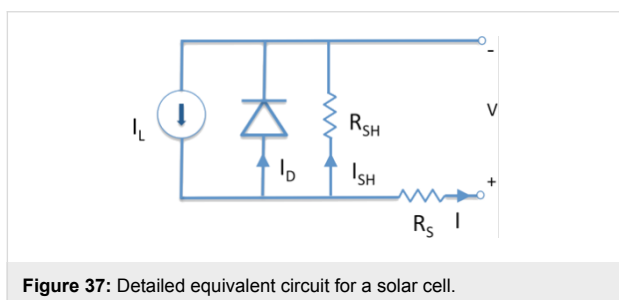
Figure 37: Detailed equivalent circuit for a solar cell.
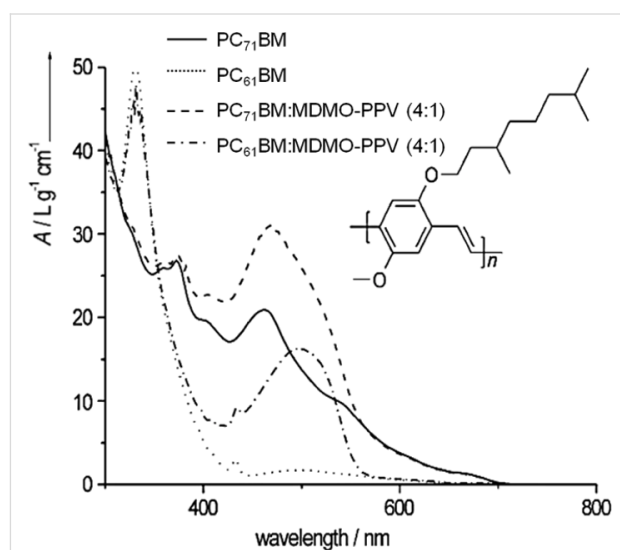
Figure 38: UV–vis spectra of $PC_{71}BM$ and $PC_{61}BM$, both in toluene. To illustrate the contribution of MDMO-PPV to the absorption, the (normalized) spectra of $PC_{71}BM$/MDMO-PPV and $PC_{61}BM$/MDMO-PPV, also in toluene, are presented. The inset shows the structure of poly(2-methoxy-5-[3',7'-dimethyloctyloxy]-p-phenylene vinylene) (MDMO-PPV). Reprinted with permission from [207]. Copyright (2015) John Wiley and Sons.

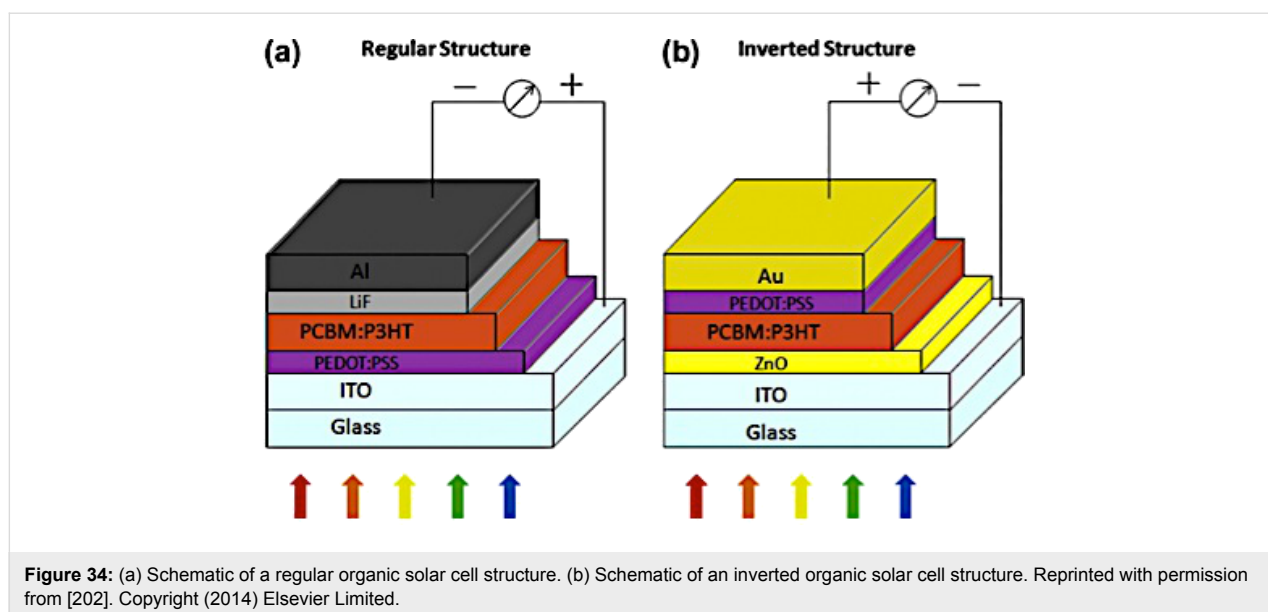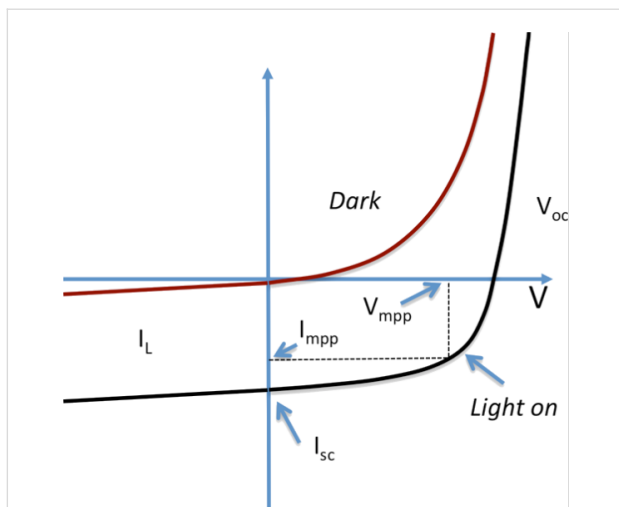cates the "squareness" of the *I–V* curve. The FF can also be calculated from Figure 36 [203]:

$$\text{FF} = \frac{V_{mp} I_{mp}}{V_{oc} I_{sc}} \qquad (4)$$

where V_{mp} and I_{mp} correspond to the maximum power point on the *I–V* curves.

The previously described, remarkable properties of carbon nanomaterials make them very attractive for use in organic photovoltaics [16]. Fullerenes (C_{60}) were the first to be proposed because they have a response typical of n-type semiconductors and are able to accept electrons coming from the photoexcitation of a conducting polymer [204]. The first heterojunction based on C_{60} was realized in 1993 [205]. Unfortunately, the performance of the device was limited by the fact that C_{60} could not be well-dispersed and could not penetrate into the conducting polymer. For this reason, C_{60} derivatives were proposed because of their ability to diffuse into the

Other fullerene derivatives and C_{60}-functionalized macromolecules have also been proposed for the preparation of all-polymer type solar cells; however, the performance to date was too low due to the presence of large solubilizing groups that decrease the charge transport [209].

Carbon nanotubes in organic solar cells
CNTs have also been used in organic solar cells to replace fullerenes as the acceptor material. Because of their high aspect ratio, electrical conductivity, and tunable optical and electronic properties, the necessary quantity of CNTs introduced into the device could be significantly lower as compared to the amount of required PCBM [210]. In fact, the ratio of PCBM and P3HT in the blend is usually 1:1. However, for CNTs, it could be much lower (≈3 wt % of the P3HT) [211]. CNTs are either

partially [212] or completely [211] replacing the PCBM compounds in organic solar cells. For example, when they are mixed with P3HT, the polymer chains tend to wrap around the CNTs with an electron transfer between the CNTs and the P3HT as demonstrated in Figure 39 [213,214] and experimentally observed in SEM and TEM images (Figure 40) [215]. This interaction is usually stronger if the SWNTs are semiconducting instead of metallic [216,217]. Heterojunctions between SWCNTs and the P3HT molecules that have been studied by means of scanning tunneling microscopy and computer simulation open possibilities for making novel solar cells [218,219]. Devices were made by blending CNTs with P3HT, resulting in a maximum efficiency of 3.36% [220]. However, by blending n-doped MWCNTs (n-MWCNTs) into a mixture of PTB7 and $PC_{71}BM$, the device reaches an efficiency as high as 8.6%. It was concluded that the incorporation of N-MWCNTs leads not only to increased nanocrystallite size but also smaller phase-seperated domain sizes of both PTB7 copolymers and $PC_{71}BM$. n-MWCNTs serve as both exciton dissociation centers and charge transfer channels. p-type SWCNTs can be easily obtained by chemical doping. A common method is the nitric acid treatment of CNTs, which introduces nitrogen dopants as well as an increase in the electrical conductivity [221,222]. The PEDOT/PSS can cause degradation of the active layer and the ITO electrode because of its hygroscopicity and acidity, which results in a decrease in the lifetime of the solar cell device [223]. Hence, the network film of p-type SWCNTs has been used to replace the PEDOT/PSS buffer layer in organic solar cells, with a device structure of ITO/SWCNTs/P3HT–PCBM/Al [223,224]. Using the SWCNT film as the hole transport layer, the energy conversion efficiency of the organic solar cell is equivalent to that of the component device with PEDOT/PSS.

Efforts have also been made toward the development of hybrid solar cells with a p-CNT/n-Si structure. By coating a transparent p-type SWCNT network film onto a Si substrate, the solar cell is formed and the energy conversion efficiency can be >11% [225]. By coating a layer of MoO_x onto the CNT film, the efficiency reaches 17% [226].

In fact, CNTs can be grown directly on the ITO substrate [227,228]. In device fabrication, the mixture of P3HT and PCBM is coated onto the substrate, and CNTs are used as 3D electrodes to collect charges from the active media. The problem is that MWCNTs grown at relatively low temperature onto the ITO glass are tens of nanometers thick and have low areal density. With such a substrate, the energy conversion efficiency of organic solar cells is lower than 1%. The best result so far, i.e., 2.1% energy conversion efficiency, was obtained in 2013 by growing CNTs onto fluorine-doped tin oxide (FTO) glass, which is more resistant to high temperature than ITO [229].

Other research groups are focusing their work on replacing ITO, which is expensive and brittle, with a carpet of CNTs in bundles because of their optical transparency, high conductivity properties and the potential to be deposited onto a flexible substrate [230,231].

Graphene and derivatives in organic solar cells

More recently, graphene and its derivatives have also been proposed for organic solar cells. In particular, pristine graphene can be used as a transparent electrode similar to the CNT carpet (Figure 41) [232-234].

Graphene is not typically found in the active or buffer layers because of its zero band gap structure, but the introduction of functional groups could open up more possibilities of graphene integration into different layers of an organic solar cell device. On the other hand, GO can easily be integrated into organic solar cells because of its semiconducting behavior that can be finely tuned as a function of the degree of oxidation.
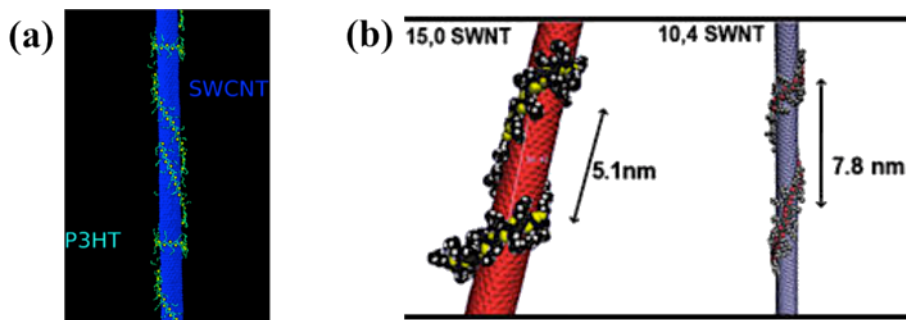
Figure 39: (a) Molecular dynamics simulations of P3HT wrapped around a SWNT (15,0). Reprinted with permission from [214]. Copyright (2010) American Chemical Society. (b) Helices form on (15,0) and (10,4) SWNTs during the folding of P3HT with orthogonal initialization. The chirality may affect the pitch distance to some extent. Reprinted with permission from [213]. Copyright (2010) American Chemical Society.
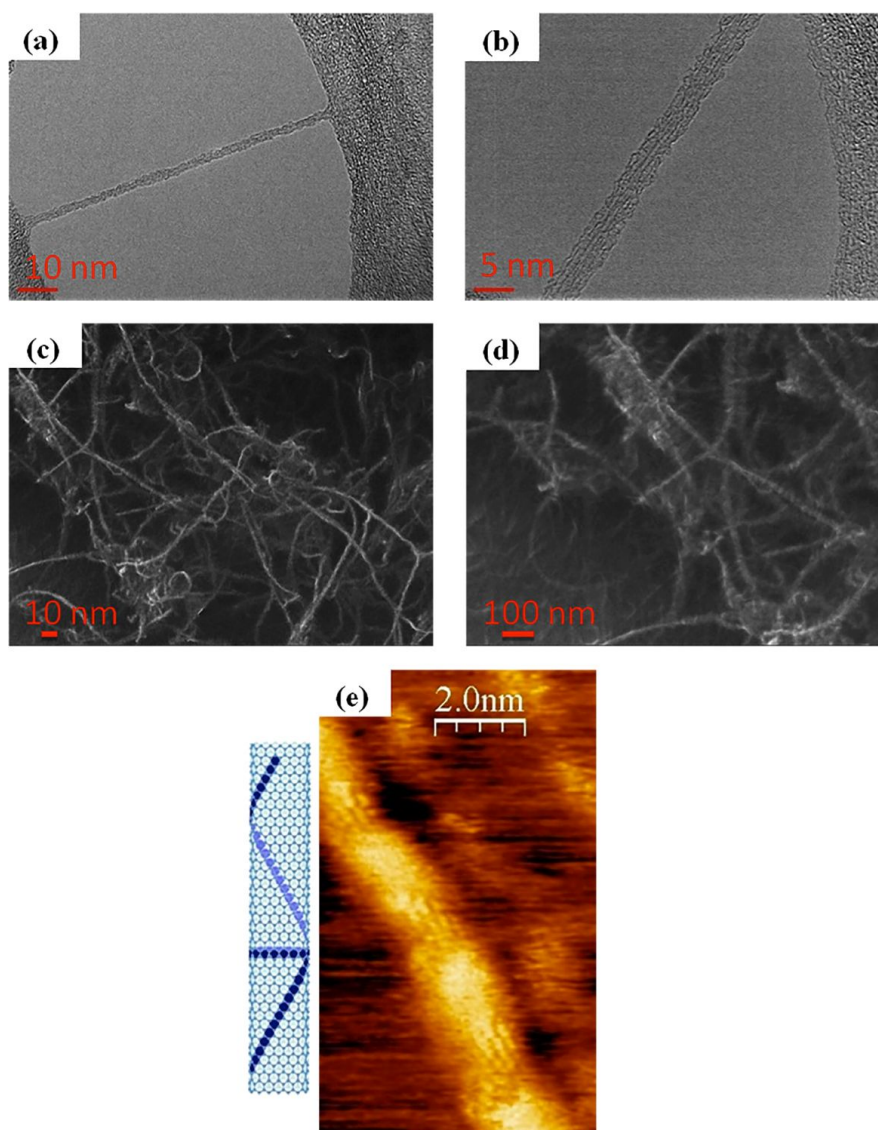
Figure 40: (a) and (b) TEM images of P3HT wrapping around a SWNT (7,6) (images taken at QUT, not yet published). (c) and (d) SEM images of P3HT wrapping around bundles of SWNTs (7,6) (images taken at QUT, not yet published). (e) STM image and schematic of P3HT wrapping around a SWNT (15,0). Reprinted with permission from [218]. Copyright (2009) AIP Publishing LLC.
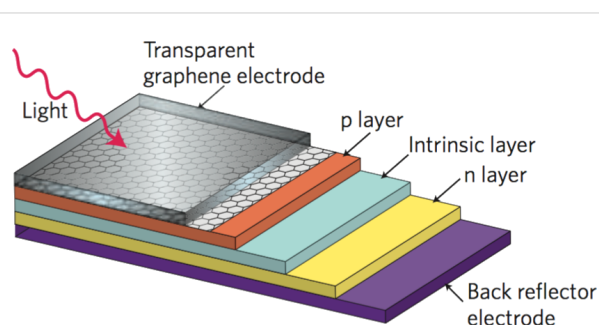
Figure 41: Schematic of an organic solar cell with a transparent graphene electrode. Reprinted with permission from [234]. Copyright (2010) Nature Publishing Group.

GO has been employed in the active layer for the effective exciton charge separation and charge transport when mixed with a conducting polymer, such as P3HT. This is due to the large surface interface area of the acceptor/donor and continuous pathway, similar to CNTs [235-237]. In order to increase the solubility in typical organic solvents (e.g., dichlorobenzene) used to disperse the conducting polymers, the GO can be functionalized with other compounds such as phenyl isothiocyanate (PITC) (Figure 42) [236].

GO has been largely used in the organic solar cell field as a buffer layer. Specifically, it could be a valid candidate to replace PEDOT/PSS as the electron blocking layer because it
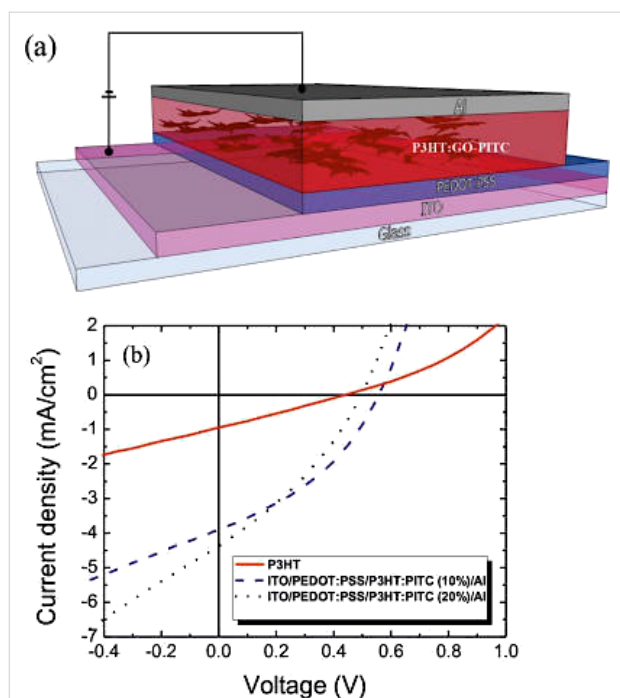
Figure 42: (a) Schematic of a photovoltaic device with a P3HT/GO–PITC thin film as the active layer and the structure ITO–PEDOT/PSS(30 nm)–P3HT/GO–PITC(110 nm)/Al(80 nm). (b) Experimental *I–V* curves of the photovoltaic devices based on P3HT (red curve) and P3HT/GO–PITC composites (dashed curve, 10 wt %; dotted curve, 20 wt %) after post fabrication thermal annealing at 160 °C for 20 min. Reprinted with permission from [236]. Copyright (2012) American Chemical Society.

presents work function values of 4.6–4.8 eV, which are very similar to PEDOT/PSS (Figure 43) [238-241].

When chemically modified with specific dopants (such as caesium (Cs) atoms), graphene could also be used as an electron-blocking layer because its work function can be reduced to 3.9–4.1 eV (Figure 44) [238,241].

Because of the high sheet resistance of GO, the addition of SWNTs into the blend can decrease the through-thickness resistance of the GO film by an order of magnitude if used as a buffer layer (Figure 45) [242].

Bernardi et al. [243] were the first to demonstrate the possibility to have a solar cell comprised of only carbon nanomaterials in the active layer without the use of any conducting polymer. In their work, the active layer was composed of only $PC_{71}BM$, semiconducting SWNTs, and reduced GO, achieving a PCE of 1.3%. They also used ab initio calculations to demonstrate efficiency limits of up to 13% for this device, which is comparable to those predicted for polymer solar cells (Figure 46).

In 2011, a research group at Stanford University proposed for the first time a solar cell based entirely on carbon nanomaterials in two architectures, one vertical and one horizontal (Figure 47) [244].
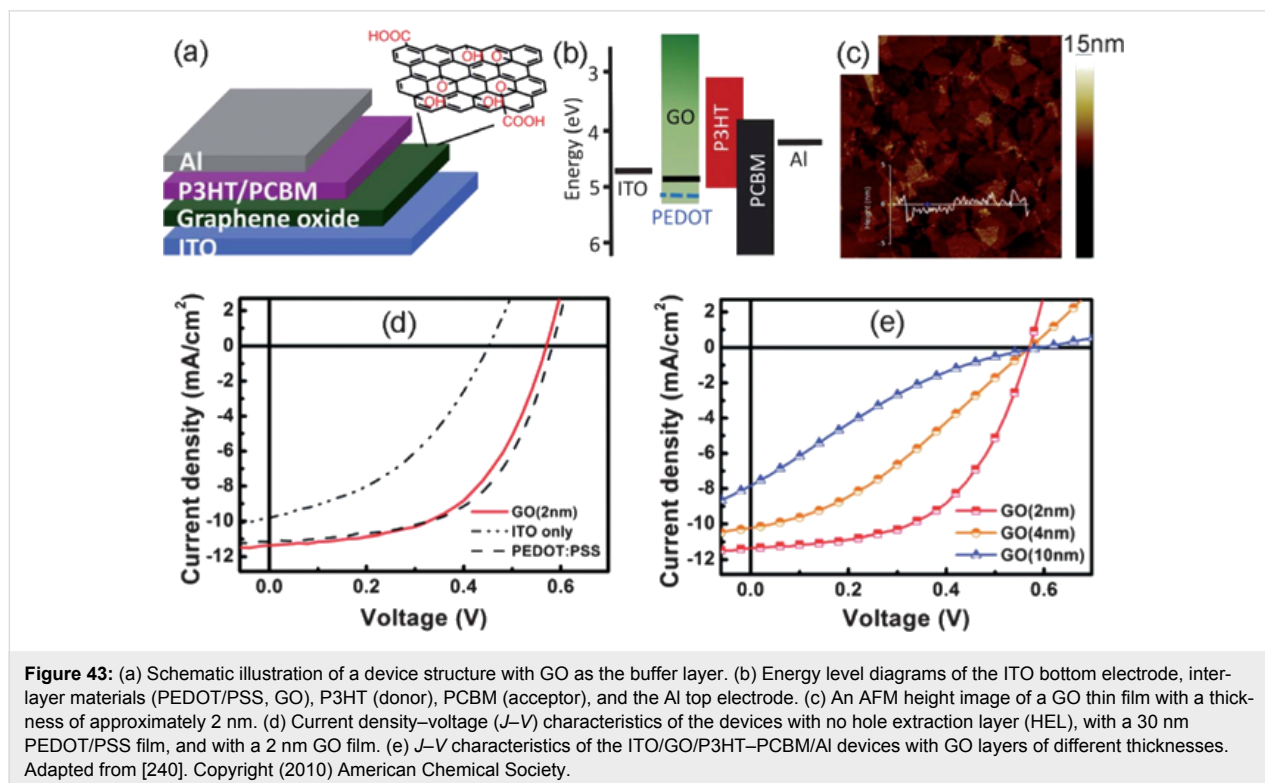
Figure 43: (a) Schematic illustration of a device structure with GO as the buffer layer. (b) Energy level diagrams of the ITO bottom electrode, interlayer materials (PEDOT/PSS, GO), P3HT (donor), PCBM (acceptor), and the Al top electrode. (c) An AFM height image of a GO thin film with a thickness of approximately 2 nm. (d) Current density–voltage (*J–V*) characteristics of the devices with no hole extraction layer (HEL), with a 30 nm PEDOT/PSS film, and with a 2 nm GO film. (e) *J–V* characteristics of the ITO/GO/P3HT–PCBM/Al devices with GO layers of different thicknesses. Adapted from [240]. Copyright (2010) American Chemical Society.
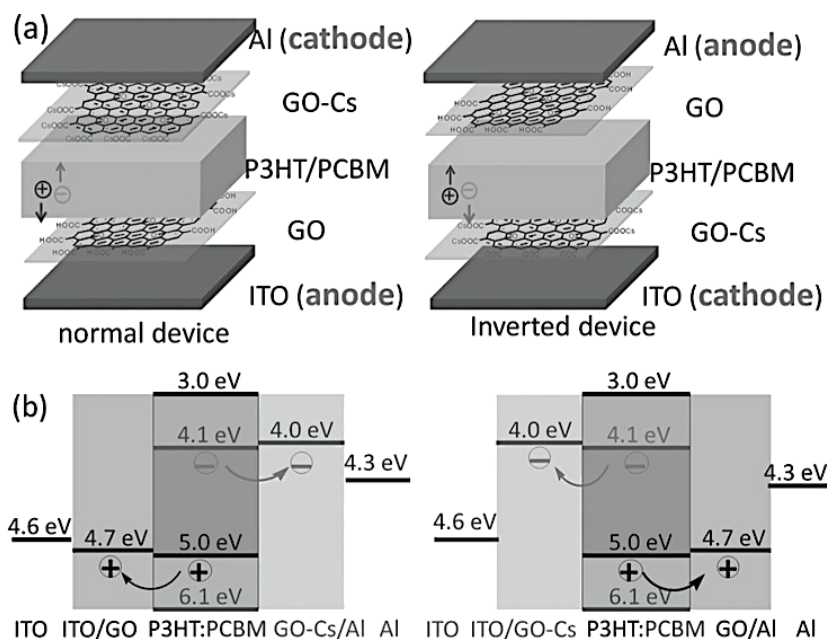
Figure 44: Device structures (a) and energy level diagrams (b) of the normal device and the inverted device with GO as the hole-extraction layer and GO/Cs as the electron-extraction layer. Reprinted with permission from [238]. Copyright (2012) John Wiley and Sons.
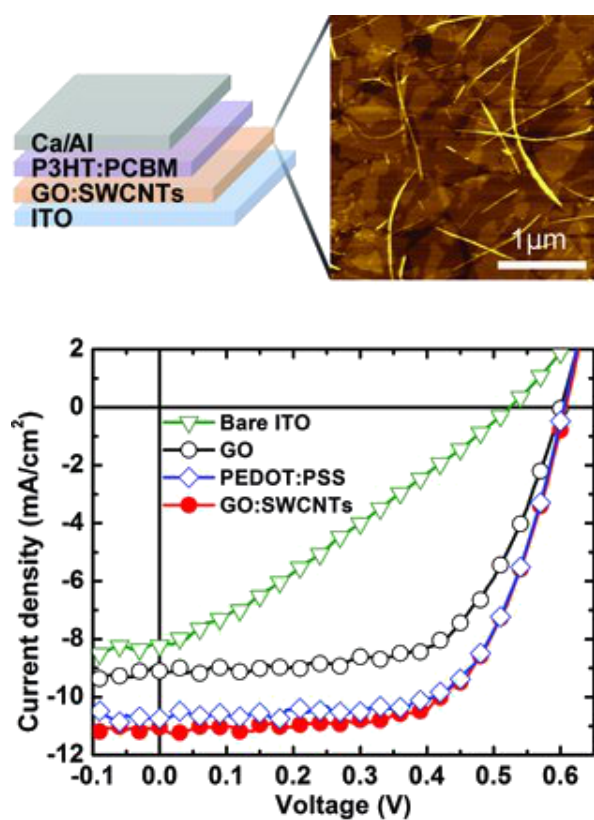
Figure 45: Addition of a small amount of SWCNTs into the GO buffer layer can increase the FF and JSC of devices with GO. Reprinted with permission from [242]. Copyright (2011) John Wiley and Sons.
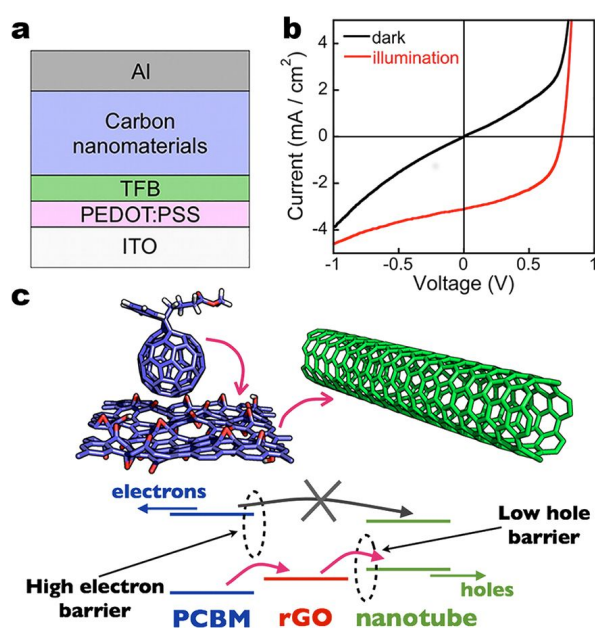
Figure 46: (a) Structure of carbon solar cells where TFB and PEDOT/PSS are the electron-blocking and hole-conducting layers, respectively, deposited on top of the ITO. For the best device efficiency, a blend of rGO, $PC_{71}BM$, and s-SWCNT with a diameter of 1.2–1.7 nm was used as the active layer, which is denoted by "carbon nanomaterials". (b) Current–voltage curves in the dark and under simulated sunlight illumination of the device. (c) Interface of $PC_{71}BM$/rGO sheet/s-SWCNT. Hole carriers photogenerated within PCBM are transferred to rGO due to a large Schottky barrier for electrons, as shown by pink arrows, and then to s-SWCNT. Reprinted with permission from [243]. Copyright (2012) American Chemical Society.
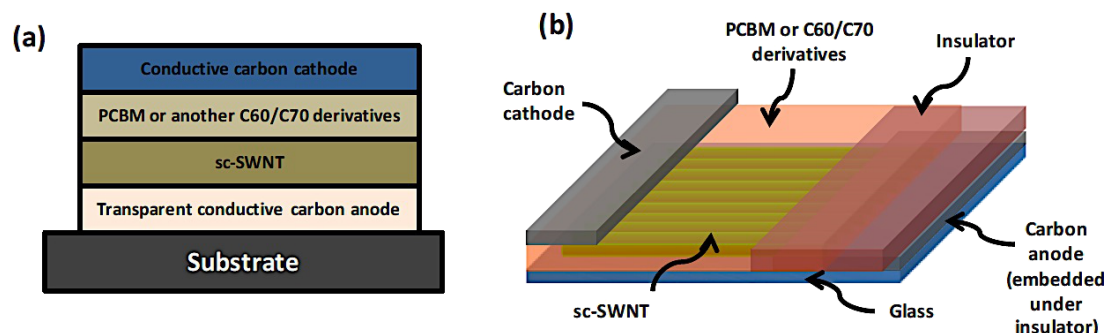
Figure 47: Schematic of the two basic all carbon nanomaterial-based solar cell device structures: (a) a typical vertical structure. An inverted vertical structure is also possible where the conductive cathode will be in contact with the substrate. (b) A horizontal structure that will take advantage of aligned SWNTs or aligned C_{60} microribbons. Reprinted with permission from the Global Climate & Energy Project, Stanford University [244].

In 2012, the same group fabricated and tested a complete carbon-based solar cell device. Although it achieved a PCE of only 5.7×10^{-3}%, they were the first worldwide to demonstrate an efficiency from a device composed solely of carbon nanomaterials [245]. A transparent electrode based on rGO was used as the anode and n-type-doped SWNTs as the cathode. Sunlight was absorbed by the semiconducting SWNTs to generate excitons that were split in the active layer composed by SWNTs and $PC_{61}BM$ [245].

To date, the PCE is still limited by the low photon absorption of the active layer. New compounds are being used in the active layer or novel carbon nanomaterials, such as fullerene derivatives and SWCNTs, and new architectures have been implemented. Although carbon nanomaterials are strong light absorbers, their percentage in the active layer is optimized to achieve the maximum PCE. Also, the thickness of the active layer is usually less than 1 μm because increased thickness is unfavorable for exciton extraction. At present, tandem organic solar cells based on the combination of high band gap and low band gap polymers represent a reliable way to achieve improved spectral range for the photoabsorption in the device. However, the challenge of trapping more incoming photons in terms of light-electron conversion [246] has not been solved.

Graphene has also been employed in solar cells other than the organic ones. By coating CVD graphene onto n-type Si, Schottky junction solar cells with efficiencies up to 1.5% were made by Li et al. [247]. The efficiency of this type of solar cell was increased to 8.6% under AM 1.5 illumination by chemically doping the graphene sheets with bis(trifluoromethane-sulfonyl)amide $((CF_3SO_2)_2NH)$ [248]. By doping the CVD graphene film coated onto n-Si with HNO_3, and subsequently spin coating a layer of colloidal TiO_2 antireflection film, Shi et al. improved the solar cell efficiency to 14.5% under standard illumination [249]. Graphene films in dye-sensitized solar cells

are mainly used as counter electrodes, which outperform platinum electrodes in some cases [250-252].

Supercapacitors

Electrochemical capacitors (ECs) have been known by different names such as "ultracapacitors" or "power capacitors" but the most recognized name today is "supercapacitors". The term supercapacitor was introduced by NEC because it was the first company to commercialize a device with the name SuperCapacitor™ in 1971 [253].

Supercapacitors have been in development since 1957 when Becker [254] first used carbon flooded with a sulfuric acid electrolyte to develop charge storage at the interface between these two materials. However, it was not until 1969 that the company SOHIO [255] first launched this technology into the market. The real success of supercapacitors started in the 1990s when government programs in the United States began giving funds for this technology to be incorporated into hybrid vehicles for providing necessary power for acceleration [256].

Supercapacitors can provide a higher power density but a smaller energy density compared to traditional chemical batteries, which make them very attractive for applications where instantaneous power is required. The other key characteristics of supercapacitors are: ability to charge–discharge within seconds; a long lifetime of more than 10^6 cycles; environmentally friendly; and stable operation at various temperatures. Figure 48 shows a typical energy density vs power density plot, also called a Ragone plot, that compares different energy storage devices. It can be seen that supercapacitors fill the gap between capacitors and batteries [257].

Today, several companies such as Maxwell, FastCap Systems, NEC, Panasonic, Tokin and even car companies such as Volvo are investing further in the development of this technology
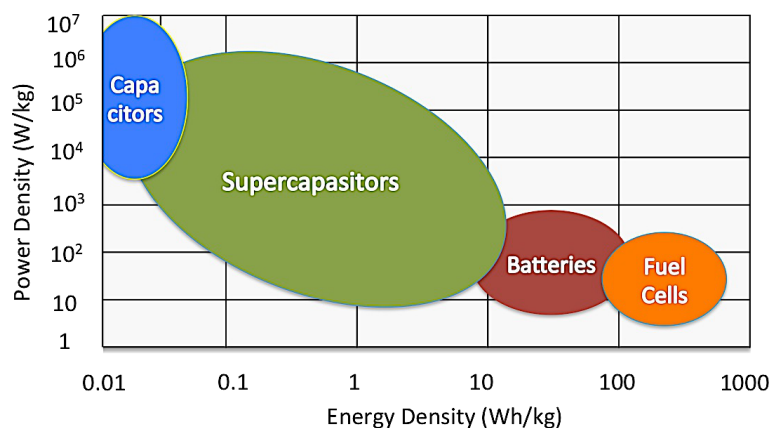
Figure 48: Energy density vs power density (Ragone plot) for various energy storage devices [257].

because of the potential large amount of energy in a small component that can be easily integrated into a device. Volvo for example is working on reducing the weight and increasing the space in a hybrid vehicle by incorporating supercapacitors in the frame of the car [258].

Supercapacitors are typically divided in two categories: electric double-layer capacitors (EDLCs) and pseudo-capacitors. A subcategory called hybrid capacitors can be identified if the EDLCs and the pseudo-capacitors are combined together into a single device (Figure 49) [253].

EDLCs typically store the energy at the electrode/electrolyte interface as shown in Figure 50. During the charging phase, an external electric field applied to the device moves the ions at the electrode/electrolyte interface [253].
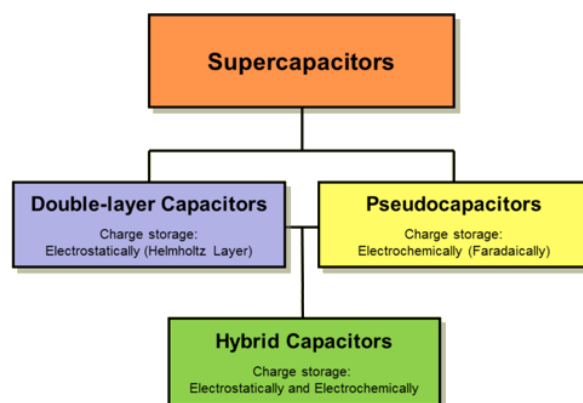
Figure 49: Hierarchical classification of supercapacitors and related types [259].
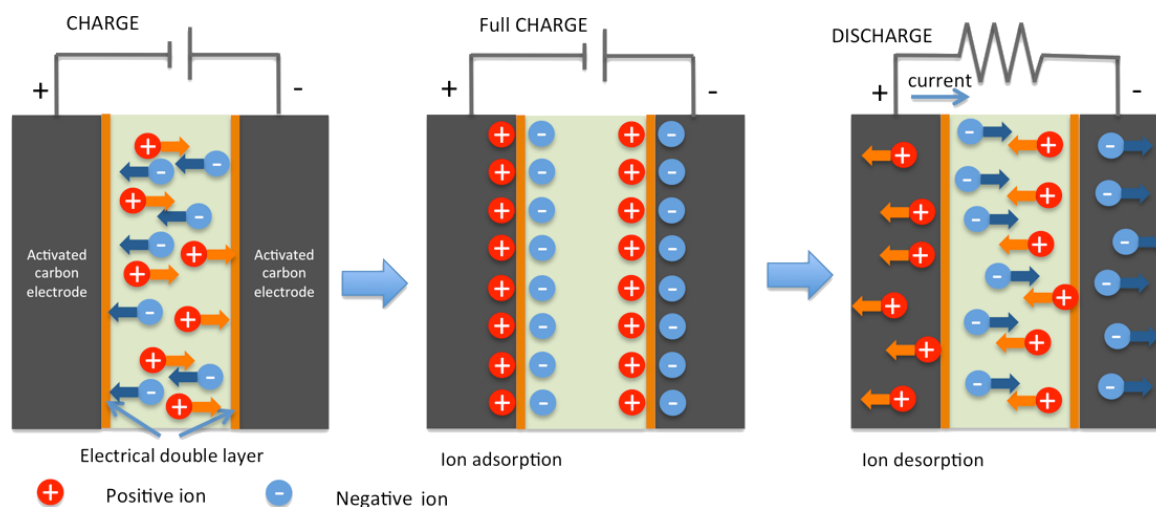
Figure 50: Charge and discharge processes of an EDLC.

Positive and negative ions are accumulated at this interface, typically on the order of 5–10 Å [260]. The conventional equation that defines the capacitance is [203]:

$$C = \varepsilon_0 \varepsilon_r \frac{A}{d}, \qquad (5)$$

where ε_0 is the permittivity of the vacuum, ε_r is the permittivity of the electrolyte and d is the thickness of the double layer with surface area A. The thickness (d) of the interface is very small (on the order of Å), as discussed previously, while the surface area (A) of the electrode is usually very due to the choice of porous structures with a large internal surface area usually chosen for supercapacitor applications. In this way, the capacitance can reach a high value (>10 μF/cm^2).

The model described to store the charge at the electrode/electrolyte interface was first derived by Helmholtz [261] in the 19th century. But only in around 1910 Gouy [262] and Chapman [263] were able to expand the model by considering the thermal motion of the electrolyte ions that lead to a diffuse layer. In 1924, Stern [264] combined the two theories in order to identify an inner plane, inner Helmholtz plane (IHP), and an outer plane, outer Helmholtz plane (OHP). The ions of the IHP are strongly bound to the IHP resulting in a strong electric field in that area (Figure 51) [265]. The capacitance established at one electrode will be given by the sum of a compact double layer capacitance (C_H) and diffusion region capacitance (C_{diff}):

$$\frac{1}{C} = \frac{1}{C_H} + \frac{1}{C_{diff}}. \qquad (6)$$

The ideal total capacitance in an EDLC is given by the sum of the capacitances established at the two electrode/electrolyte interfaces [266]:

$$\frac{1}{C} = \frac{1}{C_1} + \frac{1}{C_2}. \qquad (7)$$

Unfortunately, other parameters have to be considered in a simple equivalent circuit of an EDLC, such as the insulation resistances (R_1, R_2), the electrode resistances (Re_1, Re_2) and the interelectrode resistance (R_S) [253] (Figure 52).

Figure 51: Models of the electrical double layer at a positively charged surface: (a) the Helmholtz model, (b) the Gouy–Chapman model, and (c) the Stern model, showing the inner Helmholtz plane (IHP) and outer Helmholtz plane (OHP). The IHP refers to the distance of closest approach of specifically adsorbed ions (generally anions) and OHP refers to that of the nonspecifically adsorbed ions. The OHP is also the plane where the diffuse layer begins. d is the double layer distance described by the Helmholtz model. Ψ_0 and Ψ are the potentials at the electrode surface and the electrode/electrolyte interface, respectively. Reprinted with permission from [265]. Copyright (2009) Royal Society of Chemistry.

C_1, C_2:	Capacitor
R_{e1}, R_{e2}:	Electrode resistance
R_s:	Interelectrode resistance
R_1, R_2:	Insulation resistance

Figure 52: Simple equivalent circuit.

In contrast, pseudo-capacitors are devices where the charge is not stored electrostatically but electrochemically, similar to what happens in conventional lithium ion batteries. The materials that compose the electrode are subjected to a faradaic oxidation/reduction reaction at specific potentials during charging and discharging processes involving absorption or intercalation with the electrolyte. Pseudocapacitive materials such as conducting polymers (e.g., polyanaline (PANI) [267]) or metal oxides (e.g., ruthenium oxide (RuO_2) [268]) can have 10–100 times larger capacitance than EDLCs but they suffer from poor stability, short lifetime and are expensive to synthesize. Because of these drawbacks, they are usually combined with carbon materials creating hybrid supercapacitors. The capacitance for a pseudocapacitor is calculated using the following equation [253]:

$$\frac{C}{Q} = \frac{\frac{F}{RT}\exp\left(\Delta E \frac{F}{RT}\right)}{\left[1+\exp\left(\Delta E \frac{F}{RT}\right)\right]^2}, \tag{8}$$

by using the Nernst equation, which describes the general oxidation/reduction phenomenon. Here, E represents the equilibrium potential for the reaction and $\Delta E = (E - E^0)$, F is the Faraday constant defined as the number of coulombs per mole of electrons and Q describes the charge related to the materials subjected to oxidation or reduction.

Pseudocapacitors are not explored in this work because of the drawbacks previously described and because of the uncertainty of whether they should be categorized in the supercapacitor or in the battery family. In fact, their operating mechanism is more similar to a chemical battery than to a supercapacitor.

In order to characterize the electrical properties of a supercapacitor, three electrochemical measurement techniques are usually performed: cyclic voltammetry (CV), galvanostatic charging/discharging and electrochemical impedance measurements.

The CV technique consists of applying a potential sweep rate dV/dt from a lower limit to an upper limit and vice versa in order to measure the reversibility of the process and the stability of the device. The characteristic of the CV curve depends on the rate of the electron transfer reactions, the chemical reactivity of the electrode/electrolyte and the voltage scan rate [269]. The CV measurement is usually plotted as voltage (V) vs current (I) with an ideal supercapacitor presenting a rectangular CV curve when the capacitance (C) is constant across the different potential scan range (Figure 53). The capacitance (C) can be calcu-

lated by measuring the current (I) from the CV curves and knowing the applied potential sweep rate (dV/dt) from the equation:

$$I = C\left(\frac{\mathrm{d}V}{\mathrm{d}t}\right). \tag{9}$$
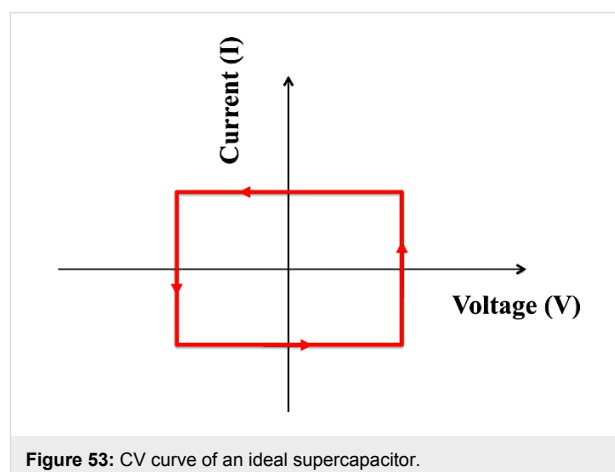
Figure 53: CV curve of an ideal supercapacitor.

Most of the real CV curves for an EDLC show deviations from the ideal shape because of the electrolyte and electrode resistance and unwanted Faradaic reactions. For example, Figure 54 shows a simulation of CV curves with increasing internal resistance at a fixed scan rate [270].
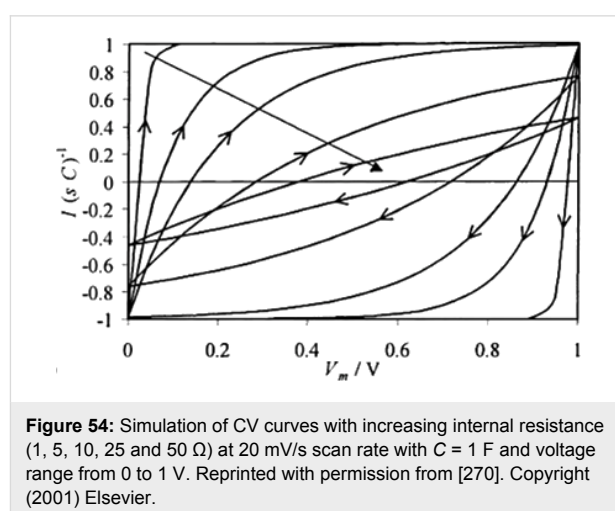
Figure 54: Simulation of CV curves with increasing internal resistance (1, 5, 10, 25 and 50 Ω) at 20 mV/s scan rate with C = 1 F and voltage range from 0 to 1 V. Reprinted with permission from [270]. Copyright (2001) Elsevier.

The galvanostatic charge/discharge measurement is instead obtained by charging/discharging the supercapacitor at a certain defined current (I) within a certain voltage window. The galvanostatic charge/discharge measurement is plotted as time (s) vs voltage (V) (Figure 55). The capacitance and the internal resistance of the device can be extracted from this measure-

ment technique. The capacitance is calculated from the slope of the charge or discharge curve with the equation [253]:

$$C = I / (-\Delta V / \Delta t). \tag{10}$$

The effective series resistance (R_{ESR}) is calculated from the voltage drop (V_{drop}) that occurs at the initial portion of the discharge with the equation [253]:

$$R_{\text{ESR}} = V_{\text{drop}} / 2I. \tag{11}$$
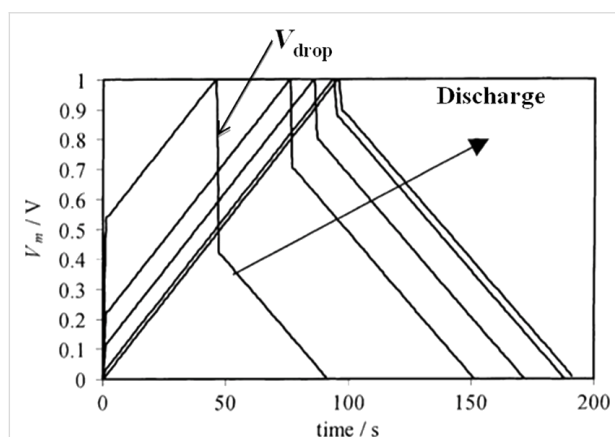
Figure 55: Simulation of the charge/discharge curves with increasing internal resistance (0, 1, 5, 10 and 25 Ω) at *I* = 10 mA. The smallest V_{drop} can be achieved with the smallest internal resistance. The longest total charging time is also achieved with the smallest internal resistance. Reprinted with permission from [270]. Copyright (2001) Elsevier.

It can be seen in Figure 55 that the total charging time for a specific voltage limit decreases with increasing the internal resistance. This occurs because the electrode has a smaller effective charge capacity within a specific voltage window [270].

Another useful measurement technique to reveal the properties of a supercapacitor is electrochemical impedance spectroscopy (EIS), which measures the impedance (*Z*) of a device over a range of frequencies. The data obtained are usually graphed as the real part of the impedance (Z_{real}) vs the imaginary part of the impedance (Z_{imag}), also called a Nyquist plot. Figure 56 shows a Nyquist plot of an ideal and a simplified supercapacitor. The ideal capacitor exhibits only a vertical line while a real one usually starts with a 45° line and then approaches a vertical line at higher frequencies. The 45° region, also called the Warburg region, is governed by the distributed resistance/capacitance in a porous electrode and by the electrolyte conductivity [253]. The effective series resistance (R_{ESR}) and the equivalent distributed resistance (R_{EDR}) can also be extracted from the Nyquist plot as shown in Figure 56 [266].
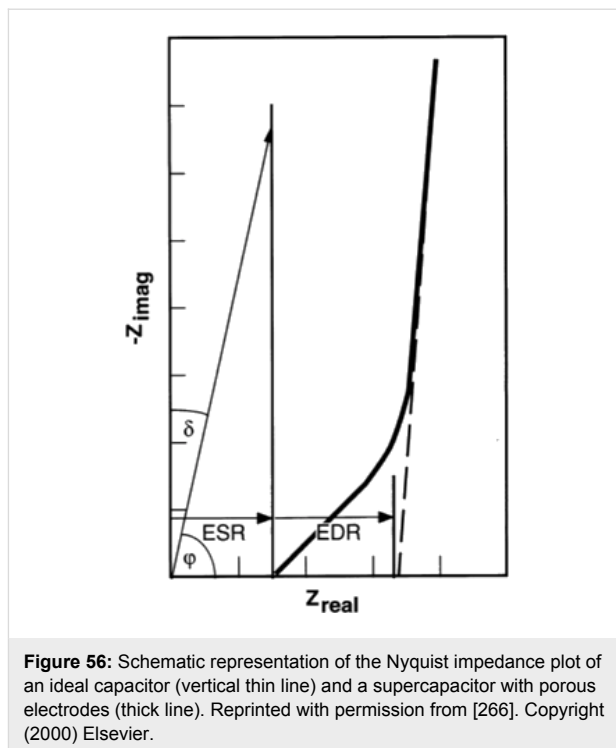
Figure 56: Schematic representation of the Nyquist impedance plot of an ideal capacitor (vertical thin line) and a supercapacitor with porous electrodes (thick line). Reprinted with permission from [266]. Copyright (2000) Elsevier.

To determine the supercapacitor performance two other important factors, apart from the capacitance, need to be considered. One is the energy density that corresponds to the amount of energy stored per unit volume or mass and the other one is the power density that combines energy density with the speed that energy can be drawn out of a device.

The energy density per unit volume, expressed in Wh/cm^3, is defined by the equation [253]:

$$E = \frac{1}{2} C_{\text{stack}} \frac{(\Delta V)^2}{3600}, \tag{12}$$

where $C_{\text{stack}} = C/V$ is the volumetric stack capacitance expressed in F/cm^3 and ΔV is the operating voltage window of the device.

The power density per unit volume, expressed in W/cm^3 is defined by the equation [253]:

$$P = \frac{(\Delta V)^2}{4 R_{\text{ESR}} Ad}, \tag{13}$$

where *A* is the area of the electrodes, *d* is the distance between the electrodes, ΔV is the operating voltage window of the device and R_{ESR} is the total effective resistance of the device that can be extracted from the galvanostatic charge/discharge curves.

The maximum energy and power densities are achieved at the maximum voltage applied to the device, which is usually determined by the maximum voltage that the electrolyte can tolerate before decomposition and breakdown of the electrode material.

Using Equation 12, the easiest way to increase the energy density is to increase the capacitance (C) of the device, but this is not the only way. The energy density can also be improved by increasing the voltage window of the electrolyte (ΔV), which follows a quadratic law. Organic electrolytes can achieve higher voltages compared to aqueous electrolytes, allowing for a dramatic increase in the energy density. Unfortunately, they also show an effective series resistance (R_{ESR}) of at least 20 times larger than the aqueous ones, which reduces the power density (Equation 13) [266].

In summary, several important characteristics of an EDLC have to be considered to maximize the performance of the device [253]:

- The specific surface area of the electrodes to increase the capacitance
- The conductivity of the electrodes to reduce the power density losses
- The resistance to any oxidation/reduction on the surface of the electrode to maintain good stability and performance
- Controlled size distribution of the pores that should match the size of the electrolyte ions
- Electrochemical stability of the electrolyte in the voltage operating window of the device
- Low interconnected resistance of the electrolyte
- Good wettability of the electrolyte on the electrode.
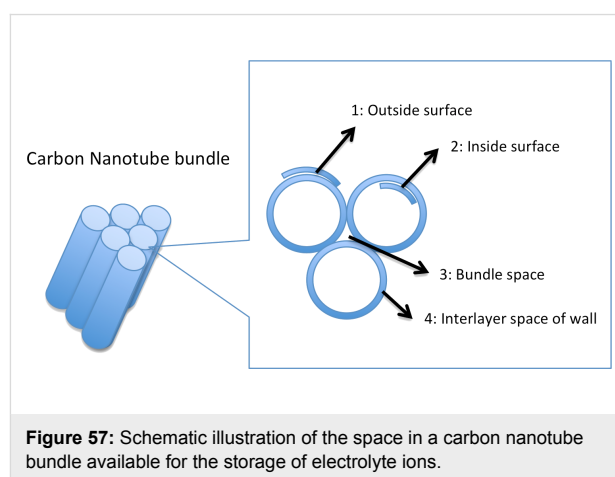
Carbon nanotubes and graphene in supercapacitors

Activated carbons (ACs) are the most commonly used materials for commercial electrodes in supercapacitors because of their stable electrical properties, large surface area and low cost. ACs can be produced by thermal and/or chemical activation of various types of materials containing carbon such as wood, coal, etc. For thermal activation, high temperatures are usually employed (from 700 to 1200 °C) in the presence of oxidizing gases. For chemical activation, the process temperatures are lower (from 400 to 700 °C) and require activating agents such as phosphoric acid, sodium hydroxide and others [265]. These two processes allow the production of a material with a high surface area (3000 m^2/g) but with a wide pore size distribution consisting of macropores (>50 nm), mesopores (2–50 nm) and micropores (<2 nm) [271,272]. Even with such a high surface area, the experimental capacitance obtained with these materials is lower (<10 μF/cm^2) when compared to the theoretical

calculations [260]. This difference indicates that not all of the pores are contributing to the charge storage mechanism and that the specific surface area is not the only parameter to be considered in a supercapacitor [273]. Pore shape and structure, pore size distribution, electrical conductivity and wettability of the electrode are other important parameters that contribute to the performance of the device as previously discussed. The pore size distribution in ACs is still a problem to be addressed [265].

Carbon nanomaterials such as CNTs and graphene are excellent candidates to replace ACs as electrode materials in supercapacitors because of their remarkable chemical stability, large specific surface area, and high electric conductivity [274,275]. Commercial supercapacitors contain metal foils such as Al, Cu, and stainless steel, as current collectors which require special techniques to passivate the metal surface to avoid corrosion effects due to the use of alkali or acidic electrolytes [276]. Because of the high conductivity of CNTs and graphene, they can function as the capacitor electrode and the current collector, leading to a more simple and lightweight device.

CNTs in the form of either arrays grown on a substrate [277,278] or network films processed from a suspension [279] have been employed in supercapacitors. CNTs show a specific capacitance of 15–200 F/g [280] with a high power capability but a low energy density due to a small specific surface area (<500 m^2 g^{-1}) caused by the entangled arrangement of the CNTs with only the outermost tubes of the bundles exposed to the electrolyte [281] (Figure 57).

Figure 57: Schematic illustration of the space in a carbon nanotube bundle available for the storage of electrolyte ions.

CNTs grown on a substrate can be very useful for high power applications when compared to ACs. In fact, the schematic in Figure 58 shows that if the CNTs are all aligned on a current collector, the resistance can be low because the path for ions and electrons is much simpler than in the typical AC electrodes [281] .

Figure 58: Comparison of conducting paths for electron and electrolyte ions in aligned carbon nanotubes and granular activated carbon.
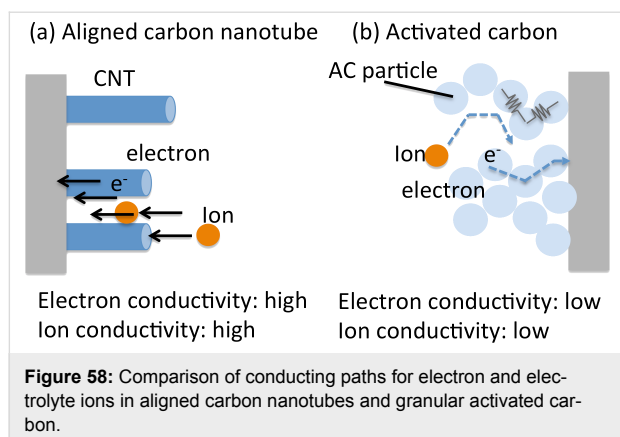
MWNTs were the first to be proposed as an electrode for an EDLC, showing a capacitance of ≈100 F/g, a low surface area of ≈400 m^2/g and a low power density value of 8 kW/kg [282]. However, apart from their high volumetric capacitance values [283] obtained by optimizing the growth process, SWNTs are preferred because they exhibit a higher surface area and consequently better overall performance [284].

Many strategies have been proposed to increase the surface area of SWNTs such as oxidizing methods, pyrolysis methods or by the use of liquid zipping effects [279,285,286]. The electrochemi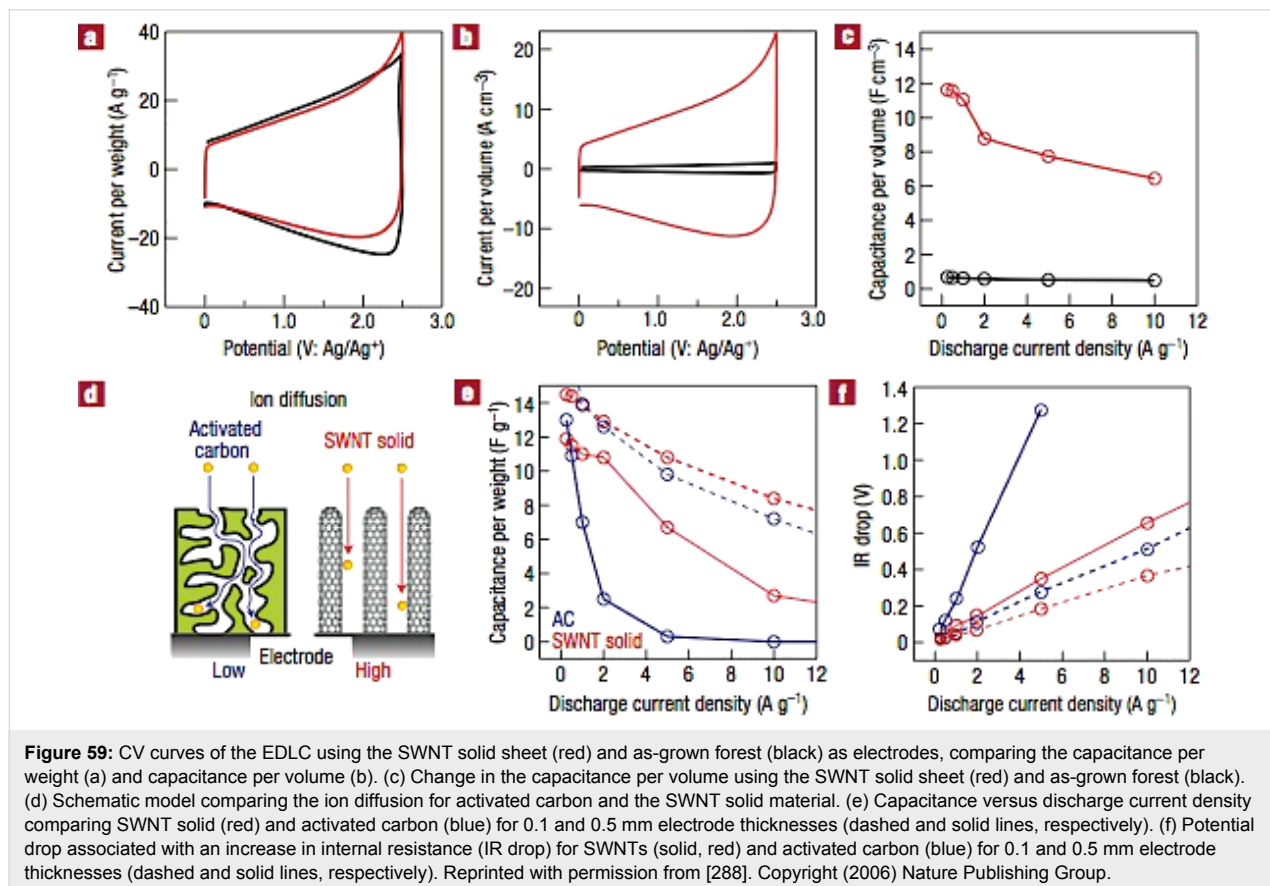cal oxidation in KOH can increase the capacitance by three times because it can facilitate the opening of some tubes, which increases the surface area. A "super growth" method has also been beneficial to increase the surface area to 1000 m^2/g as compared to the 400–800 m^2/g for commercial CNTs, proving that this material can potentially have better capacitive performance than ACs [286].

A combination of the "super growth" and oxidation methods has also been proposed in order to further increase the surface area to over 2000 m^2/g with an energy density and power density of 24.7 Wh/kg and 98.9 kW/kg, respectively [287].

Vertical SWNTs with high purity and high density have also been grown by CVD and then removed from the substrate as a single unit, uniformly densified and engineered into different shapes by the zipping effects of liquid. The surface tension of the liquids and the strong van der Waals interactions can connect the SWNTs together in near-ideal graphitic spacing. With this method, no insulating binders were needed with a conductivity 20 times larger than ACs and a higher capacitive performance than in the conventional SWNT forest (Figure 59) [288].

Figure 59: CV curves of the EDLC using the SWNT solid sheet (red) and as-grown forest (black) as electrodes, comparing the capacitance per weight (a) and capacitance per volume (b). (c) Change in the capacitance per volume using the SWNT solid sheet (red) and as-grown forest (black). (d) Schematic model comparing the ion diffusion for activated carbon and the SWNT solid material. (e) Capacitance versus discharge current density comparing SWNT solid (red) and activated carbon (blue) for 0.1 and 0.5 mm electrode thicknesses (dashed and solid lines, respectively). (f) Potential drop associated with an increase in internal resistance (IR drop) for SWNTs (solid, red) and activated carbon (blue) for 0.1 and 0.5 mm electrode thicknesses (dashed and solid lines, respectively). Reprinted with permission from [288]. Copyright (2006) Nature Publishing Group.

Another alternative, a mixture of CNTs and carbon aerogel, has been proposed to increase the surface area to 1059 m^2/g, obtaining a specific capacitance of 524 F/g (Figure 60) [289].

Recently, graphene and graphene derivatives have been considered for supercapacitor electrodes, not only for their exceptional electrical, thermal and mechanical properties previously described, but also for two other main reasons: the theoretical high surface area (2630 m^2/g) [68] and the inexpensive methods of production [81]. In fact, for supercapacitor applications, methods like the chemical exfoliation of graphite or the thermal reduction of GO are probably the most used because of the straightforward, large production quantity of quality materials for electrodes. The addition of certain functional groups can also help to disperse the material in different solvents [290].

Stoller et al. [68] were the first group to explore the possibility of using chemically modified graphene, specifically reducing GO with hydrazine hydrate for EDLCs, obtaining specific capacitance values of 135 F/g and 99 F/g for aqueous and organic electrolytes, respectively, even with a relatively low surface area of 705 m^2/g (Figure 61).

In order to maximize the performance by increasing the surface area, Wang et al. [291] proposed to reduce the GO in a gas–solid reduction process (Figure 62). In this way, they were able to obtain a capacitance of 205 F/g with a power density and energy density of 10 kW/kg and 28.5 Wh/kg, respectively.

Others, like Chen et al. [292], proposed to mildly reduce the GO with hydrobromic acid in order to maintain some oxygen functional groups that could promote the wettability of the electrode and avoid restacking of the graphene sheets, allowing better penetration of the electrolyte ions through the film. With this method, they were able to achieve a very high capacitance value of 348 F/g.

A GO exfoliation process was also explored as a method to fabricate EDLC electrodes. In particular, Lv et al. [293] showed that low temperature exfoliation of GO (200 °C) led to graphene-based electrodes with 264 F/g and 122 F/g in aqueous and organic electrolytes, respectively.

Instead, Zhu et al. [122] proposed a very inexpensive way to reduce GO for EDLC electrodes. They reduced the material in a conventional microwave oven obtaining a surface area of 463 m^2/g with a specific capacitance of 191 F/g [122]. Certainly, these are not the highest values reported but the ability to use a simple microwave creates a pathway for a scalable and inexpensive process to fabricate electrodes for supercapacitors.

A similar concept was proposed in 2012 by El-Kady et al. [294] using a standard LightScribe DVD optical drive to reduce GO with a gel electrolyte based on poly(vinyl alcohol) (PVA)-H_3PO_4 to fabricate flexible devices (Figure 63). The material showed a high surface area of 1520 m^2/g and a specific capacitance of 265 F/g.
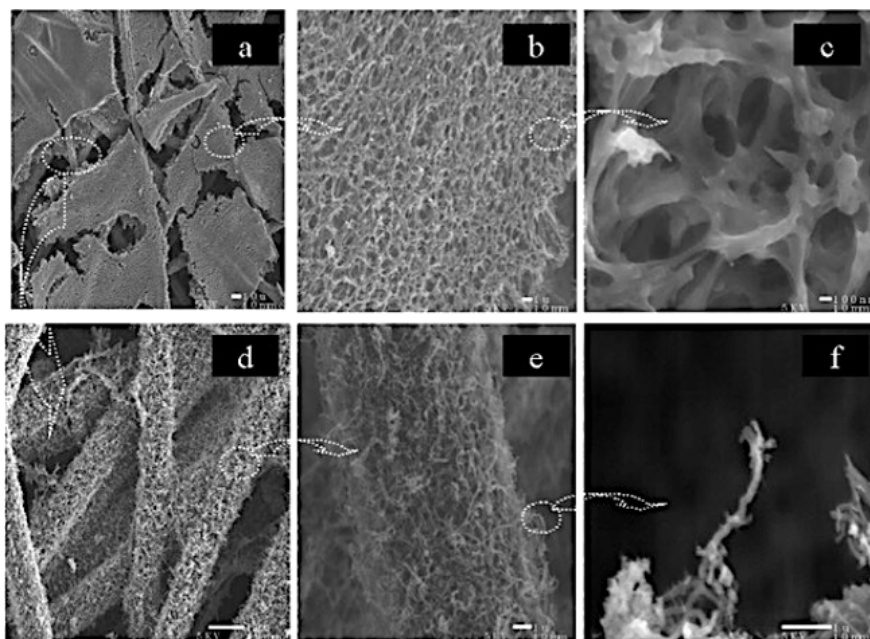
Figure 60: SEM images of CNT–carbon aerogel nanocomposites. Reprinted with permission from [289]. Copyright (2008) John Wiley and Sons.
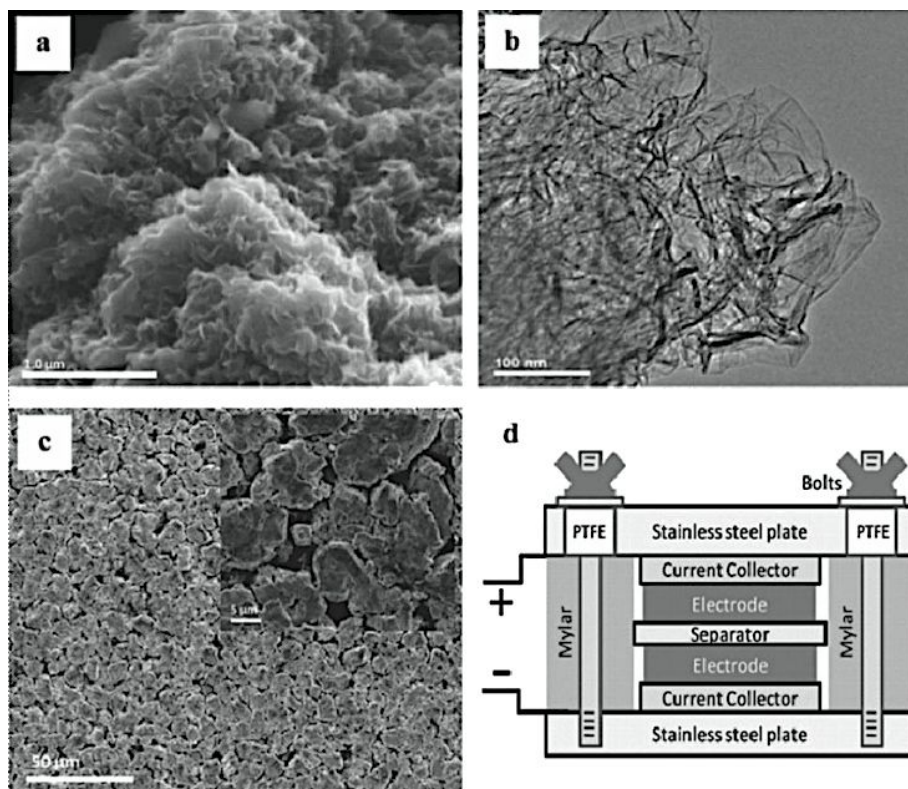
Figure 61: Graphene-based EDLCs utilizing chemically modified graphene as electrode materials. (a) Scanning electron microscopy (SEM) image of the material. (b) Transmission electron microscopy (TEM) image showing individual graphene sheets. (c) Low- and high- (inset) magnification SEM images of the electrode. (d) Schematic of test cell assembly. Reprinted with permission from [68]. Copyright (2008) American Chemical Society.

In 2013, El-Kady et al. [295] were able to further develop this technique by fabricating more than 100 micro-supercapacitors on a single DVD disc in 30 min. The devices were built on flex-ible substrates to be integrated with MEMS or CMOS technologies in a single chip (Figure 64). These micro-supercapacitors demonstrated a very high power density of 200 W/cm^3.
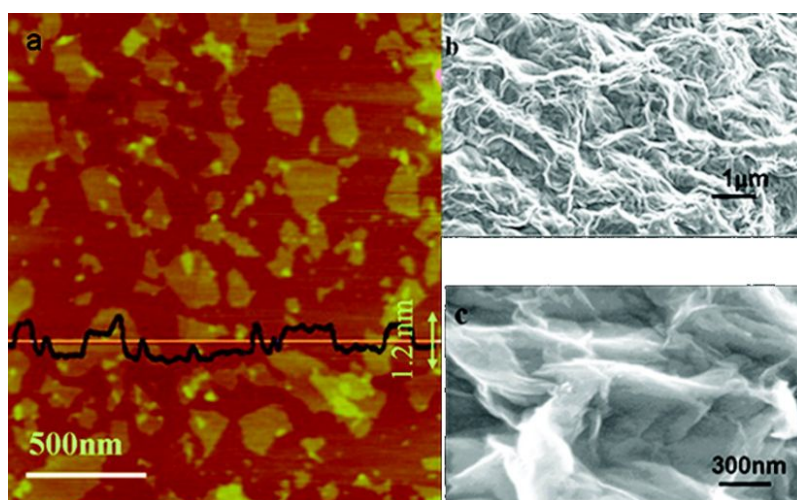
Figure 62: Morphology of graphene oxide and graphene-based materials. (a) Tapping-mode AFM image of graphene oxide and height profile plot. (b) and (c) SEM images at lower and higher magnification respectively of the graphene oxide reduced by a gas–solid reduction process. Reprinted with permission from [291]. Copyright (2009) American Chemical Society.

Figure 63: (a–d) Schematic illustration of the process to make laser-scribed graphene-based electrochemical capacitors. A GO film supported on a flexible substrate is placed on top of a LightScribe-enabled DVD media disc, and a computer image is then laser-irradiated on the GO film in a LightScribe DVD drive. (e) As shown in the photograph, the GO film changes from golden brown to black as it reduced to laser-scribed graphene. The low power, infrared laser changes the stacked GO sheets immediately into a well-exfoliated few-layered laser-scribed film, a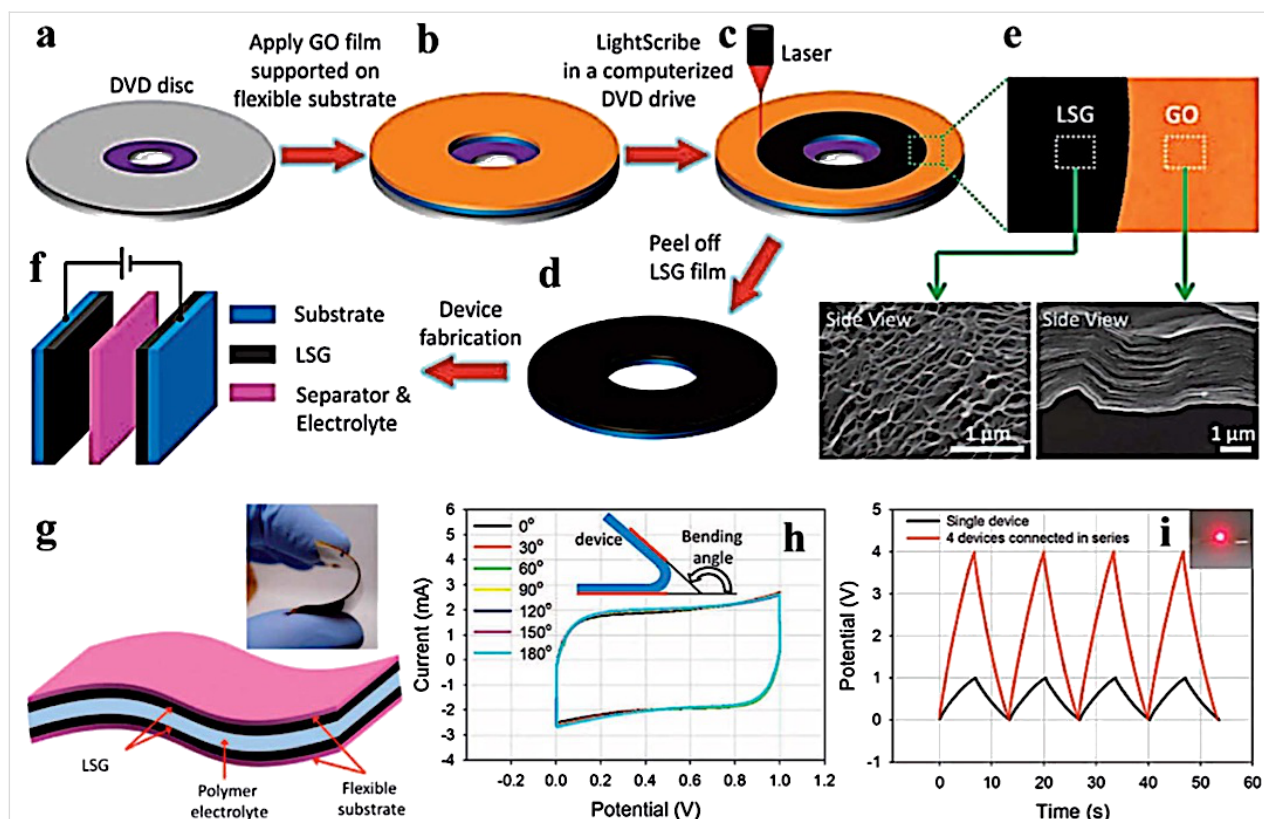s shown in the cross-sectional SEM images. (f) A symmetric supercapacitor is constructed from two identical laser-scribed electrodes, an ion-porous separator, and an electrolyte. (g) A schematic diagram of the all-solid-state device illustrates that the gelled electrolyte can serve as both the electrolyte and separator. The inset is a digital photograph showing the flexibility of the device. (h) CV curves collected at a scan rate of 1000 mV/s when the device was bent at different angles. (i) Galvanostatic charge–discharge curves for four devices connected in series. The inset image shows the glow of an LED light by the four devices in series. Reprinted with permission from [294]. Copyright (2012) The American Association for the Advancement of Science.
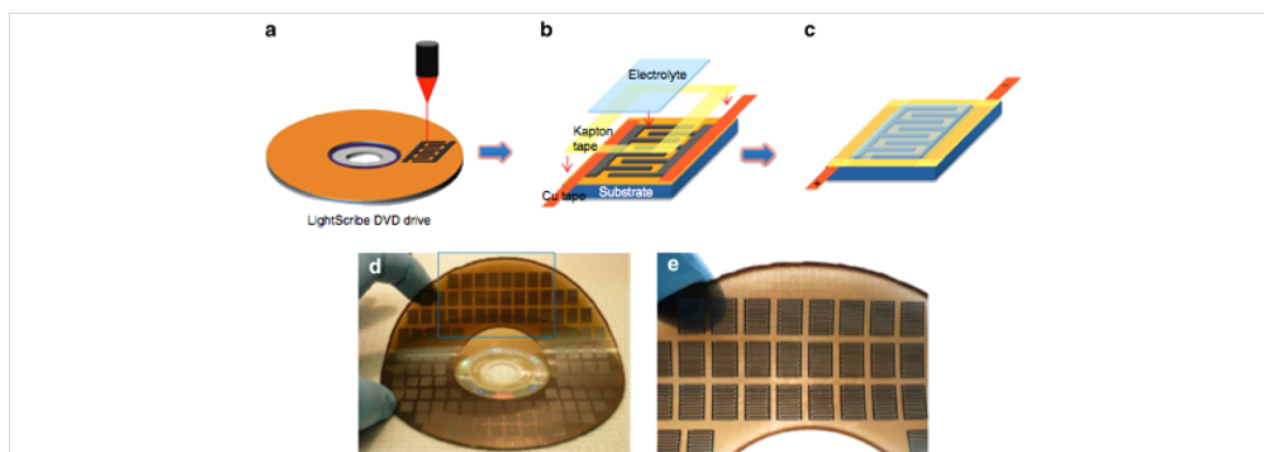
Figure 64: (a–c) Schematic diagram showing the fabrication process for a laser-scribed graphene micro-supercapacitor. A GO film supported on a PET sheet is placed on a DVD media disc. The disc is inserted into a LightScribe DVD drive and a computer-designed circuit is etched onto the film. The laser inside the drive converts the golden brown GO into black, laser-scribed graphene at precise locations to produce interdigitated graphene circuits (a). Copper tape is applied along the edges to improve the electrical contacts, and the interdigitated area is defined by polyimide (Kapton) tape (b). An electrolyte overcoat is then added to create a planar micro-supercapacitor (c). This technique has the potential for the direct writing of microdevices with a high areal density (d,e). More than 100 microdevices can be produced on a single run. The microdevices are flexible and can be produced on virtually any substrate. Reprinted with permission from [295]. Copyright (2013) Nature Publishing Group.

Planar structures have limited capacitance due to the restacking of graphene sheets, which reduces the surface area. Therefore, other graphene structures have been proposed to further boost the performance of EDLCs. Porous, 3D graphene networks have been synthetized by freezing and drying a chemically reduced GO dispersion [296,297] or by CVD on nickel foam [298,299] to overcome the limitations of planar structures.

Xu et al. [296] prepared a 3D, porous, reduced, GO hydrogel with a capacitance of 186 F/g and a capacitance decay of only 8.4% after 10,000 charge/discharge cycles in a PVA-H_3PO_4 gel polymer electrolyte (Figure 65). Even with such a high capacitance, the power density was limited to 0.5–5 kW/kg, indicating that the porous structure has a large internal resistance and needs to be combined with a Au current collector. An electrode that also functions as a bendable, high efficiency current collector is usually preferred for supercapacitor applications in order to maintain a high power density value [300,301].

Hybrid structures of CNTs and graphene electrodes have also been proposed for supercapacitors in order to combine the properties of both materials, boosting the capacitance and the energy density of the devices [302-306]. In fact, the idea is to increase the surface area and have a defined architecture for the electric transport by using graphene to store the charge and CNTs as an efficient charge transport material. Jha et al. [304] demonstrated that a device made of reduced GO mixed in a proportion of 1:1 with SWNTs achieved a specific capacitance of 222 F/g and with an energy density of 94 Wh/kg in an ionic liquid electrolyte (Figure 66).

Flexible supercapacitors have been integrated into organic solar cells in order to eliminate the energy loss in the wiring between the energy conversion device and the storage device. Wee et al. [307] demonstrated that it is possible to integrate both devices in a single, printable, all-solid device. The supercapacitor was charged by a polymer solar cell and the discharge was achieved by connecting it to a resistor (Figure 67). The capacitance obtained from the discharge was only 28 F/g but the possibility to combine both devices onto a flexible and printable surface opens up the avenue to a scalable and cheap process of a simultaneous generation and storage device.

Conclusions

The demand for energy is rapidly increasing due to dramatic population growth and technological advances worldwide. Conventional energy sources are limited and pollute the environment. Photovoltaics represent a viable solution to produce clean energy but its costs is still high due to the materials and process techniques involved. Moreover, an efficient energy storage system is required to be independent from the grid, because the sun is an intermittent energy source. Carbon, one of the most abundant materials found on earth, can be a valid material for both energy generation and storage. As was outlined in this review, it can be employed in real-world devices such as organic solar cells and supercapacitors in the form of one or more of its allotrope forms (e.g., graphene, carbon nanotubes, fullerenes) by employing inexpensive synthesis and process methods based on printing and roll-to-roll techniques.

In this paper, different approaches to synthesize and employ carbon nanomaterials for energy generation and storage applications have been explored. Carbon nanomaterials used for organic solar cells have been thoroughly reviewed. Graphene produced by electrochemical exfoliation was discussed as a viable solution to produce a large quantity of transparent electrodes for organic solar cells. Achieving a high quality material on a large scale still remains an issue in order to compete with conventional conducting transparent electrodes such as ITO. However, its potential for production on flexible substrates makes it very appealing for the organic solar cell field where roll-to-roll techniques have been recently employed to increase the production volume. Additionally, fullerene derivatives, CNTs and graphene oxide could help to boost the performance

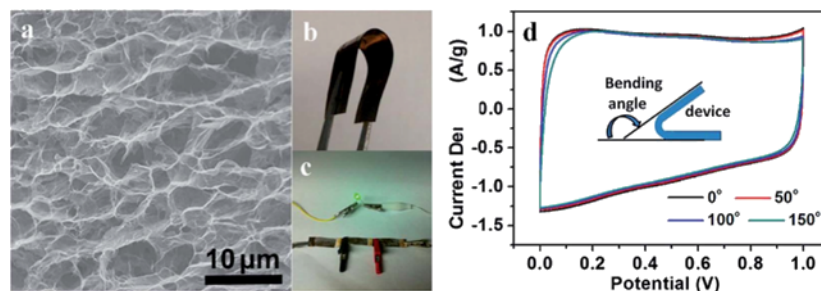**Figure 65:** (a) SEM image of the interior microstructure of a graphene hydrogel. (b) Photograph of the flexible solid-state supercapacitor based on a graphene hydrogel film. (c) Photograph of a green LED powered by the three supercapacitors in series. (d) CV curves of the flexible solid-state device at 10 mV/s for different bending angles. Reprinted with permission from [296]. Copyright (2013) American Chemical Society.
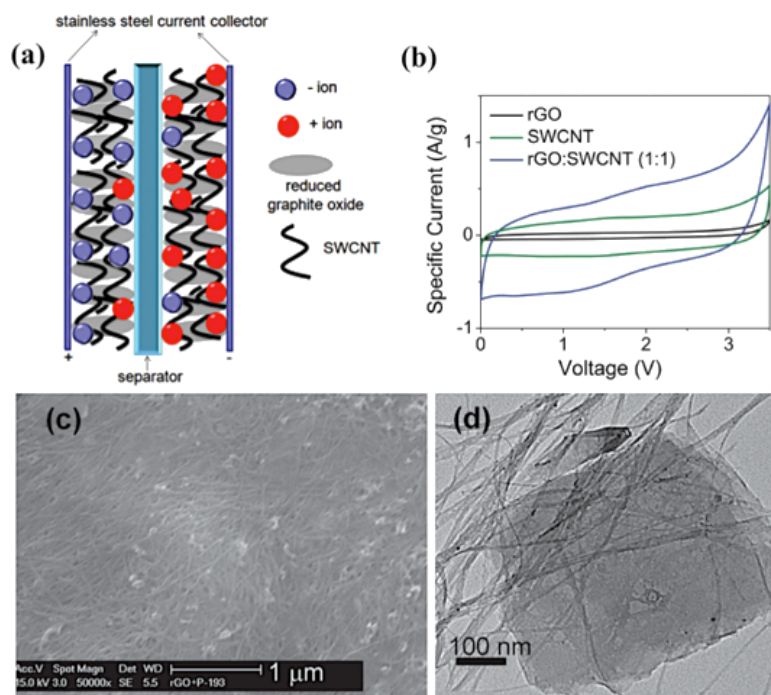
Figure 66: (a) Schematic illustration of a supercapacitor cell fabricated from reduced graphite oxide (rGO) and SWNTs. (b) CV curves of the materials at 10 mV/s. (c) SEM image of the hybrid material consisting of rGO and SWNTs in a 1:1 weight ratio. (d) TEM image of the hybrid material showing few-layer graphene sheets covering a network of SWNTs. Reprinted with permission from [304]. Copyright (2012) John Wiley and Sons.
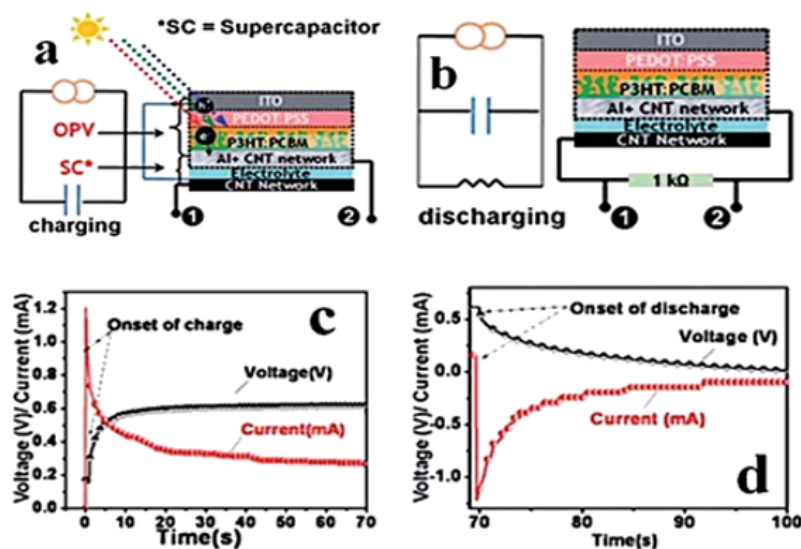
Figure 67: (a) and (b) are schematic, equivalent circuit illustrations for a polymer solar cell and a supercapacitor during charging and discharging, respectively. The voltage and current profiles versus time for the charging (c) and discharging (d) process. Reprinted with permission from [307]. Copyright (2010) Royal Society of Chemistry.

of organic solar cell devices if employed in the active or buffer layers. In fact, their semiconducting properties can be tuned by doping with other materials or by changing their physical structure in order to absorb a broader range of solar spectrum wavelengths.

Carbon nanomaterials, in particular carbon nanotubes and graphene, have also been proven to be very efficient and reliable materials for energy storage. The high specific surface area and conductivity of graphene are two key features for employing this material in supercapacitors. The ability to use a solid-

state electrolyte composed of graphene oxide or a gel polymer electrolyte allow for the possibility of printable, flexible devices that do not require encapsulation. Although carbon nanotubes generally have a relatively low specific surface area, they can still be employed in combination with graphene to increase the conductivity of the electrode or the surface roughness of the film, resulting in an increase in the number of ions stored at the electrode/electrolyte interface.

Carbon continues to surprise researchers with its extraordinary properties. Completely new carbon structures have been synthesized over the last 20 years, from 0D fullerenes to 1D nanotubes and 2D graphene. The low cost of this element, the sixth most abundant element on earth, makes it an attractive choice to replace conventional materials for energy generation and storage applications.

Acknowledgements

References

1. Gilbert, G. *World population: a reference handbook;* ABC-CLIO, 2005.
2. http://www.iea.org/Textbase/npsum/WEO2015SUM.pdf
3. Service, R. F. *Science* **2005,** *309,* 548–551. doi:10.1126/science.309.5734.548
4. Armaroli, N.; Balzani, V. *Energy for a sustainable world: from the oil age to a sun-powered future;* Wiley-VCH: Weinheim, 2011.
5. Smalley, R. E. *MRS Bull.* **2005,** *30,* 412–417. doi:10.1557/mrs2005.124
6. Smil, V. *Energy at the crossroads: global perspectives and uncertainties;* MIT Press: Cambridge, Mass., USA, 2003.
7. *Global Energy Trends – BP Statistical Review 2014.* Energy Matters, 2014; http://euanmearns.com/global-energy-trends-bp-statistical-review-2014/.
8. Holgate, S. T. *Air pollution and health;* Academic Press: San Diego, 1999.
9. Letcher, T. *Climate Change: Observed impacts on Planet Earth;* Elsevier, 2009.
10. Simmons, M. R. *Twilight In the Desert - Doubting Saudi Potential;* Petroleum Intelligence Weekly, 2005.
11. Hoffert, M. I.; Calderia, K.; Jain, A. K.; Haites, E. F.; Harvey, L. D. D.; Potter, S. D.; Schlesinger, M. E.; Schneider, S. H.; Watts, R. G.; Wigley, T. M. L.; Wuebbles, D. J. *Nature* **1998,** *395,* 881–884. doi:10.1038/27638
12. Lewis, N. S. *MRS Bull.* **2007,** *32,* 808–820. doi:10.1557/mrs2007.168
13. Armaroli, N.; Balzani, V. *Angew. Chem., Int. Ed.* **2006,** *46,* 52–66. doi:10.1002/anie.200602373
14. *What's the Value of Saudi Aramco?* http://www.texasenterprise.utexas.edu/article/whats-value-saudi-aramco (accessed Dec 14, 2015).
15. Ginley, D.; Green, M. A.; Collins, R. *MRS Bull.* **2008,** *33,* 355–364. doi:10.1557/mrs2008.71
16. Zhu, H.; Wei, J.; Wang, K.; Wu, D. *Sol. Energy Mater. Sol. Cells* **2009,** *93,* 1461–1470. doi:10.1016/j.solmat.2009.04.006
17. Frackowiak, E. *Phys. Chem. Chem. Phys.* **2007,** *9,* 1774–1785. doi:10.1039/b618139m
18. W., J. *J. Mol. Struct.* **1990,** *240,* 339. doi:10.1016/0022-2860(90)80522-L
19. Mauter, M. S.; Elimelech, M. *Environ. Sci. Technol.* **2008,** *42,* 5843–5859. doi:10.1021/es8006904
20. Osawa, E. *Kagaku (Kyoto, Jpn.)* **1970,** *25,* 854–863.
21. Bochvar, D. A.; Galpern, E. G. *Dokl. Akad. Nauk SSSR* **1979,** *209,* 610–612.
22. Kroto, H. W.; Heath, J. R.; O'Brien, S. C.; Curl, R. F.; Smalley, R. E. *Nature* **1985,** *318,* 162–163. doi:10.1038/318162a0
23. Marks, R. W. *R. Buckminster Fuller.* Encyclopaedia Britannica, Inc., 2013.
24. Taylor, R.; Hare, J. P.; Abdul-Sada, A. K.; Kroto, H. W. *J. Chem. Soc., Chem. Commun.* **1990,** 1423–1425. doi:10.1039/c39900001423
25. Dresselhaus, M. S.; Dresselhaus, G.; Eklund, P. C. *J. Mater. Res.* **1993,** *8,* 2054–2097. doi:10.1557/JMR.1993.2054
26. Hirsch, A.; Brettreich, M. *Fullerenes: Chemistry and Reactions;* Wiley-VCH, 2006.
27. Krätschmer, W.; Lamb, L. D.; Fostiropoulos, K.; Huffman, D. R. *Nature* **1990,** *347,* 354–358. doi:10.1038/347354a0
28. Hare, J. P.; Kroto, H. W.; Taylor, R. *Chem. Phys. Lett.* **1991,** *177,* 394–398. doi:10.1016/0009-2614(91)85072-5
29. Bezmelnitsin, V. N.; Eletskii, A. V.; Schepetov, N. G.; Avent, A. G.; Taylor, R. *J. Chem. Soc., Perkin Trans. 2* **1997,** 683–686. doi:10.1039/A607847H
30. Howard, J. B.; McKinnon, J. T.; Makarovsky, Y.; Lafleur, A. L.; Johnson, M. E. *Nature* **1991,** *352,* 139–141. doi:10.1038/352139a0
31. Hebgen, P.; Goel, A.; Howard, J. B.; Rainey, L. C.; Vander Sande, J. B. *Proc. Combust. Inst.* **2000,** *28,* 1397–1404. doi:10.1016/S0082-0784(00)80355-0
32. Scott, L. T.; Boorum, M. M.; McMahon, B. J.; Hagen, S.; Mack, J.; Blank, J.; Wegner, H.; de Meijere, A. *Science* **2002,** *295,* 1500–1503. doi:10.1126/science.1068427
33. Lee, H. M.; Olmstead, M. M.; Suetsuna, T.; Shimotani, H.; Dragoe, N.; Cross, R. J.; Kitazawa, K.; Balch, A. L. *Chem. Commun.* **2002,** 1352–1353. doi:10.1039/b202925c
34. Saunders, M.; Jimenez-Vazquez, H. A.; Cross, R. J.; Mroczkowski, S.; Gross, M. L.; Giblin, D. E.; Poreda, R. J. *J. Am. Chem. Soc.* **1994,** *116,* 2193–2194. doi:10.1021/ja00084a089

35. Hummelen, J. C.; Knight, B. W.; LePeq, F.; Wudl, F.; Yao, J.; Wilkins, C. L. *J. Org. Chem.* **1995,** *60,* 532–538. doi:10.1021/jo00108a012

36. Gonzalez, R.; Hummelen, J. C.; Wudl, F. *J. Org. Chem.* **1995,** *60,* 2618–2620. doi:10.1021/jo00113a049

37. Iijima, S. *Nature* **1991,** *354,* 56–58. doi:10.1038/354056a0

38. Walters, D. A.; Ericson, L. M.; Casavant, M. J.; Liu, J.; Colbert, D. T.; Smith, K. A.; Smalley, R. E. *Appl. Phys. Lett.* **1999,** *74,* 3803–3805. doi:10.1063/1.124185

39. Yu, M. F.; Files, B. S.; Arepalli, S.; Ruoff, R. S. *Phys. Rev. Lett.* **2000,** *84,* 5552–5555. doi:10.1103/PhysRevLett.84.5552

40. Gao, G.; Çagin, T.; Goddard III, W. A. *Nanotechnology* **1998,** *9,* 184–191. doi:10.1088/0957-4484/9/3/007

41. Tans, S. J.; Devoret, M. H.; Dai, H.; Thess, A.; Smalley, R. E.; Geerligs, L. J.; Dekker, C. *Nature* **1997,** *386,* 474–477. doi:10.1038/386474a0

42. Hone, J.; Whitney, M.; Piskoti, C.; Zettl, A. *Phys. Rev. B: Condens. Matter Mater. Phys.* **1999,** *59,* R2514–R2516. doi:10.1103/PhysRevB.59.R2514

43. Ajayan, P. M. *Chem. Rev.* **1999,** *99,* 1787–1800. doi:10.1021/cr970102g

44. Vidu, R.; Rahman, M.; Mahmoudi, M.; Enachescu, M.; Poteca, T. D.; Opris, I. *Front. Syst. Neurosci.* **2014,** *8,* 91. doi:10.3389/fnsys.2014.00091

45. Dresselhaus, M. S.; Dresselhaus, G.; Saito, R. *Carbon* **1995,** *33,* 883–891. doi:10.1016/0008-6223(95)00017-8

46. Wang, X.; Li, Q.; Xie, J.; Jin, Z.; Wang, J.; Li, Y.; Jiang, K.; Fan, S. *Nano Lett.* **2009,** *9,* 3137–3141. doi:10.1021/nl901260b

47. Gore, J. P.; Sane, A. Flame Synthesis of Carbon Nanotubes. In *Carbon Nanotubes - Synthesis, Characterization, Applications;* Yellampalli, S., Ed.; InTech, 2011. doi:10.5772/21012

48. Baddour, C. E.; Briens, C. *Int. J. Chem. React. Eng.* **2005,** *3.* doi:10.2202/1542-6580.1279

49. Bolshakov, A. P.; Uglov, S. A.; Saveliev, A. V.; Konov, V. I.; Gorbunov, A. A.; Pompe, W.; Graff, A. *Diamond Relat. Mater.* **2002,** *11,* 927–930. doi:10.1016/S0925-9635(01)00641-0

50. Eklund, P. C.; Pradhan, B. K.; Kim, U. J.; Xiong, Q.; Fischer, J. E.; Friedman, A. D.; Holloway, B. C.; Jordan, K.; Smith, M. W. *Nano Lett.* **2002,** *2,* 561–566. doi:10.1021/nl025515y

51. Guo, T.; Nikolaev, P.; Thess, A.; Colbert, D. T.; Smalley, R. E. *Chem. Phys. Lett.* **1995,** *243,* 49–54. doi:10.1016/0009-2614(95)00825-O

52. Arepalli, S. *J. Nanosci. Nanotechnol.* **2004,** *4,* 317–325. doi:10.1166/jnn.2004.072

53. Jorio, A.; Dresselhaus, G.; Dresselhaus, M. S. *Carbon Nanotubes: Advanced Topics in the Synthesis, Structure, Properties and Applications;* Springer-Verlag: Berlin, 2008. doi:10.1007/978-3-540-72865-8

54. Sinnott, S. B.; Andrews, R.; Qian, D.; Rao, A. M.; Mao, Z.; Dickey, E. C.; Derbyshire, F. *Chem. Phys. Lett.* **1999,** *315,* 25–30. doi:10.1016/S0009-2614(99)01216-6

55. Kumar, M.; Ando, Y. *J. Nanosci. Nanotechnol.* **2010,** *10,* 3739–3758. doi:10.1166/jnn.2010.2939

56. Sato, H.; Hata, K. *New Diamond Front. Carbon Technol.* **2006,** *16,* 163–176.

57. Alexandrescu, R.; Crunteanu, A.; Morjan, R.-E.; Morjan, I.; Rohmund, F.; Falk, L. K. L.; Ledoux, G.; Huisken, F. *Infrared Phys. Technol.* **2003,** *44,* 43–50. doi:10.1016/S1350-4495(02)00158-5

58. Smalley, R. E.; Yakobson, B. I. *Solid State Commun.* **1998,** *107,* 597–606. doi:10.1016/S0038-1098(98)00210-5

59. Nikolaev, P.; Bronikowski, M. J.; Bradley, R. K.; Rohmund, F.; Colbert, D. T.; Smith, K. A.; Smalley, R. E. *Chem. Phys. Lett.* **1999,** *313,* 91–97. doi:10.1016/S0009-2614(99)01029-5

60. Geim, A. K.; Novoselov, K. S. *Nat. Mater.* **2007,** *6,* 183–191. doi:10.1038/nmat1849

61. Seyller, T.; Bostwick, A.; Emtsev, K. V.; Horn, K.; Ley, L.; McChesney, J. L.; Ohta, T.; Riley, J. D.; Rotenberg, E.; Speck, F. *Phys. Status Solidi B* **2008,** *245,* 1436–1446. doi:10.1002/pssb.200844143

62. Mayorov, A. S.; Gorbachev, R. V.; Morozov, S. V.; Britnell, L.; Jalil, R.; Ponomarenko, L. A.; Blake, P.; Novoselov, K. S.; Watanabe, K.; Taniguchi, T.; Geim, A. K. *Nano Lett.* **2011,** *11,* 2396–2399. doi:10.1021/nl200758b

63. Morozov, S. V.; Novoselov, K. S.; Katsnelson, M. I.; Schedin, F.; Elias, D. C.; Jaszczak, J. A.; Geim, A. K. *Phys. Rev. Lett.* **2008,** *100,* 016602. doi:10.1103/PhysRevLett.100.016602

64. Lee, C.; Wei, X.; Kysar, J. W.; Hone, J. *Science* **2008,** *321,* 385–388. doi:10.1126/science.1157996

65. Liu, F.; Ming, P.; Li, J. *Phys. Rev. B* **2007,** *76,* 064120. doi:10.1103/PhysRevB.76.064120

66. Balandin, A. A. *Nat. Mater.* **2011,** *10,* 569–581. doi:10.1038/nmat3064

67. Nair, R. R.; Blake, P.; Grigorenko, A. N.; Novoselov, K. S.; Booth, T. J.; Stauber, T.; Peres, N. M. R.; Geim, A. K. *Science* **2008,** *320,* 1308. doi:10.1126/science.1156965

68. Stoller, M. D.; Park, S.; Zhu, Y.; An, J.; Ruoff, R. S. *Nano Lett.* **2008,** *8,* 3498–3502. doi:10.1021/nl802558y

69. Bunch, J. S.; Verbridge, S. S.; Alden, J. S.; van der Zande, A. M.; Parpia, J. M.; Craighead, H. G.; McEuen, P. L. *Nano Lett.* **2008,** *8,* 2458–2462. doi:10.1021/nl801457b

70. Moser, J.; Barreiro, A.; Bachtold, A. *Appl. Phys. Lett.* **2007,** *91,* 163513. doi:10.1063/1.2789673

71. Novoselov, K. S.; McCann, E.; Morozov, S. V.; Fal'ko, V. I.; Katsnelson, M. I.; Zeitler, U.; Jiang, D.; Schedin, F.; Geim, A. K. *Nat. Phys.* **2006,** *2,* 177–180. doi:10.1038/nphys245

72. Guinea, F.; Katsnelson, M. I.; Geim, A. K. *Nat. Phys.* **2010,** *6,* 30–33. doi:10.1038/nphys1420

73. Meric, I.; Han, M. Y.; Young, A. F.; Ozyilmaz, B.; Kim, P.; Shepard, K. L. *Nat. Nanotechnol.* **2008,** *3,* 654–659. doi:10.1038/nnano.2008.268

74. Novoselov, K. *Nat. Mater.* **2007,** *6,* 720–721. doi:10.1038/nmat2006

75. Geim, A. K. *Science* **2009,** *324,* 1530–1534. doi:10.1126/science.1158877

76. Wallace, P. R. *Phys. Rev.* **1947,** *71,* 622. doi:10.1103/PhysRev.71.622

77. Avouris, P.; Dimitrakopoulos, C. *Mater. Today* **2012,** *15,* 86–97. doi:10.1016/S1369-7021(12)70044-5

78. Novoselov, K. S.; Jiang, D.; Schedin, F.; Booth, T. J.; Khotkevich, V. V.; Morozov, S. V.; Geim, A. K. *Proc. Natl. Acad. Sci. U. S. A.* **2005,** *102,* 10451–10453. doi:10.1073/pnas.0502848102

79. Geim, A. K. *Usp. Fiz. Nauk* **2011,** *181,* 1284–1298. doi:10.3367/UFNr.0181.201112e.1284

80. Novoselov, K. S. *Rev. Mod. Phys.* **2011,** *83,* 837. doi:10.1103/RevModPhys.83.837

81. Novoselov, K. S.; Fal'ko, V. I.; Colombo, L.; Gellert, P. R.; Schwab, M. G.; Kim, K. *Nature* **2012,** *490,* 192–200. doi:10.1038/nature11458

82. Bae, S.; Kim, H.; Lee, Y.; Xu, X.; Park, J.-S.; Zheng, Y.; Balakrishnan, J.; Lei, T.; Ri Kim, H.; Song, Y. I.; Kim, Y.-J.; Kim, K. S.; Özyilmaz, B.; Ahn, J.-H.; Hong, B. H.; Iijima, S. *Nat. Nanotechnol.* **2010,** *5,* 574–578. doi:10.1038/nnano.2010.132

83. Li, X.; Cai, W.; An, J.; Kim, S.; Nah, J.; Yang, D.; Piner, R.; Velamakanni, A.; Jung, I.; Tutuc, E.; Banerjee, S. K.; Colombo, L.; Ruoff, R. S. *Science* **2009,** *324,* 1312–1314. doi:10.1126/science.1171245

84. Stankovich, S.; Dikin, D. A.; Piner, R. D.; Kohlhaas, K. A.; Kleinhammes, A.; Jia, Y.; Wu, Y.; Nguyen, S. T.; Ruoff, R. S. *Carbon* **2007,** *45,* 1558–1565. doi:10.1016/j.carbon.2007.02.034

85. Eda, G.; Fanchini, G.; Chhowalla, M. *Nat. Nanotechnol.* **2008,** *3,* 270–274. doi:10.1038/nnano.2008.83

86. Novoselov, K. S.; Geim, A. K.; Morozov, S. V.; Jiang, D.; Zhang, Y.; Dubonos, S. V.; Grigorieva, I. V.; Firsov, A. A. *Science* **2004,** *306,* 666–669. doi:10.1126/science.1102896

87. Allen, M. J.; Tung, V. C.; Kaner, R. B. *Chem. Rev.* **2010,** *110,* 132–145. doi:10.1021/cr900070d

88. Hernandez, Y.; Nicolosi, V.; Lotya, M.; Blighe, F. M.; Sun, Z.; De, S.; McGovern, I. T.; Holland, B.; Byrne, M.; Gun'Ko, Y. K.; Boland, J. J.; Niraj, P.; Duesberg, G.; Krishnamurthy, S.; Goodhue, R.; Hutchison, J.; Scardaci, V.; Ferrari, A. C.; Coleman, J. N. *Nat. Nanotechnol.* **2008,** *3,* 563–568. doi:10.1038/nnano.2008.215

89. Coleman, J. N. *Acc. Chem. Res.* **2012,** *46,* 14–22. doi:10.1021/ar300009f

90. De, S.; King, P. J.; Lotya, M.; O'Neill, A.; Doherty, E. M.; Hernandez, Y.; Duesberg, G. S.; Coleman, J. N. *Small* **2010,** *6,* 458–464. doi:10.1002/smll.200901162

91. Zhang, X.; Coleman, A. C.; Katsonis, N.; Browne, W. R.; van Wees, B. J.; Feringa, B. L. *Chem. Commun.* **2010,** *46,* 7539–7541. doi:10.1039/c0cc02688c

92. Du, W.; Jiang, X.; Zhu, L. *J. Mater. Chem. A* **2013,** *1,* 10592–10606. doi:10.1039/c3ta12212c

93. Nuvoli, D.; Valentini, L.; Alzari, V.; Scognamillo, S.; Bon, S. B.; Piccinini, M.; Illescas, J.; Mariani, A. *J. Mater. Chem.* **2011,** *21,* 3428–3431. doi:10.1039/C0JM02461A

94. Behabtu, N.; Lomeda, J. R.; Green, M. J.; Higginbotham, A. L.; Sinitskii, A.; Kosynkin, D. V.; Tsentalovich, D.; Parra-Vasquez, A. N. G.; Schmidt, J.; Kesselman, E.; Cohen, Y.; Talmon, Y.; Tour, J. M.; Pasquali, M. *Nat. Nanotechnol.* **2010,** *5,* 406–411. doi:10.1038/nnano.2010.86

95. Pupysheva, O. V.; Farajian, A. A.; Knick, C. R.; Zhamu, A.; Jang, B. Z. *J. Phys. Chem. C* **2010,** *114,* 21083–21087. doi:10.1021/jp1071378

96. Su, C.-Y.; Lu, A.-Y.; Xu, Y.; Chen, F.-R.; Khlobystov, A. N.; Li, L.-J. *ACS Nano* **2011,** *5,* 2332–2339. doi:10.1021/nn200025p

97. Liu, J.; Notarianni, M.; Will, G.; Tiong, V. T.; Wang, H.; Motta, N. *Langmuir* **2013,** *29,* 13307–13314. doi:10.1021/la403159n

98. Wassei, J. K.; Kaner, R. B. *Mater. Today* **2010,** *13,* 52–59. doi:10.1016/S1369-7021(10)70034-1

99. Gao, W.; Alemany, L. B.; Ci, L.; Ajayan, P. M. *Nat. Chem.* **2009,** *1,* 403–408. doi:10.1038/nchem.281

100. Szabó, T.; Berkesi, O.; Forgó, P.; Josepovits, K.; Sanakis, Y.; Petridis, D.; Dékány, I. *Chem. Mater.* **2006,** *18,* 2740–2749. doi:10.1021/cm060258+

101. Chen, D.; Feng, H.; Li, J. *Chem. Rev.* **2012,** *112,* 6027–6053. doi:10.1021/cr300115g

102. He, H.; Klinowski, J.; Forster, M.; Lerf, A. *Chem. Phys. Lett.* **1998,** *287,* 53–56. doi:10.1016/S0009-2614(98)00144-4

103. Becerril, H. A.; Mao, J.; Liu, Z.; Stoltenberg, R. M.; Bao, Z.; Chen, Y. *ACS Nano* **2008,** *2,* 463–470. doi:10.1021/nn700375n

104. Wang, S.; Chia, P.-J.; Chua, L.-L.; Zhao, L.-H.; Png, R.-Q.; Sivaramakrishnan, S.; Zhou, M.; Goh, R. G.-S.; Friend, R. H.; Wee, A. T.-S.; Ho, P. K.-H. *Adv. Mater.* **2008,** *20,* 3440–3446. doi:10.1002/adma.200800279

105. Brodie, B. C. *Philos. Trans. R. Soc. London* **1859,** *149,* 249–259. doi:10.1098/rstl.1859.0013

106. Hummers, W. S., Jr.; Offeman, R. E. *J. Am. Chem. Soc.* **1958,** *80,* 1339. doi:10.1021/ja01539a017

107. Marcano, D. C.; Kosynkin, D. V.; Berlin, J. M.; Sinitskii, A.; Sun, Z.; Slesarev, A.; Alemany, L. B.; Lu, W.; Tour, J. M. *ACS Nano* **2010,** *4,* 4806–4814. doi:10.1021/nn1006368

108. Eda, G.; Chhowalla, M. *Adv. Mater.* **2010,** *22,* 2392–2415. doi:10.1002/adma.200903689

109. Pei, S.; Cheng, H. M. *Carbon* **2012,** *50,* 3210–3228. doi:10.1016/j.carbon.2011.11.010

110. López, V.; Sundaram, R. S.; Gómez-Navarro, C.; Olea, D.; Burghard, M.; Gómez-Herrero, J.; Zamora, F. I.; Kern, K. *Adv. Mater.* **2009,** *21,* 4683–4686. doi:10.1002/adma.200990172

111. Gómez-Navarro, C.; Meyer, J. C.; Sundaram, R. S.; Chuvilin, A.; Kurasch, S.; Burghard, M.; Kern, K.; Kaiser, U. *Nano Lett.* **2010,** *10,* 1144–1148. doi:10.1021/nl9031617

112. Piloto, C.; Notarianni, M.; Shafiei, M.; Taran, E.; Galpaya, D.; Yan, C.; Motta, N. *Beilstein J. Nanotechnol.* **2014,** *5,* 1073–1081. doi:10.3762/bjnano.5.120

113. Hontoria-Lucas, C.; López-Peinado, A. J.; López-González, J. d. D.; Rojas-Cervantes, M. L.; Martín-Aranda, R. M. *Carbon* **1995,** *33,* 1585–1592. doi:10.1016/0008-6223(95)00120-3

114. Jeong, H.-K.; Lee, Y. P.; Lahaye, R. J. W. E.; Park, M.-H.; An, K. H.; Kim, I. J.; Yang, C.-W.; Park, C. Y.; Ruoff, R. S.; Lee, Y. H. *J. Am. Chem. Soc.* **2008,** *130,* 1362–1366. doi:10.1021/ja076473o

115. Mattevi, C.; Eda, G.; Agnoli, S.; Miller, S.; Mkhoyan, K. A.; Celik, O.; Mastrogiovanni, D.; Granozzi, G.; Garfunkel, E.; Chhowalla, M. *Adv. Funct. Mater.* **2009,** *19,* 2577–2583. doi:10.1002/adfm.200900166

116. Ganguly, A.; Sharma, S.; Papakonstantinou, P.; Hamilton, J. *J. Phys. Chem. C* **2011,** *115,* 17009–17019. doi:10.1021/jp203741y

117. Yang, D.; Velamakanni, A.; Bozoklu, G.; Park, S.; Stoller, M.; Piner, R. D.; Stankovich, S.; Jung, I.; Field, D. A.; Ventrice, C. A., Jr.; Ruoff, R. S. *Carbon* **2009,** *47,* 145–152. doi:10.1016/j.carbon.2008.09.045

118. Schniepp, H. C.; Li, J.-L.; McAllister, M. J.; Sai, H.; Herrera-Alonso, M.; Adamson, D. H.; Prud'homme, R. K.; Car, R.; Saville, D. A.; Aksay, I. A. *J. Phys. Chem. B* **2006,** *110,* 8535–8539. doi:10.1021/jp060936f

119. Chambers, B. A.; Notarianni, M.; Liu, J.; Motta, N.; Andersson, G. G. *Appl. Surf. Sci.* **2015,** *356,* 719–725. doi:10.1016/j.apsusc.2015.07.197

120. Wu, Z.-S.; Ren, W.; Gao, L.; Zhao, J.; Chen, Z.; Liu, B.; Tang, D.; Yu, B.; Jiang, C.; Cheng, H.-M. *ACS Nano* **2009,** *3,* 411–417. doi:10.1021/nn900020u

121. Li, X.; Wang, H.; Robinson, J. T.; Sanchez, H.; Diankov, G.; Dai, H. *J. Am. Chem. Soc.* **2009,** *131,* 15939–15944. doi:10.1021/ja907098f

122. Zhu, Y.; Murali, S.; Stoller, M. D.; Velamakanni, A.; Piner, R. D.; Ruoff, R. S. *Carbon* **2010,** *48,* 2118–2122. doi:10.1016/j.carbon.2010.02.001

123. Zhang, Y.; Guo, L.; Wei, S.; He, Y.; Xia, H.; Chen, Q.; Sun, H.-B.; Xiao, F.-S. *Nano Today* **2010,** *5,* 15–20. doi:10.1016/j.nantod.2009.12.009

124. Kotov, N. A.; Dékány, I.; Fendler, J. H. *Adv. Mater.* **1996,** *8,* 637–641. doi:10.1002/adma.19960080806

125. Stankovich, S.; Piner, R. D.; Chen, X.; Wu, N.; Nguyen, S. T.; Ruoff, R. S. *J. Mater. Chem.* **2006,** *16,* 155–158. doi:10.1039/B512799H

126. He, Q.; Sudibya, H. G.; Yin, Z.; Wu, S.; Li, H.; Boey, F.; Huang, W.; Chen, P.; Zhang, H. *ACS Nano* **2010,** *4,* 3201–3208. doi:10.1021/nn100780v

127. Zhu, Y.; Cai, W.; Piner, R. D.; Velamakanni, A.; Ruoff, R. S. *Appl. Phys. Lett.* **2009,** *95,* 103104. doi:10.1063/1.3212862

128. Fernández-Merino, M. J.; Guardia, L.; Paredes, J. I.; Villar-Rodil, S.; Solís-Fernández, P.; Martínez-Alonso, A.; Tascón, J. M. D. *J. Phys. Chem. C* **2010,** *114,* 6426–6432. doi:10.1021/jp100603h

129. Periasamy, M.; Thirumalaikumar, M. *J. Organomet. Chem.* **2000,** *609,* 137–151. doi:10.1016/S0022-328X(00)00210-2

130. Moon, I. K.; Lee, J.; Ruoff, R. S.; Lee, H. *Nat. Commun.* **2010,** *1,* 1–6. doi:10.1038/ncomms1067

131. Williams, G.; Seger, B.; Kamat, P. V. *ACS Nano* **2008,** *2,* 1487–1491. doi:10.1021/nn800251f

132. Wang, Z.; Zhou, X.; Zhang, J.; Boey, F.; Zhang, H. *J. Phys. Chem. C* **2009,** *113,* 14071–14075. doi:10.1021/jp906348x

133. Dubin, S.; Gilje, S.; Wang, K.; Tung, V. C.; Cha, K.; Hall, A. S.; Farrar, J.; Varshneya, R.; Yang, Y.; Kaner, R. B. *ACS Nano* **2010,** *4,* 3845–3852. doi:10.1021/nn100511a

134. Xu, Y.; Sheng, K.; Li, C.; Shi, G. *J. Mater. Chem.* **2011,** *21,* 7376–7380. doi:10.1039/c1jm10768b

135. Yan, Z.; Peng, Z.; Tour, J. M. *Acc. Chem. Res.* **2014,** *47,* 1327–1337. doi:10.1021/ar4003043

136. Grabke, H. J.; Paulitschke, W.; Tauber, G.; Viefhaus, H. *Surf. Sci.* **1977,** *63,* 377–389. doi:10.1016/0039-6028(77)90353-3

137. Shelton, J. C.; Patil, H. R.; Blakely, J. M. *Surf. Sci.* **1974,** *43,* 493–520. doi:10.1016/0039-6028(74)90272-6

138. Hamilton, J. C.; Blakely, J. M. *Surf. Sci.* **1980,** *91,* 199–217. doi:10.1016/0039-6028(80)90080-1

139. Hagstrom, S.; Lyon, H. B.; Somorjai, G. A. *Phys. Rev. Lett.* **1965,** *15,* 491–493. doi:10.1103/PhysRevLett.15.491

140. May, J. W. *Surf. Sci.* **1969,** *17,* 267–270. doi:10.1016/0039-6028(69)90227-1

141. Zhang, Y.; Gomez, L.; Ishikawa, F. N.; Madaria, A.; Ryu, K.; Wang, C.; Badmaev, A.; Zhou, C. *J. Phys. Chem. Lett.* **2010,** *1,* 3101–3107. doi:10.1021/jz1011466

142. Chen, S.; Cai, W.; Piner, R. D.; Suk, J. W.; Wu, Y.; Ren, Y.; Kang, J.; Ruoff, R. S. *Nano Lett.* **2011,** *11,* 3519–3525. doi:10.1021/nl201699j

143. Huang, P. Y.; Ruiz-Vargas, C. S.; van der Zande, A. M.; Whitney, W. S.; Levendorf, M. P.; Kevek, J. W.; Garg, S.; Alden, J. S.; Hustedt, C. J.; Zhu, Y.; Park, J.; McEuen, P. L.; Muller, D. A. *Nature* **2011,** *469,* 389–392. doi:10.1038/nature09718

144. Tsen, A. W.; Brown, L.; Levendorf, M. P.; Ghahari, F.; Huang, P. Y.; Havener, R. W.; Ruiz-Vargas, C. S.; Muller, D. A.; Kim, P.; Park, J. *Science* **2012,** *336,* 1143–1146. doi:10.1126/science.1218948

145. Ruiz-Vargas, C. S.; Zhuang, H. L.; Huang, P. Y.; van der Zande, A. M.; Garg, S.; McEuen, P. L.; Muller, D. A.; Hennig, R. G.; Park, J. *Nano Lett.* **2011,** *11,* 2259–2263. doi:10.1021/nl200429f

146. Yan, Z.; Lin, J.; Peng, Z.; Sun, Z.; Zhu, Y.; Li, L.; Xiang, C.; Samuel, E. L.; Kittrell, C.; Tour, J. M. *ACS Nano* **2012,** *6,* 9110–9117. doi:10.1021/nn303352k

147. Li, X.; Magnuson, C. W.; Venugopal, A.; Tromp, R. M.; Hannon, J. B.; Vogel, E. M.; Colombo, L.; Ruoff, R. S. *J. Am. Chem. Soc.* **2011,** *133,* 2816–2819. doi:10.1021/ja109793s

148. Chen, S.; Ji, H.; Chou, H.; Li, Q.; Li, H.; Suk, J. W.; Piner, R.; Liao, L.; Cai, W.; Ruoff, R. S. *Adv. Mater.* **2013,** *25,* 2062–2065. doi:10.1002/adma.201204000

149. Mohsin, A.; Liu, L.; Liu, P.; Deng, W.; Ivanov, I. N.; Li, G.; Dyck, O. E.; Duscher, G.; Dunlap, J. R.; Xiao, K.; Gu, G. *ACS Nano* **2013,** *7,* 8924–8931. doi:10.1021/nn4034019

150. Zhou, H.; Yu, W. J.; Liu, L.; Cheng, R.; Chen, Y.; Huang, X.; Liu, Y.; Wang, Y.; Huang, Y.; Duan, X. *Nat. Commun.* **2013,** *4,* 2096. doi:10.1038/ncomms3096

151. Gan, L.; Luo, Z. *ACS Nano* **2013,** *7,* 9480–9488. doi:10.1021/nn404393b

152. Hao, Y.; Bharathi, M. S.; Wang, L.; Liu, Y.; Chen, H.; Nie, S.; Wang, X.; Chou, H.; Tan, C.; Fallahazad, B.; Ramanarayan, H.; Magnuson, C. W.; Tutuc, E.; Yakobson, B. I.; McCarty, K. F.; Zhang, Y.-W.; Kim, P.; Hone, J.; Colombo, L.; Ruoff, R. S. *Science* **2013,** *342,* 720–723. doi:10.1126/science.1243879

153. Friedrichs, P.; Kimoto, T.; Ley, L.; Pensl, G. *Silicon Carbide;* Wiley-VCH, 2011.

154. Saddow, S.; Agarwal, A. *Advances in Silicon Carbide Processing and Applications;* Artech House, Inc.: Norwood, 2004.

155. Schardt, J.; Bernhardt, J.; Starke, U.; Heinz, K. *Surf. Rev. Lett.* **1998,** *5,* 181–186. doi:10.1142/S0218625X98000347

156. Luo, X.; Goel, S.; Reuben, R. L. *J. Eur. Ceram. Soc.* **2012,** *32,* 3423–3434. doi:10.1016/j.jeurceramsoc.2012.04.016

157. Forbeaux, I.; Themlin, J.-M.; Charrier, A.; Thibaudau, F.; Debever, J.-M. *Appl. Surf. Sci.* **2000,** *162–163,* 406–412. doi:10.1016/S0169-4332(00)00224-5

158. Van Bommel, A. J.; Crombeen, J. E.; Van Tooren, A. *Surf. Sci.* **1975,** *48,* 463–472. doi:10.1016/0039-6028(75)90419-7

159. Berger, C.; Song, Z.; Li, T.; Li, X.; Ogbazghi, A. Y.; Feng, R.; Dai, Z.; Marchenkov, A. N.; Conrad, E. H.; First, P. N.; de Heer, W. A. *J. Phys. Chem. B* **2004,** *108,* 19912–19916. doi:10.1021/jp040650f

160. Norimatsu, W.; Kusunoki, M. *Phys. Chem. Chem. Phys.* **2014,** *16,* 3501–3511. doi:10.1039/c3cp54523g

161. Ouerghi, A.; Marangolo, M.; Belkhou, R.; El Moussaoui, S.; Silly, M. G.; Eddrief, M.; Largeau, L.; Portail, M.; Fain, B.; Sirotti, F. *Phys. Rev. B: Condens. Matter Mater. Phys.* **2010,** *82,* 125445. doi:10.1103/PhysRevB.82.125445

162. Abe, S.; Handa, H.; Takahashi, R.; Imaizumi, K.; Fukidome, H.; Suemitsu, M. *Nanoscale Res. Lett.* **2010,** *5,* 1888–1891. doi:10.1007/s11671-010-9731-x

163. Starke, U.; Schardt, J.; Bernhardt, J.; Franke, M.; Heinz, K. *Phys. Rev. Lett.* **1999,** *82,* 2107–2110. doi:10.1103/PhysRevLett.82.2107

164. Gupta, B.; Notarianni, M.; Mishra, N.; Shafiei, M.; Iacopi, F.; Motta, N. *Carbon* **2014,** *68,* 563–572. doi:10.1016/j.carbon.2013.11.035

165. Emtsev, K. V.; Speck, F.; Seyller, T.; Ley, L.; Riley, J. D. *Phys. Rev. B* **2008,** *77,* 155303. doi:10.1103/PhysRevB.77.155303

166. Starke, U.; Bram, C.; Steiner, P.-R.; Hartner, W.; Hammer, L.; Heinz, K.; Müller, K. *Appl. Surf. Sci.* **1995,** *89,* 175–185. doi:10.1016/0169-4332(95)00024-0

167. Emtsev, K. V.; Bostwick, A.; Horn, K.; Jobst, J.; Kellogg, G. L.; Ley, L.; McChesney, J. L.; Ohta, T.; Reshanov, S. A.; Röhrl, J.; Rotenberg, E.; Schmid, A. K.; Waldmann, D.; Weber, H. B.; Seyller, T. *Nat. Mater.* **2009,** *8,* 203–207. doi:10.1038/nmat2382

168. Virojanadara, C.; Syväjarvi, M.; Yakimova, R.; Johansson, L. I.; Zakharov, A. A.; Balasubramanian, T. *Phys. Rev. B* **2008,** *78,* 245403. doi:10.1103/PhysRevB.78.245403

169. Tromp, R. M.; Hannon, J. B. *Phys. Rev. Lett.* **2009,** *102,* 106104. doi:10.1103/PhysRevLett.102.106104

170. Norimatsu, W.; Kusunoki, M. *Chem. Phys. Lett.* **2009,** *468,* 52–56. doi:10.1016/j.cplett.2008.11.095

171. Kuroki, J.; Norimatsu, W.; Kusunoki, M. *e-J. Surf. Sci. Nanotechnol.* **2012,** *10,* 396–399. doi:10.1380/ejssnt.2012.396

172. Berger, C.; Song, Z.; Li, X.; Wu, X.; Brown, N.; Naud, C.; Mayou, D.; Li, T.; Hass, J.; Marchenkov, A. N.; Conrad, E. H.; First, P. N.; de Heer, W. A. *Science* **2006,** *312,* 1191–1196. doi:10.1126/science.1125925

173. Avouris, P.; Xia, F. *MRS Bull.* **2012,** *37,* 1225–1234. doi:10.1557/mrs.2012.206

174. Lin, Y.-M.; Valdes-Garcia, A.; Han, S.-J.; Farmer, D. B.; Meric, I.; Sun, Y.; Wu, Y.; Dimitrakopoulos, C.; Grill, A.; Avouris, P.; Jenkins, K. A. *Science* **2011,** *332,* 1294–1297. doi:10.1126/science.1204428

175. Powell, C.; Bender, T.; Lawryshyn, Y. *Sol. Energy* **2009,** *83,* 1977–1984. doi:10.1016/j.solener.2009.07.009

176. Kalowekamo, J.; Baker, E. *Sol. Energy* **2009,** *83,* 1224–1231. doi:10.1016/j.solener.2009.02.003

177. Krebs, F. C. *Sol. Energy Mater. Sol. Cells* **2009,** *93,* 394–412. doi:10.1016/j.solmat.2008.10.004

178. Kippelen, B.; Brédas, J.-L. *Energy Environ. Sci.* **2009,** *2,* 251–261. doi:10.1039/b812502n

179. Heliatek. Heliatek consolidates technology leadership by establishing a new world record for organic solar technology with a cell efficiency of 12% (press release). http://www.heliatek.com/en/press/press-releases/details/heliatek-cons olidates-its-technology-leadership-by-establishing-a-new-world-record -for-organic-solar-technology-with-a-cell-effi (accessed Dec 29, 2015).

180. Best Reserach-Cell Efficiencies. http://www.nrel.gov/ncpv/images/efficiency_chart.jpg (accessed Dec 14, 2015).

181. Dennler, G.; Scharber, M. C.; Brabec, C. J. *Adv. Mater.* **2009,** *21,* 1323–1338. doi:10.1002/adma.200801283

182. Jørgensen, M.; Norrman, K.; Krebs, F. C. *Sol. Energy Mater. Sol. Cells* **2008,** *92,* 686–714. doi:10.1016/j.solmat.2008.01.005

183. Brabec, C. J.; Durrant, J. R. *MRS Bull.* **2008,** *33,* 670–675. doi:10.1557/mrs2008.138

184. Mihailetchi, V. D.; Koster, L. J. A.; Blom, P. W. M.; Melzer, C.; de Boer, B.; van Duren, J. K. J.; Janssen, R. A. J. *Adv. Funct. Mater.* **2005,** *15,* 795–801. doi:10.1002/adfm.200400345

185. Erb, T.; Zhokhavets, U.; Gobsch, G.; Raleva, S.; Stühn, B.; Schilinsky, P.; Waldauf, C.; Brabec, C. J. *Adv. Funct. Mater.* **2005,** *15,* 1193–1196. doi:10.1002/adfm.200400521

186. Guo, H.; Sreekumar, T. V.; Liu, T.; Minus, M.; Kumar, S. *Polymer* **2005,** *46,* 3001–3005. doi:10.1016/j.polymer.2005.02.013

187. Sariciftci, N. S.; Smilowitz, L.; Heeger, A. J.; Wudl, F. *Science* **1992,** *258,* 1474–1476. doi:10.1126/science.258.5087.1474

188. Umnov, A. G.; Korovyanko, O. J. *Appl. Phys. Lett.* **2005,** *87,* 113506. doi:10.1063/1.2048817

189. Krebs, F. C. *Polymeric Solar Cells: Materials, Design, Manufacture;* DEStech Publications, Inc.: Lancaster, Pennsylvania, USA, 2010.

190. Nunzi, J.-M. *C. R. Phys.* **2002,** *3,* 523–542. doi:10.1016/S1631-0705(02)01335-X

191. Halls, J. J. M.; Pichler, K.; Friend, R. H.; Moratti, S. C.; Holmes, A. B. *Appl. Phys. Lett.* **1996,** *68,* 3120–3122. doi:10.1063/1.115797

192. Theander, M.; Yartsev, A.; Zigmantas, D.; Sundström, V.; Mammo, W.; Andersson, M. R.; Inganäs, O. *Phys. Rev. B* **2000,** *61,* 12957–12963. doi:10.1103/PhysRevB.61.12957

193. Pivrikas, A.; Neugebauer, H.; Sariciftci, N. S. *Sol. Energy* **2011,** *85,* 1226–1237. doi:10.1016/j.solener.2010.10.012

194. Watkins, P. K.; Walker, A. B.; Verschoor, G. L. B. *Nano Lett.* **2005,** *5,* 1814–1818. doi:10.1021/nl051098o

195. Su, Y.-W.; Lan, S.-C.; Wei, K.-H. *Mater. Today* **2012,** *15,* 554–562. doi:10.1016/S1369-7021(13)70013-0

196. Tao, C.; Aljada, M.; Shaw, P. E.; Lee, K. H.; Cavaye, H.; Balfour, M. N.; Borthwick, R. J.; James, M.; Burn, P. L.; Gentle, I. R.; Meredith, P. *Adv. Energy Mater.* **2013,** *3,* 105–112. doi:10.1002/aenm.201200394

197. Lee, K. H.; Schwenn, P. E.; Smith, A. R. G.; Cavaye, H.; Shaw, P. E.; James, M.; Krueger, K. B.; Gentle, I. R.; Meredith, P.; Burn, P. L. *Adv. Mater.* **2011,** *23,* 766–770. doi:10.1002/adma.201003545

198. Seemann, A.; Sauermann, T.; Lungenschmied, C.; Armbruster, O.; Bauer, S.; Egelhaaf, H.-J.; Hauch, J. *Sol. Energy* **2011,** *85,* 1238–1249. doi:10.1016/j.solener.2010.09.007

199. Nelson, J. *Mater. Today* **2011,** *14,* 462–470. doi:10.1016/S1369-7021(11)70210-3

200. Bindl, D. J.; Wu, M.-Y.; Prehn, F. C.; Arnold, M. S. *Nano Lett.* **2011,** *11,* 455–460. doi:10.1021/nl1031343

201. Hau, S. K.; Yip, H.-L.; Jen, A. K.-Y. *Polym. Rev.* **2010,** *50,* 474–510. doi:10.1080/15583724.2010.515764

202. Notarianni, M.; Vernon, K.; Chou, A.; Aljada, M.; Liu, J.; Motta, N. *Sol. Energy* **2013,** *106,* 23–37. doi:10.1016/j.solener.2013.09.026

203. McEvoy, A.; Castaner, L.; Markvart, T. *Solar Cells: Materials, Manufacture and Operation;* Academic Press: UK, 2013.

204. Miller, B.; Rosamilia, J. M.; Dabbagh, G.; Tycko, R.; Haddon, R. C.; Muller, A. J.; Wilson, W.; Murphy, D. W.; Hebard, A. F. *J. Am. Chem. Soc.* **1991,** *113,* 6291–6293. doi:10.1021/ja00016a067

205. Sariciftci, N. S.; Braun, D.; Zhang, C.; Srdanov, V. I.; Heeger, A. J.; Stucky, G.; Wudl, F. *Appl. Phys. Lett.* **1993,** *75,* 585–587. doi:10.1063/1.108863

206. Dang, M. T.; Hirsch, L.; Wantz, G. *Adv. Mater.* **2011,** *23,* 3597–3602. doi:10.1002/adma.201100792

207. Wienk, M. M.; Kroon, J. M.; Verhees, W. J. H.; Knol, J.; Hummelen, J. C.; van Hal, P. A.; Janssen, R. A. J. *Angew. Chem.* **2003,** *42,* 3371–3375. doi:10.1002/anie.200351647

208. Liang, Y.; Xu, Z.; Xia, J.; Tsai, S.-T.; Wu, Y.; Li, G.; Ray, C.; Yu, L. *Adv. Mater.* **2010,** *22,* E135–E138. doi:10.1002/adma.200903528

209. Nierengarten, J.-F. *New J. Chem.* **2004,** *28,* 1177–1191. doi:10.1039/b402661f

210. Sgobba, V.; Guldi, D. M. *J. Mater. Chem.* **2008,** *18,* 153–157. doi:10.1039/B713798M

211. Ren, S.; Bernardi, M.; Lunt, R. R.; Bulovic, V.; Grossman, J. C.; Gradečak, S. *Nano Lett.* **2011,** *11,* 5316–5321. doi:10.1021/nl202796u

212. Lu, L.; Xu, T.; Chen, W.; Lee, J. M.; Luo, Z.; Jung, I. H.; Park, H. I.; Kim, S. O.; Yu, L. *Nano Lett.* **2013,** *13,* 2365–2369. doi:10.1021/nl304533j

213. Bernardi, M.; Giulianini, M.; Grossman, J. C. *ACS Nano* **2010,** *4,* 6599–6606. doi:10.1021/nn1018297

214. Caddeo, C.; Melis, C.; Colombo, L.; Mattoni, A. *J. Phys. Chem. C* **2010,** *114,* 21109–21113. doi:10.1021/jp107370v

215. Giulianini, M.; Waclawik, E. R.; Bell, J. M.; De Crescenzi, M.; Castrucci, P.; Scarselli, M.; Diociauti, M.; Casciardi, S.; Motta, N. *J. Phys. Chem. C* **2011,** *115,* 6324–6330. doi:10.1021/jp2000267

216. Kanai, Y.; Grossman, J. C. *Nano Lett.* **2008,** *8,* 908–912. doi:10.1021/nl0732777

217. Liu, L.; Stanchina, W. E.; Li, G. *Appl. Phys. Lett.* **2009,** *94,* 233309. doi:10.1063/1.3153514

218. Giulianini, M.; Waclawik, E. R.; Bell, J. M.; Scarselli, M.; Castrucci, P.; De Crescenzi, M.; Motta, N. *Appl. Phys. Lett.* **2009,** *95,* 143116. doi:10.1063/1.3241998

219. Schuettfort, T.; Nish, A.; Nicholas, R. J. *Nano Lett.* **2009,** *9,* 3871–3876. doi:10.1021/nl902081t

220. Dabera, G. D. M. R.; Jayawardena, K. D. G. I.; Prabhath, M. R. R.; Yahya, I.; Tan, Y. Y.; Nismy, N. A.; Shiozawa, H.; Sauer, M.; Ruiz-Soria, G.; Ayala, P.; Stolojan, V.; Adikaari, A. A. D. T.; Jarowski, P. D.; Pichler, T.; Silva, S. R. P. *ACS Nano* **2012,** *7,* 556–565. doi:10.1021/nn304705t

221. Vavro, J.; Llaguno, M. C.; Fischer, J. E.; Ramesh, S.; Saini, R. K.; Ericson, L. M.; Davis, V. A.; Hauge, R. H.; Pasquali, M.; Smalley, R. E. *Phys. Rev. Lett.* **2003,** *90,* 065503. doi:10.1103/PhysRevLett.90.065503

222. Jeong, H.; Park, J.-Y. *J. Phys. Chem. C* **2015,** *119,* 9665–9668. doi:10.1021/acs.jpcc.5b02633

223. Kim, S.; Yim, J.; Wang, X.; Bradley, D. D. C.; Lee, S.; deMello, J. C. *Adv. Funct. Mater.* **2010,** *20,* 2310–2316. doi:10.1002/adfm.200902369

224. Kymakis, E.; Stylianakis, M. M.; Spyropoulos, G. D.; Stratakis, E.; Koudoumas, E.; Fotakis, C. *Sol. Energy Mater. Sol. Cells* **2012,** *96,* 298–301. doi:10.1016/j.solmat.2011.09.046

225. Jung, Y.; Li, X.; Rajan, N. K.; Taylor, A. D.; Reed, M. A. *Nano Lett.* **2013,** *13,* 95–99. doi:10.1021/nl3035652

226. Wang, F.; Kozawa, D.; Miyauchi, Y.; Hiraoka, K.; Mouri, S.; Ohno, Y.; Matsuda, K. *Nat. Commun.* **2015,** *6,* 6305. doi:10.1038/ncomms7305

227. Capasso, A.; Salamandra, L.; Di Carlo, A.; Bell, J. M.; Motta, N. *Beilstein J. Nanotechnol.* **2012,** *3,* 524–532. doi:10.3762/bjnano.3.60

228. Miller, A. J.; Hatton, R. A.; Chen, G. Y.; Silva, S. R. P. *Appl. Phys. Lett.* **2007,** *90,* 023105. doi:10.1063/1.2431437

229. Capasso, A.; Salamandra, L.; Chou, A.; Di Carlo, A.; Motta, N. *Sol. Energy Mater. Sol. Cells* **2014,** *122,* 297–302. doi:10.1016/j.solmat.2013.10.022

230. Sears, K.; Fanchini, G.; Watkins, S. E.; Huynh, C. P.; Hawkins, S. C. *Thin Solid Films* **2013,** *531,* 525–529. doi:10.1016/j.tsf.2013.01.018

231. Mirri, F.; Ma, A. W. K.; Hsu, T. T.; Behabtu, N.; Eichmann, S. L.; Young, C. C.; Tsentalovich, D. E.; Pasquali, M. *ACS Nano* **2012,** *6,* 9737–9744. doi:10.1021/nn303201g

232. Kim, K.; Bae, S.-H.; Toh, C. T.; Kim, H.; Cho, J. H.; Whang, D.; Lee, T.-W.; Özyilmaz, B.; Ahn, J.-H. *ACS Appl. Mater. Interfaces* **2014,** *6,* 3299–3304. doi:10.1021/am405270y

233. Sangchul, L.; Jun-Seok, Y.; Yongsung, J.; Chunhum, C.; Dong-Yu, K.; Seok-In, N.; Byoung Hun, L.; Takhee, L. *Nanotechnology* **2012,** *23,* 344013. doi:10.1088/0957-4484/23/34/344013

234. Bonaccorso, F.; Sun, Z.; Hasan, T.; Ferrari, A. C. *Nat. Photonics* **2010,** *4,* 611–622. doi:10.1038/nphoton.2010.186

235. Liscio, A.; Veronese, G. P.; Treossi, E.; Suriano, F.; Rossella, F.; Bellani, V.; Rizzoli, R.; Samori, P.; Palermo, V. *J. Mater. Chem.* **2011,** *21,* 2924–2931. doi:10.1039/c0jm02940h

236. Stylianakis, M. M.; Stratakis, E.; Koudoumas, E.; Kymakis, E.; Anastasiadis, S. H. *ACS Appl. Mater. Interfaces* **2012,** *4,* 4864–4870. doi:10.1021/am301204g

237. Wang, J.; Wang, Y.; He, D.; Liu, Z.; Wu, H.; Wang, H.; Zhao, Y.; Zhang, H.; Yang, B. *Synth. Met.* **2010,** *160,* 2494–2500. doi:10.1016/j.synthmet.2010.09.033

238. Liu, J.; Xue, Y.; Gao, Y.; Yu, D.; Durstock, M.; Dai, L. *Adv. Mater.* **2012,** *24,* 2228–2233. doi:10.1002/adma.201104945

239. Ryu, M. S.; Jang, J. *Sol. Energy Mater. Sol. Cells* **2011,** *95,* 2893–2896. doi:10.1016/j.solmat.2011.06.008

240. Li, S.-S.; Tu, K.-H.; Lin, C.-C.; Chen, C.-W.; Chhowalla, M. *ACS Nano* **2010,** *4,* 3169–3174. doi:10.1021/nn100551j

241. Liu, J.; Durstock, M.; Dai, L. *Energy Environ. Sci.* **2014,** *7,* 1297–1306. doi:10.1039/C3EE42963F

242. Kim, J.; Tung, V. C.; Huang, J. *Adv. Energy Mater.* **2011,** *1,* 1052–1057. doi:10.1002/aenm.201100466

243. Bernardi, M.; Lohrman, J.; Kumar, P. V.; Kirkeminde, A.; Ferralis, N.; Grossman, J. C.; Ren, S. *ACS Nano* **2012,** *6,* 8896–8903. doi:10.1021/nn302893p

244. Design and Fabrication of the First All-Carbon-Based Solar Cell. http://web.stanford.edu/group/gcep/cgi-bin/gcep-research/all/design-and-fabrication-of-the-first-all-carbon-based-solar-cell/ (accessed Dec 14, 2015).

245. Ramuz, M. P.; Vosgueritchian, M.; Wei, P.; Wang, C.; Gao, Y.; Wu, Y.; Chen, Y.; Bao, Z. *ACS Nano* **2012,** *6,* 10384–10395. doi:10.1021/nn304410w

246. Ameri, T.; Dennler, G.; Lungenschmied, C.; Brabec, C. J. *Energy Environ. Sci.* **2009,** *2,* 347–363. doi:10.1039/b817952b

247. Li, X.; Zhu, H.; Wang, K.; Cao, A.; Wei, J.; Li, C.; Jia, Y.; Li, Z.; Li, X.; Wu, D. *Adv. Mater.* **2010,** *22,* 2743–2748. doi:10.1002/adma.200904383

248. Miao, X.; Tongay, S.; Petterson, M. K.; Berke, K.; Rinzler, A. G.; Appleton, B. R.; Hebard, A. F. *Nano Lett.* **2012,** *12,* 2745–2750. doi:10.1021/nl204414u

249. Shi, E.; Li, H.; Yang, L.; Zhang, L.; Li, Z.; Li, P.; Shang, Y.; Wu, S.; Li, X.; Wei, J.; Wang, K.; Zhu, H.; Wu, D.; Fang, Y.; Cao, A. *Nano Lett.* **2013,** *13,* 1776–1781. doi:10.1021/nl400353f

250. Roy-Mayhew, J. D.; Aksay, I. A. *Chem. Rev.* **2014,** *114,* 6323–6348. doi:10.1021/cr400412a

251. Wang, H.; Hu, Y. H. *Energy Environ. Sci.* **2012,** *5,* 8182–8188. doi:10.1039/c2ee21905k

252. Wang, X.; Zhi, L.; Müllen, K. *Nano Lett.* **2008,** *8,* 323–327. doi:10.1021/nl072838r

253. Lu, M.; Beguin, F.; Frackowiak, E. *Supercapacitors;* Wiley-VCH, 2013.

254. Becker, H. E. Low voltage electrolytic capacitor. U. S. Patent 2800616, 1957.

255. Boos, D. I. Electrolytic capacitor having carbon paste electrodes. U.S. Patent 3536963, 1970.

256. Murphy, T. C.; Wright, R. B.; Sutula, R. A. US Department of Energy Electrochemical Capacitor Devlopment and Testing Activities. In *Proceedings of the Symposium on Electrochemical Capacitors II;* Delnick, F. M.; Ingersoll, D.; Andrieu, X.; Naoi, K., Eds.; The Electrochemical Society, Inc.: Pennington, NJ, 1997; p 258.

257. Electrochemical Double Layer Capacitors (Supercapacitors). http://large.stanford.edu/courses/2012/ph240/aslani1/ (accessed Sept 9, 2015).

258. Gobert, Y. Volvo develops batteries (supercapacitors) integrated with body panels. http://www.technologicvehicles.com/en/green-transportation-news/2597/video-volvo-develops-batteries-supercapacitors-integrated-with-body-panels (accessed Dec 12, 2015).

259. Elcap Supercapacitor. Wikipedia http://en.wikipedia.org/wiki/Supercapacitor (accessed Dec 12, 2015).

260. Conway, B. E. *Electrohcemical Supercapacitors;* Plenum Publishing: New York, 1999.

261. Helmholtz, H. V. *Ann. Phys. (Berlin, Ger.)* **1853,** *89,* 21.

262. Gouy, G. *J. Phys. Theor. Appl.* **1910,** *9,* 457–468. doi:10.1051/jphystap:019100090045700

263. Chapman, D. L. *Philos. Mag.* **1913,** *25,* 475–481. doi:10.1080/14786440408634187

264. Stern, O. *Z. Elektrochem. Angew. Phys. Chem.* **1924,** *30,* 508–516. doi:10.1002/bbpc.192400182

265. Zhang, L. L.; Zhao, X. S. *Chem. Soc. Rev.* **2009,** *38,* 2520–2531. doi:10.1039/b813846j

266. Kötz, R.; Carlen, M. *Electrochim. Acta* **2000,** *45,* 2483–2498. doi:10.1016/S0013-4686(00)00354-6

267. Zhang, K.; Zhang, L. L.; Zhao, X. S.; Wu, J. *Chem. Mater.* **2010,** *22,* 1392–1401. doi:10.1021/cm902876u

268. Sugimoto, W.; Yokoshima, K.; Murakami, Y.; Takasu, Y. *Electrochim. Acta* **2006,** *52,* 1742–1748. doi:10.1016/j.electacta.2006.02.054

269. Wang, J. *Analytical Electrochemistry,* 3rd ed.; Wiley-VCH: Hoboken, New Jersey, 2006. doi:10.1002/0471790303

270. Pell, W. G.; Conway, B. E. *J. Power Sources* **2001,** *96,* 57–67. doi:10.1016/S0378-7753(00)00682-0

271. Qu, D.; Shi, H. *J. Power Sources* **1998,** *74,* 99–107. doi:10.1016/S0378-7753(98)00038-X

272. Raymundo-Piñero, E.; Kierzek, K.; Machnikowski, J.; Béguin, F. *Carbon* **2006,** *44,* 2498–2507. doi:10.1016/j.carbon.2006.05.022

273. Kierzek, K.; Frackowiak, E.; Lota, G.; Gryglewicz, G.; Machnikowski, J. *Electrochim. Acta* **2004,** *49,* 515–523. doi:10.1016/j.electacta.2003.08.026

274. Bose, S.; Kuila, T.; Mishra, A. K.; Rajasekar, R.; Kim, N. H.; Lee, J. H. *J. Mater. Chem.* **2012,** *22,* 767–784. doi:10.1039/C1JM14468E

275. Candelaria, S. L.; Shao, Y.; Zhou, W.; Li, X.; Xiao, J.; Zhang, J.-G.; Wang, Y.; Liu, J.; Li, J.; Cao, G. *Nano Energy* **2012,** *1,* 195–220. doi:10.1016/j.nanoen.2011.11.006

276. Yu, A. *Electrochemical Energy Storage and Conversion: Electrochemical Supercapacitors for Energy Storage and Delivery: Fundamentals and Applications;* CRC Press, 2013.

277. Azam, M. A.; Fujiwara, A.; Shimoda, T. *Int. J. Electrochem. Sci.* **2013,** *8,* 3902–3911.

278. Du, C.; Yeh, J.; Pan, N. *Nanotechnology* **2005,** *16,* 350. doi:10.1088/0957-4484/16/4/003

279. Zhang, H.; Cao, G.; Yang, Y.; Gu, Z. *J. Electrochem. Soc.* **2008,** *155,* K19–K22. doi:10.1149/1.2811864

280. Liu, C.; Li, F.; Ma, L.-P.; Cheng, H.-M. *Adv. Mater.* **2010,** *22,* E28–E62. doi:10.1002/adma.200903328

281. Inagaki, M.; Konno, H.; Tanaike, O. *J. Power Sources* **2010,** *195,* 7880–7903. doi:10.1016/j.jpowsour.2010.06.036

282. Niu, C.; Sichel, E. K.; Hoch, R.; Moy, D.; Tennent, H. *Appl. Phys. Lett.* **1997,** *70,* 1480–1482. doi:10.1063/1.118568

283. Emmenegger, C.; Mauron, P.; Sudan, P.; Wenger, P.; Hermann, V.; Gallay, R.; Züttel, A. *J. Power Sources* **2003,** *124,* 321–329. doi:10.1016/S0378-7753(03)00590-1

284. Yamada, Y.; Kimizuka, O.; Tanaike, O.; Machida, K.; Suematsu, S.; Tamamitsu, K.; Saeki, S.; Yamada, Y.; Hatori, H. *Electrochem. Solid-State Lett.* **2009,** *12,* K14–K16. doi:10.1149/1.3059010

285. Liu, C. G.; Fang, H. T.; Li, F.; Liu, M.; Cheng, H. M. *J. Power Sources* **2006,** *160,* 758–761. doi:10.1016/j.jpowsour.2006.01.072

286. Tanaike, O.; Futaba, D. N.; Hata, K.; Hatori, H. *Carbon Lett.* **2009,** *10,* 90–93. doi:10.5714/CL.2009.10.2.090

287. Hiraoka, T.; Izadi-Najafabadi, A.; Yamada, T.; Futaba, D. N.; Yasuda, S.; Tanaike, O.; Hatori, H.; Yumura, M.; Iijima, S.; Hata, K. *Adv. Funct. Mater.* **2010,** *20,* 422–428. doi:10.1002/adfm.200901927

288. Futaba, D. N.; Hata, K.; Yamada, T.; Hiraoka, T.; Hayamizu, Y.; Kakudate, Y.; Tanaike, O.; Hatori, H.; Yumura, M.; Iijima, S. *Nat. Mater.* **2006,** *5,* 987–994. doi:10.1038/nmat1782

289. Bordjiba, T.; Mohamedi, M.; Dao, L. H. *Adv. Mater.* **2008,** *20,* 815–819. doi:10.1002/adma.200701498

290. Huang, Y.; Liang, J.; Chen, Y. *Small* **2012,** *8,* 1805–1834. doi:10.1002/smll.201102635

291. Wang, Y.; Shi, Z.; Huang, Y.; Ma, Y.; Wang, C.; Chen, M.; Chen, Y. *J. Phys. Chem. C* **2009,** *113,* 13103–13107. doi:10.1021/jp902214f

292. Chen, Y.; Zhang, X.; Zhang, D.; Yu, P.; Ma, Y. *Carbon* **2011,** *49,* 573–580. doi:10.1016/j.carbon.2010.09.060

293. Lv, W.; Tang, D.-M.; He, Y.-B.; You, C.-H.; Shi, Z.-Q.; Chen, X.-C.; Chen, C.-M.; Hou, P.-X.; Liu, C.; Yang, Q.-H. *ACS Nano* **2009,** *3,* 3730–3736. doi:10.1021/nn900933u

294. El-Kady, M. F.; Strong, V.; Dubin, S.; Kaner, R. B. *Science* **2012,** *335,* 1326–1330. doi:10.1126/science.1216744

295. El-Kady, M. F.; Kaner, R. B. *Nat. Commun.* **2013,** *4,* No. 1475. doi:10.1038/ncomms2446

296. Xu, Y.; Lin, Z.; Huang, X.; Liu, Y.; Huang, Y.; Duan, X. *ACS Nano* **2013,** *7,* 4042–4049. doi:10.1021/nn4000836

297. Wu, Z.-S.; Winter, A.; Chen, L.; Sun, Y.; Turchanin, A.; Feng, X.; Müllen, K. *Adv. Mater.* **2012,** *24,* 5130–5135. doi:10.1002/adma.201201948

298. Zhang, L.; Shi, G. *J. Phys. Chem. C* **2011,** *115,* 17206–17212. doi:10.1021/jp204036a

299. Chen, J.; Sheng, K.; Luo, P.; Li, C.; Shi, G. *Adv. Mater.* **2012,** *24,* 4569–4573. doi:10.1002/adma.201201978

300. Notarianni, M.; Liu, J.; Mirri, F.; Pasquali, M.; Motta, N. *Nanotechnology* **2014,** *25,* 435405. doi:10.1088/0957-4484/25/43/435405

301. Liu, J.; Mirri, F.; Notarianni, M.; Pasquali, M.; Motta, N. *J. Power Sources* **2015,** *274,* 823–830. doi:10.1016/j.jpowsour.2014.10.104

302. Zhu, Y.; Li, L.; Zhang, C.; Casillas, G.; Sun, Z.; Yan, Z.; Ruan, G.; Peng, Z.; Raji, A.-R. O.; Kittrell, C.; Hauge, R. H.; Tour, J. M. *Nat. Commun.* **2012,** *3,* No. 1225. doi:10.1038/ncomms2234

303. Aboutalebi, S. H.; Chidembo, A. T.; Salari, M.; Konstantinov, K.; Wexler, D.; Liu, H. K.; Dou, S. X. *Energy Environ. Sci.* **2011,** *4,* 1855–1865. doi:10.1039/c1ee01039e

304. Jha, N.; Ramesh, P.; Bekyarova, E.; Itkis, M. E.; Haddon, R. C. *Adv. Energy Mater.* **2012,** *2,* 438–444. doi:10.1002/aenm.201100697

305. Fan, Z.; Yan, J.; Zhi, L.; Zhang, Q.; Wei, T.; Feng, J.; Zhang, M.; Qian, W.; Wei, F. *Adv. Mater.* **2010,** *22,* 3723–3728. doi:10.1002/adma.201001029

306. Yu, D.; Dai, L. *J. Phys. Chem. Lett.* **2010,** *1,* 467–470. doi:10.1021/jz9003137

307. Wee, G.; Salim, T.; Lam, Y. M.; Mhaisalkar, S. G.; Srinivasan, M. *Energy Environ. Sci.* **2011,** *4,* 413–416. doi:10.1039/C0EE00296H